Author:
Wheeler, Martyn David

Title:
Two novel laser-based techniques for molecular spectroscopy.

Two Novel Laser-Based Techniques for Molecular Spectroscopy

A thesis submitted to the University of Bristol in accordance with the requirement of the degree of Doctor of Philosophy in the Department of Chemistry, Faculty of Science.

Martyn David Wheeler,

November 1997.

Authors Declaration

The work described in this thesis was carried out in the Department of Chemistry, University of Bristol between October 1993 and November 1997 under the supervision of Professor M.N.R. Ashfold.

The work is original except where acknowledgement to other work is made and it has not been submitted for any other degree.

M.D. Wheeler, November 1997.

Acknowledgements

I would like to take this opportunity to thank the people that have enabled me to achieve this work:

Prof. Mike Ashfold and Dr. Andrew Orr-Ewing for their endless patience, support, and motivation throughout the course of my Ph.D. studies.

My family and Vicky for always being there to provide constant encouragement.

Stu Newman for all of his help with the CRDS experiment. Dr. Colin Western for many helpful discussions and the use of his computer programs. Keith Rosser for helping to maintain the experiments. Prof. Rob Le Roy for his invaluable advice and making available his computer programs BCONT, LEVEL, and RKR1. Dr. Ian Lambert for the many wake-up calls and his help with the TC-LIGS work. Dr. Gabriel Balint-Kurti for his help with using Molpro 96. Professors Masahiro Kawasaki and Takashi Ishiwata for their highly fruitful collaborative visits to Bristol.

Carl Otter and Ben Warren for being the most tedious flatmates imaginable (only joking boys....!). Everyone at the Highbury Vaults for all the times I don't remember for some reason. Claire, Liz, Jon, Tom, Bobbins, Jax, James, Ed and many others for all the very happy and rather late nights out.

Finally to everyone that I've worked with in the group over the past few years that have made my time in Bristol a very happy one indeed.

Abstract

Cavity Ring-Down Spectroscopy (CRDS) has been applied to investigate the predissociation mechanisms occurring in SH ($A^2\Sigma^+$), SD ($A^2\Sigma^+$), S_2 ($B^3\Sigma_u^-$) and BrO ($A^2\Pi_{3/2}$).

Spectra were recorded of the A-X (1,0) band of SH and the (1,0), (2,0) bands of SD. Linewidth measurements of transitions to individual rovibrational levels of the A state revealed increasing predissociation rates with vibrational and rotational quantum number. These and all other available data have been reproduced, quantitatively, by Fermi Golden Rule calculations employing the best (experimentally determined) analytic potential for the A state and *ab initio* repulsive potentials and spin-orbit coupling matrix elements.

The experimental spectra of the S_2 $B^3\Sigma_u^-$-$X^3\Sigma_g^-$ (v',0) bands for $10 \leq v' \leq 22$ span the wavenumber range 35480 - 39860 cm^{-1}. Extensive variation is observed in the degree of rotational structure within the vibrational bands because of lifetime broadening caused by predissociation. Fits to the band contours give homogeneous linewidths for transitions to the B-state vibrational levels for $10 \leq v' \leq 17$ that vary from $\leq$ 1 cm^{-1} for the (10,0) band to 7 $\pm$1 cm^{-1} for the (17,0) band with a maximum linewidth of 14 $\pm$ 1 cm^{-1} for the (13,0) band. For $v' \geq 18$, all bands are completely diffuse, indicating linewidths in excess of 15 cm^{-1}. The experimental results are compared with the results of a theoretical model that uses an RKR potential for the $B^3\Sigma_u^-$ state, *ab initio* calculations of the repulsive potentials that cross the B state, and Fermi Golden Rule calculations of the predissociation rates for the different repulsive potentials. Minor adjustments to the *ab initio* potentials, and an estimate of the spin-orbit coupling between the bound and repulsive states enables us to calculate predissociation rates in excellent agreement with the experimental observations. We deduce that the predissociation for $v' \leq 16$ is predominantly via a $^1\Pi_u$ state, whereas for $v' \geq 17$, coupling to a second repulsive state, suggested to be either a $^5\Sigma_u^-$ or $^5\Pi_u$ state, provides the primary mechanism for predissociation.

Using CRDS a laser-based detection scheme for BrO has been investigated using the $A^2\Pi_{3/2}$-$X^2\Pi_{3/2}$ transition. Only the (7,0) and (12,0) bands showed any degree of rotational structure due to extensive line broadening caused by predissociation throughout the A-state. Fitting the band contours gave improved spectroscopic constants and linewidths for both the $A^2\Pi_{3/2}$ v'=7 and 12 levels From a knowledge of the reaction conditions it was possible to give an upper estimate of the concentration of BrO radicals within the CRD chamber of 5×10^{12} molecules cm^{-3}.

The technique of Two-Colour Laser-Induced Grating Spectroscopy (TC-LIGS) has been demonstrated using the benchmark molecule I_2. TC-LIGS is used in a folded double resonance excitation scheme to obtain both state selected absorption spectra and SEP-like spectra of the $B(0_u^+)$ - $X(0_g^+)$ transition. Further experiments utilised TC-LIGS in a more traditional double-resonance-like scheme to investigate the high lying $E(0_g^+)$ and $f(0_g^+)$ ion-pair states of I_2 in the two-photon energy range 49100-52700 cm^{-1}.

Contents

Chapter 1: Introduction **1**

1.1. Methods of obtaining diatomic potential energy curves 5

1.1.1. Empirical molecular potential functions 5

1.1.2. Inversion of spectroscopic data 6

1.1.3. *Ab initio* methods 7

1.2. Electronic spectroscopy of diatomic molecules 12

1.2.1. The Hamiltonian for a diatomic molecule 12

1.2.2. Rotational fine structure - Hund's coupling cases 15

1.2.3. Symmetry of diatomic energy levels 18

1.2.4. Selection rules for electronic transitions 20

1.2.5. Spectral lineshapes 22

1.2.6. Perturbations and predissociation 24

1.3. Traditional methods of laser spectroscopy 33

1.3.1. Absorption spectroscopy - the Beer-Lambert law 33

1.3.2. Laser Induced Fluorescence 34

1.3.3. Resonance Enhanced Multi-Photon Ionisation 34

1.3.4. Photoacoustic spectroscopy 35

1.3.5. Intra-Cavity Laser absorption 35

1.3.6. Stimulated Emission Pumping 36

1.4. Overview of this work 37

Chapter 2: Cavity Ring-Down Spectroscopy **40**

2.1. Introduction 40

2.2. Recent applications of CRDS 41

2.3. Fundamentals of CRDS 46

2.3.1. Decay of light in an optical cavity 46

2.3.2. Conditions for recovery of a single exponential decay 48

2.4. Experimental principles 53

Chapter 3: Predissociation of the $A^2\Sigma^+$ state of SH and SD **58**

3.1. Overview 58

3.2. Experimental 64

3.3. Results 67

3.4. Calculations 72

3.5. Discussion 78

3.6. Conclusions 82

Chapter 4: Predissociation of high vibrational levels within the $B^3\Sigma_u^-$ state of S_2 **86**

4.1. Introduction 86

4.2. Experimental 95

4.3. Results 97

4.3.1. S_2 $B^3\Sigma_u^-$ v'=10 97

4.3.2. S_2 $B^3\Sigma_u^-$ v'=11-22 98

4.3.3. Spectroscopic constants 100

4.4. Calculations 103

4.4.1. Determination of S_2 potentials 103

4.4.2. Calculation of predissociation rates 108

4.5. Discussion 113

4.5.1. Mechanism of predissociation 113

4.5.2. Classification of the predissociation 115

4.5.3. Comparison with O_2 and Se_2 115

4.6. Conclusions 118

Chapter 5: CRDS Detection of the $A^2\Pi_{3/2}$-$X^2\Pi_{3/2}$ transition in the BrO radical **123**

5.1. Introduction 123

5.2. Experimental 126

5.3. Results 129

5.4. Discussion 131

5.5. Conclusions 133

Chapter 6: Four-wave mixing spectroscopy of molecular iodine **135**

6.1. Introduction 135

6.1.1. Four-wave mixing spectroscopy 135

6.1.2. Ion-pair states of I_2 140

6.1.3. Overview 141

6.2. Experimental 142

6.3. Results and Discussion 144

6.3.1. TC-LIGS of the I_2 B-X transition 144

6.3.2. Detection of the E and f ion-pairs states of I_2 147

6.4. Conclusions 149

Chapter 7: General Conclusions and Future Work **152**

Appendix 1 **153**

1. Introduction

Spectroscopy is of fundamental importance in many areas of physics and chemistry; it is arguably the most important tool for investigating molecular structure. The study of electronic spectra can provide many key insights into the fundamental electronic structure and nuclear dynamics of molecular systems and has led to an understanding of chemical valence in terms of electron motion around the vibrating-rotating nuclei. For diatomic molecules, which are the main concern of this work, an enormous amount of information may be extracted from a spectrum due to the detailed theoretical understanding of the quantum-mechanical processes associated with the interaction of a molecule with electromagnetic radiation [1,2]. Theoretical methods now exist that allow models to be derived that are capable of rationalising and understanding almost every observed spectral feature [3].

The obvious starting point for any discussion of molecular electronic spectroscopy is the fundamental concept of the *Born-Oppenheimer approximation* [2,3]. The central idea of this approximation is that since the electrons and nuclei experience similar forces within a molecule, then due to their different masses they will travel at very different speeds, thus allowing an effective uncoupling of their relative motions. This uncoupling then makes it possible to write an approximate form of the total wavefunction as the product of two functions,

$$\Psi^{BO} = \Phi_{i,\Lambda,S,\Sigma}(r,R)\chi_{v,J}(R,\theta,\phi) \qquad (1.1)$$

where the first factor is the electronic wavefunction and the second the vibration-rotation wavefunction (the subscripts i, Λ, S, Σ, v, and J, define the electronic, vibrational, and rotational state of the molecule and are discussed further below). R is the internuclear distance, θ and ϕ specify the orientation of the internuclear axis (molecule fixed coordinate system) relative to the laboratory coordinate system (see Figure 1.1), and r represents all of the electron coordinates in the molecule fixed frame.

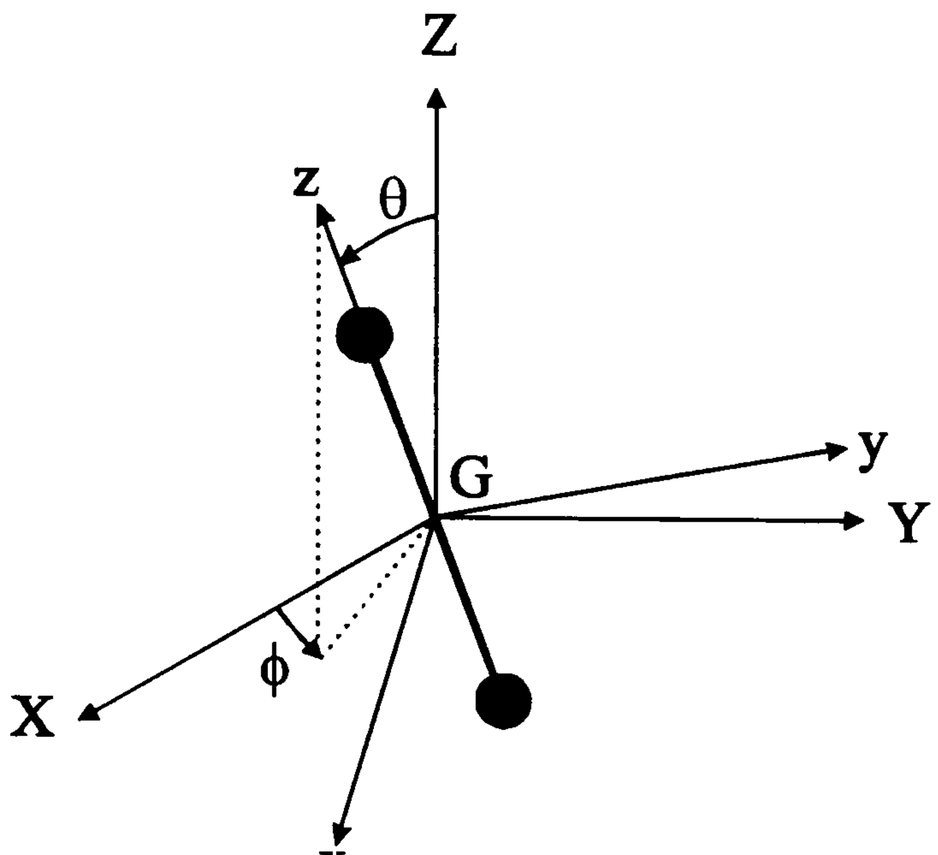

Figure 1.1. Relationship between space- (X,Y,Z) and molecule-fixed (x,y,z) frames of reference where the origin is defined by the centre of gravity, G, of the two atoms separated by a distance R.

As a consequence of the Born-Oppenheimer approximation the electronic structure may be determined by clamping the internuclear separation at fixed values and solving the purely electronic Schrödinger equation

$$\hat{H}^{el}\Phi_{i,\Lambda,S,\Sigma}(r,R) = E_i^{el}(R)\Phi_{i,\Lambda,S,\Sigma}(r,R) \qquad (1.2)$$

This process is repeated for many different values of R thereby mapping out the function $E_i^{el}(R)$ corresponding to the *purely electronic energy* which is related to the electronic energy by the addition of the nuclear-nuclear repulsion term $V_{nn}(R)$ (independent of the electronic coordinates). The function $U_i(R)=E_i^{el}(R) + V_{nn}(R)$ may be viewed as the effective potential governing the motion of the nuclei thus giving rise to the concept of the electronic potential energy curve (or surface). There are many solutions to equation 1.2, each one labelled i corresponding to a particular electronic state of the molecule. Equation (1.2) may be solved approximately by assuming that the electronic wavefunction $\Phi_{i,\Lambda,S,\Sigma}$ is made up of products of functions ϕ_j, which are referred to as molecular orbitals. These molecular orbitals are often pictured in terms of linear combinations of atomic orbitals (LCAO) of the parent atoms. This leads to the description of different molecular electronic states in terms of different electron

configurations within the molecular orbitals, and may be viewed pictorially in terms of a molecular orbital diagram.

Each particular electronic state may be classified in terms of its spin and orbital angular momenta. The important angular momenta associated with a diatomic molecule are listed in Table 1.1. Different molecular electronic states are labelled by a term symbol using the notation $^{2S+1}\Lambda_{\Omega}$.

Angular Momenta	Operator	Total quantum number	Projection of quantum number along internuclear axis
Nuclear framework rotation	$\hat{R}$	R	-
Electron orbital motion	$\hat{L}$	L	Λ
Electron spin	$\hat{S}$	S	Σ
Total angular momentum	$\hat{J} = \hat{R} + \hat{L} + \hat{S}$	J	$\Omega=\Lambda+\Sigma$
Total angular momentum excluding spin	$\hat{N} = \hat{J} - \hat{S}$	N	Λ

Table 1.1. Some of the various angular momenta associated with a diatomic molecule.

Once $U_i(R)$ has been determined it is then possible to use this potential to solve the nuclear Schrödinger equation (1.3) to obtain the rotational and vibrational eigenvalues for the particular electronic state.

$$\left[\hat{T}^N(R,\theta,\phi) + U_i(R)\right]\chi_{v,J} = E^T\chi_{v,J}\,. \qquad (1.3)$$

Here T^N is the nuclear kinetic energy operator and E^T is the total energy of the eigenstate $\chi_{v,J}$. $\chi_{v,J}$ is separable into a product of two functions, one with only radial coordinates (the vibrational wavefunction) and the other with only angular coordinates (the rotational wavefunction). The potential energy curve therefore relates the Schrödinger equation to

molecular spectroscopy, where light provides the measuring device (the operator in quantum mechanical terms) to obtain the expectation values of an ensemble of molecules.

Dunham (1932) [2] showed that the observed rovibrational eigenvalues of a given electronic state could be represented by a simple polynomial function of the rotational and vibrational quantum numbers, J and v.

$$E_{v,J} = \sum_{l,m} Y_{lm}\left(v + \tfrac{1}{2}\right)^{l}\left[J(J+1)\right]^{m} \qquad (1.4)$$

The first few Y_{lm} coefficients may be related to the equilibrium values of the molecular constants, *e.g.*,

$$Y_{10} \approx \omega_e \quad Y_{20} \approx -\omega_e x_e \quad Y_{30} \approx \omega_e y_e$$

$$Y_{01} \approx B_e \quad Y_{11} \approx -\alpha_e \quad Y_{21} \approx \gamma_e \qquad (1.5)$$

$$Y_{02} \approx -D_e \quad Y_{12} \approx -\beta_e$$

These spectroscopic constants provide a convenient and empirical way of organising a large quantity of spectroscopic data assuming a smooth v, J dependence within an electronic state. It must be emphasised, however, that the Dunham expansion has no predictive capability and will prove an inadequate representation if strong perturbations exist within the electronic state causing a rather more erratic v, J dependence.

1.1 Methods of obtaining diatomic potential energy curves

The molecular potential energy curve, although merely a concept derived from a specified set of assumptions, provides a powerful insight into understanding the nuclear dynamics and hence fundamental chemical properties of molecular systems. Therefore because of the central importance of potential energy curves in the modern description of molecular structure much effort has concentrated upon finding reliable methods of determining molecular potential energy functions from spectroscopic data [4] and by theoretical methods [5,6].

1.1.1 Empirical molecular potential functions

Clearly, being able to represent the potential using some analytic function containing only a limited number of parameters would be a very desirable situation from an intuitive perspective; this is especially true if the function is one that allows the Schrödinger equation to be solved exactly to yield the energy levels. One such function was proposed by Morse (1929) [7],

$$E(R) = D_e\left[1 - \exp\left\{-a\left(R - R_e\right)\right\}\right]^2, \tag{1.6}$$

where D_e is the dissociation energy, R_e the equilibrium bond length, and a is related to the fundamental frequency ω_e. Solving the Schrödinger equation for this potential gives vibrational energy eigenvalues G(v) of the form

$$G(v) = \omega_e\left(v + \tfrac{1}{2}\right) - \omega_e x_e\left(v + \tfrac{1}{2}\right)^2. \tag{1.7}$$

However, if spectroscopic data require terms higher than $(v+½)^2$ in the Dunham expansion then a Morse potential will prove inadequate in modelling the true potential and other more accurate methods must be sought.

1.1.2 Inversion of spectroscopic data

When spectroscopic data cannot be modelled by a suitable analytic potential function the most convenient and practical procedure for obtaining the intermolecular potential is by inversion of spectroscopic Dunham parameters. The most widely used numerical method for this inversion is the Rydberg-Klein-Rees (RKR) [8] procedure, based on the first-order semiclassical Jeffreys-Wentzel-Kramers-Brillouin (JWKB) [9] method, which yields the classical turning points, r_+ and r_-, (the points on the curve where the potential energy equals the total energy) for any desired value of v:

$$r_+ - r_- = \sqrt{\frac{h}{32\pi^2 c\mu}} \int_{-\frac{1}{2}}^{v} \frac{dv'}{\sqrt{G(v) - G(v')}} \tag{1.8a}$$

$$\frac{1}{r_-} - \frac{1}{r_+} = \sqrt{\frac{2\pi^2 c\mu}{h}} \int_{-\frac{1}{2}}^{v} \frac{B(v')dv'}{\sqrt{G(v) - G(v')}} \tag{1.8b}$$

where B(v') is the rotational constant of the vibrational level v'. v is no longer quantised within the semi-classical RKR approach and effectively becomes a continuous variable thus allowing more than one pair of turning points to be generated per vibration interval. These two equations give the full potential energy curve for the particular electronic state so long as experimental data cover a wide range of rovibrational levels.

The RKR method is a very efficient and reliable way of obtaining diatomic potential energy curves from extensive spectroscopic data, it is relatively simple to implement and many such algorithms are in existence differing primarily in the way they deal with a singularity that arises at the upper limit of integration of the two integrands given in equations 1.8a and 1.8b. The potentials generated may be tested by numerical integration of the radial Schrödinger equation in order to check that the correct values for the vibrational and rotational levels are returned.

1.1.3 *Ab initio* methods

In recent years the tools of professional quantum chemists have been made more accessible to experimental physical, inorganic, and organic chemists. There now exist packages of programs that are relatively simple to use without a detailed knowledge of the underlying theory and that do not require specialist computational skills. Indeed, the availability of programs such as MOLPRO and GAUSSIAN equip the experimentalist with a vast range of new tools for electronic structure calculations that may be used for the interpretation and prediction of spectra.

At the heart of *ab initio* quantum chemistry is the need to seek solutions of the electronic Schrödinger equation (1.2) from first principles by treating the molecule as a collection of positive nuclei and negative electrons moving under the influence of Coulombic potentials without any *a priori* knowledge of the species' chemical behaviour. However, the full Schrödinger equation has only been solved exactly for simple model systems so approximations must be made in order for *ab initio* methods to be quantitatively predictive for more challenging and chemically interesting systems. These approximations take the form of physical concepts, such as orbitals, configurations, quantum numbers and term symbols. Although a detailed understanding of modern *ab initio* methods is not necessary in order to use many commercial packages (they may be treated as a mysterious 'black-box' that hopefully yield what was asked after a couple of days), it is, however, useful to know the basis of some of the approximations in order to know the limitations of what is calculable, sources of possible error, and to become familiar with the numerous acronyms that occur in much of the literature.

Essentially all *ab initio* quantum chemistry methods start by introducing a *mean-field potential* V_{mf} that encompasses the average interactions between the N electrons within a molecule. However, in order to achieve reasonably accurate solutions to the true electronic Schrödinger equation (1.2) corrections to this mean-field are sought by introducing the concepts of molecular orbitals, electronic configurations, and electron correlation.

The most widely encountered types of mean-field are one-electron additive, *i.e.*

$$V_{mf}(r) = \sum_{j} V_{mf}(r_j) \tag{1.9}$$

Where $V_{mf}(r_j)$ is the mean-field experienced by the jth electron due to the averaged instantaneous interactions with the other j-1 electrons. Since the electronic kinetic energy operator, $\hat{T}^{el}$, is also one-electron additive then so must the mean field Hamiltonian, $\hat{H} = \hat{T}^{el} + V_{mf}$. The additivity of $\hat{H}$ implies that the mean field energy E_i is also additive and that the total electronic wavefunction $\Phi_{i,\Lambda,S,\Sigma}$ may be formed from a product of one-electron functions ϕ_j, the *molecular orbitals* with energies ε_j. The wavefunction must then be antisymmetrised to meet the requirement of the Pauli principle and each molecular orbital, ϕ_j, multiplied by either α or β to account for the intrinsic spin angular momentum of the electrons. By choosing to distribute the N electrons amongst these *spin-orbitals* in a particular manner a *configuration* is specified. Just as the one-electron mean-field Schrödinger equation has a complete set of spin-orbital solutions (ϕ_j and ε_j), the N-electron mean-field Schrödinger equation has a complete set of *configuration state functions* (CSFs) Φ_i with energies E_i.

Once a configuration has been specified an approximate description of the orbitals in the total wavefunction $\Phi_{i,\Lambda,S,\Sigma}$ may be guessed; these orbitals then implicitly define V_{mf}. This value of V_{mf} is then placed into the one-electron Schrödinger equation to generate new spin-orbitals, which in turn define an improved value of V_{mf}. This iterative process is continued until the orbitals used to define V_{mf} are the same as those returned from the electronic Schrödinger equation. The field then produced is termed as self-consistent. The most commonly used approach of generating molecular orbitals and energies in this way is the Hartree-Fock Self-Consistent Field (HF-SCF) method [5].

The HF-SCF method accounts for the majority of the total energy of a molecule with an error of around 0.5-1 %. This error, although small in magnitude compared with the total energy, can have an absolute value as large as 5 eV - a typical bond dissociation energy.

In order to obtain a more realistic and accurate description of molecular electronic structure the instantaneous interactions between electrons must be taken into account. Electrons undergoing dynamical motions tend to avoid one another due to their mutual Coulombic repulsion, in other words their motion is correlated. Hartree-Fock theory has some instantaneous correlation built in to it insofar as the wavefunction meets the requirement of the Pauli principle ensuring a vanishing probability of two electrons of the same spin occupying the same region of space. The difference between the HF energy and the exact non-relativistic energy is termed the correlation energy and much of the effort of *ab initio* quantum chemistry in recent years has concentrated on finding methods to bridge this gap. The majority of methods move beyond the simple single-configuration description of molecular electronic states by mixing in contributions from excited configurations of the same angular momentum eigenvalues and symmetry. These approaches are known as Configuration Interaction (CI) or configuration mixing. In the CI method the total wavefunction is expanded as a linear combination of configuration state functions Φ_i with appropriate symmetry generated from an SCF calculation

$$\psi = \sum_i a_i \Phi_i \qquad (1.10)$$

and the coefficients a_i are varied to minimise the total energy. The number of Configuration State Functions (CSFs) rises very rapidly with the size of basis set, b, and number of electrons, n (approximately as b^n). Therefore accurate calculations for large molecules containing many electrons will require a huge number of configurations ($>10^7$) which can pose great practical problems. Part of the art of the CI method is choosing which configurations will make the greatest contribution. Fortunately, there now exist numerous efficient approaches that may be used for treating electron correlation problems, for example, Multi-Configuration Self-Consistent field (MC-SCF) [5,6], Complete Active Space SCF (CAS-SCF) [5,6], and Multi-Reference Configuration-Interaction (MRCI) [5,6]. All of these methods involve firstly calculating HF-SCF orbitals and then using them as a first guess to generate more accurate wavefunctions and energies.

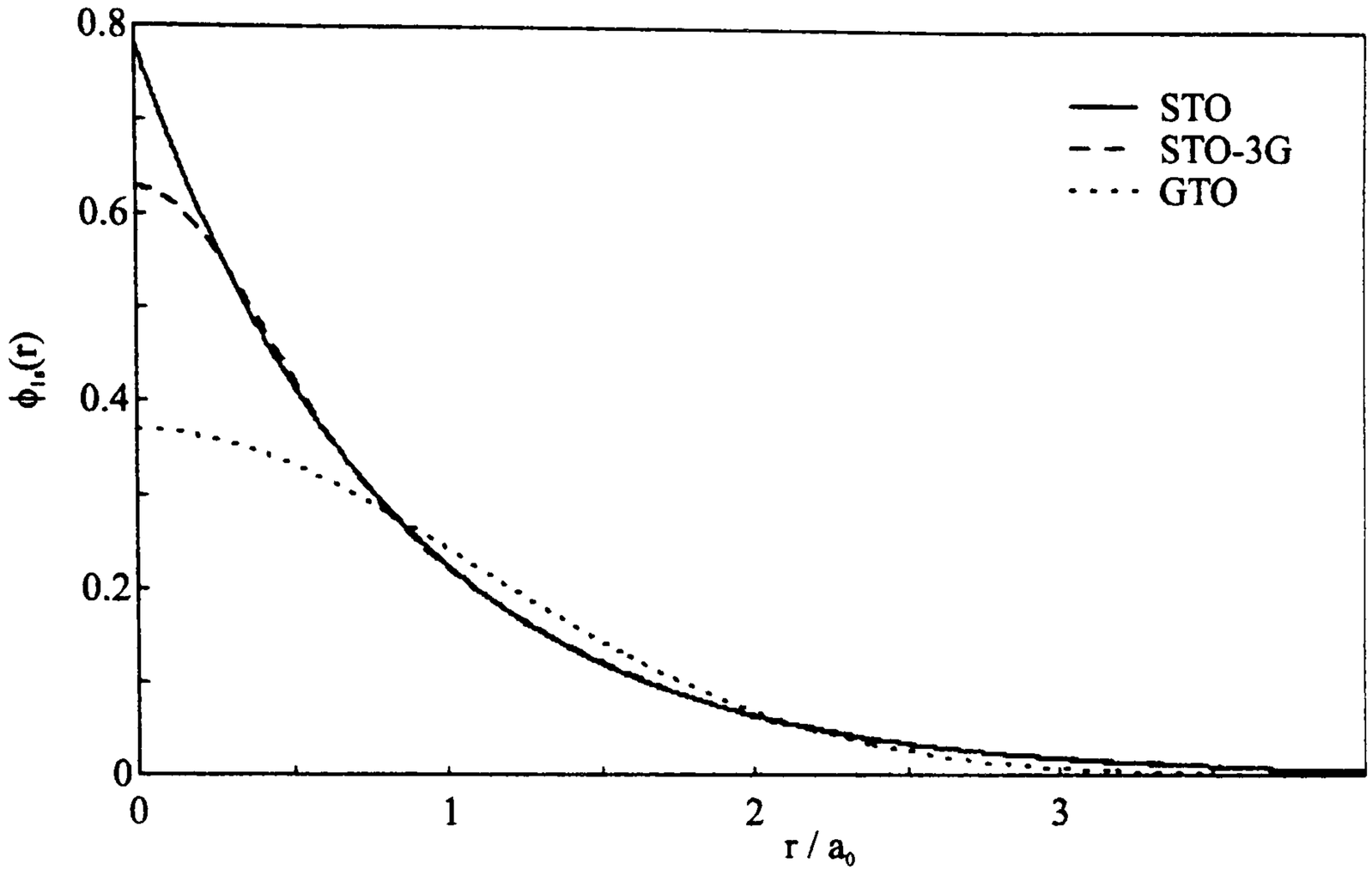

Figure 1.2. Comparison of a Slater Type Orbital (STO) with a single Gaussian Type Orbital (GTO) and a sum of three Gaussians (STO-3G) used to represent an STO.

The majority of commercially available programs express the atomic orbitals that make up the molecular orbitals as linear combinations of Gaussian basis functions (or Gaussian Type Orbitals (GTO's)),

$$G_{nlm}(r,\theta,\phi) = N_n r^{n-1} \exp(-\alpha r^2) Y_l^m(\theta,\phi) \qquad (1.11)$$

where n is the principal quantum number, N_n is a normalisation constant, $Y_l^m(\theta,\phi)$ are spherical harmonics and α an adjustable exponent. These GTO's are computationally more favourable than using Slater Type Orbitals (STO's)

$$S_{nlm}(r,\theta,\phi) = N_{nl} r^{n-1} \exp(-\zeta r) Y_l^m(\theta,\phi) \qquad (1.12)$$

since multi-centre integrals between them are much simpler to evaluate numerically. However, GTO's do not have the correct cusp behaviour at small internuclear distances (illustrated in Figure 1.2), therefore to obtain an accurate description of an atomic orbital (AO) a linear combination of several Gaussians must be used:

$$\chi_r = \sum_u d_{ur} g_u \qquad (1.13)$$

where χ_r is a contracted Gaussian type orbital (CGTO) and g_u are the primitive Gaussians. The contraction coefficients d_{ur} are calculated either by fitting Gaussians to an STO or by using a number of GTO's in an atomic SCF calculation and optimising the orbital exponents and contraction coefficients to give an accurate description of the atomic orbitals. These parameters are then held fixed in the variational calculation for the molecular energies and wavefunctions. A minimal basis set contains one CGTO for every atomic inner shell and valence orbital. This, however, does not provide an adequate description of an atomic orbital and usually a combination of two or more CGTO's are used per atomic orbital leading to the nomenclature double-zeta (two CGTO's), triple-zeta (three CGTO's) (where the zeta terminology derives from the orbital exponent of the STO which the CGTO's represent). Basis set libraries have now been developed [10] for many of the main group elements and are becoming both increasingly accurate and flexible enough to be used in various bonding environments.

1.2 Electronic Spectroscopy of Diatomic Molecules

1.2.1 The Hamiltonian for a diatomic molecule

The Born-Oppenheimer approximation allows the basic spin-free Hamiltonian for a diatomic molecule to be written as:

$$\hat{H}^{eff} = \hat{H}^{e} + \hat{H}^{v} + \hat{H}^{rot} \tag{1.14}$$

where $\hat{H}^{e}$ is the electronic part (discussed in the previous section), $\hat{H}^{v}$ is the vibrational part and $\hat{H}^{rot}$ is the rotational part of the effective Hamiltonian.

The rotational molecular Hamiltonian as defined by Hougen [11] is given below,

$$\begin{aligned}\hat{H}^{rot} &= B\hat{R}^{2} \\ &= B(\hat{R}_{x}^{2} + \hat{R}_{y}^{2}) \\ &= B[J(J+1) + S(S+1) + L(L+1) - \hat{J}_{z}^{2} - \hat{S}_{z}^{2} - \hat{L}_{z}^{2} \\ &\quad - (\hat{J}_{-}\hat{L}_{+} + \hat{J}_{+}\hat{L}_{-}) + (\hat{L}_{+}\hat{S}_{-} + \hat{L}_{-}\hat{S}_{+}) - (\hat{J}_{-}\hat{S}_{+} + \hat{J}_{+}\hat{S}_{-})]\end{aligned} \tag{1.15}$$

where $\hat{R} = \hat{J} - \hat{L} - \hat{S}$ and $\hat{J}_{\pm} = \hat{J}_{x} \pm i\hat{J}_{y}$, $\hat{L}_{\pm} = \hat{L}_{x} \pm i\hat{L}_{y}$, and $\hat{S}_{\pm} = \hat{S}_{x} \pm i\hat{S}_{y}$ are the raising and lowering operators.

The total orbital angular momentum **L** is not a conserved quantity in a diatomic molecule as a consequence of its cylindrical symmetry and therefore cannot be evaluated directly. The terms containing $L_{\pm}$ in equation (1.15) give rise to matrix elements connecting different electronic states. These off-diagonal terms can lead to perturbations between electronic states. The $J_{\pm}S_{\mp}$ terms, however, are responsible for uncoupling the spin angular momentum vector from the internuclear axis with increasing molecular rotation and may be evaluated exactly.

The basic effective Hamiltonian in equation 1.14 does not include the relativistic terms due to the interaction of the intrinsic spin angular momenta associated with the electron and the orbital angular momenta of the electrons and nuclei (see Table 1.1).

These interactions have the effect of lifting the spin degeneracy of the levels of an electronic state giving rise to multiplet splitting and again may also mix different electronic states of the same or different multiplicities giving rise to phenomena such as predissociation (discussed in section 1.2.6) and the observation of formally forbidden transitions. The following three coupling terms may be added to the basic Hamiltonian:

1.2.1.1 Spin-Orbit Coupling

The Hamiltonian given in equation 1.14 assumes that the electron orbital motion is independent of electron spin. However, if the molecule has a non-zero orbital angular momentum ($\lambda \neq 0$) then the circulating charge generates a magnetic field. This interacts with the magnetic moment associated with the intrinsic spin angular momentum, resulting in the following interaction term being added to the Hamiltonian,

$$\begin{aligned} \hat{H}^{SO} &= \sum_i \hat{a}_i \hat{l}_i . \hat{s}_i \\ &= \sum_i \hat{a}_i \left[\hat{l}_{iz} . \hat{s}_{iz} + \tfrac{1}{2}\left(\hat{l}_i^{+} . \hat{s}_i^{-} + \hat{l}_i^{-} . \hat{s}_i^{+} \right) \right] \end{aligned} \qquad (1.16)$$

where $\mathbf{l}_i$ and $\mathbf{s}_i$ are the angular momenta of the individual electrons and $\hat{a}_i$ is a one-electron spin-orbit operator. The $\hat{l}_{iz} . \hat{s}_{iz}$ term in the lower part of equation 1.16 is capable of mixing different electronic states of the same configuration. The $\hat{l}_i^{\pm} . \hat{s}_i^{\mp}$ terms cause a mixing between states of different symmetry for a given signed value of Ω. This can lead to mixing between configurations differing by one spin-orbital. However, as will be seen in chapter 3 if significant configuration mixing between states is present then the spin-orbit interaction may couple states differing by more than one spin-orbital.

For diagonal matrix elements the spin-orbit coupling constant A is defined as,

$$\left\langle \Lambda, \Sigma, S, \Omega, v \middle| \hat{H}^{SO} \middle| \Lambda, \Sigma, S, \Omega, v \right\rangle = A_{\Lambda, v} \Lambda \Sigma \qquad (1.17)$$

which gives rise to the zero-field splitting of the fine-structure levels for states with non-zero spin and orbital angular momentum into equally spaced multiplets separated by $A\Lambda$.

1.2.1.2 Spin-Rotation Coupling

This coupling originates in the interaction between the magnetic field created by the nuclear motion and the magnetic moments of the electron spins and is usually a small term since the angular velocities of the nuclei and electrons are very different. The spin-rotation Hamiltonian [3] is usually given in the form,

$$\hat{H}^{SR} = \gamma \hat{\mathbf{N}}.\hat{\mathbf{S}} = \gamma(\hat{J} - \hat{S}).\hat{S}$$

$$= \gamma\left[\hat{J}_z\hat{S}_z + \tfrac{1}{2}(\hat{J}_+\hat{S}_- + \hat{J}_-\hat{S}_+) - \hat{S}^2\right] \qquad (1.18)$$

where γ is the spin-rotation constant.

1.2.1.3 Spin-Spin Coupling

This term is only non-zero for triplet states and states of higher spin multiplicity ($S \geq 1$). It arises due to the interaction of the magnetic dipoles of two different unpaired electrons. The direct spin-spin Hamiltonian for two unpaired electrons is defined as,

$$\hat{H}^{SS} = \tfrac{2}{3}\lambda\left(3\hat{S}_z^2 - \hat{\mathbf{S}}^2\right) \qquad (1.19)$$

where λ is the effective spin-spin coupling constant. The effect of this interaction is to raise or lower in energy each multiplet component; for example, in a $^3\Sigma$ state (*e.g.* the X and B states of S_2 considered in Chapter 4) the degeneracy of the $|\Omega|$=0 and 1 components is lifted causing a splitting of 2λ between levels.

1.2.2 Rotational fine structure - Hund's Coupling Cases

Hund identified five limiting cases for the coupling of the internal electronic angular momentum within a molecule to the rotational angular momentum of the nuclear framework [1]. These different coupling regimes lead to different rotational energy level patterns depending upon the relative magnitudes of the multiplet splittings and rotational spacings. For the purposes of the present work it is necessary to consider the first three cases:

1. Case (a)

This case applies if the spin-orbit splitting of multiplet components is large compared to the rotational spacing (A>>BJ). The strong axial electrostatic field couples the orbital angular momentum, **L**, to the internuclear axis. In turn the strong spin-orbit interaction will couple the spin angular momentum, **S**, to **L** and hence the internuclear axis, as illustrated in Figure 1.3. Thus only the axial components of **L** and **S** remain well defined (good quantum numbers) and are ascribed the quantum numbers Λ and Σ. The resulting sum, $\Omega = \Lambda + \Sigma$, then couples to the nuclear framework angular momentum, **R** to form the total angular momentum vector **J**. The conserved quantities (good quantum numbers) in this case are J,Σ,Λ,Ω and S leading to the case (a) angular momentum basis set $|nJS\Omega\Lambda\Sigma\rangle$. A Hund's case (a) coupling scheme often provides a suitable basis set for describing the rotational levels of $^2\Pi$ states, for example, the ground state of SH considered in chapter 3.

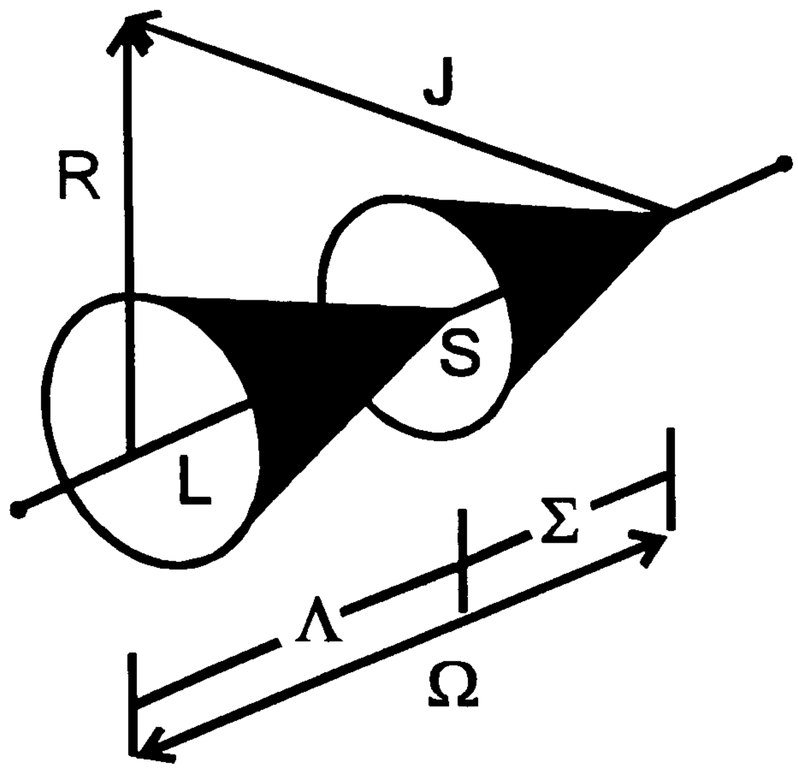

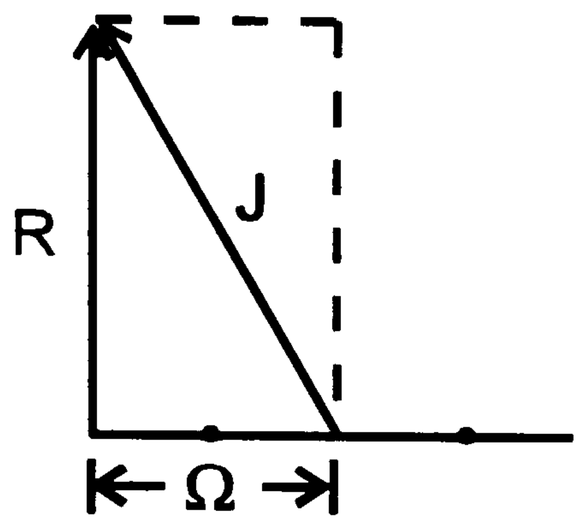

Figure 1.3. Hund's coupling case (a)

2. Case (b)

In this case the spin-orbit coupling is small compared to the rotational spacing (A<<BJ). The effect of this is to uncouple **S** from the quantisation axis as is shown in Figure 1.4. This decoupling arises due to the matrix elements of the **S**-uncoupling operator ($\hat{J}_{\pm}\hat{S}_{\mp}$) in the rotational part of the Hamiltonian (1.13) being large with respect to the energy separation between Ω components. **S** now couples to **N** (the resultant of Λ and **R**) to form the total angular momentum vector **J**. In case (b) coupling the conserved quantities are now J, N, S, and Λ and the angular momentum basis set becomes $|nJSN\Lambda\rangle$. A $^2\Sigma$ state is an example of a pure case (b) coupling scheme since there is no spin-orbit interaction due to Λ being zero. However, for a $^3\Sigma$ state, *e.g.* the X and B states of S_2 considered in chapter 4, the spin-spin splitting may be large enough relative to the rotational spacing ($\lambda > BJ$) for it to be better described as case (a) at low J. Here the large spin-spin interaction can have the effect of coupling S to the internuclear axis, resulting in case (a) being a better description.

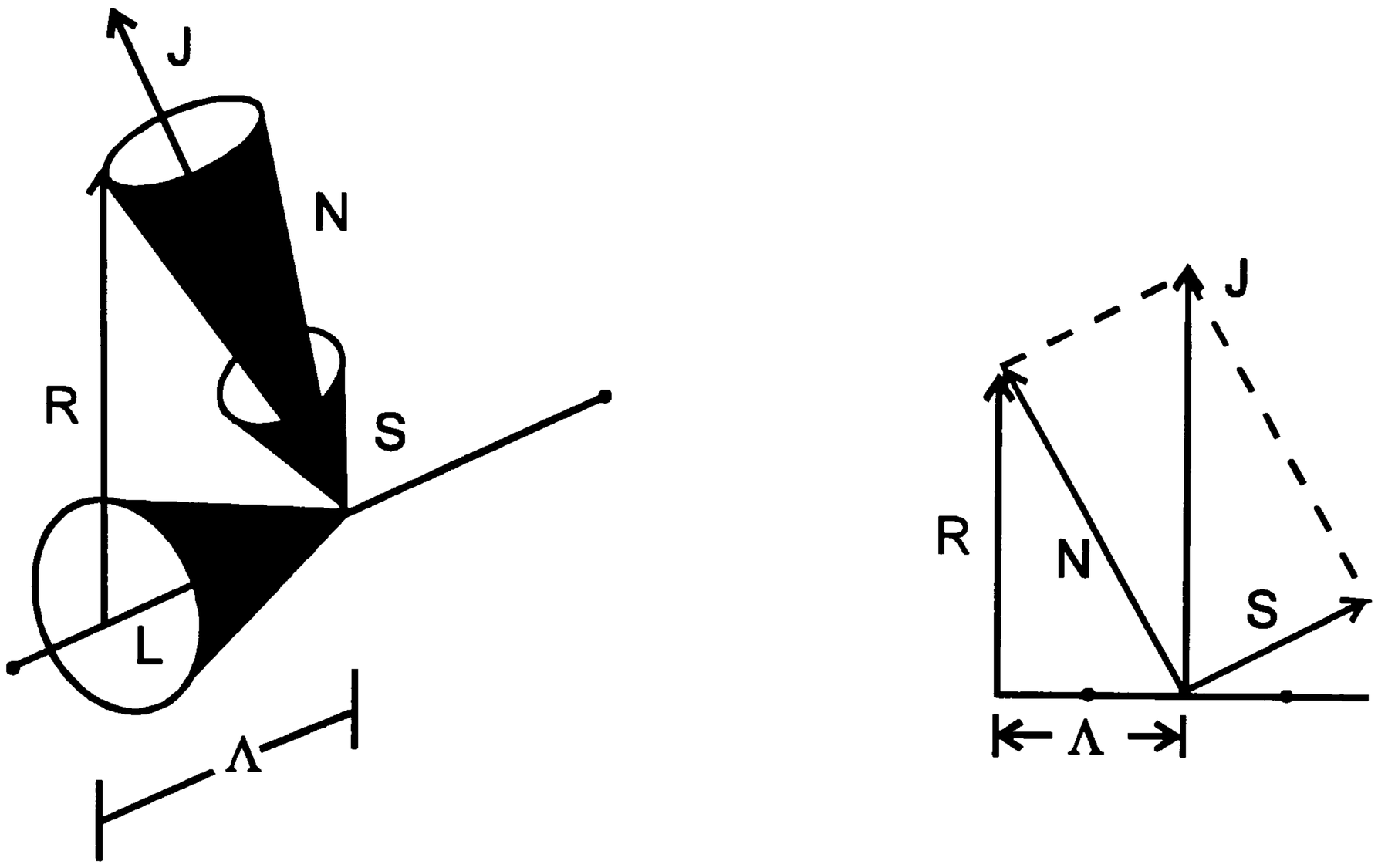

Figure 1.4. Hund's coupling case (b)

As the classification of a state in terms of case (a) or case (b) coupling regimes depends upon the comparison of the multiplet splitting to the rotational separation it is conceivable for a transition from case (a) to case (b) to occur as J is increased. Essentially, the transition from case (a) to case (b) takes place as the rotational velocity of the molecule becomes comparable with the precessional velocity of **S** about the internuclear axis, thus causing **S** to uncouple from the axis and instead couple with **N**.

3. Case(c)

This case is important for molecules containing a heavy atom where the spin-orbit coupling is very large. This strong spin-orbit interaction causes **L** and **S** to be mutually coupled together forming a new vector $\mathbf{J_a}$; this resultant then couples to the internuclear axis with a projection Ω. The total angular momentum of the molecule is now given by $\mathbf{J} = \mathbf{J_a} + \mathbf{R}$ as depicted in Figure 1.5. For case (c) the splitting between multiplet levels is comparable to the interval between electronic states and each Ω component has its own potential energy curve. In case (c) the only remaining good quantum numbers are J and Ω and the basis set is now simply $|nJ\Omega\rangle$.

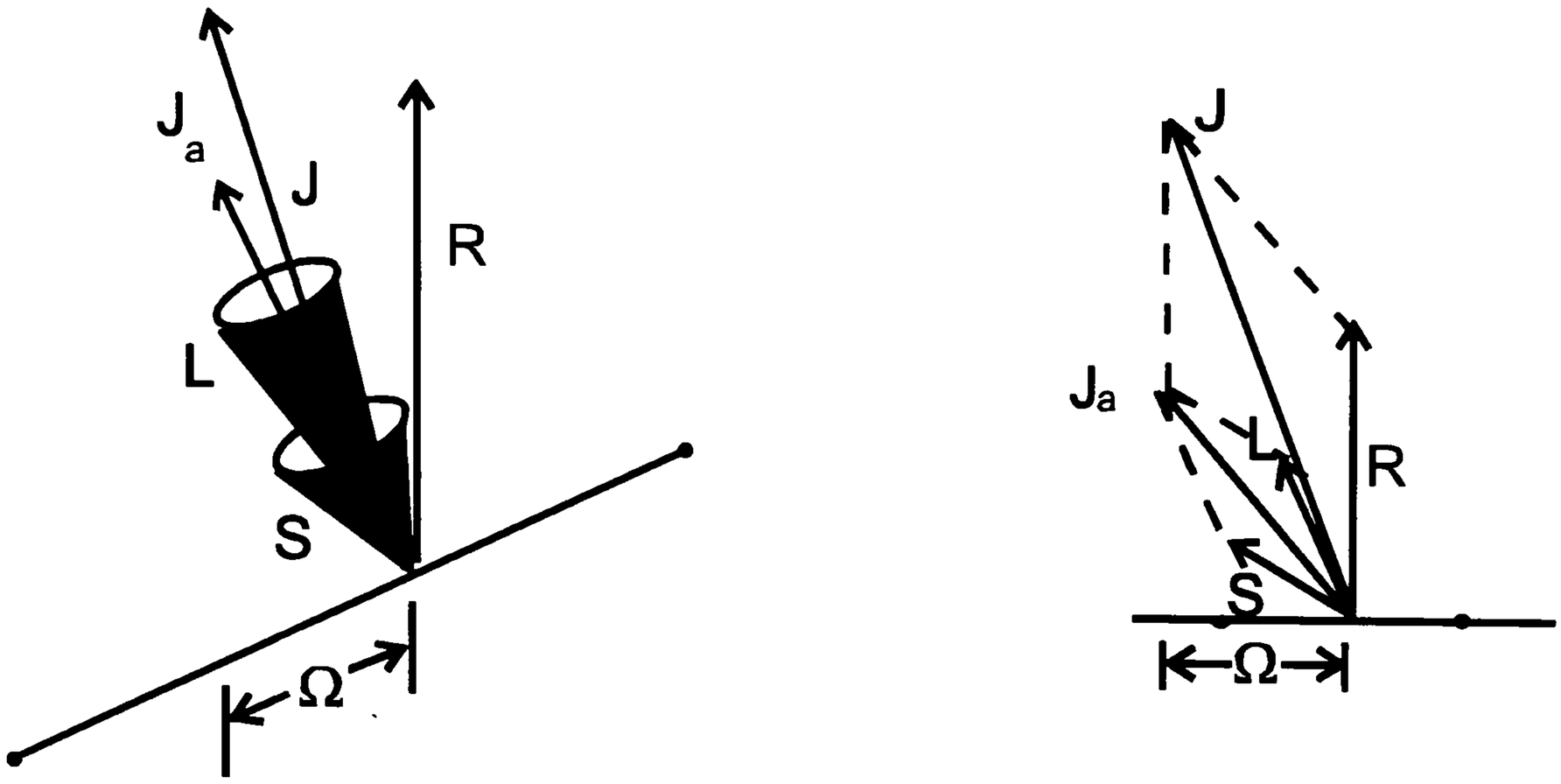

Figure 1.5 Hund's coupling case (c)

Although each coupling case has its own set of mutually commutating operators the choice for a particular situation is in fact entirely arbitrary since it is possible to represent the basis functions of any coupling scheme as a linear combination of case (a) basis functions using , for example, Clebsch-Gordan or 3-j coefficients. In the spectral analysis presented in this thesis the simulation program PGOPHER written by Dr. C.M. Western constructs a Hamiltonian expressed in symmetrised case (a) basis functions.

1.2.3 Symmetry of diatomic energy levels - parity

The *total parity* of an eigenstate of a diatomic molecule is classified as the behaviour of the total wavefunction ψ_{tot} (excluding nuclear spin) under the application of the inversion operator, $\hat{I}$, in the space-fixed frame (equivalent to the operation of $\hat{\sigma}_v(xz)$ followed by $\hat{C}_2(y)$ in the body-fixed frame) [12].

$$\hat{I}\psi_{tot} = \hat{I}(\psi_{el}\psi_{vib}\psi_{rot}) = \pm\psi_{tot} \qquad (1.20)$$

Energy levels for which the upper sign applies have (+) total parity, whereas levels for which the lower sign applies have (–) total parity. $\hat{I}$ leaves the vibrational part of ψ_{tot} unchanged and thus only the rotational and electronic components of the ψ_{tot} determine

the total parity. By considering the effect of $\hat{I}$ on each part of the wavefunction in turn it can be shown [11],

$$\hat{I}\psi_{tot} = \hat{I}\left(|n\Lambda S\Sigma\rangle|v\rangle|\Omega JM\rangle\right) = (-1)^{J-2\Sigma+S+s}|n,-\Lambda,S,-\Sigma\rangle|v\rangle|-\Omega JM\rangle \qquad (1.21)$$

For states with zero electronic orbital angular momentum (Σ states) an additional $\pm$ superscript is added to the term symbol denoting the *electronic parity* (*i.e.* $\Sigma^{\pm}$) with respect to the $\hat{\sigma}_v$ operation. This extra label is dropped for states with $\Lambda>0$ since the levels occur as $\pm$ pairs owing to the twofold orbital degeneracy. Thus in equation 1.21 s=0 for all states except Σ^- states for which s=1. It is important to note that the operation of $\hat{I}$ changes the signs of Σ, Λ, and Ω. Therefore, in order to construct eigenfunctions with well defined parity, linear combinations of the unsymmetrised basis functions are formed, *i.e.*,

$$\left|{}^{2S+1}\Lambda_{\Omega}\pm\right\rangle = \frac{\left|{}^{2S+1}\Lambda_{\Omega}\right\rangle \pm (-1)^{J-2\Sigma+S+s}\left|{}^{2S+1}\Lambda_{-\Omega}\right\rangle}{\sqrt{2}}. \qquad (1.22)$$

It is often convenient to factor out the alternation of total parity with J (introduced by the phase factor $(-1)^J$) by introducing the *rotationless* or *e/f parity* where,

$$\hat{I}\psi_{tot} = +(-1)^J\psi_{tot} \qquad \text{for } e \text{ parity} \qquad (1.23a)$$

and,

$$\hat{I}\psi_{tot} = -(-1)^J\psi_{tot} \qquad \text{for } f \text{ parity.} \qquad (1.23b)$$

If J is half-integer the exponent J is replaced by J-½. Therefore all rotational energy levels of a ${}^1\Sigma^+$ state have *e* parity, while all rotational energy levels of a ${}^1\Sigma^-$ state have *f* parity. For Π states all of the rotational levels occur as *e/f* pairs. The use of *e/f* parity also suppresses the annoying $(-1)^{J-2\Sigma+S+s}$ factor in the symmetrised parity eigenfunctions shown in equation 1.22.

Homonuclear diatomics belong to the point group $D_{\infty h}$ which contains the body-fixed inversion operation $\hat{i}$. This inversion operation is useful in classifying the

electronic orbital part of the total wavefunction since Σ, S, J, and v all remain unaffected by the application of $\hat{i}$.

$$\hat{i}|\Lambda\rangle = \pm|\Lambda\rangle \tag{1.24}$$

Eigenfunctions for which the (+) sign applies are labelled g (gerade) symmetry and those for which the (–) sign applies are classed as u (ungerade) symmetry. The u or g label is added to the term symbol of the particular state as a subscript (*i.e.* $^{2S+1}\Lambda_{g/u}$).

A further classification exists for labeling the rotational levels of a homonuclear diatomic as either s (symmetric) or a (antisymmetric). This classification derives from the Pauli exclusion principle which demands that the total wavefunction (inclusive of nuclear spin) should be either symmetric or antisymmetric with respect to the interchange of the two identical nuclei depending on whether the nuclei are bosons (zero or integer nuclear spin) or fermions (half-integer nuclear spin) respectively. If the nuclei are bosons such as for S_2 (I=0), considered in Chapter 4, then only the states with symmetric molecular wavefunctions are possible. Thus, in this case, the even (g) state levels with (+) parity are symmetric (labelled s) and the (–) parity levels are antisymmetric (labelled a), with the reverse behaviour for odd (u) states. Since the overall wavefunction must be symmetric with respect to interchange of the two sulphur nuclei and only the symmetric nuclear spin wavefunction is possible for I=0 then the (a) levels cannot exist for S_2 and hence every alternate rotational level will be absent.

1.2.4 Selection rules for Electronic Transitions

The selection rules, governing which transitions between states are allowed, may be obtained by evaluating the matrix elements of the electric dipole operator, $\mu_q^{(1)}$, connecting an initial state m with final state n,

$$R^{nm} = \langle n|\mu_q^{(1)}|m\rangle \tag{1.25}$$

For a transition to be formally allowed it must have a non-zero matrix element which requires R^{nm} to be totally symmetric. The general one-photon electric dipole selection rules that are independent of coupling case are as follows:

$\Delta J = 0, \pm 1$ where $J=0 \leftrightarrow J=0$ is forbidden

$+ \leftrightarrow -$ is allowed but $+ \leftrightarrow +$ and $- \leftrightarrow -$ are forbidden

$g \leftrightarrow u$ is allowed but $u \leftrightarrow u$ and $g \leftrightarrow g$ are forbidden.

$s \leftrightarrow s$ and $a \leftrightarrow a$ are allowed and $a \leftrightarrow s$ is forbidden.

For cases (a) and (b):

$\Delta\Lambda = 0, \pm 1$

where $\Sigma^+ \leftrightarrow \Sigma^+$ and $\Sigma^- \leftrightarrow \Sigma^-$ are allowed but $\Sigma^+ \leftrightarrow \Sigma^-$ is forbidden

$\Delta S = 0$

For case (a) only:

$\Delta\Sigma = 0$

It therefore follows $\Delta\Omega = 0, \pm 1$ from the definition of Ω. This selection rule for Ω still holds even for the case of very strong spin-orbit coupling (case (c) limit) when Λ and Σ are no longer defined. However, if $\Omega = 0$ for both electronic states there is an additional constraint,

$\Delta J = 0$ is forbidden for $\Omega = 0 \leftrightarrow \Omega = 0$.

Therefore for this type of transition no Q branch will be observed.

For case (b) only:

$\Delta N = 0, \pm 1$

with the constraint

$\Delta N = 0$ is forbidden for Σ - Σ transitions.

1.2.5 Spectral lineshapes

An important feature of the interaction of electromagnetic radiation with a molecule is the frequency dependence of the transition probability within the vicinity of a resonance. This can have the effect of broadening spectral lineshapes. There are two basic types of line-broadening mechanisms to consider: Homogeneous broadening, where *each molecule* may absorb or emit radiation over the entire linewidth and inhomogeneous broadening which arises due to *different molecules* undergoing the same nominal transition absorbing or emitting light at slightly different frequencies because of their different environments.

1.2.5.1 Lifetime broadening

This is a type of homogeneous line-broadening mechanism and gives rise to the natural linewidth of a transition. If an excited state decays spontaneously then in the absence of any other decay processes the radiative width will be determined by the reciprocal of the lifetime of the state, $1/\tau_{rad}$, *i.e.* the shorter-lived the excited state the broader the line will be. This type of broadening is essentially a reflection of the *Heisenberg Uncertainty Principle*. Other non-radiative decay processes may also contribute to this type of broadening such as collisional quenching of the excited state (pressure broadening) or predissociation (discussed in the following section). Lifetime-broadened spectroscopic transitions are in general characterised by a Lorentzian shape (see Figure 1.6),

$$\sigma_a(E) = \frac{\sigma_{max}(\Gamma/2)^2}{(E - E_r)^2 + (\Gamma/2)^2} \qquad (1.26)$$

where Γ is the full width at half maximum (FWHM), E_r the line-centre of the resonance, σ_{max} the intensity at E_r. The FWHM Γ (in cm^{-1}) is related to the natural-lifetime of the state by the expression,

$$\Gamma = \frac{1}{2\pi c\tau} \qquad (1.27)$$

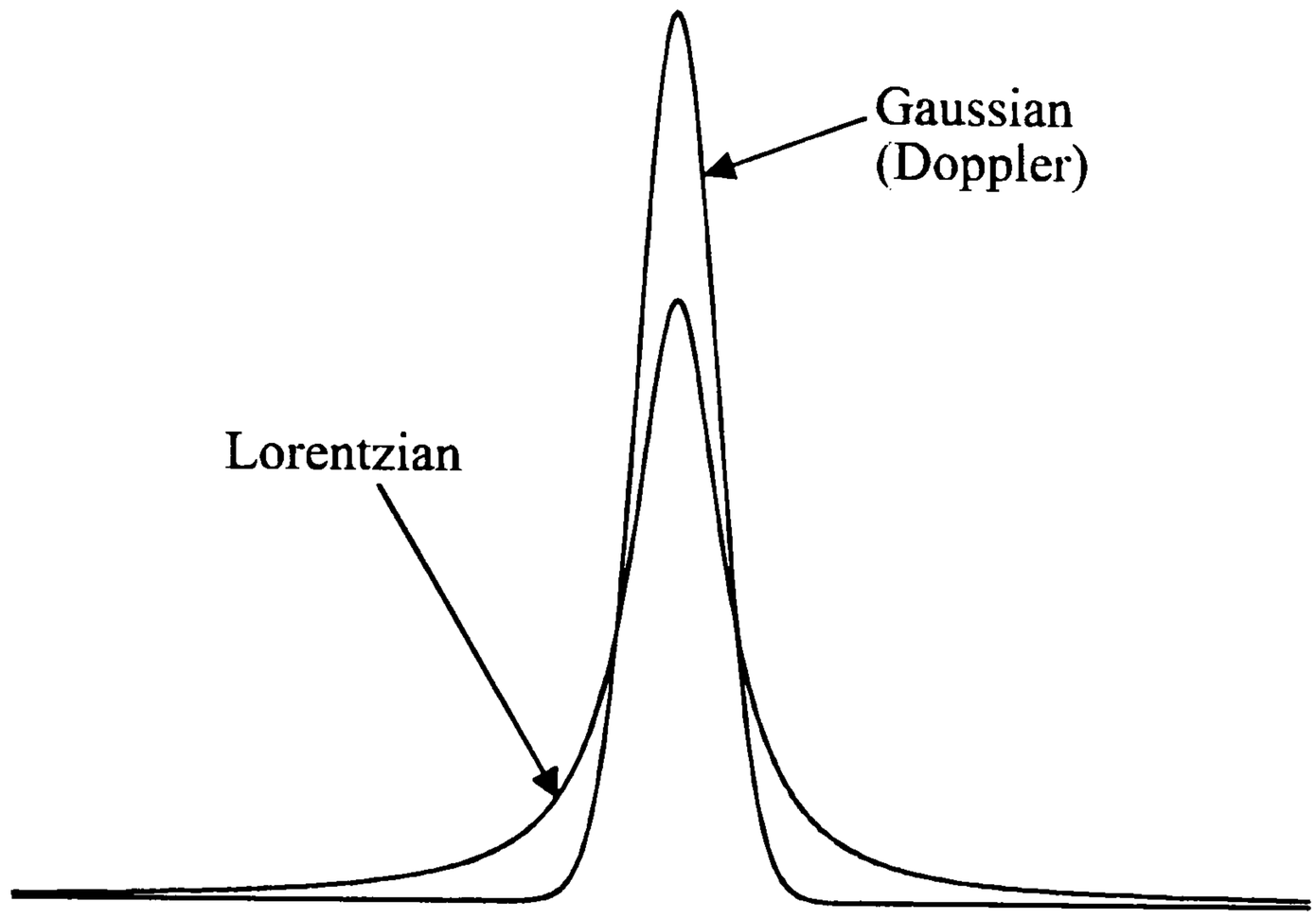

Figure 1.6. Comparison between Gaussian and Lorentzian lineshapes with the same Full-Width at Half-Maximum (FWHM).

1.2.5.2 Doppler broadening

This inhomogeneous line-broadening phenomenon arises due to a velocity distribution of molecules relative to the line of sight of the observer. Each velocity component will absorb or emit radiation at slightly different frequencies depending on the projection of the velocity along the direction of propagation of the photon (usually defined as the z-axis). The superposition of these different absorption / emission frequencies gives rise to a Gaussian lineshape with a FWHM given by:

$$\Delta\nu_D \approx 7.2 \times 10^{-7} \nu_0 \sqrt{\frac{T}{M}} \tag{1.28}$$

Here M is the molecular weight (g) of the absorbing or emitting species, T is the temperature (K) and ν_0 is the frequency of the line centre in Hz.

For the purposes of the work presented in chapters 3, 4, and 5 the laser line profile is also approximated as a Gaussian function. Experimentally it is not possible to distinguish between Doppler broadening and the laser line shape (unless $\Delta\nu_D > \Delta\nu_{laser}$) so both of these effects combine to give an overall Gaussian profile (the convolution of two

Gaussians with FWHM $\Delta\nu_D$ and $\Delta\nu_{laser}$ produces another Gaussian with FWHM $\Delta\nu=(\Delta\nu_D^2 + \Delta\nu_{laser}^2)^{½}$.

Both inhomogeneous and homogeneous lineshapes may contribute to observed spectral line profiles and their combined effect results in a non-analytic function called a Voigt profile, which is discussed in detail in chapter 3.

1.2.6 Perturbations and Predissociation

When the observed energy levels do not fit the simple Dunham energy level expression, *i.e.* there is an irregular v or J dependence of spectral line positions and intensities, the system is said to be perturbed. Perturbation phenomena can manifest themselves in a variety of ways: in addition to unexpected positions and intensities of spectral lines it may be possible to observe formally forbidden transitions, unusual radiative lifetimes, and abnormal linewidths. A perturbation may be regarded as a break-down of the Born-Oppenheimer approximation, since the cause of the deviation from 'normal behaviour' arises from couplings between angular momenta associated with the nuclear rotation, electron spin, and electron orbital motion. These couplings effectively mix different states to create new admixture states.

Perturbations may exist between discrete levels and a nearby continuum of levels, giving rise to a phenomenon known as *predissociation* [13]. The perturbation interaction mixes the wavefunctions of the two states generating a hybrid state. In this new hybrid state the system must spend some of its time in the continuum. However, once the excited molecule AB*(v', J') enters the continuum it begins to fragment into its correlated atomic components and therefore cannot return to the discrete levels.

$$AB(v'',J'') + h\nu \rightarrow AB^*(v',J') \rightarrow A + B \qquad (1.29)$$

The excited state is therefore dissociated at an energy below its normal dissociation limit and is said to be predissociated. The absorption linewidth of a transition to a predissociative level is usually broadened as a consequence of the upper state lifetime

being short compared to a non-predissociative level. The extent of the broadening or diffuseness of spectral lines is governed by the degree of overlap of the bound and continuum wavefunctions and the strength of the interaction between the states. The fragmentation of the excited species AB*(v', J') may be viewed as the most simple and fundamental chemical reaction and as such a detailed study of predissociation processes is an invaluable tool in understanding molecular dynamics at a microscopic level.

Herzberg [1] identified three possible cases of overlapping bound molecular energy levels with a continuum corresponding to the three forms of energy within the molecule:

I. Electronic predissociation - The most common type of predissociation encountered in diatomic molecules, involving the mixing of discrete levels of a given electronic state with the continuum of another electronic state.

II. Vibrational predissociation - This type of mechanism occurs in polyatomic molecules only. Excitation of a bound vibrational mode is followed by Intramolecular Vibrational Redistribution (IVR) where some of the energy is coupled into a dissociative mode causing the molecule to fragment.

III. Predissociation by rotation - The rotation of a molecule causes the addition of a centrifugal term to its potential, resulting in a centrifugal barrier to dissociation whereby the molecule can be 'quasi-bound' at levels above the dissociation limit. Tunnelling may occur through this barrier leading to decomposition of the molecule with no change of electronic state.

For the purposes of the work presented in Chapters 3, 4 and 5 of this thesis only type I predissociation is discussed further.

It is difficult to measure the rate at which the excited state predissociates directly since it requires the use of complicated techniques such as femtosecond transition-state spectroscopy (FTS) [14]. Experimentally it is a much simpler task to measure the predissociation rate relative to the radiative decay rate, as illustrated in Figure 1.7.

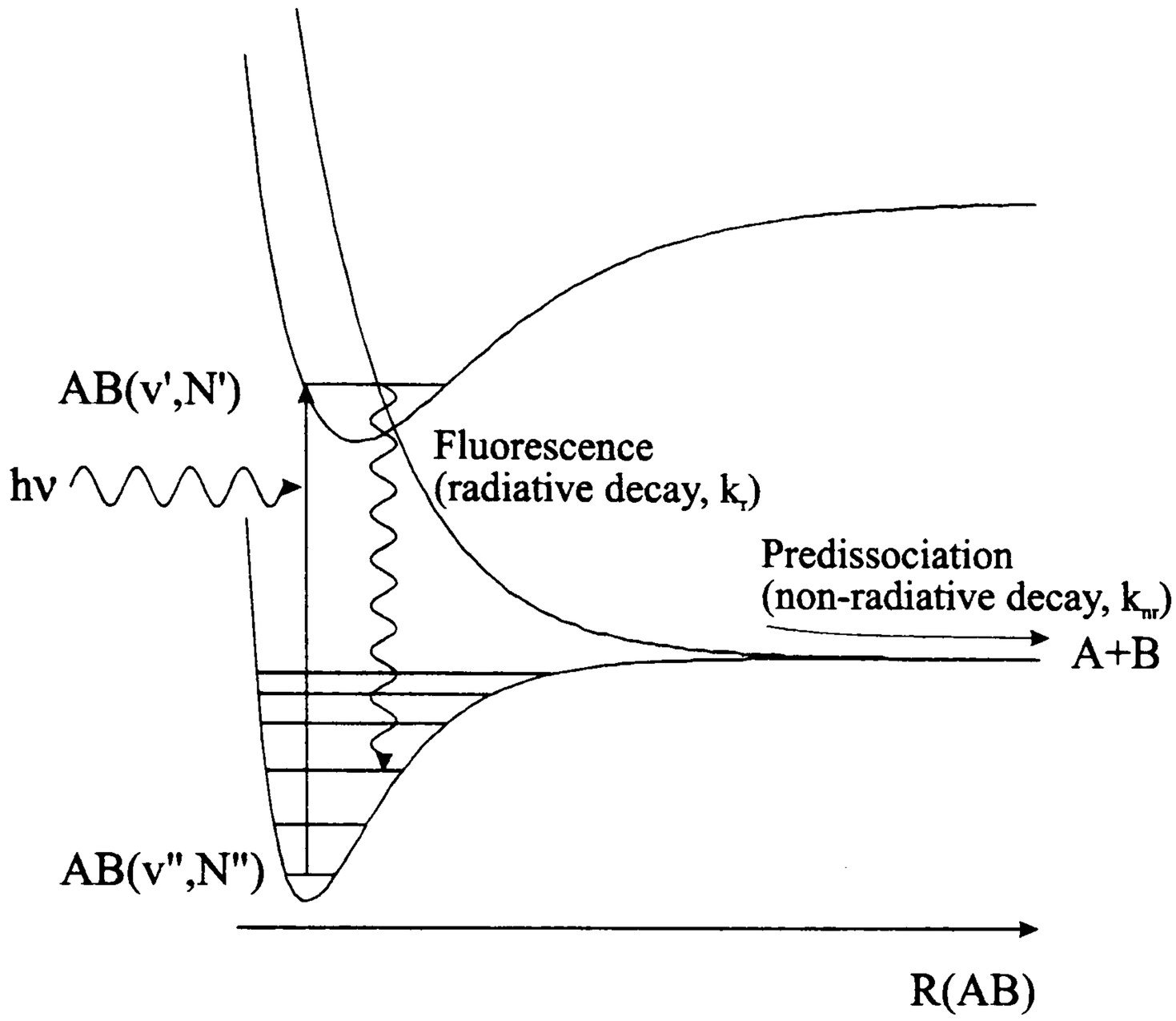

Figure 1.7. Non-radiative (k_{nr}) vs. radiative decay (k_r) routes for an excited state diatomic molecule AB*(v', J')

Provided the pressure is low enough the decay rate may be assumed to be unimolecular and the natural (or fluorescence) lifetime, τ, of the state will be given by the sum of the individual rates.

$$\frac{1}{\tau} = k_{nr} + k_r$$
$$= \frac{1}{\tau_{nr}} + \frac{1}{\tau_r} \qquad (1.30)$$

where τ_r is the radiative lifetime and τ_{nr} is the predissociative lifetime. The natural lifetime, τ, is then related to the spectral linewidth Γ by equation 1.27, some examples are given in Table 1.2.

Γ / cm^{-1}	τ
0.1	50 ps
1.0	5 ps
10	500 fs
100	50 fs

Table 1.2. Relationship between natural linewidth and natural lifetime.

Broadening of spectral lines can only occur if the predissociative lifetime is shorter than the radiative lifetime. However, the resolution of the experiment ultimately determines the extent of line broadening that can be measured. In the experiments presented in the following chapters the linewidth of the UV laser pulse is around 0.1 cm^{-1}; thus the predissociative lifetimes must be less than 50 ps in order for lifetime broadening to be sufficiently distinguishable from the laser line profile.

1.2.6.1 Theory of electronic predissociation

Fano's configuration interaction theory [15] relates the width Γ of a predissociated level to the degree of mixing between the bound ($\Psi_{1,v,J}$) and continuum ($\Psi_{2,E',J}$) states $|v,J\rangle$ and $|E',J\rangle$ which is governed by the off-diagonal interaction matrix element

$$\langle v,J|\hat{H}|E',J\rangle = H_{v,J;E',J} \tag{1.31}$$

The bound and continuum states are assumed to diagonalise their respective Hamiltonian sub-matrices,

$$\langle v,J|\hat{H}|v',J'\rangle = E_{v,J}\delta_{v,v'}\delta_{J,J'} \tag{1.32}$$

$$\langle E,J|\hat{H}|E',J'\rangle = E\delta_{J,J'}\delta(E-E') \tag{1.33}$$

The vibrational energy of the continuum is not quantised and is therefore labelled with the good quantum number E [3]. The unbound wavefunctions must be normalised to the energy density $\rho(E)$ (density of states) in the continuum since they extend to infinity thus rendering the usual spatial normalisation meaningless. At large internuclear separation the continuum wavefunctions become plane waves of the form,

$$\Psi = a_E \sin(kR - E) \tag{1.34}$$

and hence their normalisation is defined by this plane wave (asymptotic) part of the function. The product of the square of the amplitude a_E^2 and the density of states $\rho(E)$ can be shown to be a constant value $(8\mu c/hE)^{1/2}$ [16] where E is the kinetic energy (in cm^{-1}) of the fragments and μ the reduced mass. If the asymptotic amplitude is taken to be unity then the appropriate energy density is $(8\mu c/hE)^{1/2}$.

The hybrid continuum state caused by the mixing of the bound and continuum wavefunctions may be expressed as,

$$\Psi_{E,J} = a(E)\Psi_{1,v,J} + \int dE' b_{E'}(E)\Psi_{2,E',J} \tag{1.35}$$

where a(E) and $b_{E'}(E)$ are the energy dependent amplitudes of the bound and continuum wavefunctions in the hybrid state. If the energy spacings between discrete levels are much larger than the interaction matrix element $H_{v,J;E',J}$, then it is reasonable to only treat interactions between one discrete state and one continuum state, known as *the isolated resonance approximation*. The discrete amplitude, a(E), in the hybrid continuum wavefunction varies depending on the proximity of the resonance. If $H_{v,J;E',J}$ varies slowly with energy then it may be shown [3] that $|a(E)|^2$ is a Lorentzian function,

$$|a(E)|^2 = \frac{\left|H_{v,J;E',J}\right|^2}{\left(E - E_r\right)^2 + \pi^2\left|H_{v,J;E',J}\right|^4} \tag{1.36}$$

The FWHM of this Lorentzian function gives the lifetime broadened linewidth of a predissociated level in the absence of Doppler broadening as

$$\Gamma_{v,J} = 2\pi\left|H_{v,J;E',J}\right|^2 \tag{1.37}$$

where it is implied that the coupling is calculated at an energy E equal to the energy of the discrete state. An entirely equivalent expression may be written down that explicitly involves the density of states factor $\rho(E)$,

$$\Gamma_{v,J} = 2\pi\rho(E)\left|H_{v,J;E',J}\right|^2 \tag{1.38}$$

and is known as the *Fermi Golden Rule*. This expression implies a matrix element of $\hat{H}$ evaluated between space-normalised wavefunctions. If the electronic matrix element $H_{v,J;E',J}$ is assumed to vary slowly with R then it may be factored into electronic and nuclear parts

$$H_{v,J;E',J} = \left\langle \phi_1(r,R)\left|\hat{H}\right|\phi_2(r,R)\right\rangle\left\langle \chi_{v,J}(R)\middle|\chi_{E',J}(R)\right\rangle = H^e\left\langle \chi_{v,J}(R)\middle|\chi_{E',J}(R)\right\rangle \tag{1.39}$$

Where ϕ_1, ϕ_2 are the electronic wavefunctions, $\chi_{v,J}$, $\chi_{E,J}$ are the radial wavefunctions, and H^e is the electronic coupling strength (analogous to the transition dipole moment for radiative processes). H^e may be a constant interaction or in some cases a slowly varying R-dependent interaction evaluated in the region of the crossing point of the two potential curves. Using this approximation equation (1.38) becomes

$$\Gamma_{v,J} = 2\pi\rho(E)\left|H^e\right|^2\left|\left\langle \chi_{v,J}(R)\middle|\chi_{E',J}(R)\right\rangle\right|^2 \tag{1.40}$$

where, in contrast to the slow variation of H^e, the Franck-Condon factor in (1.40) may change rapidly with energy causing the predissociation rate to oscillate with v and possibly J [17]. This form of the Fermi Golden Rule will be used to interpret predissociation rates of SH / SD $A^2\Sigma^+$ (Chapter 3) and S_2 $B^3\Sigma_u^-$ (Chapter 4).

1.2.6.2 Selection rules for predissociation

For all discrete states lying within the continuum of the predissociating state the possibility of predissociation exists. As well as the condition of equal energy, the non-radiative transition must also fulfil the Kronig selection rules governing allowed interactions between different electronic states.

Regardless of coupling conditions the following selection rules hold

$$\Delta J = 0$$

$$+ \leftrightarrow + \text{ and } - \leftrightarrow -$$

$$e \leftrightarrow e \text{ and } f \leftrightarrow f$$

$$u \leftrightarrow u \text{ and } g \leftrightarrow g$$

The angular momentum J and symmetry properties are defined in the continuum as well as for discrete levels. The $\Delta J=0$ selection rule is always realisable since all J values are possible for a given energy in the continuum (due to the very large moment of inertia associated with the separated atoms).

For Hund's cases (a) and (b),

$$\Delta\Lambda = 0, \pm 1$$

$$\Delta S = 0$$

If both states are case (a) or both case (b) then the additional rules are respectively

$$\Delta\Sigma = 0$$

$$\Delta N = 0$$

In Hund's case (c)

$$\Delta\Omega = 0, \pm 1$$

1.2.6.3 Classification of electronic predissociation

Mulliken [18] demonstrated that the location of the curve crossing (E_c, R_c) relative to the dissociation energy, D_0, of the predissociating state and the equilibrium bond length, R_e, of the predissociated state would have a significant effect on the observed variation of predissociation rate with the quantum numbers v and J. Based on this illustration a further sub-classification of electronic predissociation was formulated; when the asymptote of a dissociative state lies approximately at, above, or below the crossing point it is defined as case a, b, and c respectively. The superscripts -, i, and + are further added to indicate the position of the crossing point relative to the equilibrium bond length of the bound state $R_c < R_e$, $R_c = R_e$, and $R_c > R_e$. If the potentials are non-crossing then an o superscript is added. Some examples are given in Figure 1.8.

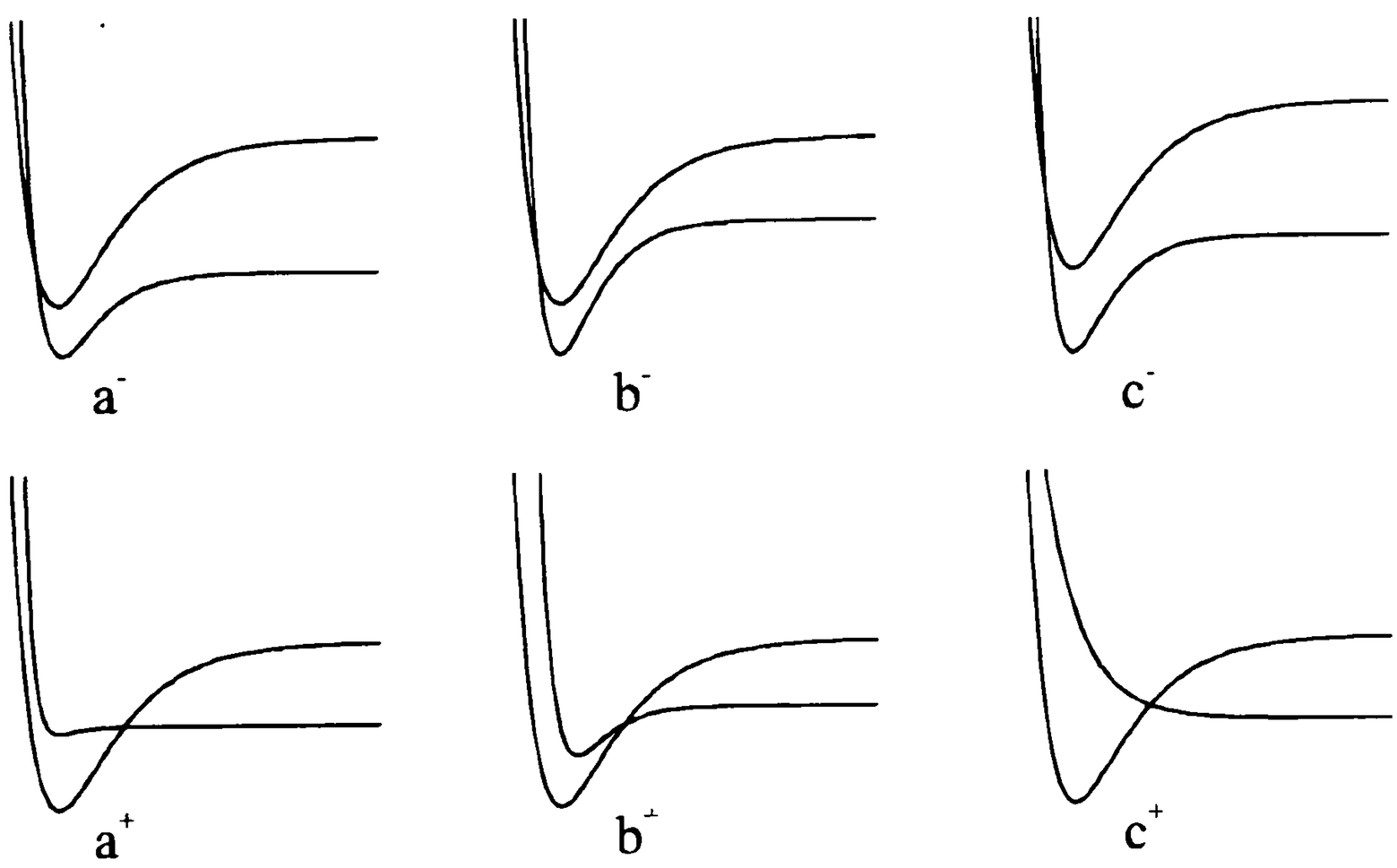

Figure 1.8. Examples of different sub-cases of electronic predissociation.

If experimental data concerning the variation of linewidth with v, J and isotope or the breaking-off in emission are obtained for a number of vibrational bands it is often possible to classify accurately the predissociation as belonging to a particular case. For instance, an inner wall (– superscript) crossing will show little variation of Γ with v since the slopes of the potentials will be very similar; thus the innermost maximum of the discrete wavefunction will move to smaller R very slowly. In contrast, outer wall (+ superscript) crossings often show an oscillatory variation of Γ with v due to rapid

variation of the Franck-Condon factor in equation 1.40. The classification determined from experimental data may then be used as a guide when attempting to model theoretically the predissociation mechanism.

Predissociation may also be classified in terms of the interactions responsible for the mixing of the bound and continuum levels. In the rotational Hamiltonian (equation 1.15) the terms $J_{\pm}L_{\mp}$ and $L_{\pm}S_{\mp}$ can give rise to matrix elements off-diagonal in electronic state, all of which may cause predissociation. However, the most frequently encountered interaction responsible for predissociation of diatomic molecules is the J-independent spin-orbit interaction, especially between different spin states. This interaction originates from the $\hat{l}_i^{\pm}.\hat{s}_i^{\mp}$ terms in both the rotational Hamiltonian (equation 1.15) and the spin-orbit part of the Hamiltonian (equation 1.16) with the contribution from $\hat{H}_{SO}$ dominating. In this limit the $\Delta S=0$ selection rule often quoted for predissociation is no longer valid and the interaction arises between states of the same Ω.

1.3 Traditional methods of Laser Spectroscopy

1.3.1 Absorption - The Beer-Lambert Law

The absorption and emission of electromagnetic (EM) radiation by atoms or molecules are the key physical processes used in spectroscopic analysis. The absorption of light by a sample is described by the Beer-Lambert Law [19] which gives a quantitative relationship between the intensity of a spectral feature and the frequency dependent absorption properties of the sample:

$$I = I_0 \exp[-\sigma C \ell] \qquad (1.41)$$

Here, I_0 and I are the intensities of light entering and leaving the sample respectively, C is the concentration of the absorber, ℓ is the sample path length, and σ is the absorption cross-section of the sample at the particular wavelength of the light. The product of C and σ is the absorption coefficient, α, and the absorbance is defined as $\sigma C \ell$.

Conventional (non-laser) implementations of absorption spectroscopy require broad-band or continuum light sources, with the wavelength dependence of absorption obtained by dispersing the light that exits the sample through a monochromator. To achieve high resolution, narrow monochromator slits must be used and the light is dispersed over a large distance (of the order of metres) before reaching the detector (traditionally a photographic plate, but more recently a diode array or ccd camera), thereby decreasing the throughput. The inherent non-linearities in detection of light using photographic plates makes quantitative interpretation of spectral lineshapes and linewidths unreliable. Using tunable laser sources, however, it is possible to record absorption spectra by detecting the change in intensity of the beam emerging from the sample as the laser wavelength is varied. The sensitivity of any absorption technique is ultimately governed by the path length of the beam through the sample, and thus the sensitivity may be increased by using a multiple-pass (*e.g.*, White cell) arrangement, [20] *e.g.*, 50 traversals of a 20-cm cell results in an *effective path length* of 10 m.

The main problem with laser absorption spectroscopy when detecting inherently weak absorptions (*e.g.*, electric-dipole forbidden but magnetic-dipole allowed transitions such as the O_2 $b^1\Sigma_g^+$-$X^3\Sigma_g^-$ system, or trace gas detection) is that the change in intensity of the light as it passes through the sample is very small compared with the initial laser intensity, so the sensitivity is generally limited by fluctuations in I_0. Several other laser-based methods of obtaining absorption-like spectra exist, however, which rely upon some subsequent side effect of the excitation process; some examples of such are briefly outlined below.

1.3.2 Laser-Induced Fluorescence (LIF)

Following the absorption of a photon of light, an electronically excited molecule may decay to its ground state by emission of radiation, a process known as fluorescence. By monitoring this fluorescence (generally at 90° to the laser beam) molecular absorption can be detected as the input laser wavelength is scanned [21]. LIF is, at least in theory, a zero-background technique, but some sources of noise are inevitable, the principal one usually being scattered laser light from optical surfaces. LIF is thus a highly sensitive absorption technique: for example, for detection of tropospheric OH, a sensitivity of 1.8×10^6 molecules cm^{-3} was recently demonstrated and further improvements have since been made [22]. Detection of fluorescence is ultimately limited by the quantum efficiency of the photomultiplier tube (PMT). A primary limitation of LIF is the requirement that the excited state have a large fluorescence quantum yield. Many excited electronic states decay via other competing pathways such as predissociation or collisional quenching and thus show little or no fluorescence. Also, LIF is generally restricted to excitation wavelengths in the visible and UV regions of the electromagnetic spectrum since fluorescence rates are much slower at longer wavelengths. Examples of small molecules and radicals commonly probed by LIF include I_2, NO, OH, CH, CN, NO_2 and CO.

1.3.3 Resonance-Enhanced Multiphoton Ionisation (REMPI)

A molecule can be induced to absorb two or more photons simultaneously provided the intensity of light is sufficiently high to compensate for the very small cross sections for such processes. Typically, small molecules composed of light atoms will

have ionisation potentials around 10-15 eV [1] corresponding to the absorption of three UV photons from the ground state of the neutral molecule. The cross section of this process is greatly enhanced if there is a real excited state resonant at the energy of one or two absorbed photons. By monitoring the photoionisation yield as the laser is scanned, a spectrum corresponding to absorption to the resonant state is obtained.[23-25] REMPI has certain advantages over single photon spectroscopy; in particular different selection rules for multiphoton transitions allow many previously unobservable transitions to be seen (*e.g.*, for a 2-photon absorption, g↔g and u↔u transitions in a centrosymmetric molecule), and it can be mass selective if used in combination with time-of-flight (TOF) detection. If the resonant state is heavily predissociated, however, little or no ion formation will occur. Key species detected by REMPI include H_2, HCl and CH_3.

1.3.4 Photoacoustic Spectroscopy

Absorption of EM radiation raises the internal energy of the molecules in a sample. This energy can be dissipated to a bath gas via collisions that cause vibrational to translational (V→T) energy transfer, resulting in a local, thermally induced pressure increase. A pulsed laser will thus generate pressure waves when tuned to be resonant with an absorption feature of the sample gas, and these pressure waves may be monitored by a piezoelectric detector or a microphone placed within the sample cell. The intensity of the sound detected depends on the degree of heating which in turn is related to the strength of the absorption: hence, plotting sound level versus laser frequency yields an absorption spectrum [26] Photoacoustic spectroscopy is a highly sensitive form of laser absorption spectroscopy, for example, Zare and coworkers [27] specified a limiting absorption coefficient of 4×10^{-10} /cm. The technique has thus found extensive applications in the study of high vibrational overtones of small hydride molecules.

1.3.5 Intra-Cavity Laser Absorption Spectroscopy (ICLAS)

An absorber placed within a laser cavity can alter the gain and hence the output of the laser. Therefore by placing a narrow band absorber into the cavity of a laser and determining the gain at different wavelengths, an absorption spectrum can be obtained. The wavelength-dependent gain can be determined either by tuning the (narrow-band)

laser or by using a broad-band multimode laser and dispersing the output light with a high resolution spectrograph. Quantitative intensity measurements may be extracted from these spectra, allowing concentrations or oscillator strengths to be determined. ICLAS is a very sensitive technique which may be performed in the visible using a dye laser or the infra-red using a colour-centre laser, and has been applied to a number of species to measure high overtone spectra [28] and absolute concentrations, such as for HCO in a methane/air flame [29].

1.3.6 Stimulated Emission Pumping (SEP)

The principle of the SEP technique [30] is as follows: one laser (the PUMP laser) is used to prepare a single rovibrational level in an excited electronic state. The spontaneous fluorescence is monitored while a second laser (the DUMP laser) is scanned over the region of interest. On resonance the DUMP laser stimulates emission back to the ground electronic state levels and causes a drop in the intensity of spontaneous emission (since the stimulated emission comes out parallel to the DUMP laser and therefore will not reach the detector mounted perpendicular to the laser beam axis). The SEP technique has found enormous use in studying a wide range of rotation-vibration levels of ground electronic states and other low lying electronic states of diatomic and polyatomic molecules [31,32]. It is particularly useful for studying polyatomic molecules where it can complement overtone spectroscopy by providing information on otherwise inaccessible parts of the potential (if a suitable intermediate electronic state is chosen that differs in geometry from the ground state thus accessing high lying vibrational levels or bending modes). Also the resultant spectra are greatly simplified since only transitions from one excited state rovibrational level are observed. The technique does, however, suffer the limitation of the requirement of the excited state to fluoresce thus ruling out many predissociating states. Another practical limitation is caused by fluctuations in the PUMP laser intensity; thus if the depletion in fluorescence is very small it will not be seen over the background noise (depletions of around 1% of the total fluorescence are the lower limit).

1.4 Overview of this work

The aim of the following work was to test the applicability of two novel laser-based spectroscopic techniques for studying the electronic spectroscopy and dynamics of several diatomic species.

Chapter 2 introduces the technique of Cavity Ring-Down Spectroscopy (CRDS) and reviews some of the advantages and potential drawbacks compared with other more traditional laser absorption spectroscopies. In Chapters 3 and 4 CRDS is used to provide an investigation of the predissociation mechanisms occurring in SH / SD($A^2\Sigma^+$) and $S_2(B^3\Sigma_u^-)$ by the measurement of lifetime broadened linewidths. To complement the experimental investigations detailed theoretical analysis is also presented to rationalise the observations and gain an insight into which states are involved in the predissociations. Chapter 5 demonstrates a possible detection scheme using CRDS for the atmospherically important radical, BrO.

In Chapter 6 the non-linear technique of Two-Colour Laser-Induced Grating Spectroscopy (TC-LIGS) is discussed in the context of the benchmark system of molecular iodine. Various ways of using TC-LIGS are demonstrated resembling the more traditional spectroscopic methods of Stimulated Emission Pumping (SEP) and UV-visible double-resonance.

The general merits and disadvantages of both CRDS and TC-LIGS for molecular spectroscopy are summarised in Chapter 7 and some recent developments and future possibilities are highlighted.

References

1. G. Herzberg, *Molecular Spectra and Molecular Structure*, Volume I - Spectra of Diatomic Molecules, Van Nostrand Reinhold Company Inc. (1950) and references therein.
2. J. I. Steinfeld, *Molecules and Radiation, An Introduction to Modern Molecular Spectroscopy*, MIT Press, (1974) and references therein.
3. H. Lefebvre-Brion and R.W. Field, *Perturbations in the Spectra of Diatomic Molecules*, Academic, New York, (1986) and references therein.
4. C.M. Western, *Chem. Soc. Rev.*, **24** (1995) 299.
5. I.N. Levine, *Quantum Chemistry*, Prentice-Hall, (1991).
6. J. Simons, *J. Phys. Chem.*, **95** (1991) 1017.
7. P.M. Morse, *Phys. Rev*, **34** (1929) 57.
8. J. Tellinguisen, *J. Mol. Spec.*, **44** (1972) 194.
9. A. Messiah, *Quantum Mechanics* Wiley, New York, (1964) Vol. I, Sec, VI-6.
10. T.H. Dunning, *J. Chem. Phys.*, **53** (1970) 2823.
11. J. T. Hougen, *'The Calculation of Rotational Energy Levels and Rotational Energy Levels in Diatomic Molecules'*, NBS monograph 115, Washington D.C., 1970.
12. R.N. Zare, *Angular Momentum (Understanding Spatial Aspects in Chemistry and Physics)*, John Wiley and Sons, Inc., (1988).
13. H. Katô and M. Baba, *Chem. Rev.*, **95** (1995) 2311 and references therein.
14. A.H. Zewail, *J. Phys. Chem.*, **100** (1996) 12701 and references therein.
15. U. Fano, *Phys. Rev.*, **124** (1961) 1866
16. A. Messiah, *Quantum Mechanics* (Wiley, New York, 1964) Vol. II, Sec, XVII-4.
17. J. Tellinguisen, *Adv. Chem. Phys.*, **60** (Photodissociation and Photoionisation, ed. K.P. Lawley) (1985) 299.
18. R.S. Mulliken, *J. Chem. Phys.*, **33** (1960) 247.
19. P.F. Bernath, *Spectra of Atoms and Molecules*, Oxford University Press, New York (1995).
20. J. Ballard, K. Strong, J.J. Remedios, M. Page and W.B. Johnston, *J. Quant. Spectrosc. Radiat. Transfer*, **52** (1994) 677.
21. J. Pfab in *Applied Laser Spectroscopy: Techniques, Instrumentation and Applications*, ed. D.L. Andrews, VCH Publishers Inc., New York (1992).
22. D.J. Creasey, P.A. Halford-Maw, D.E. Heard, M.J. Pilling, and B.J. Whitaker, *J. Chem. Soc. Faraday Trans.*, **93** (1997) 2907; D.E. Heard and M.J. Pilling, private communication.
23. M.N.R. Ashfold, S.G. Clement, J.D. Howe, and C.M. Western, *J. Chem. Soc. Faraday Trans.*, **89** (1993) 1153.

24. M.N.R. Ashfold and J.D. Howe, *Ann. Rev. Phys. Chem.*, **45** (1994) 57.
25. M.N.R. Ashfold, *Mol. Phys.*, **58** (1986) 1.
26. W. Demtroder, *Laser Spectroscopy*, Springer-Verlag, Berlin (1981).
27. J. Davidson, J.H. Gutow, and R.N. Zare, *J. Phys. Chem.*, **94** (1990) 4069 and references therein.
28. A. Campargue, F. Stoeckel, M. Chenevier, *Spectrochimica Acta Reviews*, **13** (1990) 69.
29. V.A. Lozovsky, S. Cheskis, A. Kachanov, F. Stoeckel, *J. Chem. Phys.*, **106** (1997) 8384.
30. Hai-Lung Dai, *Nonlinear Spectroscopy for Molecular Structure Determination*, ed. by E. Hirota, R.W. Field, J.P. Maier, and S. Tsuchiya (IUPAC, 1997), chapter 3, 54.
31. C.E. Hamilton, J.L. Kinsey, and R.W. Field, *Ann. Rev. Phys. Chem.*, **37** (1986) 493.
32. F.J. Northrup and T.J. Sears, *Ann. Rev. Phys. Chem.*, **43** (1992) 127.

2. Cavity Ring-Down Spectroscopy

2.1 Introduction

In recent years a new, ultra sensitive laser absorption spectroscopy technique has developed [1], evolving from previous techniques used, for example, to measure mirror reflectivities [2,3]. The technique is most widely known as Cavity Ring-Down Spectroscopy (CRDS), although the alternative, but more cumbersome, Cavity Ring down Laser Absorption Spectroscopy (CRLAS) is preferred by some authors. The CRDS technique is a direct absorption spectroscopy that eliminates the effect of shot-to-shot intensity fluctuation of the source laser, and which benefits from tremendously long path lengths (up to 30 km) through a sample on a bench top apparatus. In CRDS, a laser pulse is trapped inside a high finesse optical cavity containing the sample, and the pulse decay time as a function of wavelength is measured by monitoring light exiting one of the mirrors with a photosensitive detector. It is relatively simple to implement experimentally but, until recently, progress has been hampered by the lack of commercially available ultra high reflectivity mirrors required for the experiments

In this chapter, some of the recent applications of CRDS are briefly discussed, followed by an outline of the basic principles and experimental considerations involved in the implementation of the technique.

2.2 Recent applications of CRDS

2.2.1 Kinetics Measurements

Lin and co-workers first applied CRDS to the study of rates of chemical reactions using laser pump and probe techniques, with the traditional probe methods such as LIF or laser absorption replaced by CRDS detection [4,5,6,7]. They performed extensive studies of the reactions of the phenyl radical with species such as O_2, [8] CCl_4, [9] cycloalkanes, [10] and HBr [11,12]. These studies were conducted over a range of temperatures, and relied on detection either of C_6H_5 at 504.8 nm or $C_6H_5O_2$, formed by adding small amounts of O_2 to the reaction mixture, at 496.4 nm. The same group has since studied the reaction of NH_2 with NO by photolysing NH_3 at 193 nm in the presence of NO and monitoring the loss of absorption by NH_2 at 537.6 nm [13].

Atkinson and Hudgens [14] compared measurements of the rates of reaction of $C_2H_5 + C_2H_5$, $C_2H_5O_2 + C_2H_5O_2$, and $O_2 + C_2H_5 + Ar$ using CRDS detection with rates determined by alternative methods and found good agreement, thereby demonstrating the validity of CRDS as a tool for measurement of reaction rate coefficients. These experiments used XeCl excimer laser photolysis of Cl_2 to initiate a sequence of reactions in a mixture of Cl_2, ethane, O_2 and argon, with Cl-atom abstraction of H from C_2H_6 forming C_2H_5. A combination of a cylindrical lens and a beam mask in the path of the photolysis laser provided a well-defined pathlength over which the CRDS detection of reactive species occurred. More recently, the same authors [15] have determined the rate of self reaction of the propargyl radical (CH_2CCH), formed by the 193-nm photolysis of methyl acetylene.

2.2.2 High Overtone Spectroscopy

High vibrational excitation of molecules may be used to characterise the topology of ground state potential energy surfaces in regions energetically distant from the bottom of the potential well. Information can also be obtained about intramolecular energy flow and the possible evolution of regular to chaotic energy level structure. High-overtone transitions are inherently weak, however, and therefore require very sensitive probe

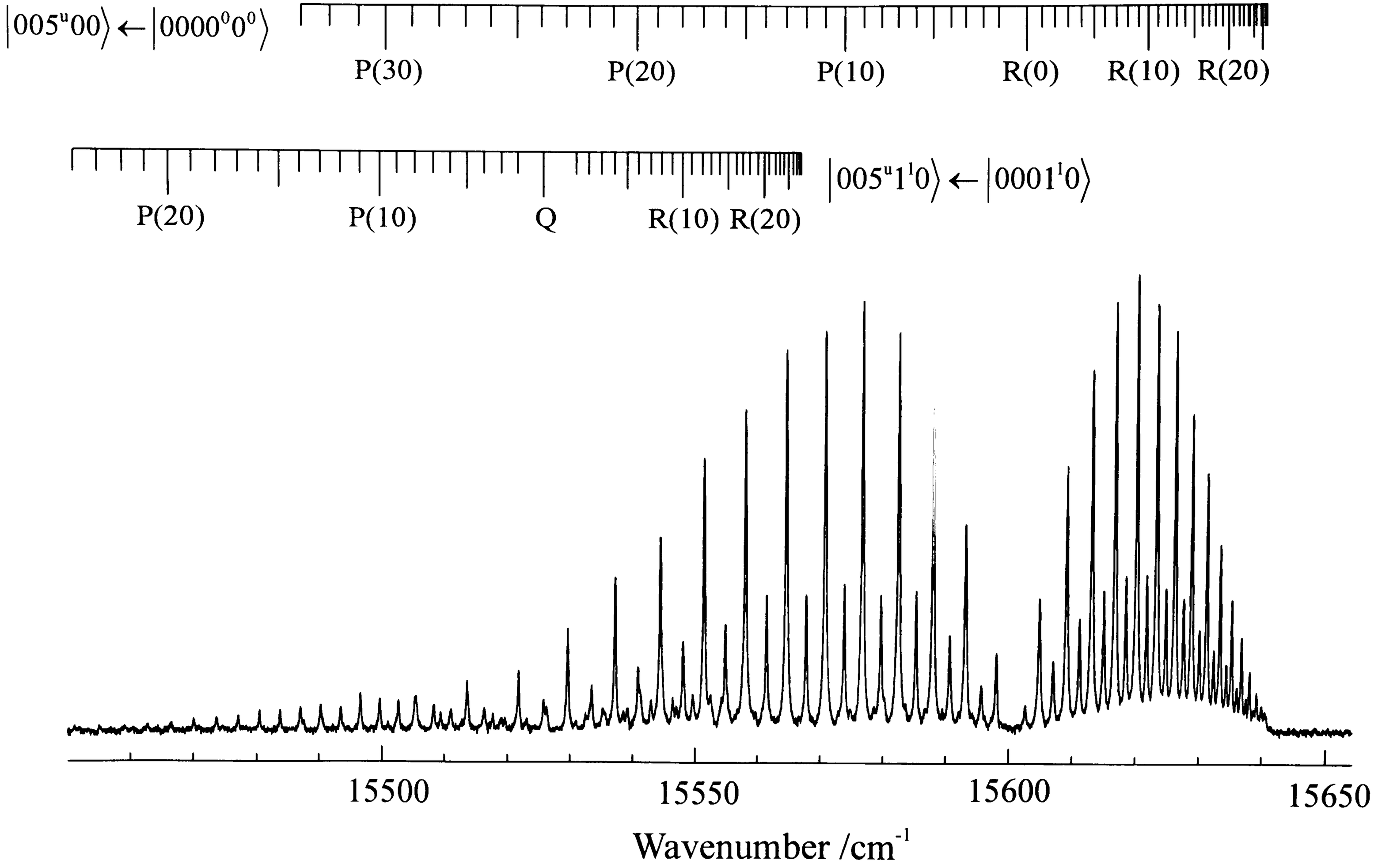

Figure 2.1. CRD Spectrum of the 4th C-H Stretching Overtone of C_2H_2

techniques. Photoacoustic spectroscopy has, until recently, been the probe method of choice, but CRDS also has sufficient sensitivity and has the distinct advantage of being a direct absorption technique allowing quantitative studies of transition intensities. In our lab CRDS and photoacoustic spectra have been recorded of the 4th C-H stretching overtones of C_2H_2 (see Figure 2.1) and C_2HD. We observe similar signal-to-noise ratios for similar pressures of the gases in the two experiments. The validity of an absolute comparison of the relative sensitivities is not well addressed by our experiments since in neither case did we try hard to optimise the signal-to-noise ratio. We note, however, that for the CRDS detection, much lower laser intensities are required, and because only a very small percentage of the laser intensity enters the ring-down cavity, power broadening effects evident in the photoacoustic spectrum are entirely absent in the CRD spectrum.

The observed line positions and intensities for overtone spectra are strongly dependent on the shape of the portion of the potential energy surface probed and may be compared with theoretical values obtained using *ab initio* or empirically determined potentials in order to test and further refine these potentials. Romanini and Lehmann [16,17] have used CRDS to extend the range of observed C-H stretching overtones in HCN up to six, seven and eight stretching quanta for various isotopomers, and compared their observed spectroscopic frequencies and constants with those derived from various calculated potential energy surfaces. They found few perturbed bands despite the very high vibrational excitation.

CRDS is now being extended to the spectroscopy of the fundamental vibrations of molecules lying in the infra-red region of the spectrum. Rakestraw and coworkers observed the IR-active ν_3 mode of CH_4 via its fundamental transition in a static cell [18] and determined concentrations of CH_3 in a laminar flame [19], and Saykally and coworkers have reported IR CRDS spectra of the $(H_2O)_n$ n=1-6 clusters [20,21,22].

2.2.3 Electronic spectroscopy

The exceptional sensitivity of CRDS makes it ideally suited to the investigation of weak molecular transitions or of molecules present at low concentrations, and the

technique has the added advantage of providing quantitative spectral intensities. These features have been exploited in studies of electronic transitions of a range of gas-phase molecules.

Slanger *et al.*[23,24] observed and characterized five new bands of the O_2 Herzberg system in the 40950-41300 cm^{-1} region, namely the (12,0) and (13,0) bands of the $A'^3\Delta_u$-$X^3\Sigma_g^-$ transition, the $c^1\Sigma_u^-$-$X^3\Sigma_g^-$ (17,0) and (18,0) bands, and the $A^3\Sigma_u^+$-$X^3\Sigma_g^-$ (12,0) band, and were able to determine improved spectroscopic constants. Engeln *et al.* [25] demonstrated the utility of phase shift cavity ring-down spectroscopy by obtaining a spectrum of the very weak $b^1\Sigma_g^+$-$X^3\Sigma_g^-$ (2,0) band of $^{18}O_2$. A combination of CRDS with a hollow cathode discharge enabled Maier and coworkers to observe the N_2^+ $A^2\Pi_u$-$X^2\Sigma_g^+$ (6,0) band [26] and a $^2\Pi$-$X^2\Pi$ transition of C_6H (and C_6D) [27] The C_6H radical is of interest in radioastronomy, and pairs of bands due to the $^2\Pi_{1/2}$ -$X^2\Pi_{1/2}$ and $^2\Pi_{3/2}$ -$X^2\Pi_{3/2}$ components were identified. Band origins were accurately determined, improving on values from previous matrix-isolation studies. Lehr and Hering [28] recently made comparisons of the linear CRDS and non-linear Degenerate Four-Wave Mixing (DFWM) techniques using the spectrum of NaH as a test case. They reported sensitivities of 10^9 molecules per cm^3 per quantum state.

CRDS offers an ideal approach to studying electronic spectroscopy of small and even medium-sized cluster systems where rapid internal conversion and predissociation processes often occur upon excitation. Saykally and coworkers have to date applied CRDS spectroscopy to a variety of bare metal dimers and trimers such as Cu_2, Cu_3[29], and Al_2 [30] and metal silicides such as CuSi [31], AgSi [32], AuSi [33], and PtSi [34] using a novel, long path length, pulsed slit-valve apparatus [35,36].

In our laboratory the primary application of CRDS to date has been the study of predissociation in excited electronic states of diatomic and triatomic radicals. The HNO molecule is of particular interest in the field of molecular dynamics both for its complicated predissociation behaviour and for the comparisons that can be drawn between it and the HCO and HO_2 radicals. Earlier work at Bristol by Dr. Jon Pearson [37] consisted of an investigation of several vibrational bands (v_1,v_2,v_3) (v_1 is the N-H

stretch, v_2 the N=O stretch, and v_3 the H-N=O bend) of the $\tilde{A}\ ^1A''$- $\tilde{X}\ ^1A'$ transition and their underlying K' sub-structure using CRDS. The spectra revealed perturbations of the $\tilde{A}$ -state levels and, for excitation to levels of the $\tilde{A}$ -state lying above the dissociation limit, showed J' dependent line broadening occurring within several of the bands. This latter observation indicated a rotationally induced predissociation mechanism.

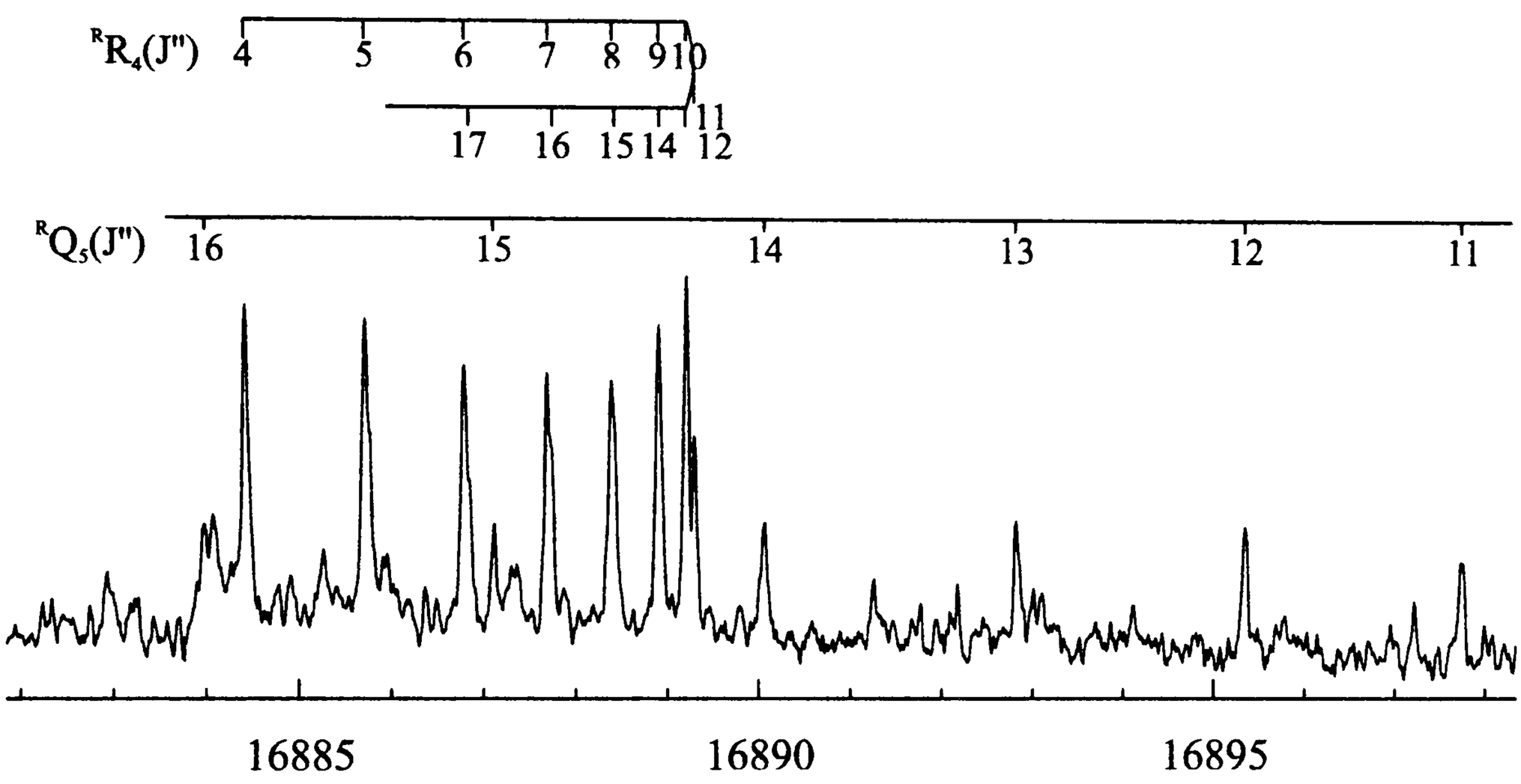

Figure 2.2. Portion of the CRD spectrum of the $\tilde{A}\ ^1A''$- $\tilde{X}\ ^1A'$ (110)-(000) transition of DNO showing the $^RR_4$ and $^RQ_5$ sub-bands.

To complement this work CRD spectra were recorded of the deuterated analogue DNO in order to investigate isotopic effects on the dynamics and spectroscopy. Dixon and Rosser [38] measured a J-dependent breaking-off in fluorescence in a total of six sub-bands within three vibronic transitions (020)-(000), (021)-(000), and (110)-(000). By extrapolation to J=0 they determined a limiting curve for predissociation with limit of 17030 ± 10 cm^{-1}. The difference (580 cm^{-1}) in the predissociation limits for the two isotopomers is due to the difference in zero point energies of the two ground states. Many perturbations were observed with much smaller shifts (<0.3 cm^{-1}) than are observed in HNO (up to 1.4 cm^{-1}). Using our CRDS apparatus spectra of DNO were

recorded in order to investigate any line broadening above the predissociation threshold, an example spectrum of part of the (110)-(000) band is shown in Figure 2.2 in the range 16880-16900 cm^{-1}. Only three K' sub-bands were seen above the threshold for this vibronic transition K'=5 - K"=4, K'=6 - K"=5, and K'=7 - K"=6 - this is mainly a consequence of poor Franck-Condon factors rather than lines becoming broader due to predissociation. There is no observable line-broadening in any of our spectra suggesting that the coupling between the $\tilde{A}$ and $\tilde{X}$ states is much weaker than in HNO. This observation is entirely consistent with the predissociation model proposed for HNO, since the second order a-axis Coriolis coupling is proportional to A^2, therefore if the linewidths scale in accordance with this the maximum expected linewidth for DNO would be only 0.08 cm^{-1} rather than 0.3 cm^{-1}.

2.3 Fundamentals of Cavity Ring-Down Spectroscopy

Traditional absorption spectroscopy measurements determine the attenuation of a light beam passed through a sample and measure absorption coefficients from the ratio of intensities of the light exiting and entering the sample container via the Beer-Lambert law (equation 1.41). As such, these methods must measure a small change in a large intensity and hence require very stable light sources with small time-dependent intensity fluctuations. The approach used in a CRDS experiment differs because the quantity determined experimentally is the rate of decay of the light intensity within the cavity, and hence CRDS is much less sensitive to variations in the laser pulse intensity. In the following section the form of the decay of the light intensity, and how absorbances and absorption coefficients can be extracted from the decay rate are outlined together with the possible complications arising from cavity mode effects. Careful consideration of the cavity mode structure is important because the sample cell used in the CRDS apparatus is bounded by two high reflectivity mirrors without intervening surfaces and, just as in an etalon, the separation of the two fixed mirrors determines the mode structure and frequency spacing for light trapped within the cavity.

2.3.1 Decay of light in an optical cavity

As a first consideration of the behaviour of the light within the cavity, the etalon-like nature of the cavity will be ignored and just the decay of the intensity of the light at a particular wavelength will be considered. For an empty cavity bounded by two mirrors of reflectivity R, separated by a distance ℓ, the light intensity within the cavity will decay with an exponential time profile according to [16]:

$$I(t) = I_0 \exp\{-t/\tau\} \tag{2.1}$$

Here, $\tau = \ell/c\,|\ln R| \approx \ell/c(1\text{-}R)$ is the empty cavity ring-down time (RDT), the time for the intensity to decay to 1/e of its original value. Cavity losses by mirror transmission (T) and other processes such as diffraction and Rayleigh scattering are equal to (1-R). The empty cavity RDT is thus determined by these loss processes, and depends strongly on the reflectivity of the mirrors. For a cavity bounded by two mirrors of reflectivity R,

the number of round trips, N, performed in the time taken for the intensity to fall to 1/e of its initial value is obtained by solving $R^{2N} = 1/e$, or $N = -1/[2 \ln(R)]$. Thus, for example, for a mirror reflectivity of 0.999, N = 500, whereas for R = 0.99999, N = 50,000, giving a pathlength in a 1-m cavity of 100 km. The extreme sensitivity of CRDS is a consequence of these very long pathlengths for the probe light through a sample.

If the wavelength of the light within the cavity matches an absorption of a sample gas held between the mirrors, the additional mechanism for loss of light from the cavity by sample absorption speeds up the decay of the trapped light intensity. For absorption conditions corresponding to Beer-Lambert law behaviour, the decay of the light intensity will still be exponential, with time dependence given by [16]:

$$I(t) = I_0 \exp\left\{-\frac{t}{\tau} - \alpha c t\right\} \qquad (2.2)$$

Here α is the molecular absorption coefficient (with units of cm^{-1}) and c is the speed of light. The product of c and t is the pathlength, L, over which the absorption is measured. The decay rate is now given by $1/\tau' = 1/\tau + c\alpha$. The conditions under which equation (2.2) applies will be discussed in the next section.

If the empty cavity RDT, τ, is known, measurement of the decay rate of the light intensity as the wavelength of the laser is scanned gives the absorption coefficient for each laser wavelength, and hence the absorption spectrum. For a discrete spectrum, τ can be determined from the baseline level between absorption features (where $\alpha = 0$). Note that the quantity obtained is the absorption coefficient (or absorbance) and thus a knowledge of the partial pressure of the absorbing species within the cavity is required to extract absorption cross sections. Two simple methods for extracting spectra from the exponential decays recorded at each laser wavelength are:

(i) Direct fitting (e.g., least-squares fitting) of the exponential decay or of its logarithm [1]. The time region of the exponential fitted determines the effective pathlength through the sample. The fit will give the decay time τ'. This is the most satisfactory and

direct method, but it does, however, have the disadvantage that it requires a relatively fast computer in order to sample and fit the decay at the laser repetition rate of 10 Hz.

(ii) Romanini and Lehmann [16] have suggested an alternative method which involves setting two gates of equal width, t_w, on the exponential at some time separation Δt as shown in Figure 2.3. This time separation then determines the effective path length, and the signal is measured as [16]:

$$S = \ln\left\{\frac{S_A}{S_B}\right\} = -\frac{\Delta t}{\tau} - L\alpha \qquad (2.3)$$

where S_A and S_B are the signals measured in the first and second time gates. Clearly this manipulation of the S_A and S_B values gives a value that is directly proportional to the absorption coefficient. However, in practice it is necessary to correct for fluctuations and drifts in the baseline, this is achieved by setting a third gate at some sufficiently long delay such that the signal has decayed to zero. The signal from this third gate is then subtracted from S_A and S_B before taking the logarithm.

Both methods rely on the decay being a true exponential in order to extract accurate α values. In the work presented in the following chapters both of the above procedures were used and found to give essentially the same results. As Hudgens [39] has pointed out, care must be taken in any averaging procedure as it is mathematically incorrect to average out shot-to-shot fluctuations by adding a series of exponential decays for multiple laser shots at a particular wavelength and then to fit the resultant decay to obtain an absorption coefficient. The correct procedure must be to fit each decay separately and average the resultant absorption coefficients.

2.3.2 Conditions for recovery of a single exponential decay

Direct fitting of the decay of the light intensity exiting a CRDS cavity allows a constant check of the true single-exponential nature of the intensity decay. If Beer-Lambert behaviour for a single pass of the light through the cavity is violated, or if interference effects between the longitudinal and transverse modes of the cavity become

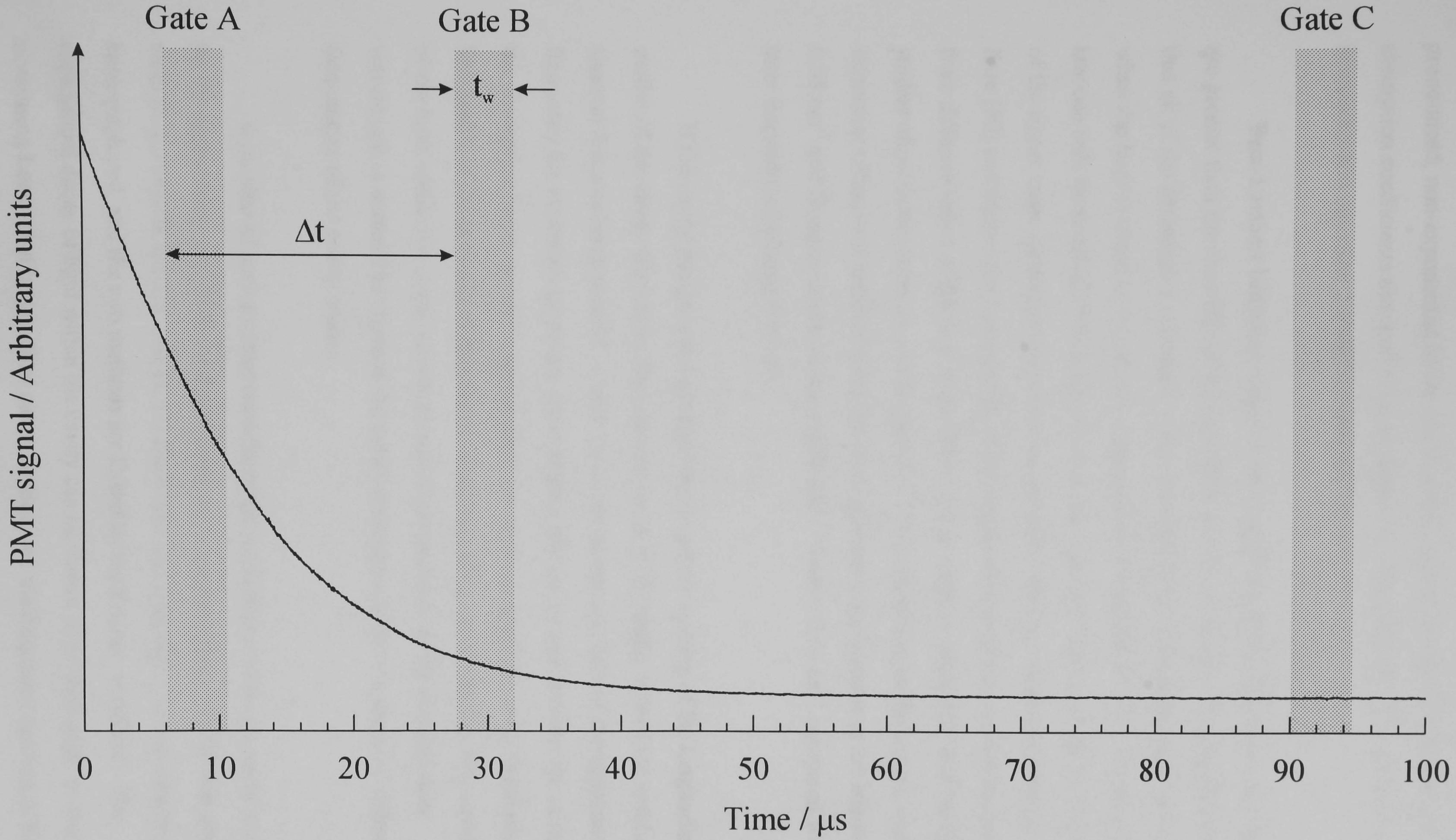

Figure 2.3. The decay of light in the ring down cavity monitored by the photomultiplier tube. The shaded areas represent the three gates of width t_w that are used to determine the absolute absorption as described in the text.

pronounced, non-exponential decay can be observed and spectral intensities and absorption coefficients obtained using analysis of a single exponential will become inaccurate and equation 2.2 will become invalid.

Beer-Lambert behaviour requires that the widths of the absorption spectral lines are greater than the linewidth of the laser light within the cavity. This condition ensures that all of the frequencies contained within the laser pulse are attenuated by absorption when the laser is tuned to the central frequency of the absorption line. The Beer-Lambert law can only be satisfied if the pulse duration, t_p, is greater than T_2, with T_2, the lifetime of the upper state, determined by radiative and non-radiative decay rates. Zalicki and Zare [40] considered the inaccuracies of the extracted absorption coefficients arising from different ratios of the laser linewidth to the absorption linewidth. For the CRDS studies of predissociation on a timescale of < 100 ps described in the current work, this important criterion is satisfied since the homogeneous contributions to the linewidth is $>$ 0.05 cm^{-1} and Doppler widths in the visible and UV are > 0.04 cm^{-1} compared with a laser linewidth of around 0.07 cm^{-1}.

If the cavity design is not optimal, the frequency spacing of the longitudinal modes of the cavity (the cavity free spectral range, FSR) might exceed the widths of the spectral features being studied. Under these circumstances, light of the appropriate frequency for excitation of certain spectral lines will not be injected into the cavity and the absorption features will be absent from the resultant spectrum [41]. Similarly, if the bandwidth of the probe laser is narrower than the cavity mode spacing, the wavelength of the light within the cavity cannot be tuned continuously as the external laser wavelength is scanned but instead the cavity response will show a series of spikes at the frequencies of the cavity modes.

A number of authors have considered the implications of cavity mode structure on the applicability of CRDS for determining accurate absorption coefficients and for recording complete spectra. [40,41,42] Both time and frequency domain treatments have been employed, and the two methods are linked by the Fourier transform. The exponential decay of light within the cavity can be shown to be equivalent to the cavity possessing Lorentzian longitudinal cavity modes, and the frequency spacing of these

cavity modes, $\Delta\nu$, depends on the round-trip time, t_r, of light within the cavity (and hence the separation of the cavity mirrors, ℓ) according to:

$$\Delta\nu = \frac{1}{t_r} = \frac{c}{2\ell} \tag{2.4}$$

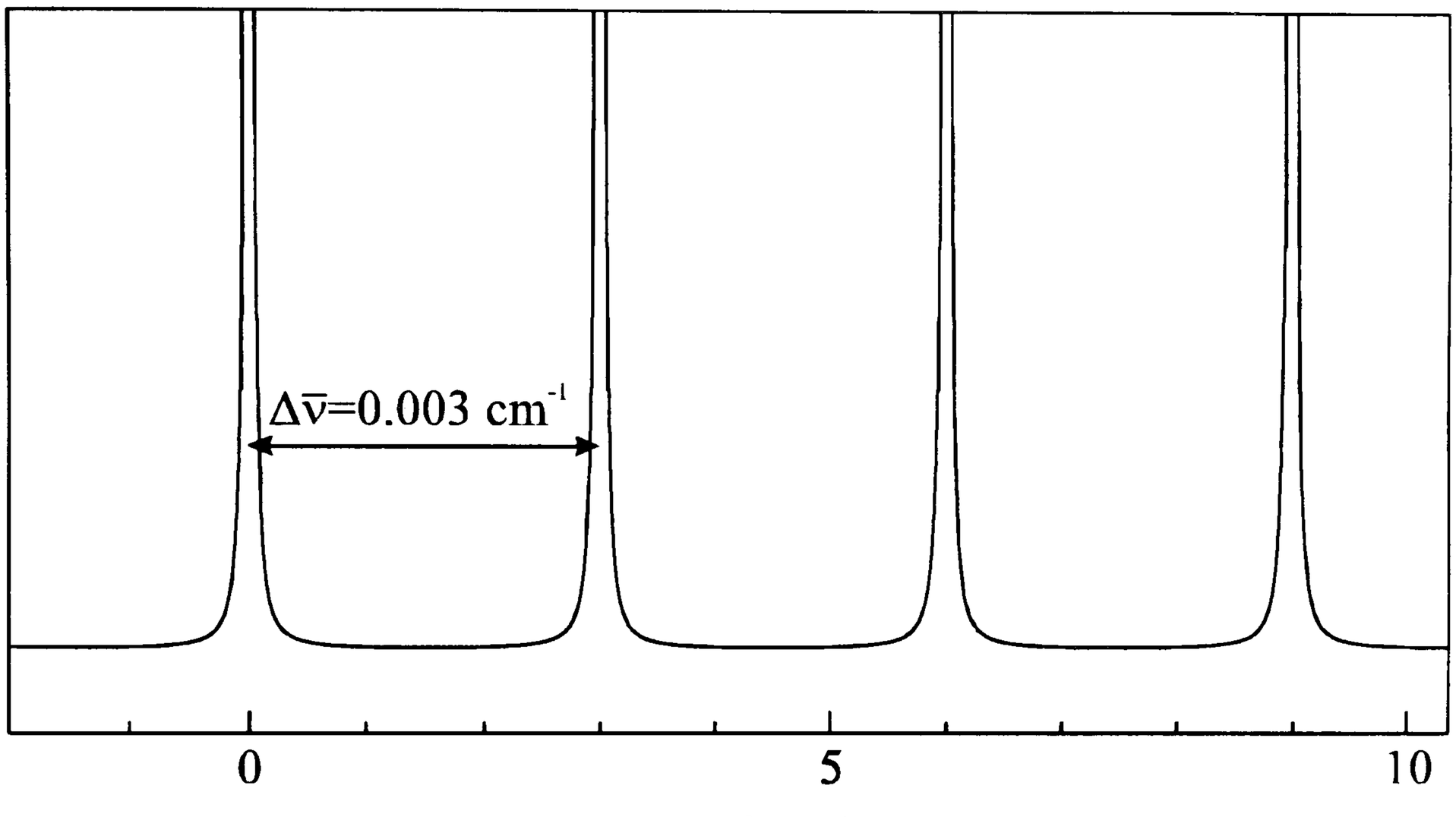

Figure 2.4. The calculated mode structure of a 1.6 m long cavity.

Thus for the 1.6-m cavity used in our experiments, the longitudinal mode spacing for the TEM_{00} transverse mode is 94 MHz (or in wavenumber units $\Delta\bar{\nu} = 0.003\ cm^{-1}$), as shown in Figure 2.4. The sharpness of these cavity modes and the contrast of the transmittivity of the cavity for frequencies at and between the mode maxima depends on the mirror reflectivity and hence the decay time. For experiments in which the laser light pulse is not carefully tailored to match the TEM_{00} mode of the cavity, or is not injected perfectly axially into the cavity, transverse cavity modes will be established that have frequencies lying between those of the longitudinal cavity modes. As discussed by Lehmann and Romanini [41] and Hodges *et al.* [42], even in the impulsive limit of a laser pulse having a duration shorter than the cavity round-trip time (so that the front end of the pulse doesn't overlap the rear end propagating in the same direction) the frequency

components of the pulse within the cavity must still match cavity mode frequencies for transmission into and through the cavity. Provided the bandwidth of the light injected into the cavity spans several cavity modes, however, the probe laser can be scanned continuously and give a ring-down intensity at all nominal laser wavelengths. In practice, the frequency restrictions imposed by cavity longitudinal modes are considerably relaxed by transverse mode structure and by cavity instabilities, so that the frequencies supported by a cavity are essentially continuous. If the coherence length of the laser pulse is less than the round trip time within the cavity, the laser bandwidth will exceed the cavity longitudinal mode spacing. A dye laser bandwidth of ~ 0.07 cm^{-1} means that in our 1.6-m cavity at least 22 cavity longitudinal modes are spanned for each dye laser wavelength setting. For higher resolution lasers, such as cw seeded pulse-amplified dye lasers and optical parametric oscillators (OPOs), or cw ring dye lasers, however, a careful consideration of the effects of cavity modes becomes more critical. Molecular absorption features must also overlap one or more cavity modes to contribute to the decay of light within the cavity (i.e., to feature in the recorded spectrum).

Excitation of a single, Lorentzian cavity mode will result in exponential decay of the light intensity within the cavity. The effect of exciting numerous cavity modes is to give a multiple exponential decay unless the different modes have the same losses per round trip. Even in this instance, beating between the different frequency components can result in a modulation of the exponential decay. In addition, for a cavity excited on numerous transverse cavity modes, the light emitted from the cavity can experience temporal interference because of beating between the slightly different decay rates of the separate TEM_{mn} modes. This mode beating can lead to non-exponential decays, and oscillatory structure superimposed on the decay envelope, as demonstrated by Zare and coworkers [43] for the excitation of a 50-cm cavity using transform-limited pulses from an IR OPO. The laser pulses had a coherence time and pulse duration greater than the round trip cavity time, and the resultant decays show severe oscillations in amplitude. Generally, however, this mode beating is much faster than the decay time of the exponential and hence can be filtered electronically or averaged out in the fitting. Under most circumstances, the amplitude of oscillations caused by mode-beating is small compared to the decay trace of interest, however, and the exponential decay rate can be extracted by fitting the decay envelope. Collection of the entire cross section of the

beam at the detector is important to suppress transverse mode beating effects. Transverse modes can also be suppressed either by spatially matching the input laser beam to the TEM_{00} mode of the cavity or by placing apertures in the cavity. If the mirror coatings are not of uniform reflectivity across the different profiles of the different transverse cavity modes, multiple-exponential decays can arise as a result of different losses for the different modes.

A final potential pitfall that merits mention here is the coherent interaction of molecules with the recurring laser pulse if the lifetime of the excited molecular state (with dephasing time T_2) exceeds the cavity round trip time. This regime of timescales has been discussed at length [40], and for the studies of predissociation in the following work, the lifetimes of the upper state are typically < 100 ps and we need not concern ourselves with the effect of recurrent pulses within the cavity. Note that if $T_2 < t_r$ the absorption feature will span many cavity modes, and similarly for $T_2 < t_p$, the requirement that the laser bandwidth is narrower than the absorption feature will be satisfied for transform limited pulses.

The general conclusion of detailed considerations of the possible causes of spectral inaccuracies in CRDS, however, is that in the bulk of experiments performed to date, cavity mode effects have not significantly distorted the measured spectra. The method is most prone to mode effects when either the absorption lines are very sharp or the bandwidth of the laser is comparable to or less than the free spectral range of the cavity.

2.4 Experimental Principles

The CRDS apparatus used in the following work consisted of a pulsed dye laser system, a glass flow tube bounded by high reflectivity mirrors, signal detection and acquisition electronics, and wavelength calibration equipment. A schematic diagram of the ring-down apparatus is shown in Figure 2.5.

The laser system consisted of a Nd:YAG (Quantel YG680 (10 ns pulse width at10 Hz)) laser, operating at either 532 nm or 355 nm, pumping a dye laser (Spectra Physics PDL-3) to generate tuneable light in the range 500-680 nm using a number of dyes. This light was frequency doubled in either a KDP or BBO crystal to produce the required UV light over the range 250-340 nm. The phase match angle of the doubling crystal was controlled by a homebuilt autotracker. Typically, UV pulse energies were a few mJ of which only a small fraction (a few μJ) entered the ring-down cell due to the very high mirror reflectivities.

The ring-down cavity consisted of a pair of high reflectivity mirrors mounted in PTFE disks connected to a glass flow cell by flexible bellows. Fine control of the mirror positions is essential for accurate alignment of the cavity and was achieved using micrometer screws mounted alongside the bellows allowing complete translational freedom. The mirrors were manufactured from a quartz substrate 7.75 mm diameter, 4 mm thickness, and 1 or 2 m radius of curvature, with the coating laid down on the curved sides of the mirrors. This arrangement can cause etaloning effects between the two surfaces of the mirror [16], but was found not to be problem in our experiments. To facilitate easy alignment of the mirrors a 632.8 nm Helium-Neon laser was used to define the axis of the cavity and the UV beam was counter-propagated along this axis using a number of irises placed along the beam path. This rough alignment was then finely adjusted in order to maximise the decay time by monitoring the time extent of the trace on the oscilloscope. The trace was then transferred to a PC for inspection in order to test for purely single exponential behaviour. The (1/e) ring-down times varied according to which mirror set was used but were typically in the range of 6 -10 μs over the whole wavelength region scanned corresponding to effective absorption pathlength of 1.8 -

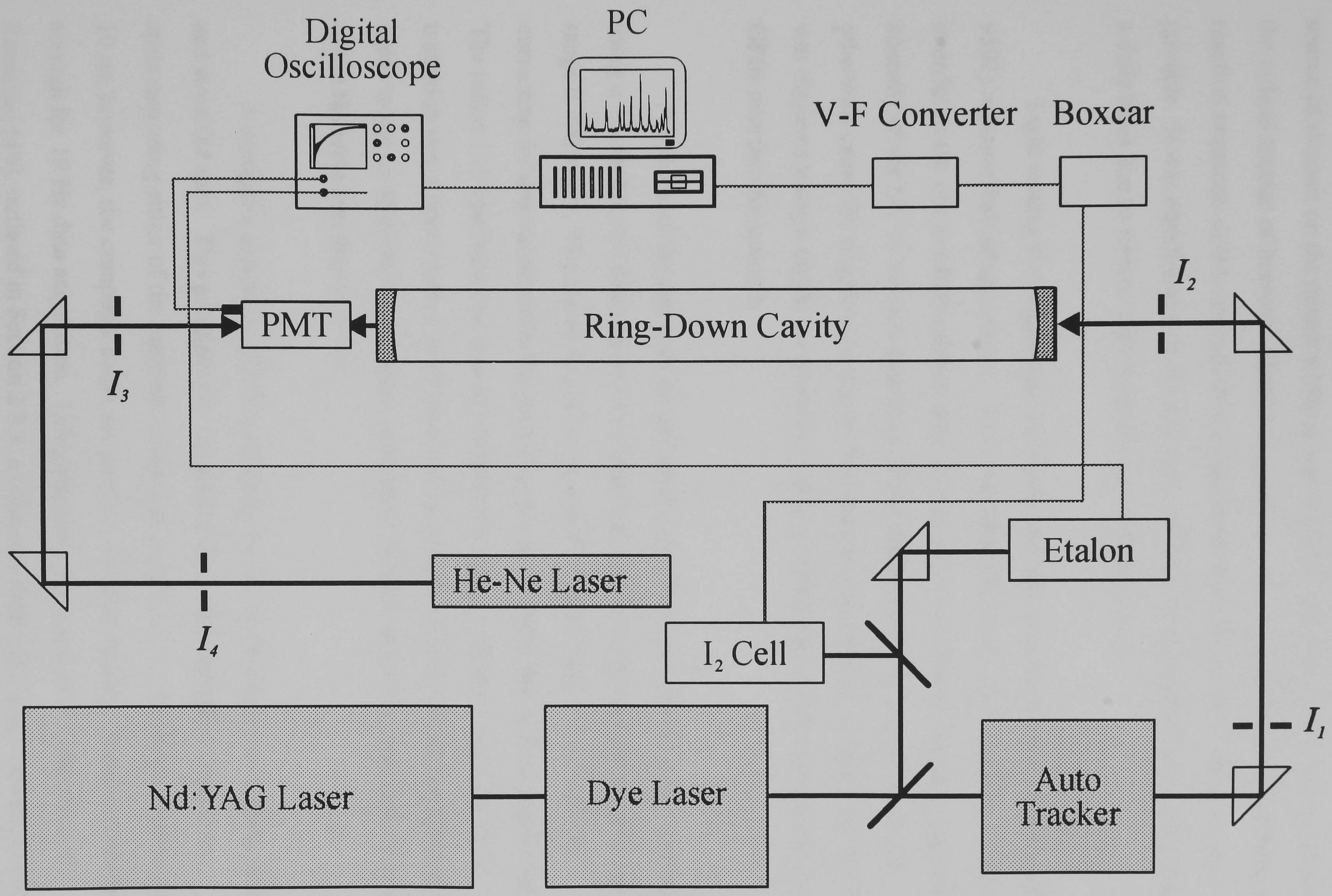

Figure 2.5. Schematic diagram of the CRDS experiment.

3.0 km and mirror reflectivity of >99.9 %. The mirrors required frequent cleaning as the ring-down time was greatly reduced if any material was deposited on them. The main source of deposit on the mirror surfaces was from the reactions being used to generate the radical species of interest. Therefore great care needed to be taken in selecting a reaction sequence so that the radical species could be produced in as clean a way as possible. It was also found that the alignment of the mirrors needed to be reoptimised on a daily basis due to temperature fluctuations in the laboratory.

Light exiting the ring-down cavity was detected by a fast photo-multiplier (EMI 9592) mounted behind one mirror. A UV bandpass filter was placed in front of the PMT in order to cut out any fluorescence arising from mirror substrates, and to reduce the intensity of the UV to prevent saturation of the photomultiplier; saturation would otherwise cause the ring down decay to become non-exponential. Signal from the PMT was digitised using a digital oscilloscope (LeCroy 9400) and transferred to a PC via a GPIB interface for analysis.

A portion of the dye laser fundamental was separated from the main laser beam using a quartz flat and directed into an iodine cell and a Fabry-Perot etalon (free spectral range 0.492 cm^{-1}). The etalon fringes were used to obtain a linear scale, thereby correcting for any variations in the scan control motor speed during data acquisition. The iodine LIF spectrum can then be compared with the well documented I_2 B-X transition and a least squares fit of observed vs. calculated line positions performed in order to get an absolute wavenumber calibration for each spectrum; standard deviations of the fits were less than 0.05 cm^{-1}.

A computer program DRIVE written by Dr. C. M. Western was used to collect and store the data. This program was capable of obtaining the cavity-ring down spectrum using either of the methods outlined in section 2.3.1. For decays longer than 10 μs, however, the computer could not perform the least-squares fitting procedure fast enough for 10 Hz data acquisition. Using the collection method of Lehmann and Romanini [16], outlined in Section 2.3.1, a total of 6 data collection channels needed to be used; 3 channels to record the gates on the ring-down decay (via the oscilloscope), a channel each for both the etalon fringes (again via the oscilloscope) and the iodine LIF

signal (via a boxcar, Stanford Research Systems SR250), and a channel to calculate the actual absorption spectrum from the three gates. Each point on the CRD spectrum corresponds to an averaging of 3-5 laser shots to minimise shot-to-shot variation caused by the laser. Typical raw and transformed data is shown in Figure 2.6.

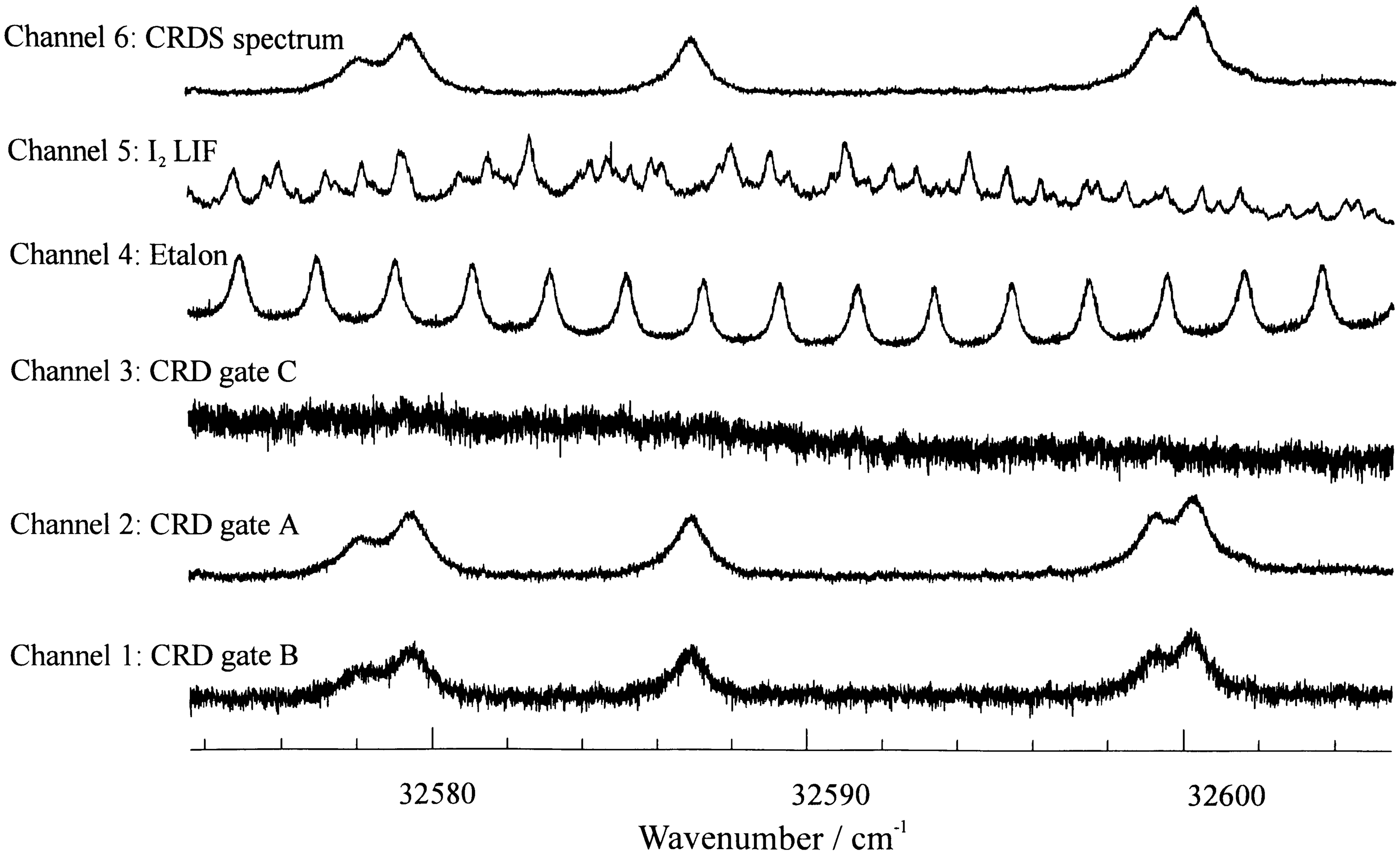

Figure 2.6. Illustration of the six channels required to record the CRD spectra using the method of reference [16].

References

1. A. O'Keefe and D.A.G. Deacon, *Rev. Sci. Instrum.*, **59** (1988) 2544.
2. J.M. Herbelin, J.A. McKay, M.A. Kwok, R.H. Uenten, D.S. Urevig, D.J. Spencer, and D.J. Bernard, *Appl. Opt.*, **19** (1980) 144.
3. D.Z. Anderson, J.C. Frisch, and C.S. Masser, *Appl. Opt.*, **23** (1984) 1238.
4. T. Yu and M.C. Lin, *J. Am. Chem. Soc.*, **115** (1993) 4371.
5. T. Yu, M.C. Lin and C.F. Melius, *Int. J. Chem. Kinet.*, **26** (1994) 1095.
6. T. Yu and M.C. Lin, *J. Phys. Chem.*, **98** (1994) 2105.
7. T. Yu, A.M. Mebel, and M.C. Lin, *J. Phys. Org. Chem.*, **8** (1995) 47.
8. T. Yu and M.C. Lin, *J. Am. Chem. Soc.*, **116** (1994) 9571.
9. T. Yu and M.C. Lin, *J. Phys. Chem.*, **98** (1994) 9697.
10. T. Yu and M.C. Lin, *J. Phys. Chem.*, **99** (1995) 8599.
11. T. Yu and M.C. Lin, *Int. J. Chem. Kinet.*, **25** (1993) 875.
12. T. Yu and M.C. Lin, *Int. J. Chem. Kinet.*, **26** (1994) 771.
13. E.W. Diau, T. Yu, M.A.G. Wagner, and M.C. Lin, *J. Phys. Chem.*, **98** (1994) 4034.
14. D.B. Atkinson and J.W. Hudgens, *J. Phys. Chem. A*, **101** (1997) 3901.
15. D.B. Atkinson and J.W. Hudgens, manuscript in preparation.
16. D. Romanini and K.K. Lehmann, *J. Chem. Phys.*, **99** (1993) 6287.
17. D. Romanini and K.K. Lehmann, *J. Chem. Phys.*, **102** (1995) 633.
18. J.J. Scherer, D. Voelkel, D.J. Rakestraw, J.B. Paul, C.P. Collier, R.J. Saykally, and A. O'Keefe, *Chem. Phys. Lett.*, **245** (1995) 273.
19. J.J. Scherer, K.W. Aniolek, N.P. Cernansky, and D.J. Rakestraw, *J. Chem. Phys.*, **107** (1997) 6196.
20. J.J. Scherer, J.B. Paul, C.P. Collier, A. O'Keefe, D.J. Rakestraw and R.J. Saykally, *Spectroscopy*, **11** (1996) 46.
21. J.B. Paul, J.J. Scherer, A. O'Keefe, and R.J. Saykally, *Laser Focus World*, **33** (1997) 71.
22. J.B. Paul, C.P. Collier, R.J. Saykally, J.J. Scherer, and A. O'Keefe, *J. Phys. Chem. A*, **101** (1997) 5211.
23. T.G. Slanger, D.L. Huestis, P.C. Cosby, H. Naus, and G. Meijer, *J. Chem. Phys.*, **105** (1996) 9393.
24. D.L. Huestis, R.A. Copeland, K. Knutsen, T.G. Slanger, R.T. Jongma, M.G.H. Boogaarts, and G. Meijer, *Can. J. Phys.*, **72** (1994) 1109.
25. R. Englen, G. von Helden, G. Berden, and G. Meijer, *Chem. Phys. Lett.*, **172** (1996) 105.
26. M. Kotterer, J. Conceicao, and J.P. Maier, *Chem. Phys. Lett.*, **259** (1996) 233.
27. M. Kotterer and J.P. Maier, *Chem. Phys. Lett.*, **266** (1997) 342.

28. L. Lehr and P. Hering, *IEEE J. Quantum. Electron.*, **33** (1997) 1465.
29. A. O'Keefe, J.J. Scherer, A.L. Cooksy, R. Sheeks, J. Heath and R.J. Saykally, *Chem. Phys. Lett.*, **172** (1990) 214.
30. J.J. Scherer, J.B. Paul, and R.J. Saykally, *Chem. Phys. Lett.*, **242** (1995) 395.
31. J.J. Scherer, J.B. Paul, C.P. Collier, and R.J. Saykally, *J. Chem. Phys.*, **102** (1995) 5190.
32. J.J. Scherer, J.B. Paul, C.P. Collier, and R.J. Saykally, *J. Chem. Phys.*, **103** (1995) 113.
33. J.J. Scherer, J.B. Paul, C.P. Collier, A. O'Keefe, and R.J. Saykally, *J. Chem. Phys.*, **103** (1995) 9187.
34. J.B. Paul, J.J. Scherer, C.P. Collier, and R.J. Saykally, *J. Chem. Phys.*, **104** (1996) 2782.
35. J.J. Scherer, J.B. Paul, A. O'Keefe, and R.J. Saykally, *Adv. Metal and Semiconductor Clusters*, **3** (1995) 149.
36. J.B. Paul and R.J. Saykally, *Anal. Chem.*, **69** (1997) 287 A.
37. J. Pearson, A.J. Orr-Ewing, M.N.R. Ashfold and R.N. Dixon, *J. Chem. Soc. Faraday Trans.*, **92** (1996) 1283.
38. R.N. Dixon and C.A. Rosser, *Chem. Phys. Letts.*, **108** (1985) 323
39. J.W. Hudgens, private communication.
40. P. Zalicki and R.N. Zare, *J. Chem. Phys.*, **102** (1995) 2708.
41. K.K. Lehmann and D. Romanini, *J. Chem. Phys.*, **105** (1996) 10263.
42. J.T. Hodges, J.P Looney and R.D. van Zee, *J. Chem. Phys.*, **105** (1996) 10278.
43. J. Martin, B.A. Paldus, P. Zalicki, E.H. Wahl, T.G. Owano, J.S. Harris Jr., C.H. Kruger, and R.N. Zare, *Chem. Phys. Lett.*, **258** (1996) 63.

3. Predissociation of the $A^2\Sigma^+$ state in SH and SD

3.1 Overview

The spectroscopy [1-7] and reaction kinetics [8,9] of the SH (or mercapto) radical have been the subject of many investigations over the years because of its importance in coal combustion processes and as an intermediate in many reactions producing sulphur-based pollutants. It is produced from the photodissociation of H_2S in the upper atmosphere, the H_2S being generated both by the burning of fossil fuels and also naturally by bacteria and volcanic activity. However, the subsequent chemistry of SH in the atmosphere has not been well characterised. It has been suggested that it should form a weakly bound adduct with O_2 via the reaction [8],

$$SH + O_2 + M \rightarrow HSOO + M \qquad (3.1)$$

The HSOO species has not been observed directly, but the rate coefficient for the reaction of SH + NO_2 in the presence of 100 Torr of O_2 [10] is approximately 40 % lower than that measured in the absence of O_2 [11] suggesting that reaction 3.1 may be important. If equilibration occurs in the SH + O_2 reaction, the adduct may be difficult to observe and may have gone unnoticed. Theoretical calculations [12] suggest that HSOO formation is thermochemically unfavourable at 298 K due to the weak SO bond, but the reaction becomes more favourable at lower temperatures. If SH does in fact add to O_2 and the adduct reacts further, to form SO_2 for example, the current proposed mechanism for the atmospheric oxidation of H_2S may need revision.

The SH radical and its deuterated isotopomer SD should be detectable in interstellar space due to the relatively high cosmic abundance of elemental sulphur and H_2S [13]. Rotational transitions arising from the upper spin-orbit component of the ground state (see below) should only be detectable from hot interstellar sources and may provide a good indication of star formation. SH is also thought to constitute one of the building blocks of larger molecules found within dense molecular clouds which are often the site of active star formation.

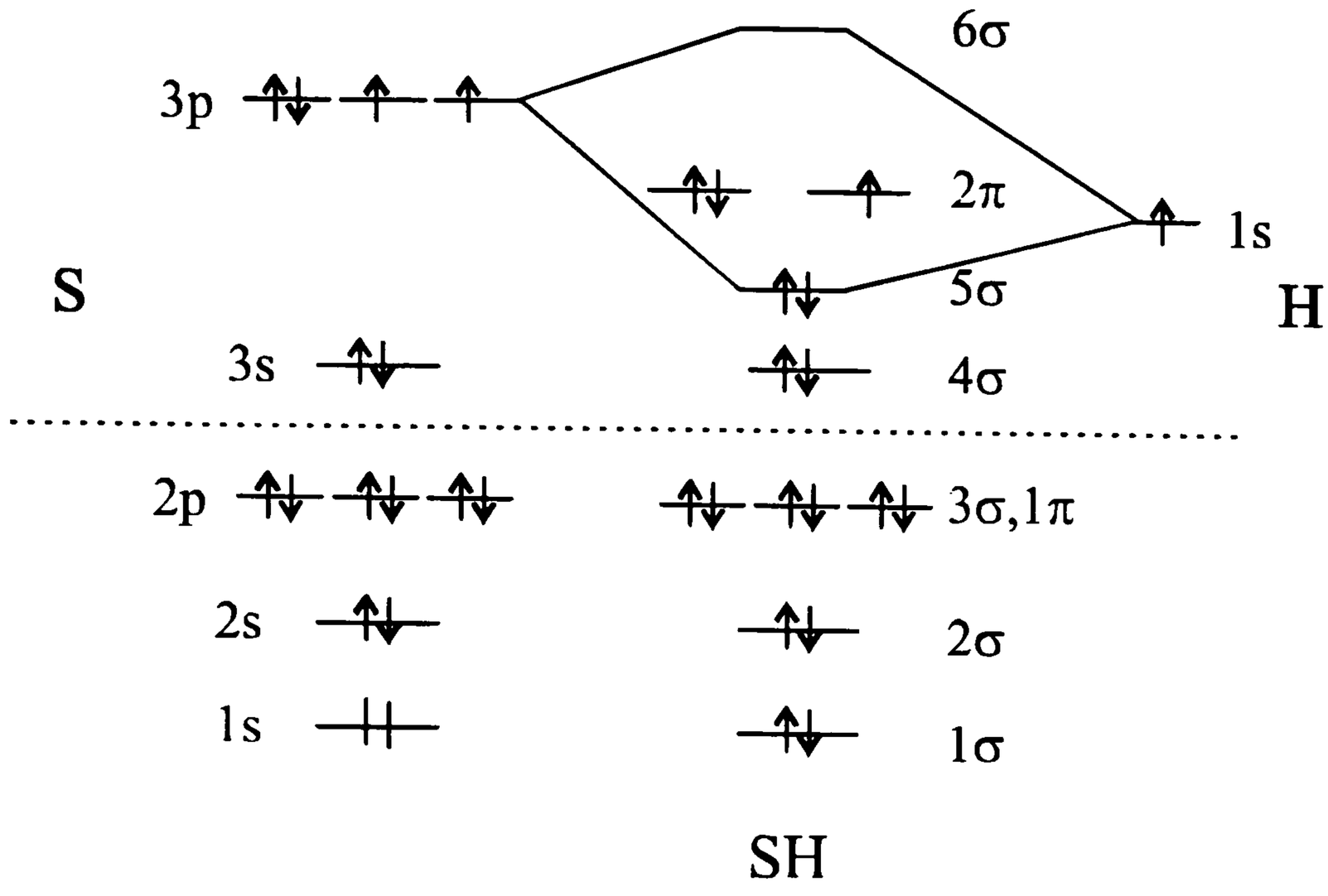

Figure 3.1 Molecular orbital diagram of the SH(SD) radical showing the ground $^2\Pi$ electronic state with a configuration ....$4\sigma^2 5\sigma^2 2\pi^3$.

A schematic molecular orbital diagram for the ground state electronic configuration ....$4\sigma^2 5\sigma^2 2\pi^3$ of SH(SD) is given in Figure 3.1. This configuration gives rise to an inverted $^2\Pi$ ground state, with a spin-orbit splitting constant A = –379 cm^{-1} for SH. At low rotational energies this state is well described by a Hund's case (a) coupling scheme (since A>>BJ for low J) giving the rotational energy level pattern shown in the bottom half of Figure 3.2. The spectroscopic parameters for this state in both SH and SD are by now well established from a combination of microwave and infrared data [14-17]. The first excited state configuration ....$4\sigma^2 5\sigma^1 2\pi^4$ is generated by a perpendicular transition promoting a 5σ electron to a 2π orbital, giving rise to the $A^2\Sigma^+$ state. The rotational energy levels for a $^2\Sigma^+$ state are pure case (b) since there is no spin-orbit or spin-spin interaction and are shown in the top half of Figure 3.2. By consideration of the selection rules from a case (a) ground state to a case (b) excited state, $\Delta J=0, \pm 1, + \leftrightarrow -$ six rotational branches are expected to arise from each spin-orbit component of the $^2\Pi$ ground state; these allowed transitions together with their nomenclature are also illustrated in figure 3.2 [18]. Transitions from the upper spin-orbit state will be intrinsically weaker since it is substantially less populated at normal temperatures.

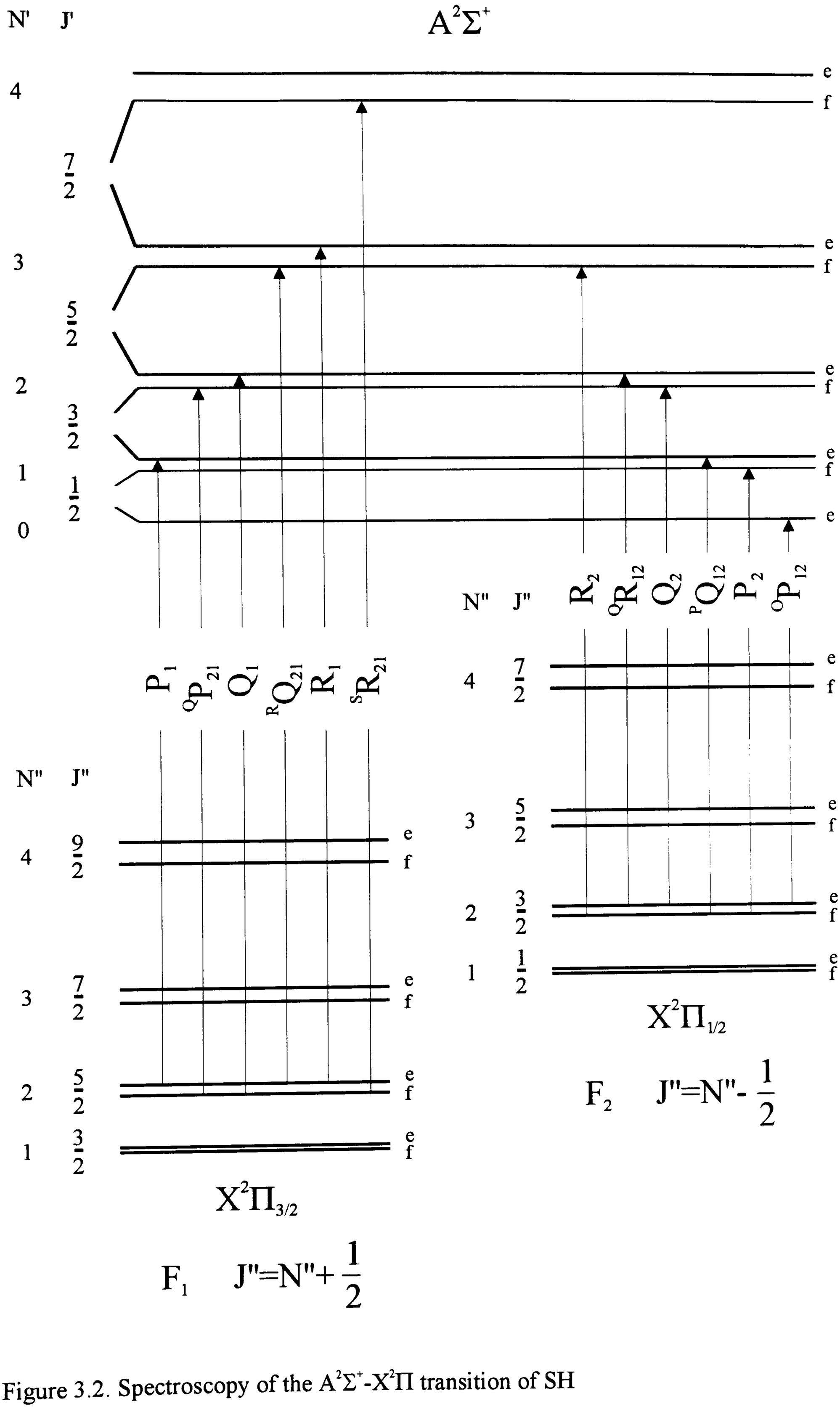

Figure 3.2. Spectroscopy of the $A^2\Sigma^+$-$X^2\Pi$ transition of SH

The $A^2\Sigma^+$-$X^2\Pi$ band system of the SH radical was first observed in absorption by Lewis and White [1] in 1939 using a pulsed electric discharge through H_2S. In 1950 Porter [6] observed bands at 3236.6 Å and 3060 Å via flash photolysis of H_2S and assigned them as the (0,0) and (1,0) bands. A more thorough investigation was carried out by Ramsay [19] and continued by Johns and Ramsay [20] by means of a 21 ft concave grating spectrometer and again observing the flash photolysis products of H_2S. Accurate constants were obtained for the A state of SH and SD by least squares fitting data from the (0,0), (1,0), and (2,0) bands; these derived molecular constants are summarised in Table 3.1. A Birge-Sponer extrapolation based on the observed v' = 0, 1 and 2 band origins suggested an $A^2\Sigma^+$-state well depth $D_e = 8020 \pm 1000$ cm^{-1}.

	SH	SD
B_e / cm^{-1}	8.521	4.392
α_e / cm^{-1}	0.46	0.172
γ_e / cm^{-1}	-0.02	-0.005
D_e / cm^{-1}	6.3×10^{-4}	1.7×10^{-4}
β_e / cm^{-1}	0.6×10^{-4}	0.1×10^{-4}
r_e / Å	1.423	1.423
ω_e / cm^{-1}	1979.8	1417
$\omega_e x_e$ / cm^{-1}	97.6	48.8

Table 3.1. Equilibrium molecular constants for the $A^2\Sigma^+$ state of SH taken from Johns and Ramsay [20].

Ramsay observed that the (0,0) bands of both SH and SD exhibited sharp rotational fine structure but that the lines became progressively more diffuse in bands involving the higher v' levels; linewidth measurements suggested that the v' > 0 levels of SH $A^2\Sigma^+$ have lifetimes with respect to predissociation of *ca.* 50ps. Further evidence for the predissociation of the $A^2\Sigma^+$ state came from flame emission spectra [21] with SH(SD) made in a extremely exothermic reaction energetically capable of producing high

vibrational levels of the A-state. Emission was observed from the SH A-X (0,0) band and the SD A-X (0,0) and (0,1) bands only, but none was seen for v'>0 in either molecule. From these experiments it was also noted that the observed emission intensity from v'=0 of SD was greater than that of SH by more than could be explained by the effects of isotopic substitution on the radiative lifetime. This observation indicates the onset of predissociation even in the lowest vibrational manifold of SH. Similarly, laser induced fluorescence (LIF) studies of SH and SD have failed to detect fluorescence from v'>0 levels of the $A^2\Sigma^+$ state [22,23].

More recently the hyperfine and spin-rotation structure of the $A^2\Sigma^+$ v' = 0 state of SH has been determined using high-resolution molecular beam cw laser-induced fluorescence (LIF) [24,25]. The narrow laser linewidth (0.5 MHz FWHM) used in these experiments allowed measurement of lifetime-broadening in levels of the v' = 0 state. Predissociation rates were observed to increase with increasing rotational quantum number; the corresponding lifetimes decrease from 3.2 ns (N' = 0) to 0.95 ns (N' = 9), with e-parity levels (corresponding to the F_1 components of the $A^2\Sigma^+$ state) having slightly shorter lifetimes than the f-parity (F_2) levels. These lifetimes are in good agreement with other (generally less precise) values determined via quenching [26] and time resolved fluorescence decay measurements [27], but are substantially longer than those determined from Hanle effect measurements [28] - a discrepancy subsequently attributed to saturation effects [25,29]. Kawasaki *et al.* [30] measured fluorescence lifetimes of SD $A^2\Sigma^+$, v'=0, N'=0-13 and observed a monotonic decrease with increasing N' from 198 ± 7 ns to 44 ± 1 ns, with e-parity levels again having slightly shorter lifetimes. The radiative lifetimes of SH and SD $A^2\Sigma^+$, v'=0 have been experimentally deduced as 820 ± 240 ns and 730 ± 180 ns respectively [27], with *ab initio* calculations for SH giving a value of 704 ns [31]. Excitation of SH on the A-X transition has been used to study SH-Ar and SH-Ar_2 van der Waals complexes [32] and SH embedded in matrices of argon and krypton [33]. The presence of one or more Ar atoms bound to SH $A^2\Sigma^+$ increased the fluorescence lifetime of v'=0 levels to as long as 600 ns; for Ar-SH the increase in the natural lifetime depended on the number of quanta of excitation of the Ar-SH stretch. This effect has been reproduced theoretically in terms of a ballistic model [34] using an empirical potential energy surface. SH contained within a rare-gas matrix

showed complete suppression of the electronic predissociation of the A-state. More recently the SH A-X transition has been employed as a probe to measure nascent rotational distributions arising from the 266 nm photolysis of H_2S using the technique of degenerate four-wave mixing (DFWM) [35] which, unlike LIF as a detection scheme, should not suffer from signal loss due to non-radiative processes such as predissociation.

Electronic structure calculations [31,36-38] suggest that the interactions resulting in predissociation of the $A^2\Sigma^+$ states of SH and SD are similar to those occurring in the analogous system OH. Predissociation of the OH $A^2\Sigma^+$ state has been much studied both experimentally [39,40] and theoretically [41,42]. The $A^2\Sigma^+$ state of OH is crossed by three repulsive electronic states that dissociate to the atomic fragments $O(^3P_j) + H(^2S)$. These repulsive $^4\Sigma^-$, $^2\Sigma^-$ and $^4\Pi$ states are coupled to the bound $A^2\Sigma^+$ state via spin-orbit coupling, and the extent to which these states affect the predissociation rate varies with the vibrational level of the OH $A^2\Sigma^+$ and the rotational quantum number; for example, for OH $A^2\Sigma^+$, v'=3 rates are 0.33×10^{10} s^{-1} for N'=0 and 1.58×10^{10} s^{-1} for N' = 14, with rates for e-parity (F_1) levels up to 10% higher than for f-parity (F_2) levels. Recent Fermi Golden Rule calculations of the predissociation rates of OH $A^2\Sigma^+$, v',N' levels employing *ab initio* electronic wavefunctions for the $A^2\Sigma^+$, $^4\Sigma^-$, $^2\Sigma^-$ and $^4\Pi$ states and computed values of the spin-orbit coupling between these states showed excellent agreement with the available experimental data [42].

The SH $A^2\Sigma^+$ state is similarly crossed by $^4\Sigma^-$, $^2\Sigma^-$ and $^4\Pi$ repulsive states that correlate with $S(^3P_j)$ and $H(^2S)$ at large internuclear separation. Riad Manaa [38] performed detailed *ab initio* electronic structure calculations of the potential energy curves for the SH $X^2\Pi$, $A^2\Sigma^+$, $^4\Sigma^-$, $^2\Sigma^-$ and $^4\Pi$ states, shown in Figure 3.3, and for the spin-orbit and Coriolis couplings between all of these states. Predissociation rates based on these *ab initio* results were not, however, calculated. The experimental data with which to compare such calculated rates has, until now, been sparse, and measurement of accurate lifetimes for SH and SD $A^2\Sigma^+$, v',N' levels has been restricted to v'=0. A comparison of predissociation rates of SH $A^2\Sigma^+$ with the much-studied OH $A^2\Sigma^+$ should highlight the effects of the different spin-orbit interactions in these first- and second-row hydride radicals. It is therefore the intention of this work to use CRDS to extend the

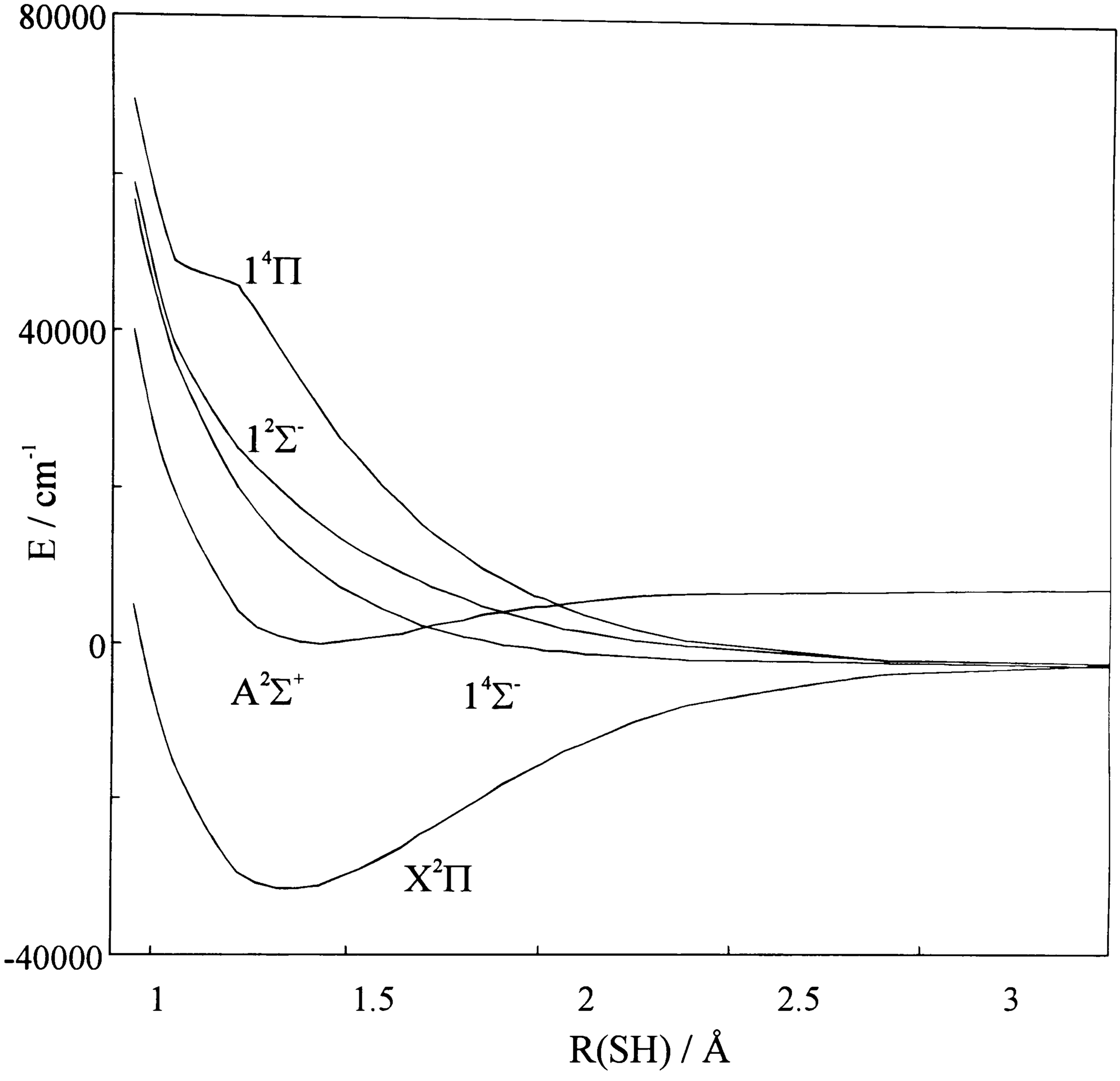

Figure 3.3. Potential energy curves for the five lowest states of SH from CI calculations. Taken from reference [38]. The potentials are plotted with the zero of energy taken as the bottom of the $A^2\Sigma^+$ well.

range of experimental data available for SH(SD), and to perform detailed Fermi-golden rule calculations using the most recent *ab initio* and experimental potentials for comparison, thereby producing a unified experimental and theoretical picture of the mechanism of predissociation of SH/SD $A^2\Sigma^+$ $v' \leq 2$, as well as predictions for the predissociative behaviour of higher v' levels.

3.2 Experimental

The cavity ring-down experiment used for this work is described in detail in chapter 2. Two sets of UV mirrors were required to extend over the observable A-X band system of SH(SD), 298 - 328 nm, the first centred at 320 nm (Research Electro-Optics) and the second at 290 nm (Lightning Optical Corporation). Both sets were manufactured from a quartz substrate 7.75-mm diameter, 4-mm thick and 2-m radius of curvature, the optical coating was laid down on the curved sides of the mirrors and had a specified reflectivity of >99.9% at the mirror centre.

The flow tube consisted of a 1.6-metre long, 25-mm diameter glass tube with several ports along its length to allow connection of pressure gauges and gas cylinders / bulbs. The flow tube was evacuated by a rotary pump (Edwards), through a porous filter to prevent pump oil dirtying the mirrors and connected close to one end of the cell by vibration-isolating bellows. The pressure in the cell was monitored by two capacitance gauges (0-1000 Torr and 0-10 Torr) and could be regulated by the use of a throttle valve placed in front of the rotary pump.

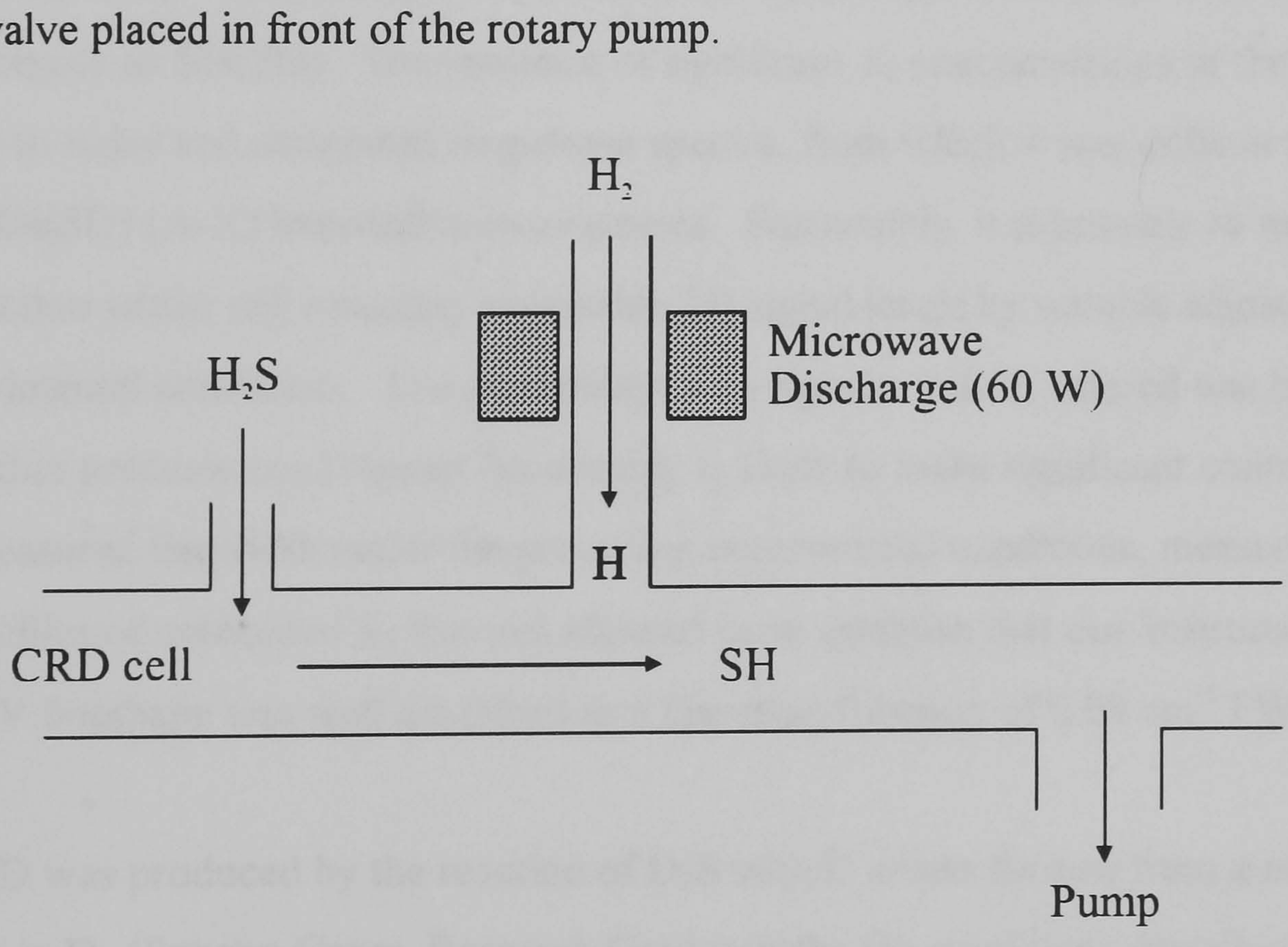

Figure 3.4. Discharge flow-tube apparatus used to generate the SH(SD) radicals.

The SH radicals were produced in continuous flow system, as illustrated in Figure 3.4, by the reaction,

$$H + H_2S \rightarrow SH + H_2. \qquad (3.1)$$

The hydrogen atoms were generated by a microwave discharge of H_2 (BOC High Purity) in a phosphoric-acid coated mullite tube (10-cm long, 12-mm o.d.) and were passed into the cavity ring-down (CRD) cell 33-cm from one end; they reacted in the RDC with a few mTorr of H_2S (Matheson, 99.5 % purity) introduced further upstream. Microwave power (typically around 40-50 W) was fed from a generator (Microtron 200) to a cavity surrounding the mullite tube close to the inlet of the RDC to maximise the concentration of H atoms reaching the flow tube. The flow rates of the gases were carefully controlled by needle valves and the optimum pressures were typically around 0.5 -1.0 Torr of H_2 and 1 - 2 mTorr of H_2S. The H_2S and H_2 were both passed through 10 μm filters to prevent any dust reaching the mirrors. A number of side reactions can accompany the reaction given in Equation (3.1), resulting in a variety of other sulphur containing species including S_2, which has a complex structured absorption spectrum [43] in the same UV spectral region as SH(SD). The presence of significant S_2 concentrations in the present work led to noisy and congested ring-down spectra, from which it was difficult to make reliable SH(SD) (A-X) linewidth measurements. Fortunately, it is possible to minimise S_2 production whilst still retaining reasonable SH signal levels by suitable adjustment of the experimental conditions. The availability of S_2 signals, in fact, offered one benefit: since neither pressure nor Doppler broadening is likely to make significant contributions to any measured linewidth under the prevailing experimental conditions, measurements of the profiles of unblended S_2 features allowed us to establish that our 'instrumental' (laser) UV lineshape was well described as a Gaussian function of 0.09 cm^{-1} FWHM.

SD was produced by the reaction of D_2S with D atoms formed from a microwave discharge in D_2 (Spectra Gases, Research Grade) under the conditions described above. D_2S was synthesised by the reaction of D_3PO_4 in D_2O with FeS in a deuterated vacuum line and was stored in a 5-litre glass bulb. Prior to studying SD, the entire vacuum apparatus was deuterated by overnight exposure to D_2O, and the microwave discharge tube was coated with deuterated phosphoric acid. Although reaction of H atoms with

D_2S should cleanly produce SD, the reaction with D atoms was found to give better SD signal with less SH contamination.

3.3 Results

Spectra were recorded of the SH $A^2\Sigma^+$-$X^2\Pi$ (1,0) band and of the SD $A^2\Sigma^+$-$X^2\Pi$ (1,0) and (2,0) bands and span a total wavelength range 298-317 nm. Unfortunately, attempts to record the (2,0) band were foiled by a combination of two effects; poor Franck-Condon factors for the transition (see Table 3.2) compared with the equivalent SD band and a very strong overlapping S_2 $B^3\Sigma_u^-$ - $X^3\Sigma_g^-$ (6,0) band that could not be eliminated by adjustment of the H_2S and H atom mixing ratios. In addition the reflectivity of our mirror set at wavelengths appropriate to the (2,0) band of SH was substantially less than the maximum mirror reflectivity. The maximum ring-down time we could achieve at 290 nm was around 4 μs.

	Franck-Condon Factor	
v'	SH v"=0	SD v"=0
0	0.749	0.687
1	0.202	0.242
2	0.042	0.058
3	0.008	0.012
4	0.001	0.002

Table 3.2. Franck-Condon factors for the SH(SD) A-X transition taken from Johns and Ramsay [20]

Figure 3.5 shows the CRD spectrum of the SH $A^2\Sigma^+$-$X^2\Pi$ (1,0) band over the wavenumber range 32390 - 32670 cm^{-1} together with a simulation derived using the literature values for the ground [14,16] and excited [20,24] state constants. The simulation assumes a temperature of 300 K, a Gaussian instrument function of FWHM 0.09 cm^{-1} (mostly laser line profile, see below), and a Lorentzian component of the line profile of FWHM 1.0 cm^{-1} to allow for homogeneous lifetime broadening. The simulation reproduces the observed positions, intensities and widths of the spectral lines very well, but to interpret the effects of predissociation as precisely as possible, we fitted

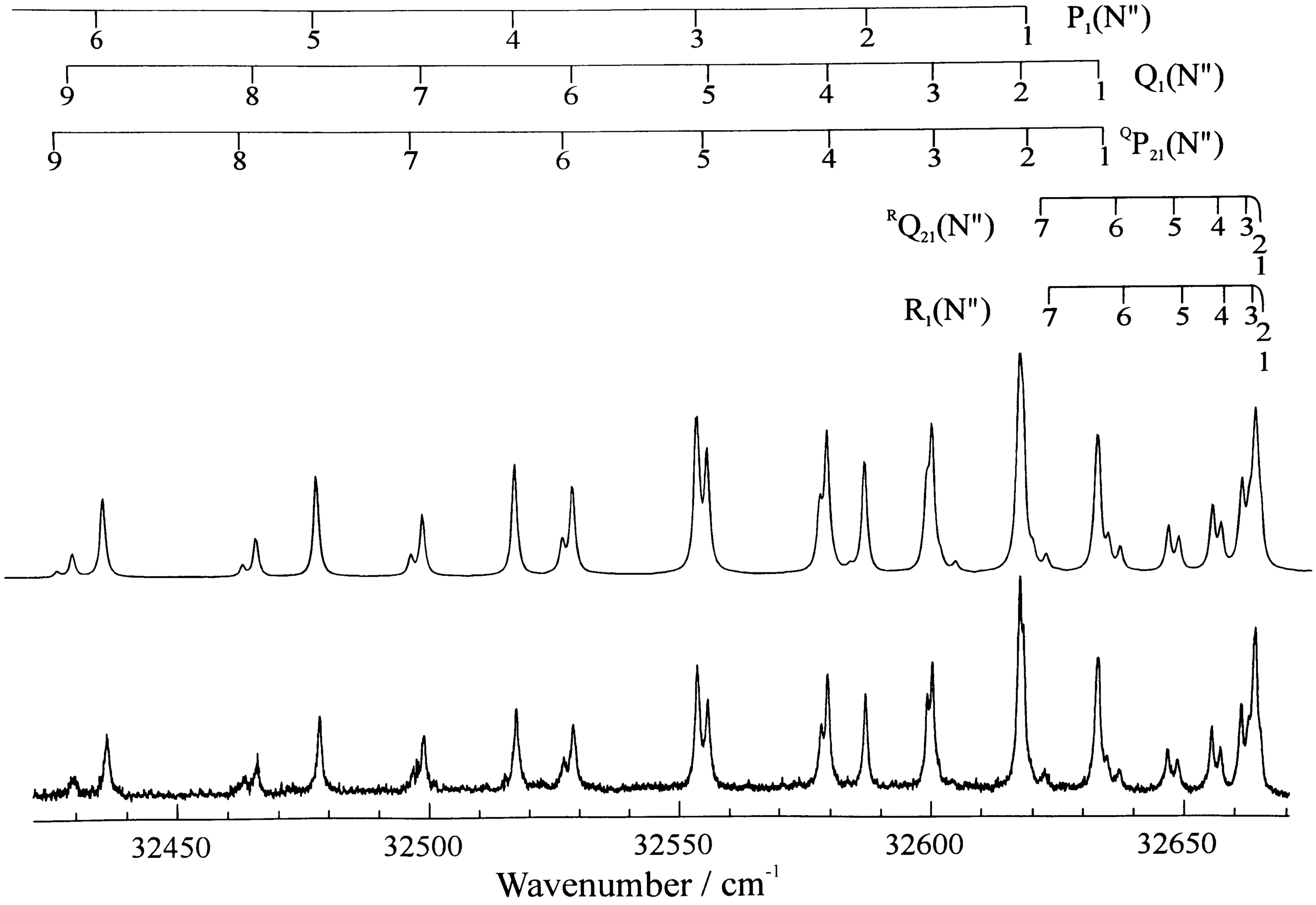

Figure 3.5. CRD spectrum and simulation of the A-X (1,0) band of SH. The combs above the spectra indicate rotational line assignments.

unblended spectral lines as described below to determine accurately the homogeneous widths of individual rotational levels.

The excited states of SH (SD) can, in principle, decay via two routes, radiative decay and predissociation. If the rate constants for these two processes are denoted as k_{rad} and k_{pre} respectively, the total rate of decay of the excited state is determined by an overall rate constant $k = k_{rad} + k_{pre}$, as discussed in Chapter 1. The natural lifetime of the excited state, τ (=1/k) is related to the associated radiative and predissociative lifetimes, τ_{rad} and τ_{pre} respectively, via:

$$\frac{1}{\tau} = \frac{1}{\tau_{rad}} + \frac{1}{\tau_{pre}} \qquad (3.2)$$

The deduced radiative lifetimes of SH $A^2\Sigma^+$ v'=0 and SD $A^2\Sigma^+$ v'=0 are of the order of 700 - 800 ns [27] whereas the natural lifetimes measured in this study are less than 100 ps. Since it is reasonable to assume only a small R-dependence in the A-X electronic transition moment and thus a small v'-dependence to the radiative lifetime of the A state, we can thus safely equate the measured natural lifetimes with the predissociative lifetimes of the $A^2\Sigma^+$ v'>0 levels.

In order to extract quantum state dependent lifetimes from experimental CRD spectra such as that shown in Figure 3.5 we determine the Lorentzian contribution to the linewidth of individual rotational lines corresponding to transitions to various upper state N'. Each line was fitted to a Voigt profile with a fixed Gaussian component of 0.09 cm^{-1} (FWHM). Figure 3.6 shows one example of such a fit. The Voigt profile is a convolution of a Gaussian function (corresponding to the combined effects of the laser lineshape and Doppler broadening) and a Lorentzian function (corresponding to the effects of lifetime broadening). The FWHM of the Gaussian function is determined by fitting S_2 transitions that overlap the SH and SD spectra. Although the Doppler components due to SH and S_2 will differ slightly, the bandwidth of the UV laser beam dominates the Gaussian "instrument" function and we determine a FWHM of 0.09 cm^{-1} that we attribute primarily to the bandwidth of the frequency doubled dye laser contribution. This Gaussian contribution to the Voigt profile is held fixed during the line

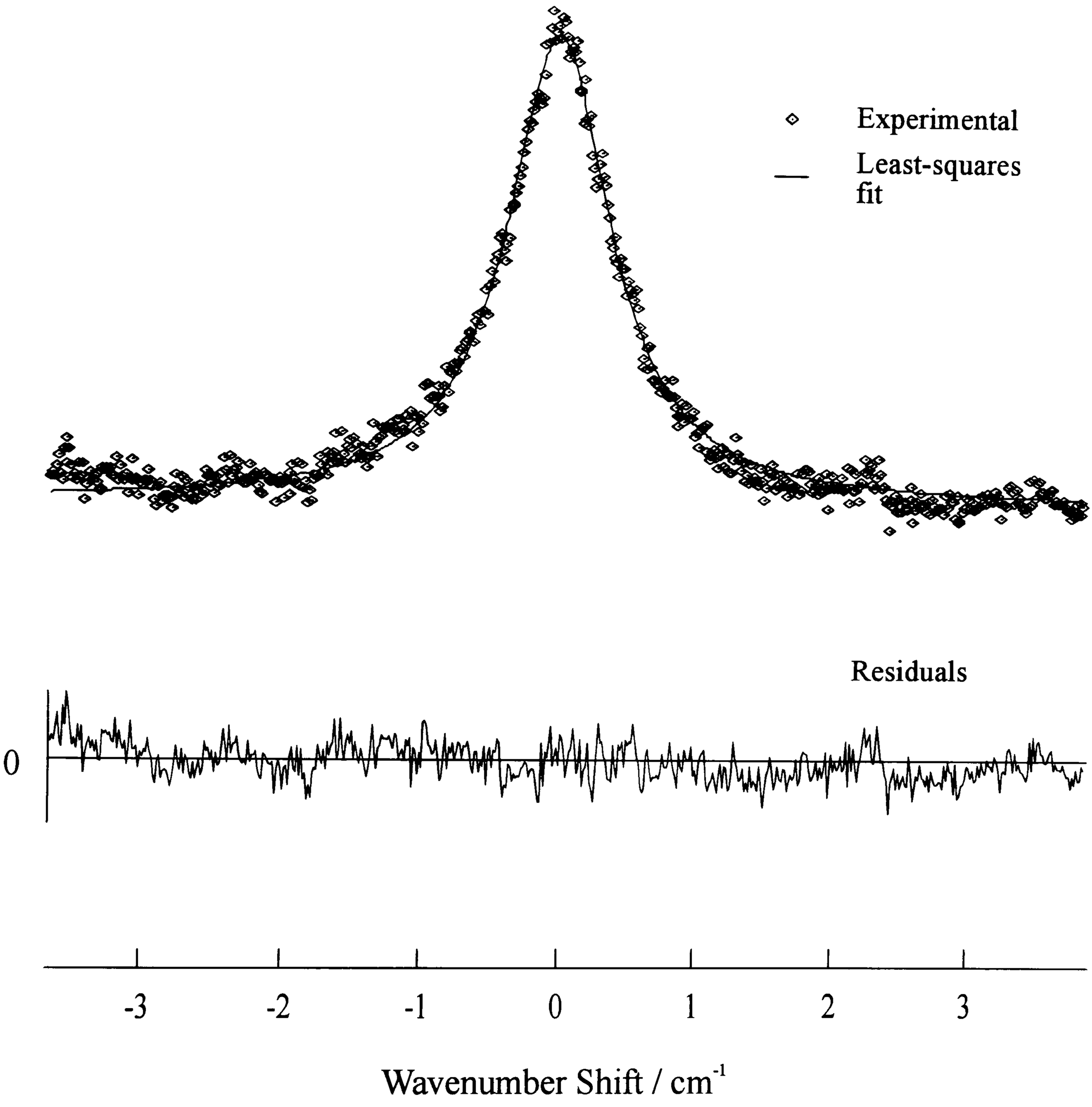

Figure 3.6. The experimentally determined line profile of the SH A-X (1,0) $P_1(2)$ rotational transition together with a least squares fit Voigt profile (solid line). Shown beneath the fitted line profile are the residuals to the fit on the same vertical scale. The Voigt profile has a fixed Gaussian component of FWHM 0.09 cm^{-1}, and the fit gave a Lorentzian component of FWHM 0.98 cm^{-1}.

fitting, and this fitting then determines the FWHM of the Lorentzian component, Γ, which may in turn be related to the predissociation lifetime. The results of this fitting process are listed in Table 3.3 for SH $A^2\Sigma^+$, v'=1, N'=0-8. Within the errors of the measurements, we observe no difference in predissociation rates for the e- and f-parity rotational levels of v'=1. The error limits give an indication of the spread of lifetime values determined from fitting lineshapes of transitions involving the same N' level accessed via different rotational sub-branches and from recording the various line profiles under different experimental conditions (*i.e.* varying the total pressure, the H_2S/H_2 mixing ratio, the microwave power and/or the laser pulse energy). The fitting assumes that unresolved hyperfine structure and pressure broadening make negligible contributions to the lineshapes. Hyperfine splittings of < 0.03 cm^{-1} have been measured for SH $A^2\Sigma^+$ v'=0, N'=14 while, at the pressures of < 1 Torr used in our experiments, pressure broadening is expected to result in a linewidth contribution of < 0.001 cm^{-1}.

	Lifetime / ps	
N'	*e*-parity	*f*-parity
0	$5.45^{+0.24}_{-0.22}$	
1	$5.45^{+0.24}_{-0.22}$	
2		
3	$4.93^{+0.36}_{-0.32}$	$5.10^{+0.36}_{-0.32}$
4	$5.19^{+0.37}_{-0.33}$	$4.64^{+0.51}_{-0.42}$
5	$4.97^{+0.25}_{-0.23}$	$4.70^{+0.65}_{-0.51}$
6	$4.65^{+0.31}_{-0.27}$	$4.08^{+0.27}_{-0.24}$
7	$4.59^{+0.42}_{-0.36}$	
8	$4.61^{+0.73}_{-0.55}$	

Table 3.3 SH $A^2\Sigma^+$ v'=1,N' lifetimes. Error limits in the quoted lifetimes correspond to 2σ in the fit of the experimental linewidths, as described in the text.

Figure 3.7 shows a portion of the spectrum of the SD $A^2\Sigma^+$-$X^2\Pi$ (1,0) band in the wavenumber range 32310 - 32350 cm^{-1}. The signal-to-noise ratio in this spectrum is

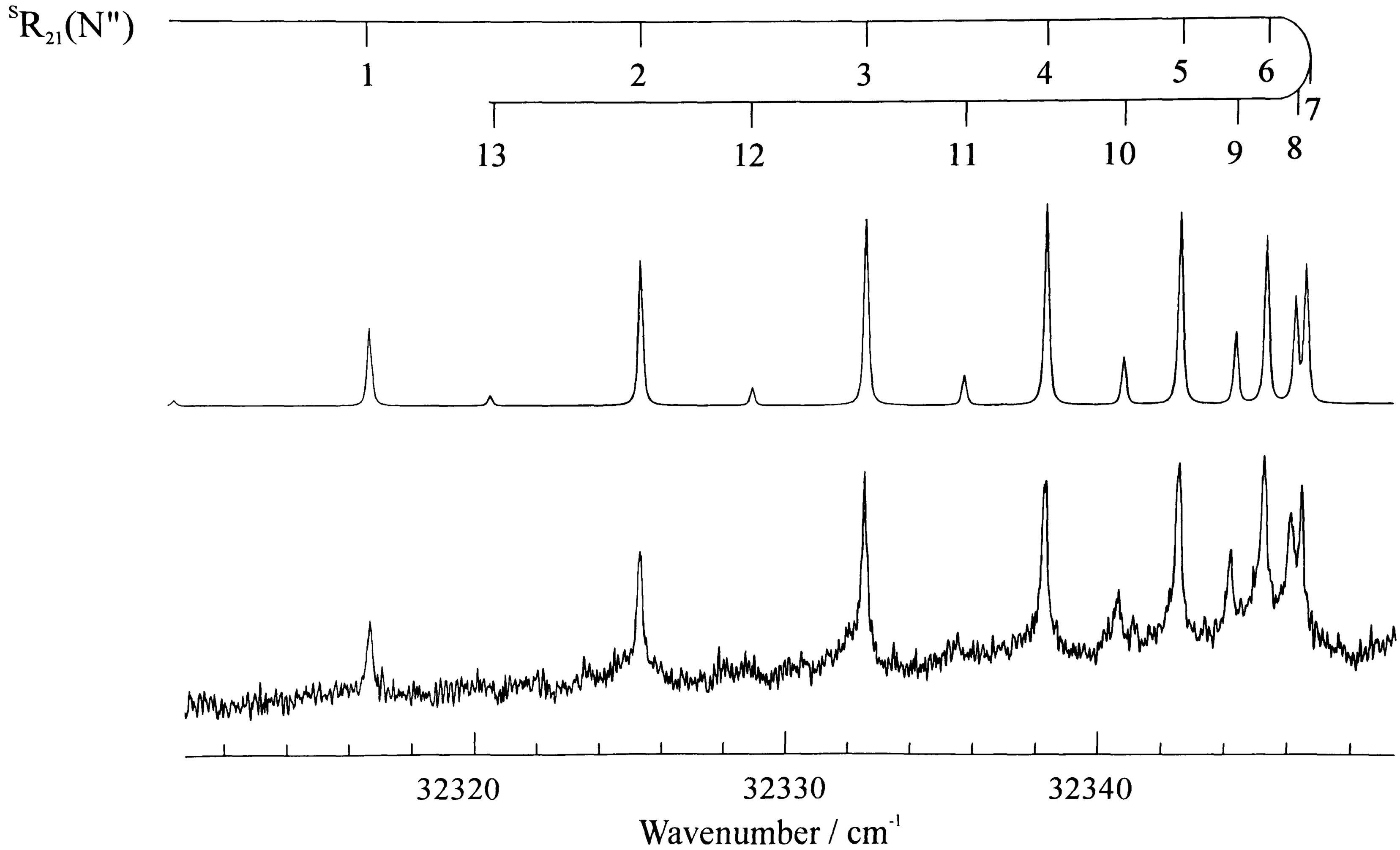

Figure 3.7. Experimental and simulated spectra of part of the SD A-X (1,0) band, with rotational line assignments indicated by the comb above the spectra.

worse than in the equivalent SH band, presumably because of the less efficient production of SD in our discharge flow system. Shown with the experimental spectrum is a simulated spectrum calculated using the spectroscopic constants for SD in its $X^2\Pi$ [14,21,15] and $A^2\Sigma^+$ states [20]. The closest correspondence between the observed and measured lineshapes is obtained if the 0.09 cm^{-1} FWHM Gaussian instrument function is convoluted with a Lorentzian profile of $\Gamma = 0.14$ cm^{-1} (FWHM). This homogeneous broadening is equivalent to an upper state lifetime of ~ 30 ps. The signal-to-noise ratio and the modest homogeneous broadening prevent accurate fitting of unblended spectral lines to determine the N' dependence of the predissociation rate. The linewidths are virtually at the limit we can determine reproducibly with our UV laser bandwidth and hence we restrict ourselves to the observation that the lifetimes of the SD $A^2\Sigma^+$ v'=1 rotational levels are ≥ 30 ps.

As mentioned already, we were unable to record spectra of the SH A-X (2,0) band because of a combination of unfavourable factors. It was, however, possible to observe portions of the SD A-X (2,0) band and part of this spectrum in the wavenumber range 33430 - 33520 cm^{-1} is shown in Figure 3.8. The Figure also shows a simulation of the band calculated as described above and including a homogeneous contribution to the spectral lineshapes with $\Gamma = 2.3$ cm^{-1} FWHM. This value of Γ was determined by fitting the complete experimental spectrum to a simulation with the linewidth as a floated parameter. The spectrum is overlapped by a band of the S_2 B-X transition, and much of the apparent "noise" in the spectrum is in fact sharp, unbroadened S_2 spectral lines. The procedure used to determine Γ precludes measurement of the N' dependence of the predissociation rate from SD $A^2\Sigma^+$ v'=2. Direct fitting of single lines to establish this N' dependence is not feasible because the widths of the features mean there are in fact no isolated lines in the spectrum. A value of $\Gamma = 2.3$ cm^{-1} corresponds to an SD $A^2\Sigma^+$ v'=2 lifetime of 2.3 ps.

In Table 3.4 the available experimental information on SH and SD $A^2\Sigma^+$ v' predissociative lifetimes has been collected together for direct comparison. The variation of the predissociation rate with v' and with hydrogen isotope can be understood in terms of the proximity of the vibrational energy levels of the $A^2\Sigma^+$ state to the crossing points

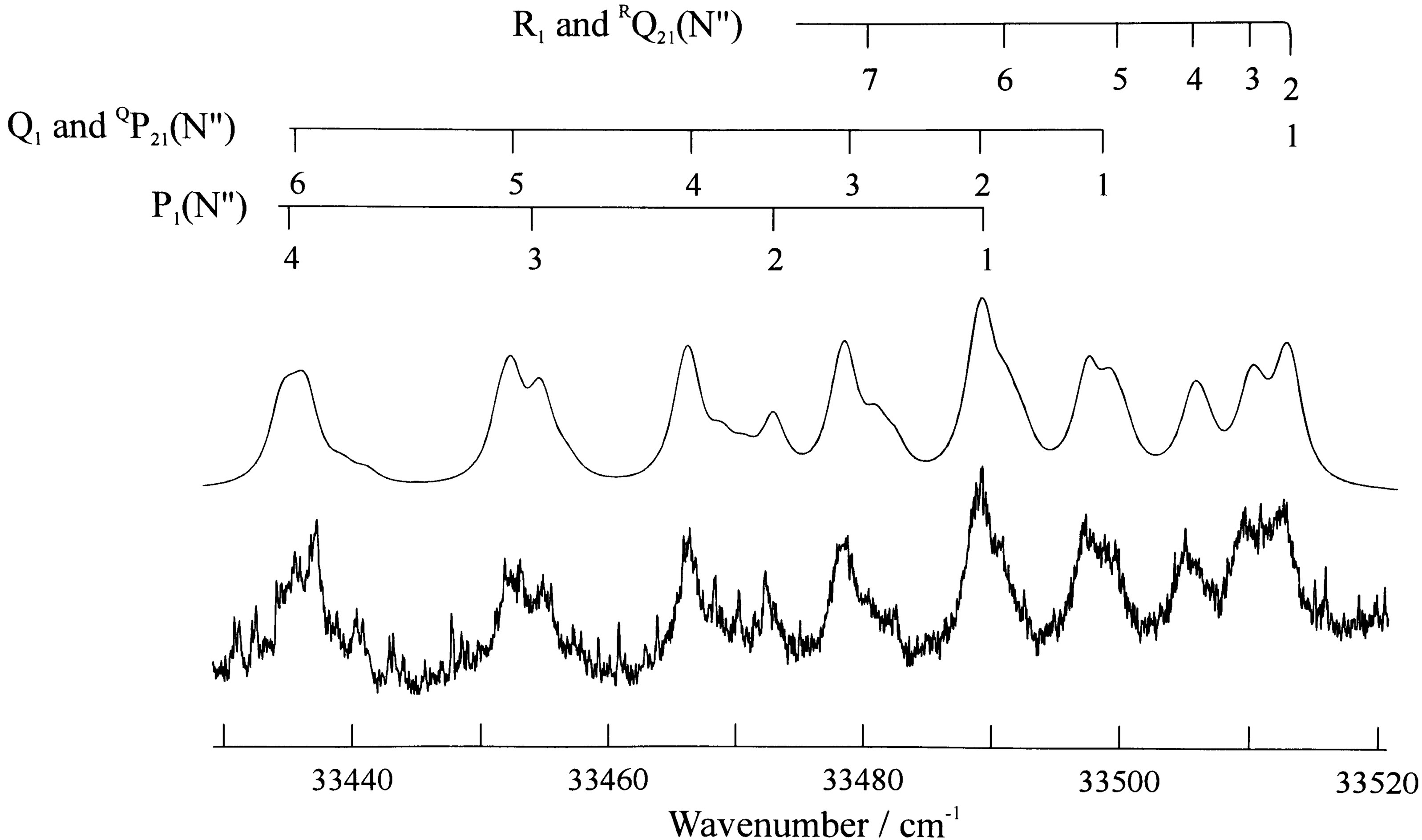

Figure 3.8. Experimental and simulated spectra of part of the SD A-X (2,0) band, with rotational line assignments indicated by the comb above the spectra.

of the $A^2\Sigma^+$ and repulsive $^4\Sigma^-$, $^2\Sigma^-$ and $^4\Pi$ potentials. This point will be addressed in more detail in the following sections.

	Lifetime	
v'	SH	SD
0	3.20-0.95 ns [a]	247 - 38 ns [b]
1	5.45-4.61 ps	35 - 30 ps
2	-	2.3 ps

Table 3.4 Summary of the variation of SH/SD $A^2\Sigma^+$ v' lifetimes for experimentally observed levels typically over the range $N' \approx 0 - 10$. a and b are taken from references [24], [30] respectively.

3.4 Calculations

The availability in the literature of *ab initio* potentials for the various electronic states of SH and for the R-dependence of the spin-orbit coupling between the electronic states has permitted us to perform detailed calculations of the rates of predissociation of individual v', N' states of SH and SD $A^2\Sigma^+$ and to compare these calculations with our experimental data. The results of this analysis clarify the relative roles of the different repulsive states in the predissociation mechanism and make apparent the origins of the observed variations of the predissociation rates with v' and N' for this system. The calculations presented here neglect the effects of the parity of the rotational levels but this point will be addressed in Section 3.5.

As mentioned previously, the observed predissociation of the lowest vibrational levels of the $A^2\Sigma^+$ state of SH is generally attributed to interaction with a nearby repulsive $1^4\Sigma^-$ state. A similar interaction has been invoked as the main contributor to the predissociation of low v' levels of the corresponding $A^2\Sigma^+$ state of both OH and OD [42]. The electronic potential energy curves for the three dissociative states - the $1^4\Sigma^-$, $1^2\Sigma^-$, and $1^4\Pi$ states arise (predominantly) from the electron configurations

$$[1\sigma^2 - 3\sigma^2\, 1\pi^4]\,\{4\sigma^2\, 5\sigma^2\, 6\sigma^1\, 2\pi^2\}; \qquad 1^4\Sigma^-,\ 1^2\Sigma^- \qquad (3.3)$$

$$[1\sigma^2 - 3\sigma^2\, 1\pi^4]\,\{4\sigma^2\, 5\sigma^1\, 6\sigma^1\, 2\pi^3\}; \qquad 1^4\Pi. \qquad (3.4)$$

Since the $A^2\Sigma^+$ state arises from the $\ldots 4\sigma^2\, 5\sigma^1\, 2\pi^4$ configuration it can be seen from equation 3.3 the $1^4\Sigma^-$, $1^2\Sigma^-$ states differ from the $A^2\Sigma^+$ state by two spin-orbitals, suggesting a significant departure from the single-configuration picture if predissociation is to take place via interactions between these states. The most accurate information available on the form of these repulsive potentials comes from a recent *ab initio* study by Riad Manaa [38]. In these calculations the molecular orbitals and energies were determined by a Complete Active Space State-Averaged Multi-Configuration Self-Consistent Field (SA-MCSCF) procedure based on electrons and orbitals partitioning $[1\sigma - 3\sigma, 1\pi]^{10}\,\{4\sigma - 6\sigma, 2\pi - 3\pi\}^7$, with the square brackets denoting the frozen core orbitals and the curly brackets denoting the active orbital space. The electronic energies

of the repulsive states were obtained as a function of internuclear distance and were calculated to cross the outer limb of the $A^2\Sigma^+$ state potential at $R_c(1^4\Sigma^-) = 1.71$ Å , $R_c(1^2\Sigma^-) = 1.90$ Å and $R_c(1^4\Pi) = 2.04$ Å, respectively [38].

For our model calculations it proved most convenient to fit the *ab initio* repulsive potential points to analytic exponential functions of the form

$$V_{rep}(R) = D + A\exp\{-[b_1(R - R_x) + b_2(R - R_x)^2]\}, \qquad (3.5)$$

where D, the energy at the potential asymptote was fixed at -564 cm^{-1}, measured relative to the A state minimum (taken to be the zero in energy), so as to be in agreement with the known [44] asymptotic splitting between the ^{1}D and ^{3}P states of atomic sulphur (9239 cm^{-1}). A, b_1, and b_2 are fitted parameters defining the curvature, whilst R_x defines the S–H bond length about which we expand the potential and, for simplicity, was initially chosen to be the *ab initio* value for the crossing point, R_c. The fitting was done using the computer program GNUPLOT with a non-linear least squares routine. However, having fitted each potential using the appropriate value of R_x (and thus determined A, b_1 and b_2 for each repulsive state), it is then possible to 'tune' each crossing point by letting R_x be an adjustable parameter, thus moving the potential inwards or outwards, as described further below.

The *ab initio* potential for the $A^2\Sigma^+$ state proved too inaccurate for the purposes of our calculation since it did not reproduce the known vibrational frequencies and energies of SH (SD) nor did it asymptotically give the correct energy of S(^{1}D) relative to S(^{3}P). Consequently, we chose to fit available experimental data to obtain a more accurate A-state potential. We used two sources of experimental data: the results of 121.6 nm photolysis of H_2S (and D_2S) [45,46] and of rotationally and vibrationally resolved spectroscopic studies of the A-X transitions of SH and SD [19,20]. The former experiments, using the technique of H (Rydberg) atom photofragment spectroscopy, established the well depth, D_e, of the bound $A^2\Sigma^+$ state potential as -8675 ± 100 cm^{-1} (relative to the asymptotic products H + S($^1D_2$)) as well as the energies of several SH (SD) $A^2\Sigma^+$ v' levels not observed in absorption spectroscopy. The A-state potential energy curve was constructed using an extended Rydberg function [47],

$$V(R) = -D_e\left[1 + a_1\rho + a_2\rho^2\right]\exp(-a_1\rho) \qquad (3.6)$$

where $\rho = R\text{-}R_e$, the distortion from the equilibrium bond length (R_e = 1.423Å) and a_1 and a_2 are fitted parameters describing the shape of the potential. We note, however, that the best-fit values of a_1 (2.97 $Å^{-1}$) and a_2 (–3.02 $Å^{-2}$) reported previously [46] do not reproduce the observed rovibrational eigenvalues. We refitted the previously tabulated experimental data for both SH and SD, simultaneously, to yield the following unified values of the parameters: a_1 = 2.90 $Å^{-1}$, a_2 = -2.33 $Å^{-2}$, using a suitably modified version of the program LEVEL [48]. This program solves the one-dimensional Schrödinger equation for a given potential function and was adapted by the addition of a fitting routine which minimises the squares of the residuals between the observed and calculated term values. The A-state potential used in subsequent calculations reported in this work was shifted upwards in energy by D_e so that the reference zero of energy for all potential functions is taken as the bottom of the A-state well.

Figure 3.9 shows the bound $A^2\Sigma^+$ and repulsive $1^4\Sigma^-$, $1^2\Sigma^-$, and $1^4\Pi$ potentials used in the subsequent analysis (prior to shifting the repulsive curves by 0.03 Å (see below)), along with the calculated vibrational levels of the A state for SH and SD. From this figure it may be seen that the predissociation will proceed via a case c^+ type mechanism, see Figure 1.8. As already mentioned, the most significant contribution to the predissociation rate of low v' levels of the A state is likely to be from interaction with the $1^4\Sigma^-$ state and a similar interaction has been invoked as the main contributor to the predissociation of low v' levels of the corresponding $A^2\Sigma^+$ states of both OH and OD [42]. To quantify the contributions to the predissociation from the three different repulsive states, $1^4\Sigma^-$, $1^2\Sigma^-$, and $1^4\Pi$, we have taken the calculated spin-orbit coupling matrix elements $H^{SO}(A^2\Sigma^+,1^4\Sigma^-)$, $H^{SO}(A^2\Sigma^+,1^2\Sigma^-)$ and $H^{SO}(A^2\Sigma^+,1^4\Pi)$ which are a sensitive function of S-H bond length in the region of the respective crossing points [38]. We paramaterised these matrix elements as a Taylor expansion in the shifted distance co-ordinate, $(R - R_x)$, to yield an effective coupling function $H^{SO}(R)$,

$$H^{SO}(R) = m_0 + m_1(R - R_x) + m_2(R - R_x)^2 \qquad (3.7)$$

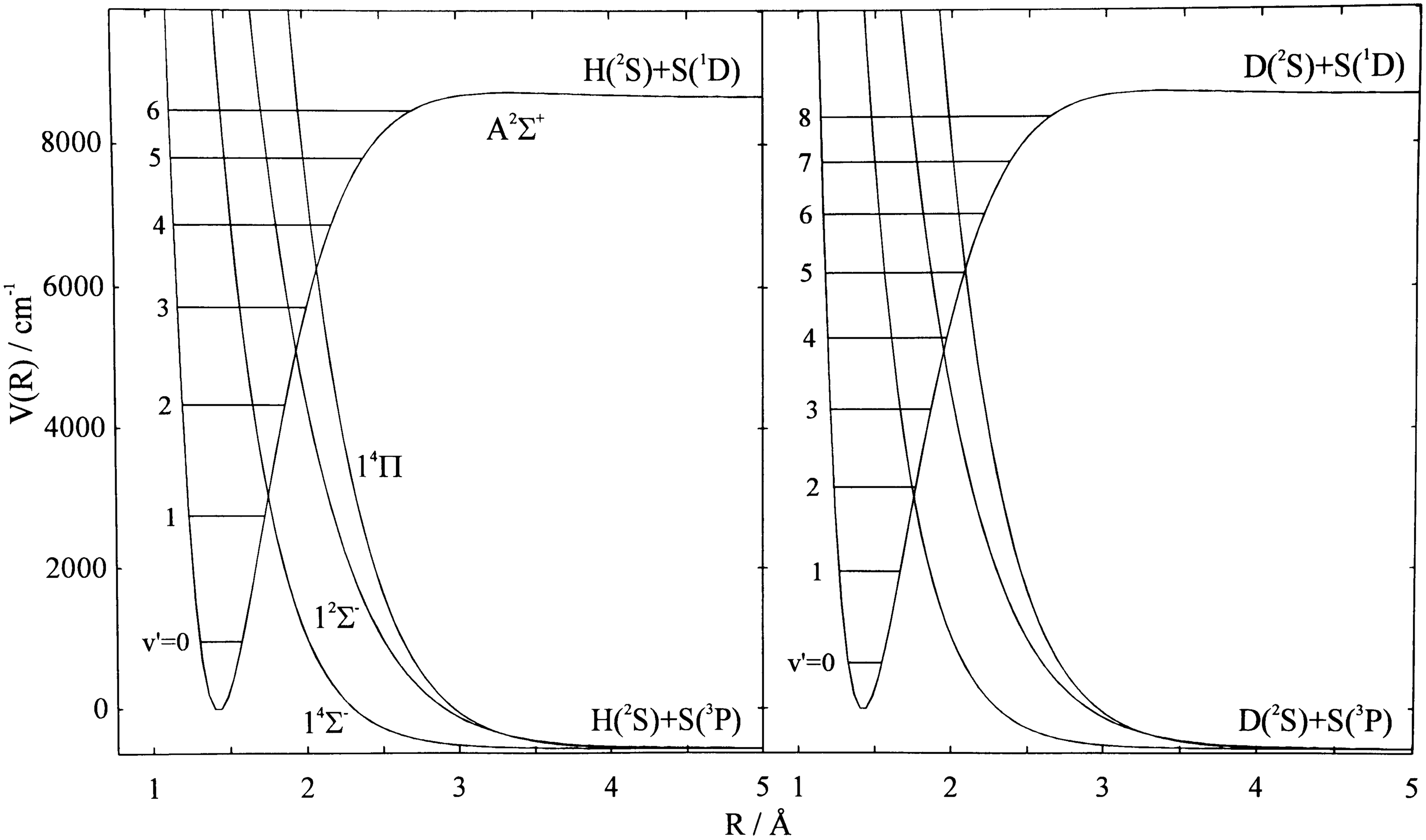

Figure 3.9. Potential energy curves used in the calculation of SH and SD predissociation rates. The horizontal lines show the energies of the vibrational levels of the $A^2\Sigma^+$ states of SH (left) and SD (right). The zero of energy is defined as the minimum of the $A^2\Sigma^+$ state potential.

This parameterisation procedure was carried out using the shareware program GNUPLOT. Figure 3.10 shows the calculated spin-orbit coupling matrix elements $H^{SO}(A^2\Sigma^+, 1^4\Sigma^-)$ taken from [38] together with the fitted coupling function $H^{SO}(R)$ superimposed on the region of the $A^2\Sigma^+$ and $1^4\Sigma^-$ state crossing. The fitted values of all parameters required for Equations 3.5 and 3.7 are listed in Table 3.

	b_1 / Å^{-1}	b_2 / Å^{-2}	D / cm^{-1}	A / cm^{-1}	R_x / Å	m_0 / cm^{-1}	m_1 / Å^{-1} cm^{-1}	m_2 / Å^{-2} cm^{-1}
$1^4\Sigma^-$	3.26	0.13	-564	4626.17	1.68	44	140	60
$1^2\Sigma^-$	2.20	0.17	-564	6730.83	1.87	50	109	-37
$1^4\Pi$	2.53	0.27	-564	8494.46	2.00	-162	67	54

Table 3. Parameters for the potentials and coupling functions used in the calculations of the SH/SD $A^2\Sigma^+$ v', N' predissociation rates. All parameters are defined in the text.

In Chapter 1 it was shown that the predissociation rate is proportional to the square of the matrix element coupling the bound and continuum states, known as the Fermi Golden Rule. Therefore in order to calculate predissociation rates for SH(SD) $A^2\Sigma^+$ (v', N') it is our goal to evaluate the spin-orbit coupling matrix element between the eigenfunctions $\langle v', N'|$ for the bound $A^2\Sigma^+$ state levels and the energy normalised continuum wavefunctions $\langle E, N'|$ of the $^4\Sigma^-$, $^2\Sigma^-$ and $^4\Pi$ dissociative states. Both the bound and continuum state wavefunctions are solutions of the radial Schrödinger equation

$$\left[-\frac{\hbar^2}{2\mu}\frac{d^2}{dR^2} + V(R)\right]\Psi = E\Psi \qquad (3.8)$$

where U(R) is the effective electronic potential energy curve including a centrifugal term that depends upon the rotational quantum number. Equation 3.8 may be integrated analytically by the method of Cooley [49], Cashion [50] and Zare [51] to yield tabulated solutions for the wavefunctions. In this method equation 3.8 is replaced by an equivalent

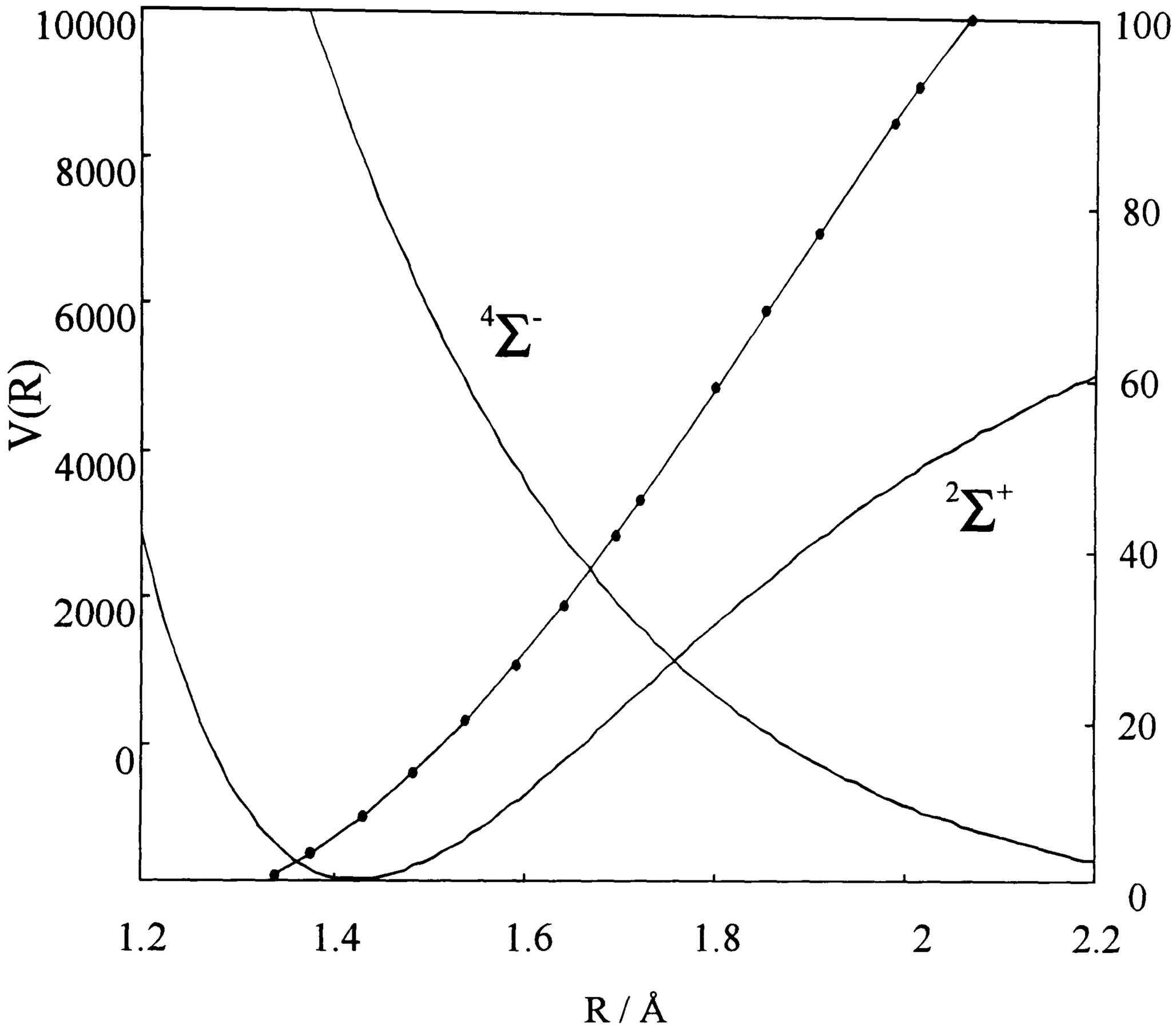

Figure 3.10. Potential energy curves of the bound $A^2\Sigma^+$ and repulsive $^4\Sigma^-$ state of SH shown with the calculated spin-orbit coupling function (•) on the right hand axis, taken from reference [38].

finite difference equation which is solved for the eigenvalue E of the total energy and the wavefunction Ψ by employing a Numerov [52] method of integration. The solution is obtained in two segments, by inward and outward integration, and is carried out iteratively starting with a trial eigenvalue then using a predictor-corrector formula [53] to adjust the eigenvalue to achieve continuity in the first derivative at the connection point to give the nearest true eigenvalue and wavefunction. This method is equally applicable to both the bound and continuum wavefunctions the only difference is in how the wavefunctions are normalised. In the case of the bound state the resulting wavefunctions are (space) normalised to unity once the solution has converged. The continuum wavefunctions, however, must be normalised with respect to energy, as discussed in chapter 1. This is achieved by normalising the amplitude of the outgoing function at some sufficiently large R (by which point the amplitude has stabilised for a number of successive maxima) to a unit amplitude and introducing the density of states factor $\rho(E)$. The matrix elements are then evaluated by pointwise summation of the product of the two wavefunctions and the R-dependent coupling term using an extended Simpson's rule formula. Finally the matrix elements are related to the predissociation rate by Fermi's Golden Rule. The above calculations were carried out using a slightly modified version of the computer program BCONT (Bound-Continuum Intensities) written by R. J. Le Roy [54].

Predissociation rates were calculated, as a function of the bound state v' and N' quantum numbers, for interaction with each of the three repulsive curves. As expected, the rates obtained for the SH and SD $A^2\Sigma^+$ $v' \leq 1$ levels interacting with the higher lying $1^2\Sigma^-$ and $1^4\Pi$ states were several orders of magnitude smaller than those from interaction with the $1^4\Sigma^-$ state. For SD $A^2\Sigma^+$ $v'=2$ the rates of predissociation via the $1^2\Sigma^-$ and $1^4\Pi$ states are calculated to be 10^3 and 10^5 times slower than for predissociation via the $1^4\Sigma^-$ state, but for SH $A^2\Sigma^+$ $v'=2$ the corresponding rates are both only one order of magnitude slower, suggesting the onset of significant predissociation via routes other than crossing to the $1^4\Sigma^-$ potential.

Figures 3.11 to 3.14 show a comparison of the calculated and experimental predissociation lifetimes for SH $A^2\Sigma^+$ $v'=0,1$ and SD $A^2\Sigma^+$ $v'=0,1,2$. The experimental

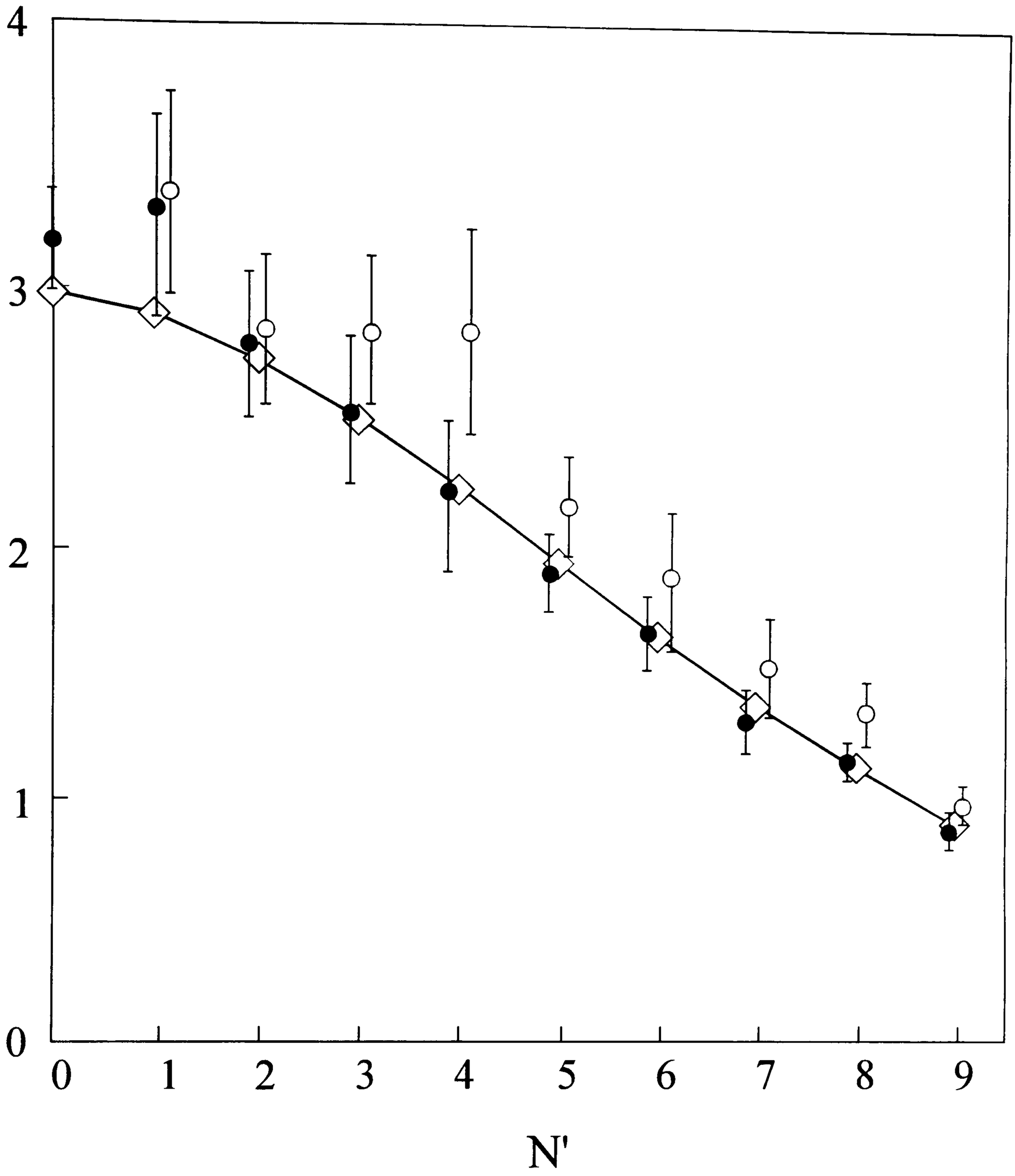

Figure 3.11. Lifetimes of SH $A^2\Sigma^+$ v'=0: Experimental results are shown by circles: ● *e* parity, ○ *f* parity; diamonds are the results of calculations described in the text. Experimental data are taken from references [24] and [25].

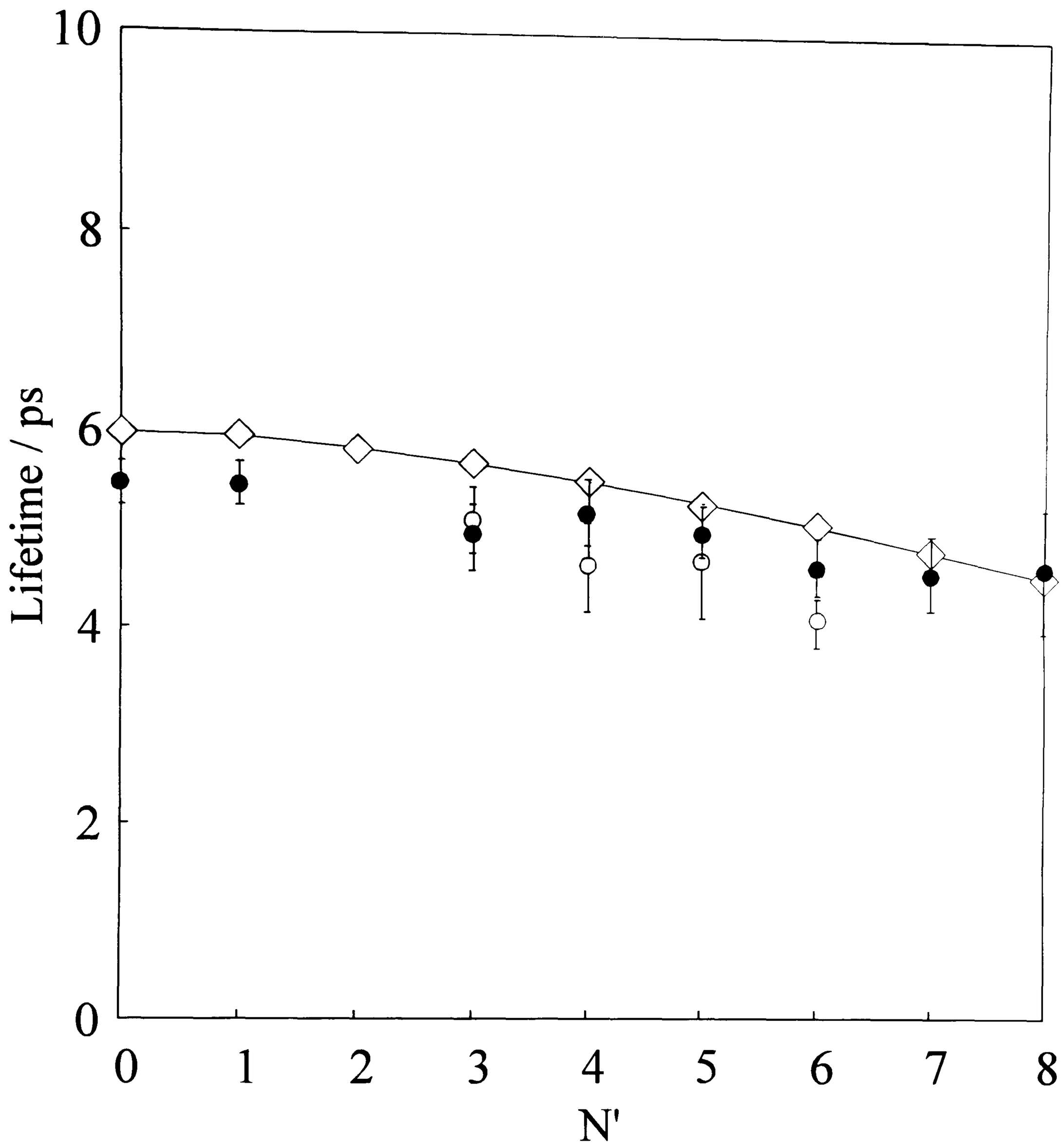

Figure 3.12. Lifetimes of SH $A^2\Sigma^+$ v'=1: Experimental results are shown by circles: ● *e* parity, ○ *f* parity; diamonds are the results of calculations described in the text.

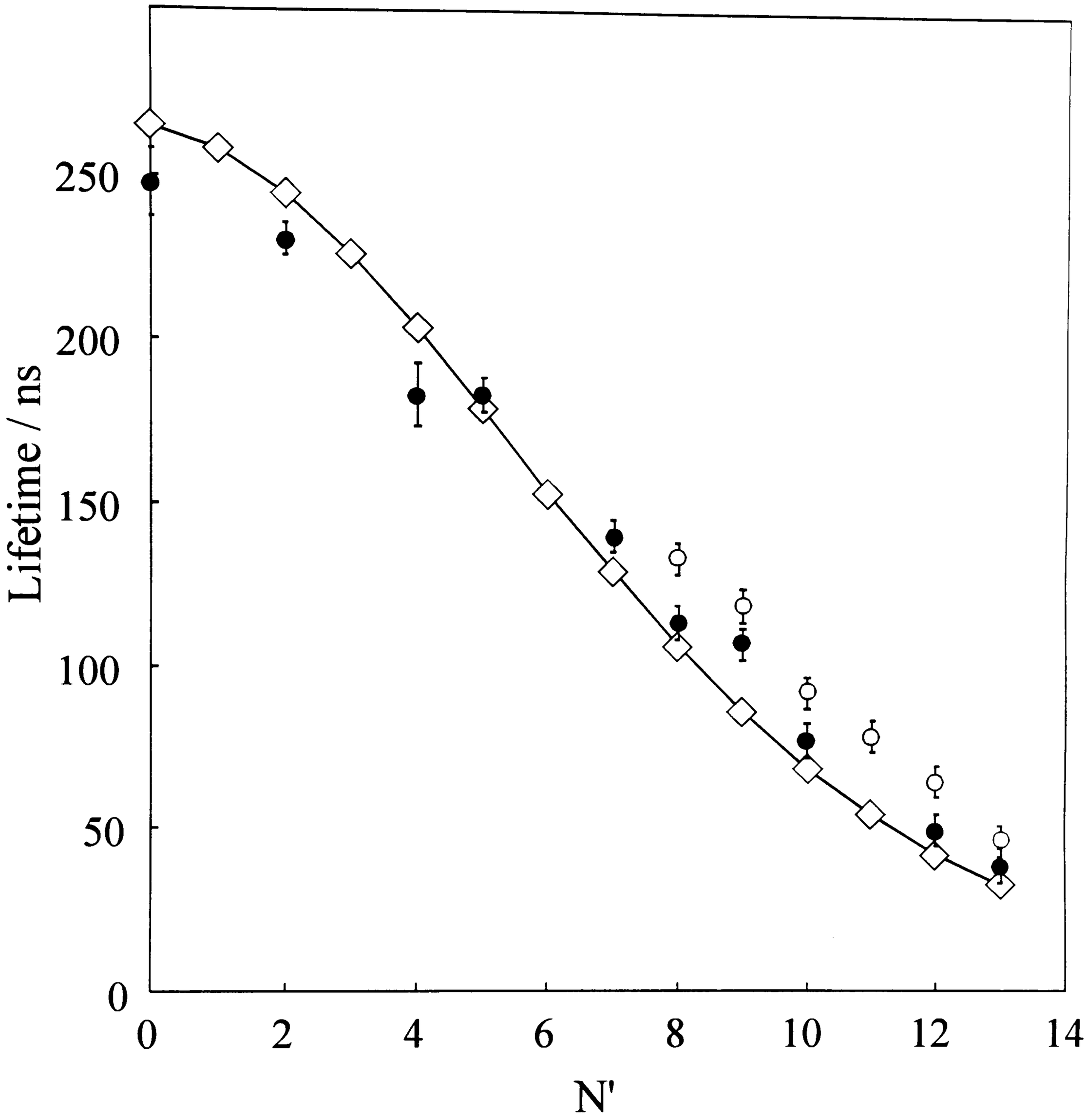

Figure 3.13. Lifetimes of SD $A^2\Sigma^+$ v'=0: Experimental results are shown by circles: ● *e* parity, ○ *f* parity; diamonds are the results of calculations described in the text. Experimental data are taken from reference [30].

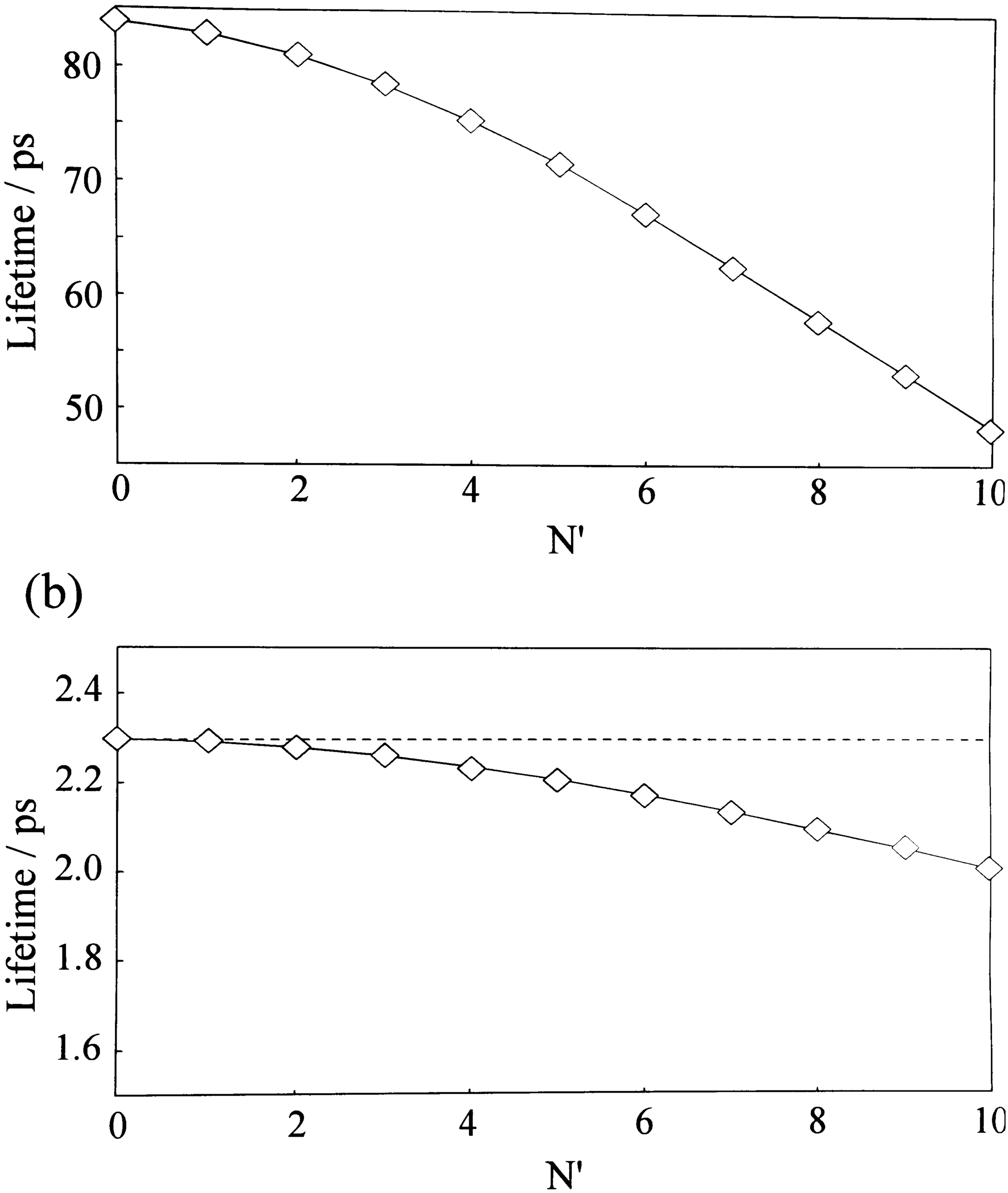

Figure 3.14. Calculated lifetimes of (a) SD $A^2\Sigma^+$ v'=1 and (b) SD $A^2\Sigma^+$ v'=2. For reasons outlined in the text it is not possible to give an experimental variation of lifetime with N' for these vibrational levels. SD $A^2\Sigma^+$ v'=1 has an experimentally measured lifetime of > 30 ps whilst that for SD $A^2\Sigma^+$ v'=2 is 2.3 ps (shown by dashed line in (b)).

data in Figures 3.11 and 3.13 are from Ubachs *et al.* [24,25] and Kawasaki *et al.* [30] respectively. The data for SD v'=0 has been converted from fluorescence lifetimes to predissociative lifetimes using the known radiative lifetime of SD $A^2\Sigma^+$ [27].

The calculated data were obtained as described above after optimisation of the precise form of the repulsive potentials to give the shown match with the N'-dependent SH $A^2\Sigma^+$ v'=1 experimental data. It was found that moving the repulsive potentials up and down in energy so as to be asymptotically correlated with the correct $S(^3P_j)$ spin-orbit components made only a negligible difference to the calculated data and hence all the repulsive potentials were set to be in agreement with the splitting between $S(^1D)$ and $S(^3P)$ (9239 cm^{-1}) as previously mentioned. The optimisation was done in a trial-and-error fashion by making minor adjustments to the $1^4\Sigma^-$ state potential from which we find, by inspection, that the experimentally measured SH (A) v'=1 lifetimes are reproduced best if the whole $1^4\Sigma^-$ state potential is shifted by -0.03 Å from the *ab initio* value, i.e., if R_x is decreased from 1.71 Å to 1.68 Å. This new value of R_x is also used in equation 5 for the coupling function. The crossing point of the $A^2\Sigma^+$ and $1^4\Sigma^-$ potentials then occurs at R_c = 1.75 Å. The repulsive potentials shown in Figure 3.9 are all shifted inwards by 0.03 Å from their *ab initio* crossing points with the A state, and all other calculated results displayed in Figures 3.11 - 3.14 make use of these slightly shifted *ab initio* $1^4\Sigma^-$, $1^2\Sigma^-$ and $1^4\Pi$ potentials and coupling functions and were not optimised for each experimental data set. The potentials and coupling functions we have chosen for the calculations are probably not unique in being able to model the experimental data but, as is apparent from the Figures, the agreement between experiment and calculations for all data sets is very good. The calculations for SH and SD match not just the absolute rates and lifetimes for different v' states, which vary by about five orders of magnitude, but also reproduce the N' dependence for the different v'. The greatest discrepancies are for SD v'=1 but, as pointed out in section 3.3, the linewidths in the SD A-X (1,0) band are very close to our experimental instrument function so precise determination of the homogeneous contributions to the linewidths is particularly difficult for this transition.

3.5 Discussion

We are now in a position to compare the variation of the predissociation rates of SH and SD $A^2\Sigma^+$ with hydrogen isotope and with vibrational and rotational level. The calculations described in the previous section reproduce quantitatively the magnitudes and variation of these rates and we can use the potentials, energy levels and wavefunctions from the calculations to interpret our experimental observations and to make predictions about the predissociation for levels with $v' > 2$.

The predissociation rate for a particular state depends on the extent of overlap of the bound state and continuum wavefunctions [55,56] and this overlap will be greatest for energy levels in close proximity to the energy of the crossing point between the $A^2\Sigma^+$ and repulsive-state potentials. The variation of the predissociation rate with v' is summarised in Table 3.3, and Figure 3.10 shows a plot of the shifted (as discussed earlier) potentials for the $A^2\Sigma^+$, $1^4\Sigma^-$, $1^2\Sigma^-$ and $1^4\Pi$ states used in the calculations. These calculations demonstrate that the predissociation of the v' = 0, 1, and 2 levels is dominated both for SH and SD by crossing to the $1^4\Sigma^-$ state and it is clear from the Figure that the large increase in predissociation rate for SH as v' increases from 0 to 1 is caused by the closeness of v'=1 to the energy of the crossing. Likewise, because of isotopic effects, the vibrational levels of SD lie lower in the potential than those of SH with the same vibrational quantum number. Hence, we observe a faster predissociation for SH v'=1 than for SD v'=1. The energy of SD v'=2, however, is greater than that of SH v'=1 and the former state predissociates about twice as quickly as the latter. Our calculations of the rate for predissociation of SD v'=2 predict a lifetime of ~ 2.3 ps in extraordinarily good agreement with the experimental result. To illustrate the influence of the overlap of the bound ($A^2\Sigma^+$) and continuum ($1^4\Sigma^-$) nuclear radial wavefunctions on the predissociation rate, Figure 3.15 shows plots of the calculated SD $A^2\Sigma^+$ v'=0 and v'=2 wavefunctions together with continuum wavefunctions of the same energy: it is evident that proximity to the crossing of the $A^2\Sigma^+$ and $1^4\Sigma^-$ potentials substantially enhances this overlap in the latter case.

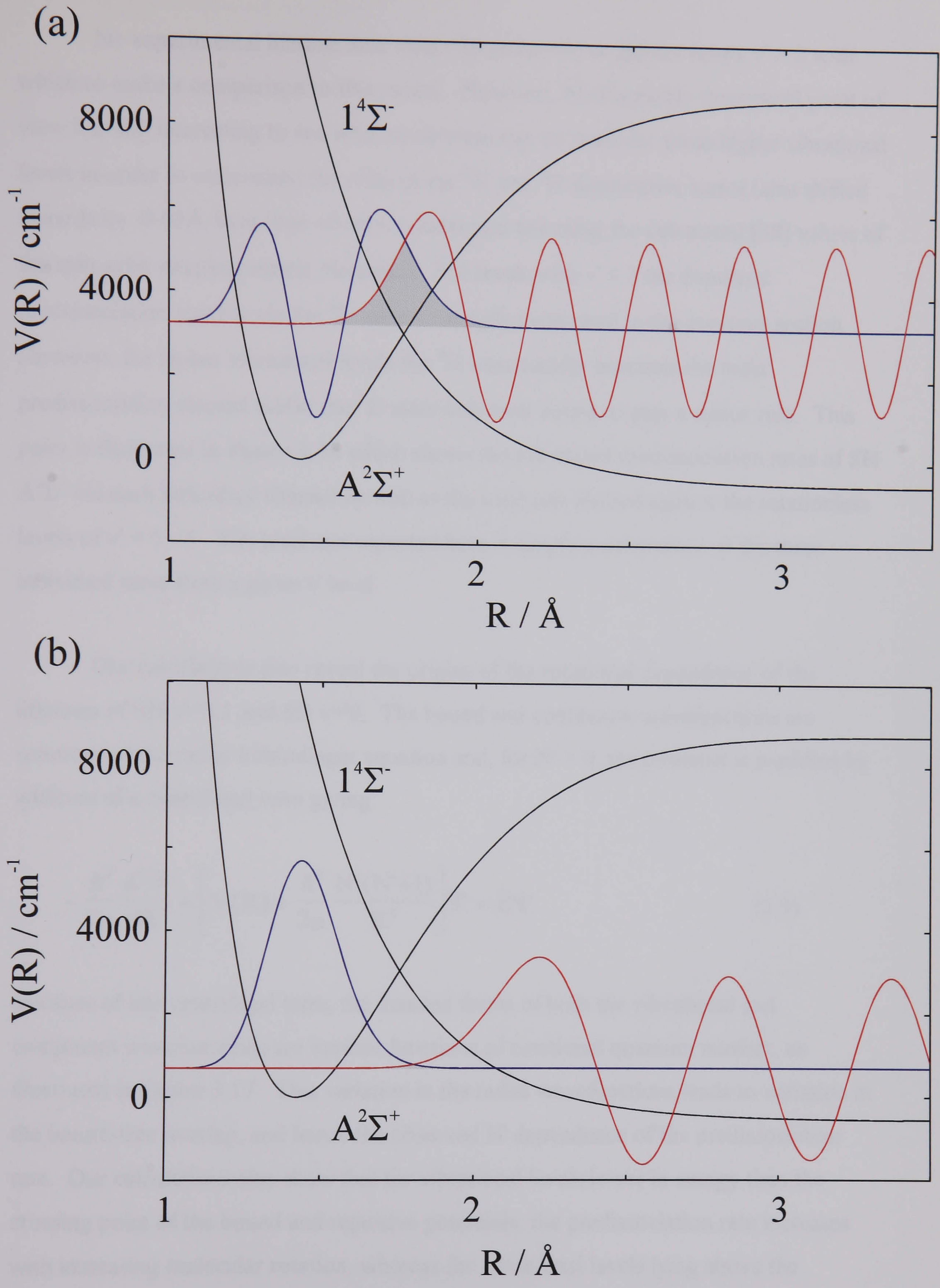

Figure 3.15. Calculated bound ($A^2\Sigma^+$) and continuum ($1^4\Sigma^-$) nuclear radial wavefunctions for SD. The bottom panel shows the SD $A^2\Sigma^+$ v'=0 wavefunction and the $1^4\Sigma^-$ wavefunction of the same energy. The top panel shows the SD $A^2\Sigma^+$ v'=2 wavefunction and the $1^4\Sigma^-$ wavefunction of the same energy. The very different overlaps (shaded areas) in the two cases are clearly apparent.

No experimental lifetime data exists for either SH or SD for levels v' > 2 with which to make a comparison to this model. However, from a purely theoretical point of view it is still interesting to see what predictions can be made for these higher vibrational levels in order to understand the roles of the $^2\Sigma^-$ and $^4\Pi$ dissociative states (also shifted inwards by -0.03Å from their *ab initio* values and assuming the calculated [38] values of the spin-orbit coupling matrix elements). For levels with v' ≤ 2 the dominant predissociation route is via the $^4\Sigma^-$ state as already mentioned in the previous section. However, for higher vibrational levels the $^4\Pi$ state rapidly becomes the main predissociation channel whilst the $^2\Sigma^-$ state only ever seems to play a minor role. This point is illustrated in Figure 3.16 which shows the calculated predissociation rates of SH $A^2\Sigma^+$ via each individual channel as well as the total rate plotted against the rotationless levels of v' = 0 - 5. The total rate reported here is simply a summation of the three individual rates from a given v' level

Our calculations also reveal the origins of the rotational dependence of the lifetimes of SH v'=0,1 and SD v'=0. The bound and continuum wavefunctions are solutions of the radial Schrödinger equation and, for N' > 0, the potential is modified by addition of a centrifugal term giving:

$$-\frac{\hbar^2}{2\mu}\frac{d^2\Psi}{dR^2}+\left[V(R)+\frac{\hbar^2}{2\mu}\frac{N'(N'+1)}{R^2}\right]\Psi=E\Psi \qquad (3.9)$$

Because of this centrifugal term, the detailed forms of both the vibrational and continuum wavefunctions are implicit functions of rotational quantum number, as illustrated in Figure 3.17. This variation in the radial wavefunctions leads to variation in the bound-free overlap, and hence the observed N' dependence of the predissociation rate. Our calculations also show that for vibrational levels lower in energy than the crossing point of the bound and repulsive potentials, the predissociation rate increases with increasing molecular rotation, whereas for vibrational levels lying above the crossing point e.g. SH (v'=2), the effect of increased rotation is to decrease the predissociation rate, this is illustrated in Figure 3.18.

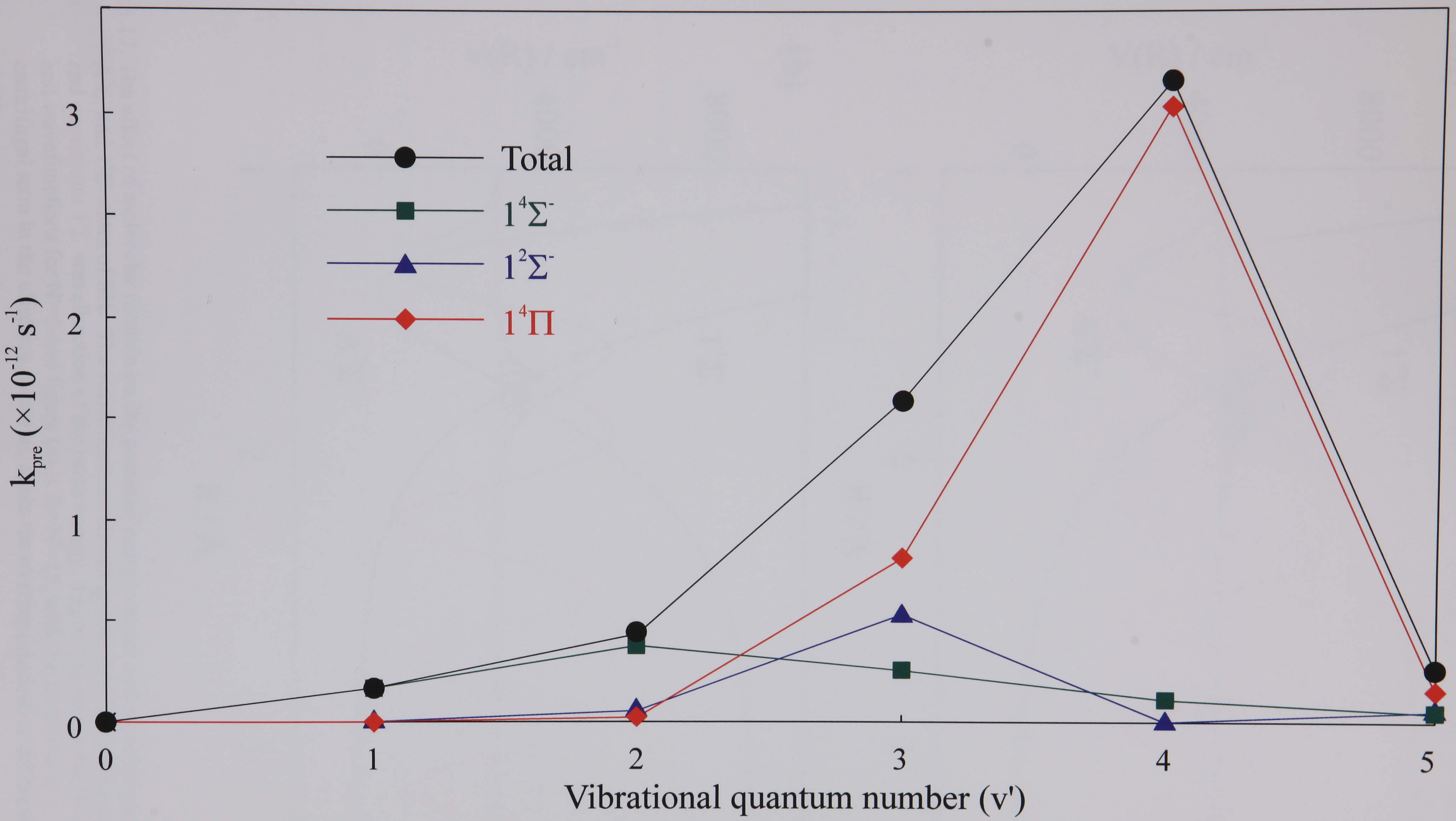

Figure 3.16. Variation of predissociation rate due to each dissociative state and the total predissociation rate for the first six vibrational levels of SH $A^2\Sigma$

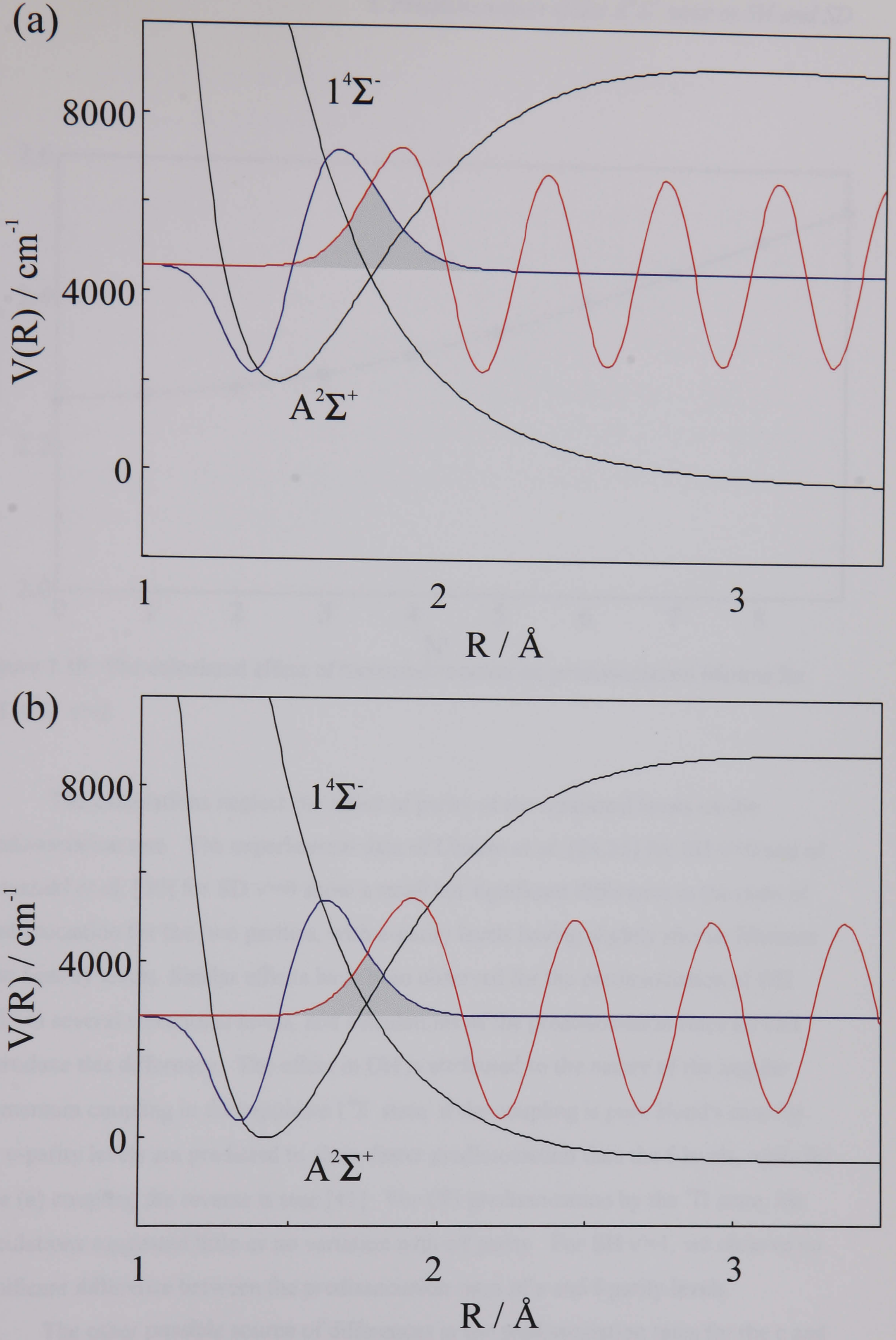

Figure 3.17. The effect of molecular rotation on the potential energy curves and wavefunctions of the $A^2\Sigma^+$ and $1^4\Sigma^-$ states of SH. The wavefunctions shown are the calculated bound $A^2\Sigma^+ v'=1$ and continuum $1^4\Sigma^-$ wavefunction of the same energy. Figure (b) shows the potentials and wavefunctions for N'=0 and figure (a) is for N'=15, with the inclusion of a centrifugal term in the effective potential, again the overlap (shaded) is different in both cases.

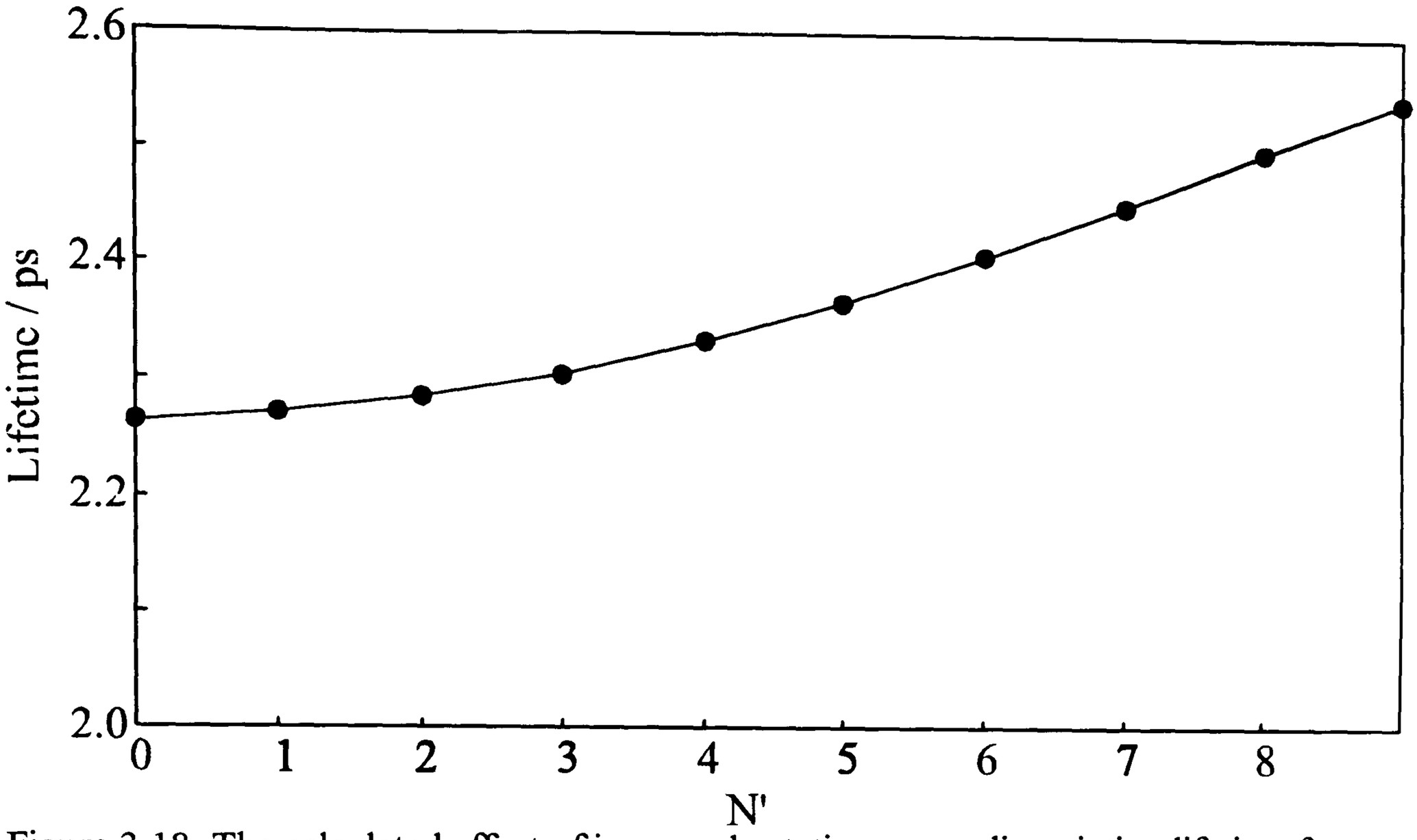

Figure 3.18. The calculated effect of increased rotation on predissociation lifetime for SH $A^2\Sigma^+$ v'=2.

The calculations neglect the effect of parity of the rotational levels on the predissociation rate. The experimental data of Ubachs *et al.* [24,25] for SH v'=0 and of Kawasaki *et al.* [30] for SD v'=0 show a small but significant difference in the rates of predissociation for the two parities, with e-parity levels having slightly shorter lifetimes than f-parity levels. Similar effects have been observed for the predissociation of OH $A^2\Sigma^+$ in several vibrational levels, and calculations of the predissociation rates for OH reproduce this difference. The effect in OH is attributed to the nature of the angular momentum coupling in the repulsive $1^4\Sigma^-$ state: if the coupling is pure Hund's case (b) the e-parity levels are predicted to show faster predissociation than the f-levels, while for case (a) coupling the reverse is true [41]. For OH predissociation by the $^4\Pi$ state, the calculations suggested little or no variation with e/f parity. For SH v'=1, we observe no significant difference between the predissociation rates of e and f-parity levels.

The other possible source of differences in the predissociation rates for the e and f-parity rotational levels is the difference in energy: for SH or SD $A^2\Sigma^+$ the e-parity level lies slightly higher in energy than the f-parity level of the same N' quantum number. We

have investigated the effect of this very small energy shift on the calculated predissociation rates and find it to be negligible.

It is interesting to compare the lifetime data for the A states of SH, SD with those of OH, OD to see the effects of a heavier nucleus on the magnitude of the spin-orbit interaction. In OH the crossing point of the $A^2\Sigma^+$ and $1^4\Sigma^-$ states occurs between v'=3 and v'=4 and, as a result, the lowest few rotational levels in v'=0 and 1 show no predissociation at all. Even in v'=3, however, the lifetime of the highest observed [39,40] rotational level is still as long as 33 ns in contrast with SH (v=1) for which $\tau < 5$ ps. This is largely a reflection of the smaller spin-orbit coupling matrix elements associated with the first row hydride.

3.6 Conclusions

Using a combination of experimental and theoretical methods it has been possible to understand the predissociation of the low vibrational states of SH and SD $A^2\Sigma^+$. As is the case with OH, the first electronically excited state of SH is predissociated by three repulsive states, the $1^4\Sigma^-$, $1^2\Sigma^-$ and $1^4\Pi$ states, which all correlate with $S(^3P) + H(^2S)$ at large internuclear separation. CRDS measurements of the A-X (1,0) bands of SH and SD and the (2,0) band of SD reveal the rates of predissociation through homogeneous broadening of spectral lines. The lifetimes determined from the predissociation rates have been compared with Fermi Golden Rule calculations that make use of an experimentally derived empirical potential for the $A^2\Sigma^+$ state and *ab initio* values for the $1^4\Sigma^-$, $1^2\Sigma^-$ and $1^4\Pi$ potentials and for the spin-orbit coupling between the bound and repulsive states. The comparison of experimental and theoretical results reveals that the predissociation of the A state levels with $v' \leq 2$ is dominated by coupling to the $1^4\Sigma^-$ state, but that the other repulsive potentials should start to contribute to the predissociation of higher v' levels. The rotational dependence of the predissociation rates determined by us for the v'=1 level of SH (A) and by others for the v'=0 levels of the A state of SH and SD is reproduced quantitatively by the calculations which show the variation to be the result of centrifugal contributions to the potential energy functions. The value of CRDS as a method of studying fast molecular predissociation is clearly demonstrated.

References

1. M.N. Lewis and J.U. White, *Phys. Rev.* **55** (1939) 894
2. A.G. Gaydon and G. Whittingham, *Proc. Roy. Soc. (London)*, **A189** (1947) 313.
3. P.J. Dyne and D.W.G. Style, *Nature*, **167** (1951) 899.
4. S. Leach, *Compt. rend.*, **230** (1950) 2181.
5. S. Leach, *Disc. Faraday Soc.*, **9** (1950) 81.
6. G. Porter, *Disc. Faraday Soc.*, **9** (1950) 60.
7. G. Herzberg and D.A. Ramsay, *Disc. Faraday Soc.*, **9** (1950) 80.
8. G.S. Tyndall and A.R. Ravishankara, *Int. J. Chem. Kinet.* **23** (1991) 483.
9. W.B. DeMore, S.P. Sander, D.M. Golden, R.F. Hampson, M.J. Kurylo, C.J. Howard, A.R. Ravishankara, C.E. Kolb, and M.J. Molina, *Chemical Kinetics and Photochemical Data for use in Stratospheric Modeling, Evaluation no. 10*, JPL Publications 92-20, Pasadena, 1990.
10. R.A. Stachnik and M.J. Molina, *J. Phys. Chem.*, **91** (1987) 4603.
11. N.E. Wang and E.R. Lovejoy, *J. Phys. Chem.*, **91** (1987) 5743.
12. A. Gourmi, J.D.R. Rocha, and P. Marshall, *J. Phys. Chem.*, **99** (1995) 10834.
13. E. Klisch, T. Klaus, S.P. Belov, A. Dolgner, R. Schieder, G. Winnewisser, and E. Herbst, *Astrophys. J.* **473** (1996) 1118.
14. W.L. Meerts and A. Dymanus, *Can. J. Phys.*, **53** (1975) 2123.
15. D. Zeitz, W. Bohle, J. Werner, A. Hinz, and W. Urban, *Mol. Phys.*, **54** (1985) 953.
16. S.H. Ashworth and J.M. Brown, J. Mol. Spec. **153** (1992) 41.
17. R.S. Ram, P.F. Bernath, R. Engleman Jr., and J.W. Braults, *J. Mol. Spec.*, **172** (1995) 34.
18. G. Herzberg, *Molecular Spectra and Molecular Structure*, Volume I - Spectra of Diatomic Molecules, Van Nostrand Reinhold Company Inc. (1950) and references therein.
19. D.A. Ramsay, *J. Chem. Phys.*, **20** (1952) 1920.
20. J.W.C. Johns and D.A. Ramsay, *Can. J. Phys.*, **39** (1961) 210.
21. C.M. Pathak and H.B. Palmer, *J. Mol. Spectrosc.*, **32** (1969) 157.
22. W.G. Hawkins and P.L. Houston, *J. Chem. Phys.*, **73** (1980) 297; ibid, **76** (1982) 729.
23. B.R. Weiner, H.B. Levene, J.J. Valentini, and A.P. Baronavski, *J. Chem. Phys.*, **90** (1989) 1403.
24. W. Ubachs, J.J. ter Meulen, and A. Dymanus, *Chem. Phys. Lett.*, **101** (1983) 1.
25. W. Ubachs and J.J. ter Meulen, *J. Chem. Phys.*, **92** (1990) 2121.
26. J.J. Tiee, M.J. Ferris, and F.B. Wampler, *J. Chem. Phys.*, **79** (1983) 130.
27. R.R. Friedl, W.H. Brune, and J.G. Anderson, *J. Chem. Phys.* **79** (1983) 4227.

28. G.W. Loge and J.J. Tiee, *J. Chem. Phys.*, **89** (1988) 7167.
29. G.W. Loge and J.J. Tiee, *J. Chem. Phys.*, **93** (1990) 2122.
30. M. Kawasaki, H. Sato, G. Inoue, and M. Suzuki, *J. Chem. Phys.*, **91** (1989) 6758.
31. J. Senekowitsch, H.J. Werner, P. Rosmus, E.A. Reinsch, and S.V. O'Neil, *J. Chem. Phys.*, **83** (1985) 4661.
32. M.-C. Yang, A.P. Salzberg, B.-C. Chang, C.C. Carter, and T.A. Miller, *J. Chem. Phys.*, **98** (1993) 4301.
33. J. Zoval, D. Imre, and V.A. Apkarian, *J. Chem. Phys.*, **98** (1993) 1.
34. A.B. McCoy, *1997 Conference on the Dynamics of Molecular Collisions*
35. T.W. Wasserman, A.A. Arias, T. Müller, and P. H. Vaccaro, *Chem. Phys. Lett.*, **262** (1996) 329.
36. D.M. Hirst and M.F. Guest, *Mol. Phys.* **46** (1982) 427.
37. P.J. Bruna and G. Hirsch, *Mol. Phys.* **61** (1987) 1359.
38. M. Riad Manaa, *Int. J. Quantum Chemistry: Quantum Chemistry Symposium*, **29** (1995) 577.
39. D.E. Heard, D.R. Crosley, J.B. Jeffries, G.P. Smith, and A. Hirano, *J. Chem. Phys.*, **96** (1992) 4366.
40. J.A. Gray and R.L. Farrow, *J. Chem. Phys.*, **95** (1991) 7054 and references therein.
41. M.L. Sink, A.D. Bandrauk, and R. Lefebvre, *J. Chem. Phys.*, **73** (1980) 4451.
42. D.R. Yarkony, *J. Chem. Phys.*, **97** (1992) 1838 and references therein.
43. M.E. Green and C.M. Western, *J. Chem. Phys.*, **104** (1996) 848.
44. C.E. Moore, *Atomic Energy Levels*, NSRDS-NBS 35 vol. 1 (1971).
45. L. Schnieder, W. Meier, K.H. Welge, M.N.R. Ashfold, and C.M. Western, *J. Chem. Phys.*, **92** (1990) 7027.
46. G.P. Morley, I.R. Lambert, D.H. Mordaunt, S.H.S. Wilson, M.N.R. Ashfold, R.N. Dixon, and C.M. Western, *J. Chem. Soc. Faraday Trans.*, **89** (1993) 3865.
47. J.N. Murrell, S. Carter, S.C. Farantos, P. Huxley, and A.J.C. Varandas, *Molecular Potential Energy Functions*, Wiley, New York (1984).
48. R.J. LeRoy, LEVEL 6.1, University of Waterloo Chemical Physics Research Report CP-555R (1996).
49. J. W. Cooley, *Math. Comp.*, **15** (1961) 363
50. J. K. Cashion, *J. Chem. Phys.*, **39** (1963) 1872
51. R. N. Zare, *J. Chem. Phys.*, **40** (1964) 1934
52. B. Numerov, *Publ. Obs. Central Astrophys. Russ.*, **2** (1933) 188.
53. P.-O. Löwdin, *J. Mol. Spec.*, **10** (1963) 12.
54. R.J. LeRoy, *Comp. Phys. Comm.* **52** (1989) 383; BCONT 1.4, University of Waterloo Chemical Physics Research Report CP-329R (1993).

55. H. Lefebvre-Brion and R.W. Field, *Perturbations in the Spectra of Diatomic Molecules.*, Academic Press, Inc., (1986)

56. J. Tellinguisen, *Adv. Chem. Phys.*, **60** (*Photodissociation and Photoionization*, K.P. Lawley, editor), 299 (1985).

4. Predissociation of high vibrational levels within the $B^3\Sigma_u^-$ state of S_2.

4.1 Introduction

The $B^3\Sigma_u^-$-$X^3\Sigma_g^-$ system of S_2 contains many bands spanning a wavelength range of 250 - 700 nm and is analogous to the extensively studied Schumann-Runge band system of O_2 [1]. Unlike O_2, S_2 is not a stable molecule; it is produced only transiently in sulphur containing flames and discharges [2,3,4], and also high temperature (>800 K) sulphur vapour. The B-X transition is very intense and is responsible for the blue colour arising from flames and discharges containing sulphur. Since its first observation by Graham in 1910 [5] many attempts have been made to interpret this heavily perturbed band system and only recently [6,7,8] has a full rotational analysis been carried out. A complete understanding of this band system is desirable for a number of reasons: The strength of the transition makes S_2 a useful probe for studying combustion processes of sulphur-containing fossil fuels via LIF. It is also of interest in molecular dynamics studies as it is a product of photodissociation processes such as CS_2 photolysis [9], and reactions e.g. $S(^1D)$ + OCS [10], thus a detailed knowledge of the B-X band system may provide information on energy disposal in the fragments / products. The recent observation by the Hubble space telescope of the impact of the comet Shoemaker-Levy with Jupiter revealed S_2 to be transiently produced in its atmosphere following the collision [11]. Other observations have revealed the presence of S_2 within cometary atmospheres [12,13] and it is believed to play an important role in the sulphur chemistry of dense molecular clouds [14,15]. At high temperatures the large number of bands overlap to cause a virtual continuum of levels throughout the UV and visible part of the spectrum, it is for this reason that this transition has been put forward as a possible candidate for a chemical laser. The population inversion is achieved via optical pumping of the B state [16] and the subsequent lasing transitions are to high vibrational levels of the ground state which are unpopulated at the 500 °C operating temperature. Another important application of the S_2 B-X transition that is currently being developed is for the

production of mercury-free discharge lamps and daylight-simulation light bulbs using low-pressure rf sulphur discharges [17].

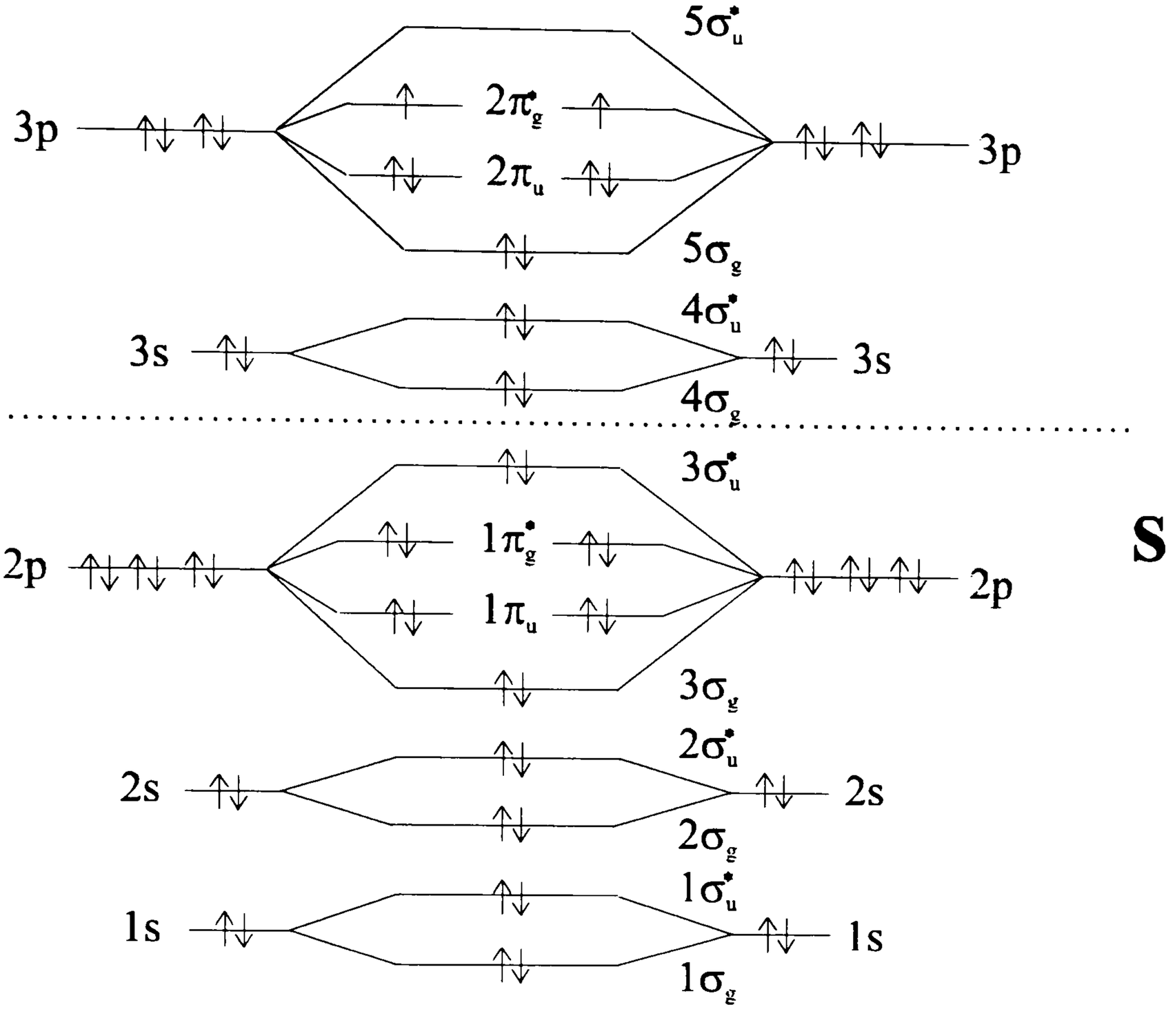

Figure 4.1. Molecular orbital diagram of the $X^3\Sigma_g^-$ state of S_2. The dotted line shows the distinction of essentially core and valence orbitals.

The ground $X^3\Sigma_g^-$ state of S_2 has the electronic configuration $\ldots 5\sigma_g^2\, 2\pi_u^4\, 2\pi_g^2$ as illustrated in the molecular orbital diagram of Figure 4.1, and has been well characterised by a combination of epr [18] and microwave [19] studies. The value of the spin-spin splitting constant, $\lambda = 11.8\ cm^{-1}$ observed in the ground state is surprisingly large, as the direct spin-spin splitting usually tends to become smaller with increasing molecular weight. This observation may be understood by the realisation that the effective spin-spin coupling parameter is actually composed of two contributions, the direct spin-spin splitting parameter λ_{SS}, and the second order spin-orbit parameter λ_{SO} due to interaction of the ground state with an electronic state of the same configuration. The magnitude of

the effective value of λ observed in the $X^3\Sigma_g^-$ state of S_2 is dominated by the second order spin-orbit interaction with the isoconfigurational $b^1\Sigma_g^+$ state. Only the Ω=0 component of the $X^3\Sigma_g^-$ state can interact with the $^1\Sigma_g^+$ state via spin-orbit coupling, and since the $^1\Sigma_{0g}^+$ state is at higher energy than the $^3\Sigma_{0g}^-$ state it will have the effect of pushing the Ω=0 component of the ground state to lower energy hence increasing the effective value of λ as shown in Figure 4.2. The magnitude of this shift has been calculated from second order perturbation theory to be around 13.5 cm^{-1} compared with an experimentally determined value of 11.8 cm^{-1} [20].

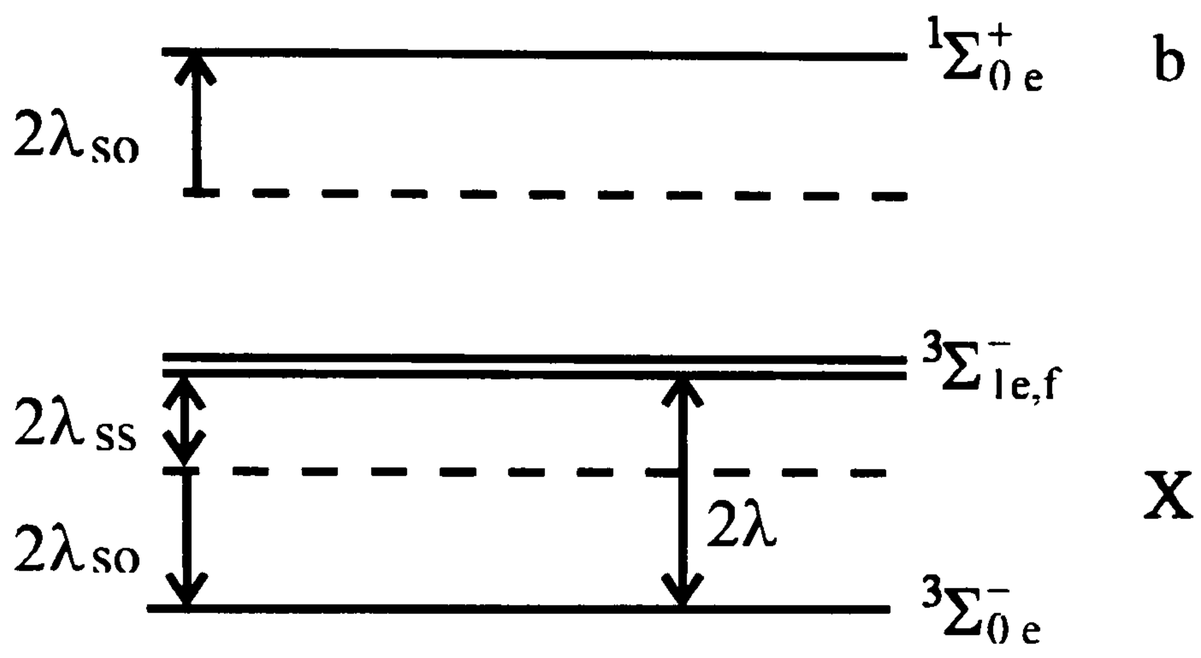

Figure 4.2. The shifts in energy level caused by the interaction between the b and the X state. This results in a second order spin-orbit splitting which contributes to the effective spin-spin splitting for the X state. The dashed lines are the deperturbed energy levels.

Due to this large spin-spin splitting, a Hund's case (a) coupling scheme provides the best description of the rotational energy levels at low J, since the different Ω components are well separated compared with the rotational energy levels ($|\lambda| >> BJ$). However, as J increases, a transition from case (a) to case (b) coupling (S-uncoupling interaction) occurs since the rotational energy level spacing becomes comparable to the multiplet splitting. The energy level patterns for the $X^3\Sigma_g^-$ state at both low and high J are shown in Figure 4.3. The rotational energy levels for a $^3\Sigma$ state have been derived, including contributions arising from spin-spin splitting, and the spin-rotation interaction, γ. These energy levels, neglecting centrifugal distortion, are given by the Schlapp expression [21],

$$
\begin{aligned}
F_1(N) &= BN(N+1) - (2N-1)B - \lambda + [\lambda^2 - 2B\lambda + B^2(2N-1)^2]^{\frac{1}{2}} - \gamma N + \tfrac{1}{2}\gamma \\
F_2(N) &= BN(N+1) \\
F_3(N) &= BN(N+1) + (2N+3)B - \lambda - [\lambda^2 - 2B\lambda + B^2(2N+3)^2]^{\frac{1}{2}} + \gamma(N+1) + \tfrac{1}{2}\gamma
\end{aligned}
\qquad (4.1)
$$

where the F_i labels are determined by the ordering of the different Ω components in the high J (case (b)) limit. F_1 refers to components where J=N-1, F_2 refers to those where J=N, and F_3 to those where J=N+1.

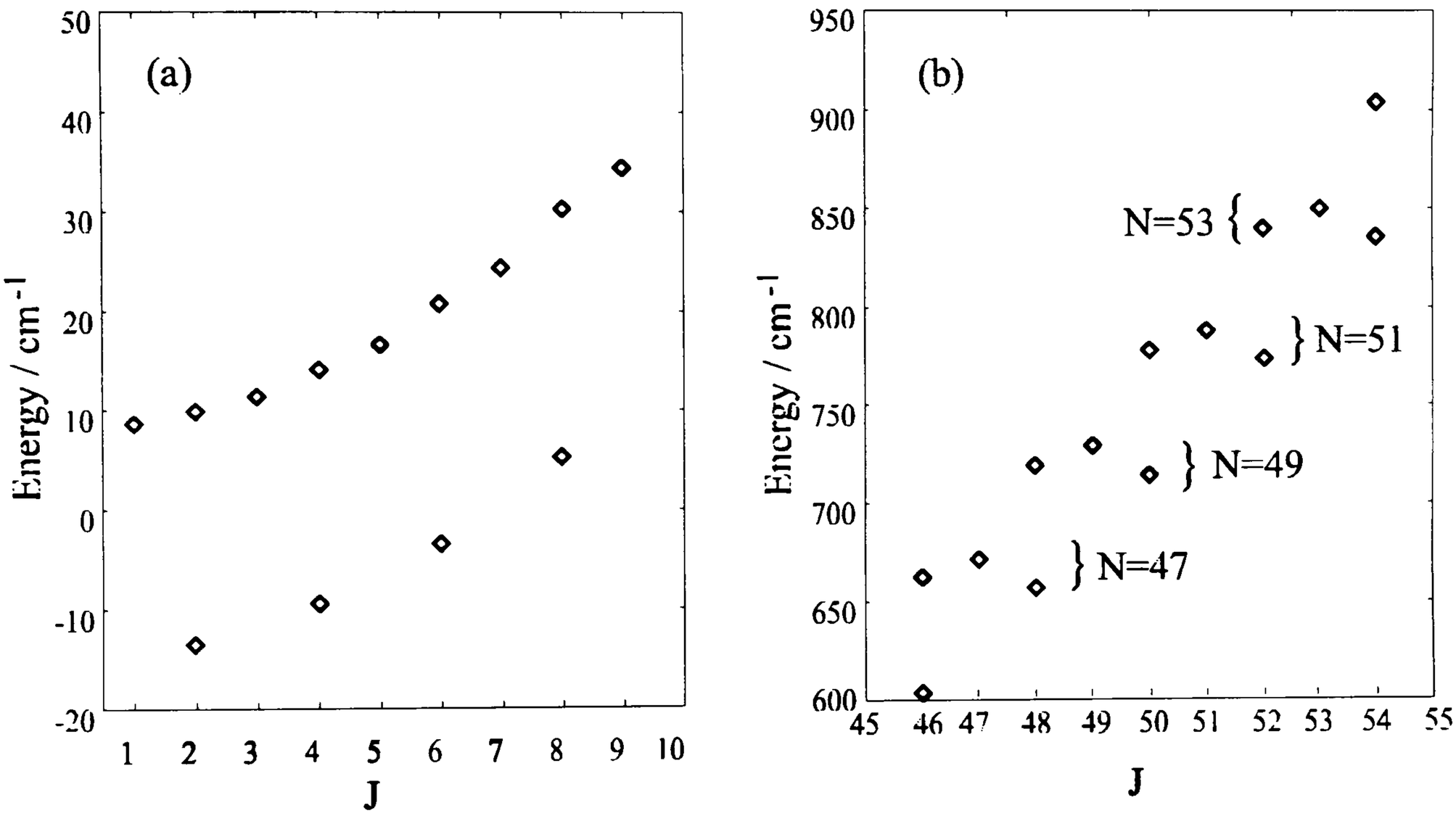

Figure 4.3. Energy level pattern for the S_2 X $^3\Sigma_g^-$ state (λ = 11.8 cm^{-1}) at (a) low J and (b) high J.

Also arising from this configuration are the $x^1\Delta_g$ and $b^1\Sigma_g^+$ both of which have also been observed experimentally.

The first excited molecular configuration $\ldots 5\sigma_g^2\, 2\pi_u^3\, 2\pi_g^3$ gives rise to the $B^3\Sigma_u^-$ state, which is the main concern of this work, and another five possible excited electronic states $c^1\Sigma_u^-$, $A'^3\Delta_u$, $A^3\Sigma_u^+$, $b^1\Delta_u$ and $^1\Sigma_u^+$ of which the first four have been identified via spectroscopic transitions.

The configuration $\ldots 5\sigma_g^{\,2}\, 2\pi_u^{\,4}\, 2\pi_g^{\,1}\, 5\sigma_u^{\,1}$ is also of some importance in this study since it gives rise to the $B''^3\Pi_u$ and $^1\Pi_u$ states. The former gives rise to the extensive perturbations observed in the B state and has been identified spectroscopically [22] in rare gas matrix studies and by virtue of its long lifetime (0.1-3.9 μs) [23,24], whereas the latter has been invoked by many authors [25,26] to be responsible for the onset of the first predissociation in the B state at high vibrational energies. Two other repulsive states, $^5\Pi$ and $^5\Sigma$ that may contribute to the predissociation arise from the configurations $\ldots 5\sigma_g^{\,2}\, 2\pi_u^{\,2}\, 2\pi_g^{\,3}\, 5\sigma_u^{\,1}$ and $\ldots 5\sigma_g^{\,1}\, 2\pi_u^{\,4}\, 2\pi_g^{\,2}\, 5\sigma_u^{\,1}$ respectively.

Many other states including Rydberg [27] and ion-pair states [28] have been identified and Figure 4.4 shows all of the observed transitions within the S_2 molecule to date.

The work presented in this chapter is concerned with the B-X transition in $^{32}S_2$. The selection rules governing the transition between two case (a) $^3\Sigma$ states are $\Delta J=0,\pm1$, with the restriction that if both states have $\Omega = 0$ the $\Delta J=0$ transitions are forbidden. Thus for the $^3\Sigma_{0u}^- - {}^3\Sigma_{0g}^-$ transition within the case (a) limit only P and R branches are expected whereas for the other transitions where at least one of the states has $\Omega > 0$ then P, Q, and R branches are expected. However, for higher rotational excitation the states are better described within the case (b) limit thus obeying the selection rules $\Delta N=\pm1$, and $\Delta J=0,\pm1$ resulting again in P, Q, and R branches being formally allowed. It has been found previously that the Q branches in S_2 are intrinsically very weak and are not observed experimentally. The allowed transitions for both case (a) and case (b) limits for the case when the upper state spin-spin constant is positive are shown in Figure 4.5.

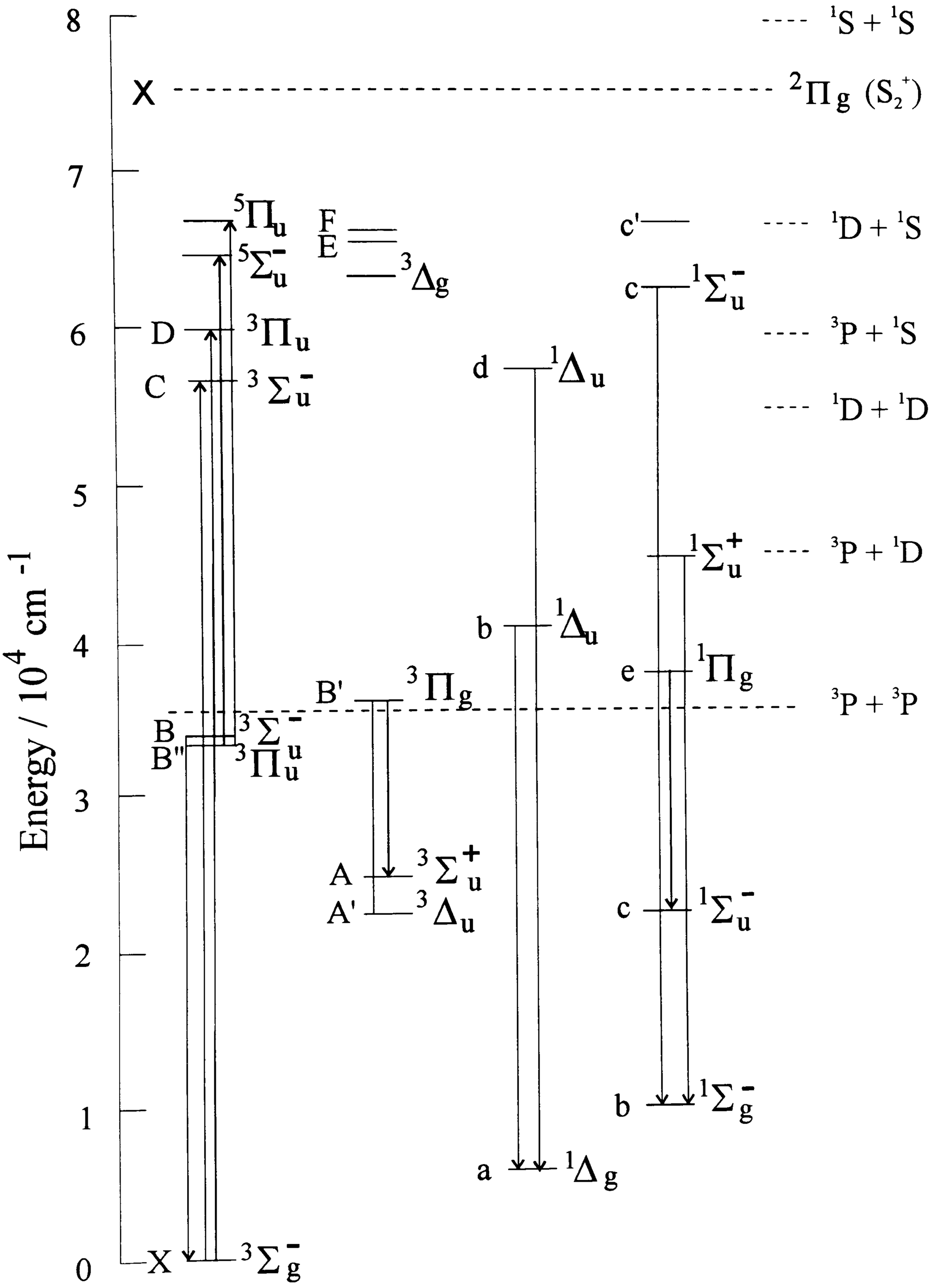

Figure 4.4. Observed transitions in S_2 to date.

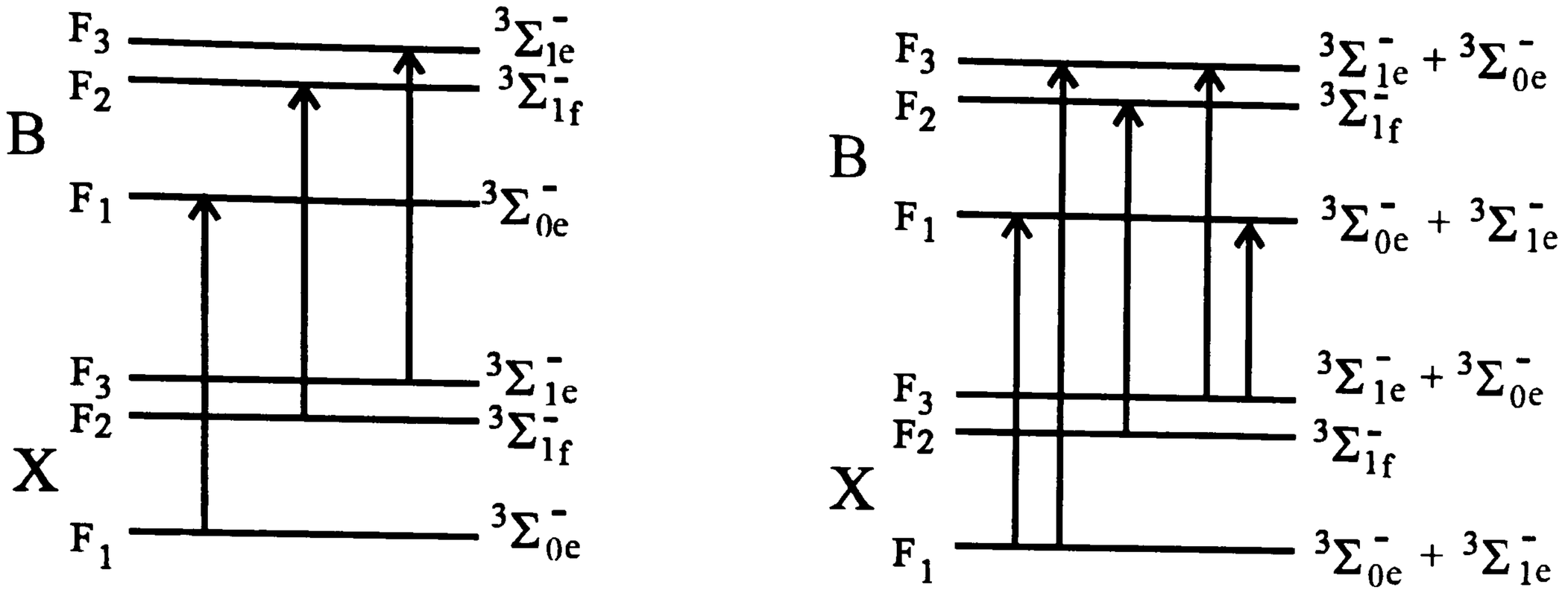

Figure 4.5. The allowed $B^3\Sigma_u^- - X^3\Sigma_g^-$ transitions when λ' is positive (a) at low J and (b) at high J.

Much effort has been put in over the past 80 years to try to understand the extensively perturbed rotational structure of the B-X transition. The coarse vibrational structure of the B-X system is approximated by the Dunham expansion [29],

$$G_v / cm^{-1} = 31835 + 434.0(v + \tfrac{1}{2}) - 2.75(v + \tfrac{1}{2})^2 \qquad (4.2)$$

Early attempts to elucidate the perturbed nature of the B state mainly consisted of partial rotational analysis of isolated pairs of vibrational bands [30]. Many rotational perturbations were observed in vibrational levels v'=7,8. From this analysis the nature of the perturbing state was deduced to be $^3\Pi_u$ and was ascribed the spectroscopic label B". Further studies [31], revealed erratic variation of values of the molecular constants with vibrational level, such as the spin-spin splitting constant λ having values of around -4.7 cm^{-1} for v'=0,2,4 and around +9.5 cm^{-1} for v'=1,3,5. Attempts have been made to provide a deperturbation model in terms of mixing between the B and B" states [32,33] in order to understand the observed rotational structure of the B state $0 < v' < 10$. The most recent and thorough analysis by Green and Western [6,7,8] considered the system as a whole, rather than deperturb two or three bands in isolation, in order to account for interactions from far off states. From this work deperturbed constants were obtained up to v=9 by using experimental results from both rotationally cold and hot spectra.

In his original study of the absorption spectrum of the B-X band system, Graham [5] noted that there were two points where the lines became diffuse: the first beginning with the (11-0) band and the second with the (18-0) band. The first specific studies of predissociation effects within high vibrational levels of the $B^3\Sigma_u^-$ state were conducted in 1937 by Olsson [34] and further investigated by Herzberg and Mundie [35]. Prior to these works it had already been established [36,37] that emission from the $B^3\Sigma_u^-$ state abruptly breaks off at high rotational levels within the v'=8 and 9 manifolds whilst no emission was seen from the v'=10 level indicating a limit for predissociation lying somewhere between some high rotational level of the v'=9 state and the origin of the v'=10 state. Herzberg's experiments utilised a 6-meter long absorption cell to photograph the whole of the B-X band system. The spectrum revealed an intensity distribution quite different from what one would expect from interpretation based on the Franck-Condon principle, with a sudden increase in intensity at around v'=10. This anomalous intensity distribution was explained in terms of the predissociation setting in at v'=10; lines corresponding to transitions to this level were still sharp at the experimental resolution, whereas those for transitions to v'=11 become obviously diffuse. In fact the v'=9 band seems to have a greater than expected intensity at high rotational energies indicating that predissociation has already set in by this point in agreement with earlier emission studies.

From these observations Herzberg attributed the predissociation mechanism to a type Ic (see Figure 1.8), i.e. the predissociation limit lies appreciably higher in energy than the true dissociation energy of the predissociating state, thereby giving an upper limit for the dissociation energy of S_2 D_0=35500 cm^{-1}. This result was contrary to the conclusions drawn from the work of Rosen, Désirant and Duchesne [37] who from the breaking-off of bands with v'=8 and 9 in emission assigned the predissociation to a case Ib using the method of Herzberg [38]. However, these authors had not analysed the fine structure of the bands in detail and both of these bands are subject to large rotational perturbations thus making use of the above-mentioned method unreliable. In 1969 Ricks and Barrow [39] re-examined predissociation within the B states v'=8,9, and 10 using a 3.4 metre plane-grating spectrograph. In this work they carefully analysed the breaking off in emission due to predissociation of $^{32}S_2$, $^{34}S_2$, and $^{32}S^{34}S$ and were able to obtain

three limiting curves of predissociation corresponding to the F_1, F_2, and F_3 components (only the F_1 component was observed for v'=10), all of which extrapolated to the same limit of 35999.0 ± 2.5 cm^{-1} above the ground state minimum (see Figure 4.6). From their data they were able to estimate the energy of the crossing point, E_c, again using the method of Herzberg and interpreted the predissociation as a case Ib as had Rosen, Désirant and Duchesne [37] some 34 years earlier. Therefore, the limiting value of predissociation they obtained, 35999.0 ± 2.5 cm^{-1}, should correspond to the true dissociation limit. Since the last observed value of J' decreased with increasing vibrational level they were able to assign the predissociation as type Ib^+ in Mulliken's classification, i.e. an outer wall (attractive branch) crossing, thus eliminating the repulsive inner wall of the B" state as a candidate. The limiting curves for predissociation of all three Ω-components, F_1, F_2 , and F_3, of the B state tend toward the same limit indicating that they were all predissociated by the same state. From this investigation they postulated that the first predissociating state was probably a 1_u state correlating with $S(^3P_2) + S(^3P_1)$ and proposed the $^1\Pi_u$ state as a likely candidate since it would be capable of predissociating all three Ω-components of the $B^3\Sigma_u^-$ state. By making use of the known spin-orbit splitting between $S(^3P_2)$ and $S(^3P_1)$ of 396.8 cm^{-1} they were also able to obtain an improved estimate of the ground state dissociation energy D_0 = 35216.4 ± 2.5 cm^{-1}.

Emission from the lowest rotational levels of the $B^3\Sigma_{0u}^-$ v'=10 level has been studied in detail more recently [7,23], the lifetime calculated from fluorescence decay rate was found to be less than 3 ns compared with a lifetime of around 32 ns for lower non-predissociated vibrational levels. In these studies no emission was observed for v' > 10. It should be noted that transitions have been observed from v'=10,11, and 12 when S_2 is formed from the reaction of H atoms with H_2S (v'=10,11) [40,41] and in an electrical discharge of SF_6/He mixtures (v'=10,11,12) [42]. The observed emission is attributed to inverse predissociation, i.e. atomic recombination in the absence of a third body quencher.

Theoretical investigations of the B state of S_2 to date have been limited. In fact, only two such investigations are to be found in the literature. Swope *et al.* [43]

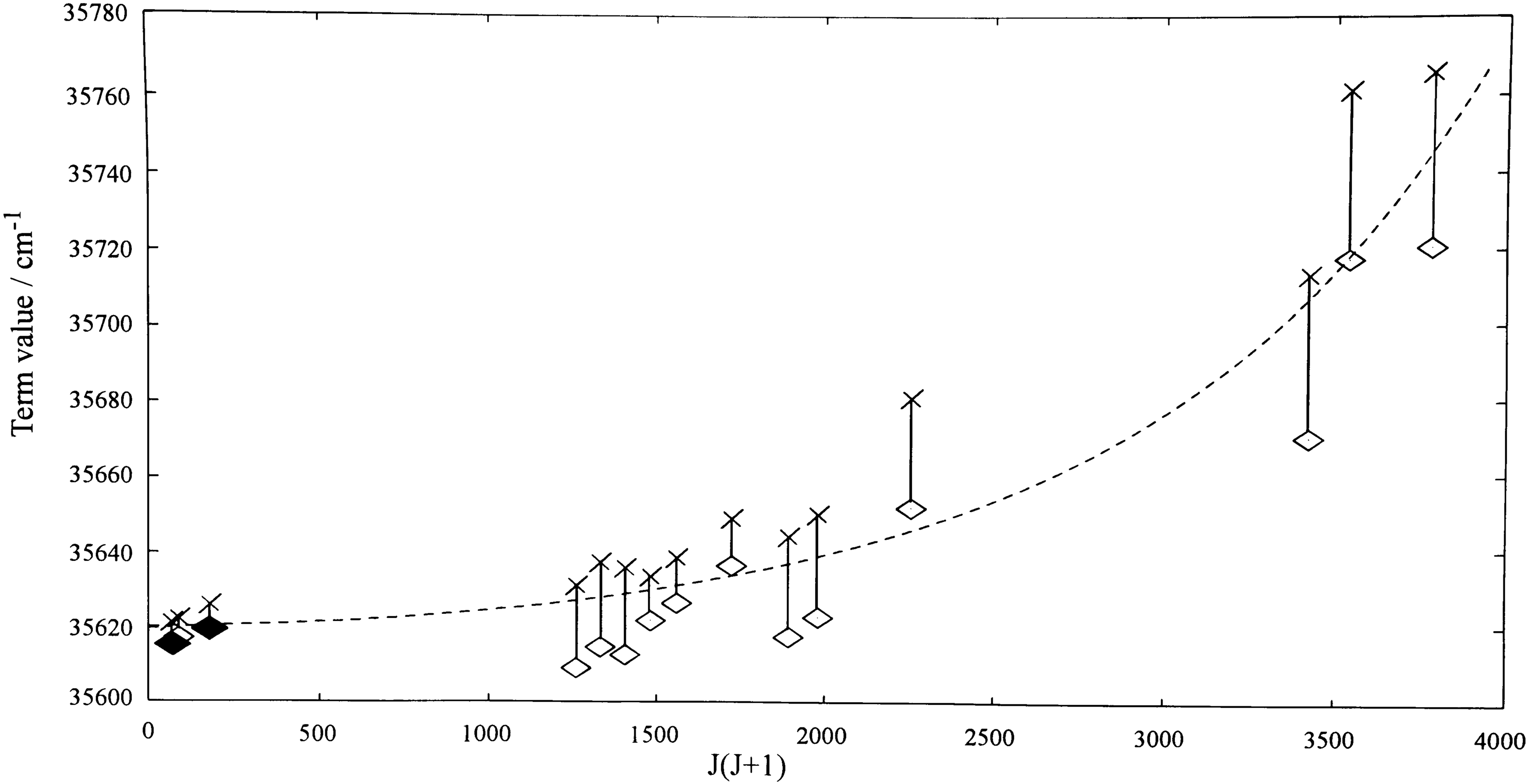

Figure 4.6. Plot of term values against J(J+1) for the last rotational levels, (◇) observed by Ricks and Barrow [39] for the B v'=8-10 state,. (◆) observed by Green and Western [7,8] for the B' v''=20 and 21. The crosses (×) represent the first predissociated level for each point and the dashed line drawn represents the limiting curve of predissociation.

performed self-consistent-field (SCF) followed by configuration-interaction (CI) calculations using an augmented double zeta basis set on thirteen low-lying electronic states including the $X^3\Sigma_g^-$, $B^3\Sigma_u^-$, $B''^3\Pi_u$, and $^1\Pi_u$ states. From these calculations it was concluded that the $^1\Pi_u$ state was weakly bound, lying at an energy of around 37600 cm^{-1} and dissociates into two ground state sulphur atoms. More recently a complete theoretical study of the B-X and B"-X band systems, including calculation of transition dipole moments, has been carried out by Pradhan and Partridge [44]. In this work wavefunctions and potentials were obtained via multireference configuration-interaction (MRCI) calculations. Oscillator strengths, transition probabilities, and radiative lifetimes were calculated from these wavefunctions and were all shown to be in good agreement with experimental data.

To date much of the work on the S_2 B-X band system has focused on the lower lying non-predissociated vibrational levels. Therefore the motivation behind this work is to concentrate on the predissociated levels above v'=10. Currently, only plate spectra exist of these higher vibrational levels and hence extraction of dynamical information such as linewidth variation with vibrational excitation is somewhat hindered. The nature of the second predissociation does not seem to have been investigated a great deal, Barrow and du Parcq [26] attribute it to an inner wall predissociation (Mulliken's type c) via the $B''^3\Pi_u$ state. In the work presented in the following sections the B-X band system of S_2 is experimentally investigated further over the range of excited state vibrational levels $10 < v' < 22$, by the use of CRDS. Along with this experimental investigation, complementary *ab initio* calculations are conducted in order to clarify the nature and ordering of the possible states responsible for the observed predissociations within the B state. These potentials are then used along with an improved RKR potential for the B state to estimate the strength of the interstate interactions by the use of a Fermi Golden Rule calculation and to thus rationalise the experimental observations.

4.2 Experimental

The experimental arrangement used to record the CRD spectra of S_2 was essentially the same as was used to record the SH (SD) spectra in the previous chapter. Spectra of the B-X (10,0), (11,0), and (12,0) bands were recorded using the frequency-doubled output of a dye laser (Spectra Physics PDL-3) operating with Fluorecein 548 and pumped by the 532-nm output of a Nd:YAG laser (Quantel YG680). To record spectra of the (v',0) bands with v'=13-22, the dye laser, operating with Coumarin 500, 540 and 540A dyes, was pumped with the 355-nm third harmonic of the Nd:YAG laser. The dye-laser fundamental was frequency doubled in a BBO or KDP crystal to generate the necessary UV light between 250 and 282 nm. In this wavelength region it is not possible to calibrate all of the resulting spectra using I_2 LIF as was used for the work in the previous chapter because the I_2 spectrum starts to become diffuse and unstructured. Spectral calibration of the dye-laser fundamental was therefore performed by simultaneously recording optogalvanic lines of neon excited in a hollow cathode discharge in regions where I_2 LIF calibration was unsuitable. To cover the complete spectral range of the experiments, two HR mirror sets were required, the first having maximum reflectivity at a central wavelength of 290 nm (Virgo Lightning Optical Corp.), and the second centred at 243 nm (Research Electro Optics). At the central wavelength for the high-reflectivity mirrors, the 1/e ring-down time was typically 10 μs. Absorption spectra were obtained by direct least-squares fitting of the logarithm of the exponential decay function to obtain the variation of the ring-down time with wavelength.

As was mentioned in chapter 3, the continuous flow reaction system used to generate the SH / SD radicals also produced S_2 as a minor contaminant as a consequence of our experimental arrangement. However, by changing the reaction conditions slightly (i.e. increasing the gas pressures slightly) it was possible to increase the concentration of S_2 being produced, possibly via the radical-radical reaction mechanism,

$$\begin{aligned} H_2S + H &\rightarrow SH + H_2 \\ H + SH &\rightarrow H_2 + S \\ S + S + M &\rightarrow M + S_2 \end{aligned} \qquad (4.3)$$

where M corresponds to the surrounding gas mixture. The H atoms are produced by passing a microwave discharge across H_2 (BOC High Purity) flowing through a length of mullite tube. Again it was found that the efficiency of S_2 production could be increased by lightly coating the mullite tubing with a solution containing phosphoric acid, methanol, and water. Typically pressures of 1.0 - 2.0 Torr of H_2 were flowed continuously through the mullite tube with the microwave generator operating at an input power of approximately 30-40 Watts. The H_2S (Matheson 99.5 % purity) was gradually introduced into the ring-down cell further upstream. In order to check that S_2 was being produced only in relatively low concentrations, since too much could cause non-linear behaviour in the CRD spectrum, the ring-down time (RDT) at an expected S_2 B-X band origin was monitored on the oscilloscope as the H_2S was added until the RDT was seen to decrease slightly, typically this corresponded to only a few mTorr of H_2S. Again, as in the work involving production of SH, care had to be taken when adding the H_2S so as to suppress formation of other sulphur products within the ring-down cavity as this caused the mirrors to become dirty and decreased the ring down time dramatically.

4.3 Results

Using the CRDS apparatus, spectra were taken of the S_2 $B^3\Sigma_u^-$-$X^3\Sigma_g^-$ (v',0) band system with v' ranging from 10 to 22 spanning a total wavelength range of 282-250 nm. Levels with v' > 18 are diffuse and completely unstructured and, for v' > 20, the experimental spectra showed only weak signals.

4.3.1 S_2 $B^3\Sigma_u^-$ v'=10

Figure 4.7(a) shows the CRDS spectrum of the $B^3\Sigma_u^-$-$X^3\Sigma_g^-$ (10,0) band over the wavenumber range 35480 - 35800 cm^{-1}. The LIF spectrum of this region shows the lowest J' (i.e., J'=1) of the $\Omega'=0$ component, with other, higher J' levels appearing only weakly [7], but the CRDS spectrum shows extensive rotational structure. Attempts were made to simulate this spectrum by extrapolating the deperturbed constants obtained from the previous vibrational bands seen in earlier, high resolution LIF studies [7]. However, these attempts were largely unsuccessful owing to strong rotational perturbations by the $B''^3\Pi_u$ state which are still evident in much of the spectrum: the $B^3\Sigma_u^-$ v'=10 level lies close to the dissociation limit of the B'' state. A combination of the room temperature spectrum shown in Figure 4.7(a) and an ongoing fluorescence-depletion study [45] should clarify the observed structure. From the spectrum, however, the full width at half maximum height (FWHM) values for the rotational linewidths are estimated to be $\Gamma<1$ cm^{-1} since the spectrum clearly shows sharp structure: the homogeneous broadening results from predissociation and indicates a natural lifetime > 5 ps. These linewidths should be compared with the instrument resolution of the CRD experiment, determined from the last chapter to be well described by a Gaussian function of FWHM 0.09 cm^{-1}; this instrumental resolution is limited by the UV laser linewidth. The estimates of S_2 B-X (10,0) linewidths and v'=10 lifetimes cannot be quantified more precisely because fitting to individual lines was prevented by the high density of overlapping rotational lines.

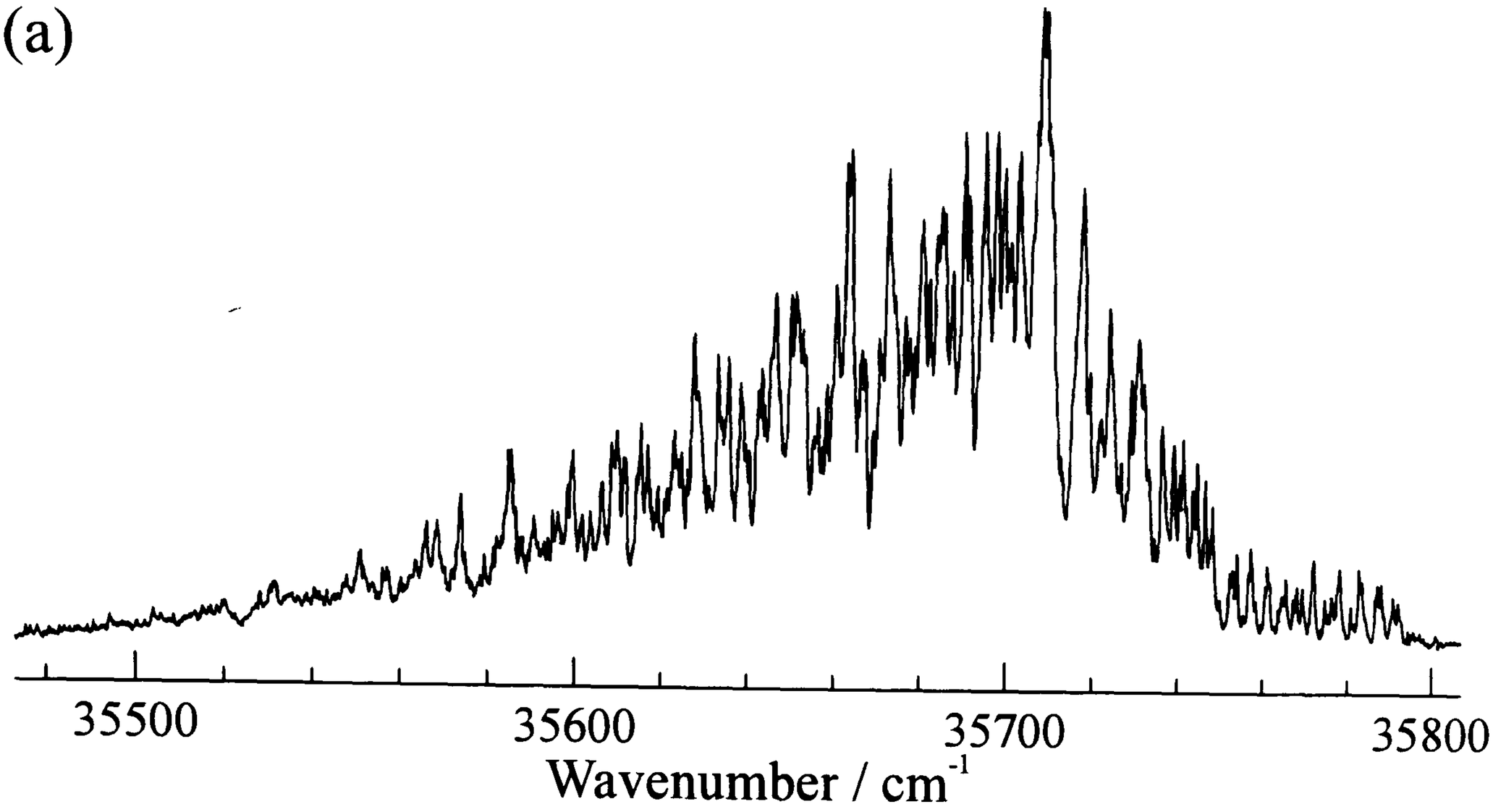

Figure 4.7. CRD spectrum of (a) (10,0) band and (b) the (11,0) band (with simulation) of the B-X transition of S_2.

4.3.2 S_2 $B^3\Sigma_u^-$ v'=11-22

4.3.2.1 Spectral linewidths

Figure 4.7(b) shows a CRD spectrum of the (11,0) band of the B-X transition over the wavenumber range 35800 -36160 cm^{-1}. It is clear from this spectrum that the predissociation is much more pronounced for v'=11 of the $B^3\Sigma_u^-$ state than for v'=10 since now the rotational fine structure is almost entirely washed away by homogeneous broadening, leaving only a small ripple on top of an almost continuous band profile. Also shown in the Figure is a simulation of the $B^3\Sigma_u^-$-$X^3\Sigma_g^-$ (11,0) band assuming a rotational temperature of 300 K. This simulation was derived using the quoted literature values for the $X^3\Sigma_g^-$ state constants [6] and improved values of the B-state constants deduced from a least-squares fitting procedure described in the next section. Along with the spectroscopic constants in the Hamiltonian matrix, the spectral linewidth (assumed independent of rotational quantum number and Ω) was included as a parameter in the fitting procedure, with the broadening of the spectral lines described by a Lorentzian function with FWHM Γ. The spectral fits to the (11,0) band returned a value of Γ=10 ± 1 cm^{-1} corresponding to a predissociative lifetime of 530^{+60}_{-50} fs. The absence of marked structure in the spectrum meant that no rotational dependence for the linewidth could be deduced, and this lack of variation is reflected in the relatively large (10 %) error in the estimated linewidth.

Figures 4.8 - 4.11 show CRD spectra of the B-X (v',0) bands with v'=12 - v'=19, together with simulations derived using the least-squares fitting procedure. All simulations assume a temperature of 300 K. It is evident from Figure 4.8(a) that predissociation has become still more rapid at v'=12 of the B state since the rotational structure is even less pronounced than for the (11,0) band. The Lorentzian component of the spectral linewidth reaches a maximum FWHM value of 14 ± 1 cm^{-1} at v'=13 (Figure 4.8(b)) indicating a lifetime of 380 ± 30 fs, though again there is probably some rotational dependence to this value which cannot be resolved in the spectrum. As the vibrational energy of the B state is increased beyond v'=13 the rotational structure gradually becomes sharper and more pronounced, as is illustrated in Figures 4.9(a) and 4.9(b), indicating that the rate of predissociation decreases for v'>13. The signal-to-

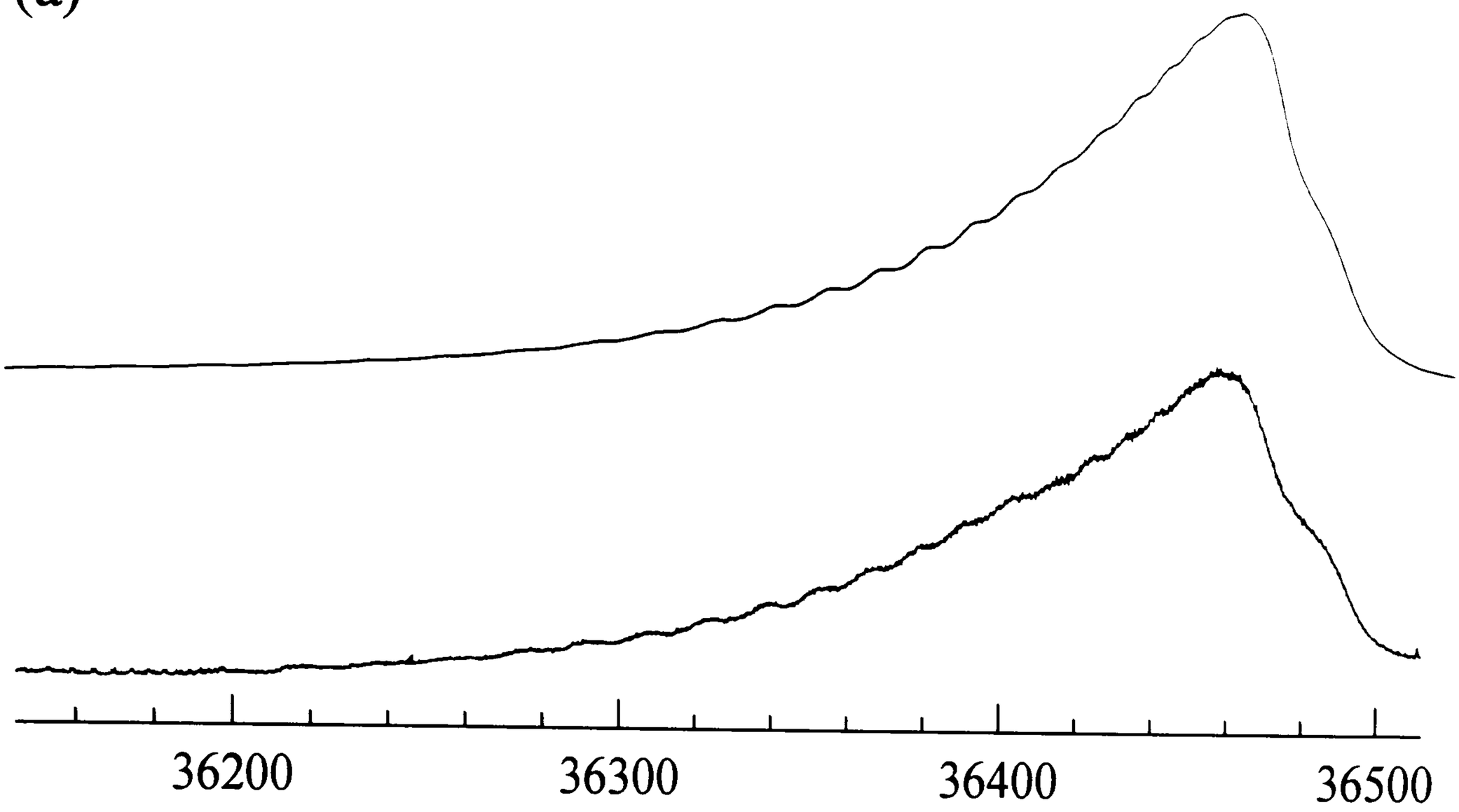

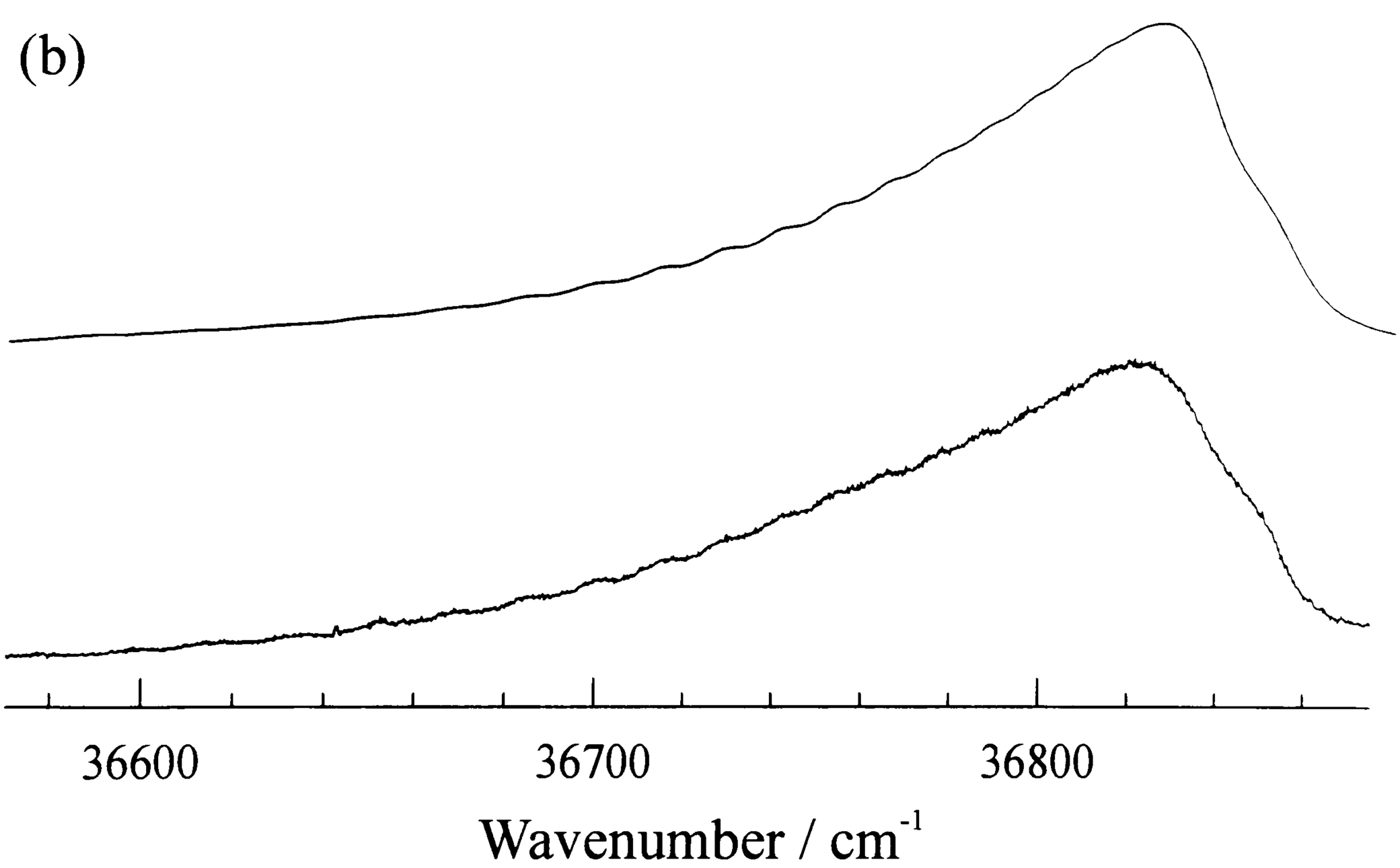

Figure 4.8. CRD spectrum and simulation of (a) the (12,0) band and (b) the (13,0) band of the B-X transition of S_2

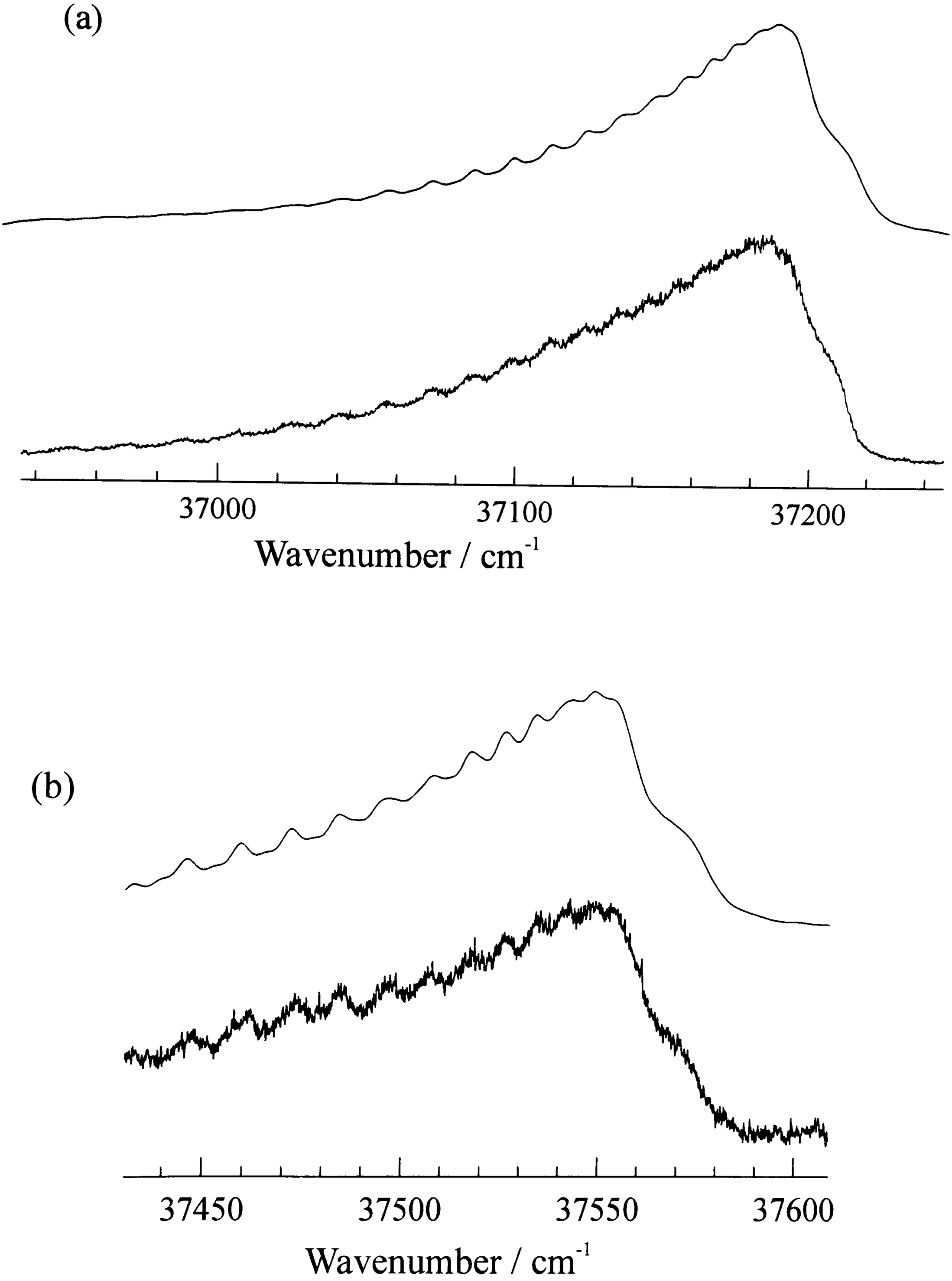

Figure 4.9. CRD spectrum and simulation of (a) the (14,0) band and (b) the (15,0) band of the B-X transition of S_2

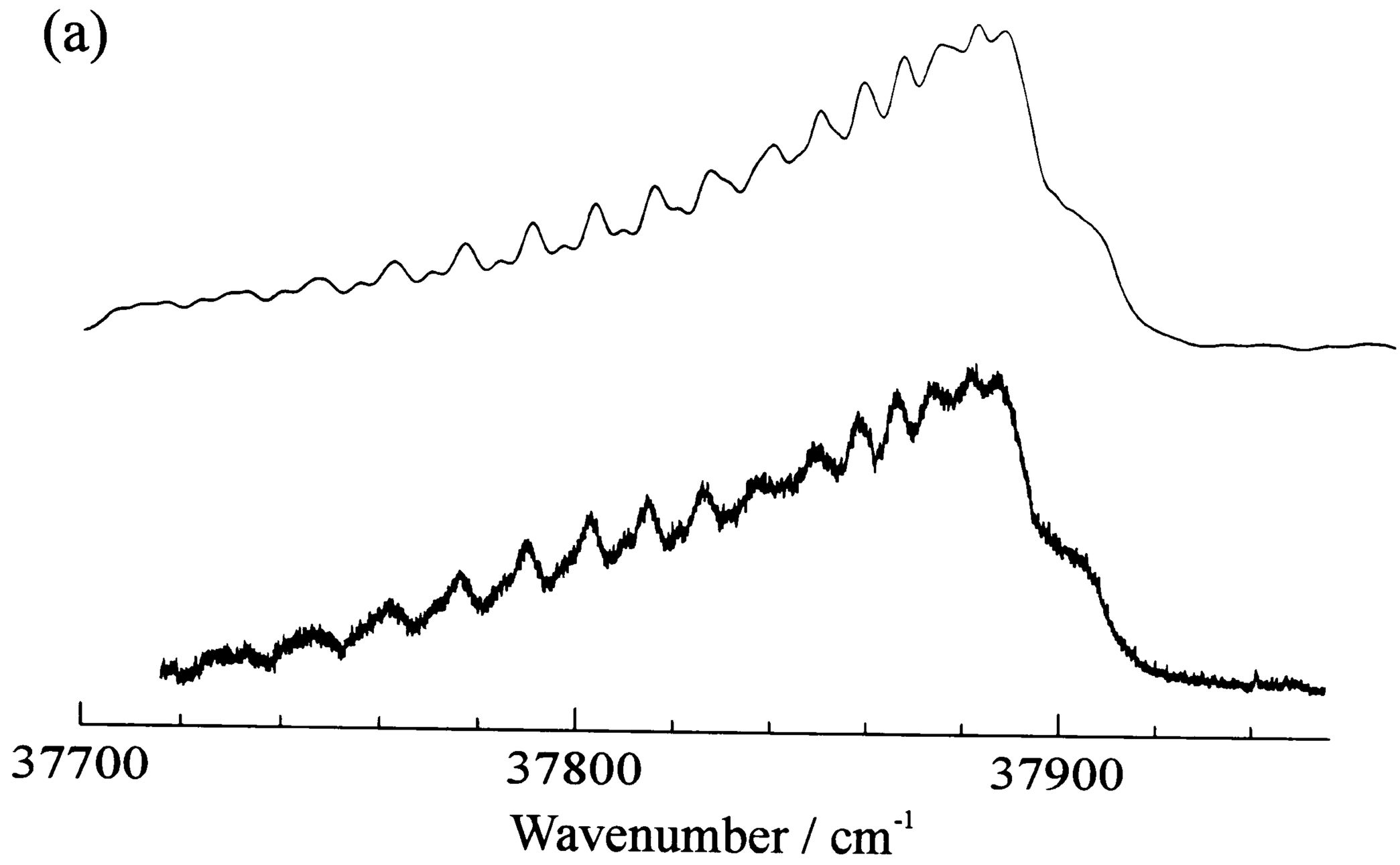

Figure 4.10. CRD spectrum and simulation of (a) the (16,0) band and (b) the (17,0) band of the B-X transition of S_2

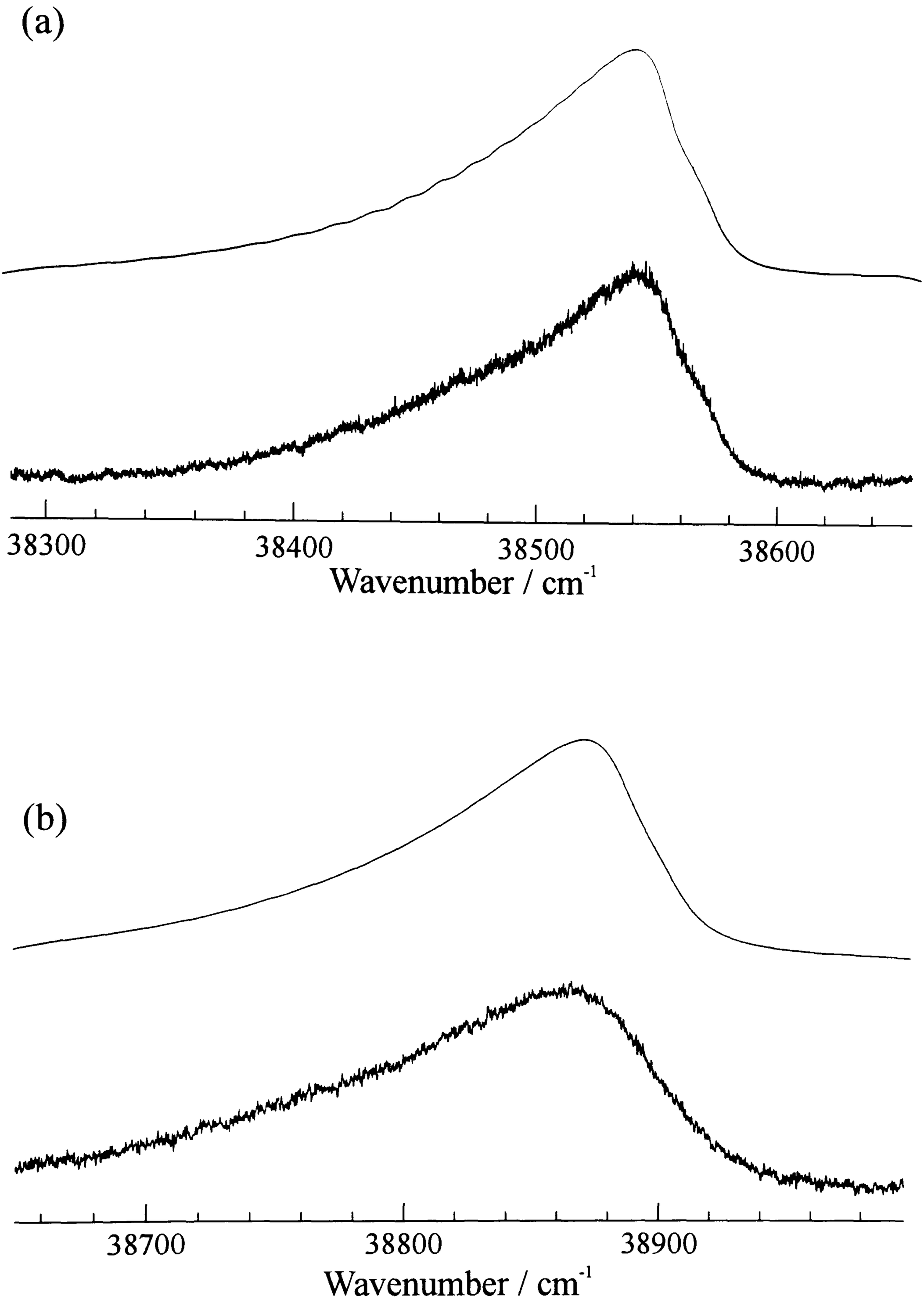

Figure 4.11. CRD spectrum and simulation of (a) the (18,0) band and (b) the (19,0) band of the B-X transition of S_2

noise ratio is poorer in the spectrum of the B-X (15,0) band (Figure 4.9(b)) than in the rest of the B-X spectra and the spectrum is cut off at 37430 cm^{-1}; the reason being that the reflectivities of both the mirror sets used are comparatively low in this spectral region, therefore decreasing the ring down time to less than 1 μs and degrading the experimental sensitivity. The linewidth reaches a minimum value (for $v' > 10$) of 6 ± 1 cm^{-1} at $v'=16$ of the B state (Figure 4.10(a)), and this linewidth corresponds to a predissociative lifetime of 880^{+60}_{-180} fs. Again, how the predissociation rates are affected by molecular rotation was unable to be assessed.

For excitation to vibrational levels above $v'=16$, the FWHM of the Lorentzian lifetime-broadened component of the spectral lineshapes once more increases: for $v'=17$ (Figure 4.10(b)) $\Gamma = 7 \pm 1$ cm^{-1}, and for the (18,0) band (Figure 4.11(a)), all rotational structure is lost and the band becomes diffuse indicating linewidths in excess of 15 cm^{-1} (lifetime < 350 fs). For levels with $v' > 18$, the slight step at the start of the band (arising from transitions to the different Ω components of the B state) which was clearly apparent in earlier spectra, is now lost, indicating that the bands become even more diffuse. Gradually the spectra become very weak and bands with $v' > 22$ were not looked for. The linewidths derived from the least-squares fitting procedure for the $B^3\Sigma_u^-$ $-X^3\Sigma_g^-$ band progression $10 \leq v' \leq 19$ are summarised in Table 4.1.

4.3.3 Spectroscopic constants

B v'	T_v	B_v	λ_v	Γ_v
10				≤ 1
11	36109.9(3)	0.204(3)	1.3(4)	10(1)
12	36477.4(5)	0.201(2)	1.5(5)	12(1)
13	36843.3(7)	0.198(3)	1.7(4)	14(1)
14	37201.0(6)	0.196(5)	1.9(4)	10(1)
15	37563.5(6)	0.194(4)	2.2(3)	8(1)
16	37896.7(5)	0.193(2)	2.4(2)	6(1)
17	38230.9(4)	0.191(1)	2.7(4)	7(1)
18	38558.9(7)			>15
19	38890(2)			>20

Table 4.1. Values of the $^{32}S_2$ $B^3\Sigma_u^-$ state constants and linewidths for the vibrational levels $11 < v' < 19$ derived from the least-squares fitting procedure outlined in the text. All values are in cm^{-1}. Values in parenthesis are the standard deviation (2σ) of the parameters obtained from the fit.

The fits to the band contours for $v' > 10$ give values not only for the spectral linewidths, but also for band origins, rotational constants and spin-spin splitting constants. The fitting process was performed using the computer program PGOPHER written by Dr. C.M. Western in which adjustable parameters (the rotational constant B, the band origin T_v, and the spin-spin splitting constant, λ) of a rigid-rotor Hamiltonian matrix were floated in order to minimise the squares of the differences between the observed and calculated spectra. The ground state constants were fixed at previously determined values [6]. Since the bands show no individually resolved rotational structure, the whole band contour was fitted until the total standard deviation reached a minimum. It was possible to model band contours successfully without the complications caused by the extensive perturbations evident for $v' \leq 10$ because the predissociated bands lie above the dissociation limit of the $B''^3\Pi_u$ state. Derived values of the spectroscopic constants are shown in Table 4.1 and vary smoothly with vibrational level, confirming that the perturbations experienced in the lower part of the vibrational progression ($v' \leq 10$) have switched off. The values of the constants obtained from the

CRD experiment, together with deperturbed constants from references [6,7,8] were used to obtain combined values for the equilibrium molecular constants T_e, ω_e, $\omega_e x_e$, B_e, and α_e for the B state levels extending from v'=0-19 (excluding v'=10). Figure 4.12(a) shows a plot of the vibrational term value against (v'+½) together with the line of best fit obtained using the expansion

$$G(v) = T_e + \omega_e\left(v+\tfrac{1}{2}\right) - \omega_e x_e\left(v+\tfrac{1}{2}\right)^2 . \qquad (4.4)$$

T_e is defined as the energy separation of the minima of the Ω=0 components of the ground and excited states, consistent with previous authors [39]. Term values are obtained from T_e by adding the vibrational energy in the B state (from the potential minimum) and subtracting the $X^3\Sigma_g^-$ state zero point energy of 362.11 cm^{-1} and a value of 4/3 λ = 15.78 cm^{-1} corresponding to the ground-state spin-spin splitting.

A plot of rotational constant B_v versus (v'+½) is shown in Figure 4.12(b) along with the line of best fit obtained using the expression,

$$B(v) = B_e - \alpha_e\left(v+\tfrac{1}{2}\right) + \gamma_e\left(v+\tfrac{1}{2}\right)^2 . \qquad (4.5)$$

The improved values of the equilibrium constants obtained from the above fitting procedures are given in Table 4.2 and for the purposes of comparison, previous values listed by Huber and Herzberg [29] and those calculated by Pradhan and Partridge [44] are included in the table. The values obtained here from the combination of our results and other recent work [6,7,8] differ slightly from the quoted literature values, reflecting in part the higher resolution and accuracy of the LIF [6,7] spectra compared to the original photographic-plate studies, and partly the nature of the deperturbation analysis used for v'≤9. The vibrational term values are reproduced to accuracies of ±6 cm^{-1} by these constants, which is less than the experimental precision to which they can be determined because of incomplete deperturbation for v'≤9. Our objective in obtaining these equilibrium spectroscopic constants was to enable the construction of an RKR potential for the $B^3\Sigma_u^-$ state, as discussed in the following section.

(a)

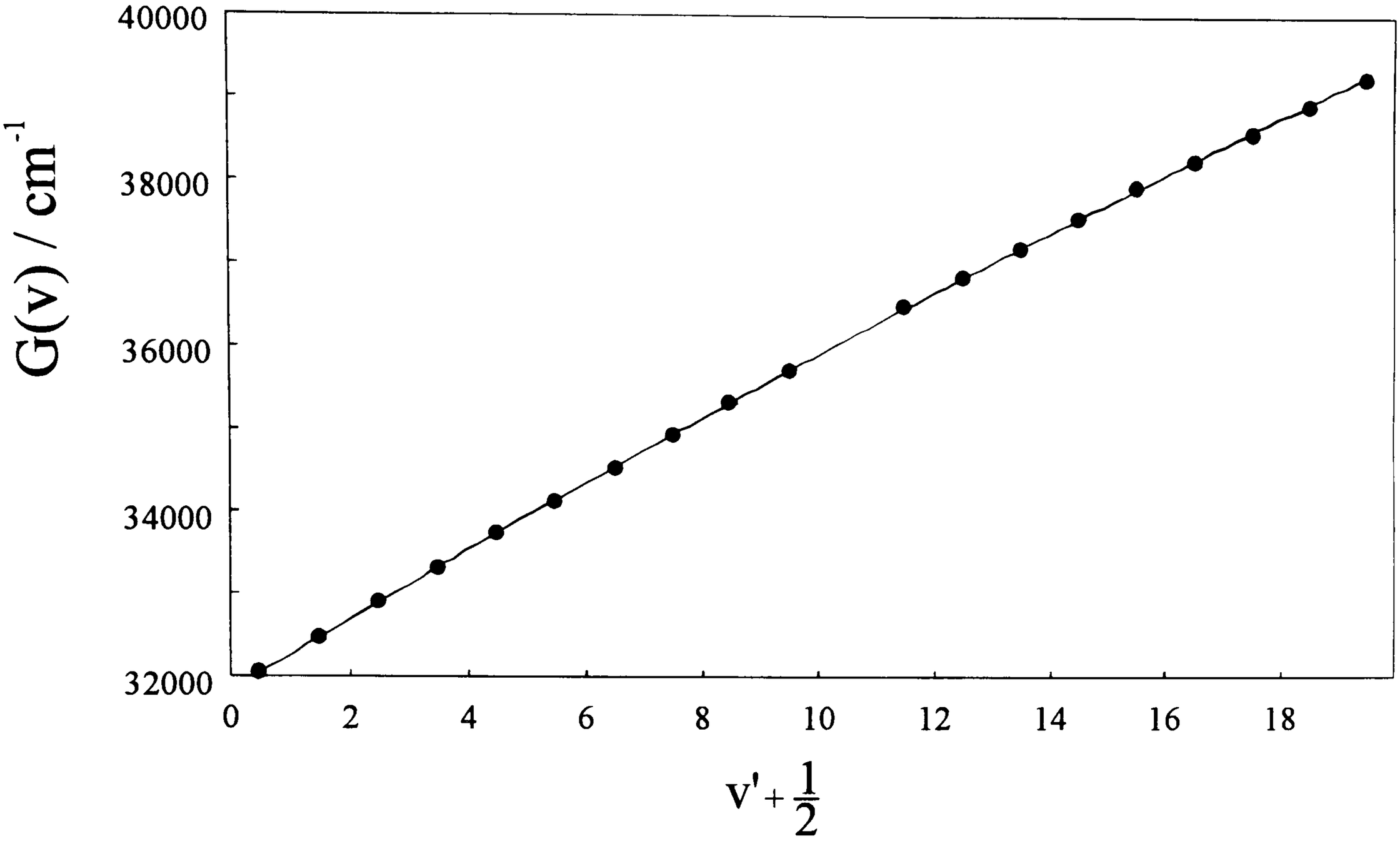

(b)

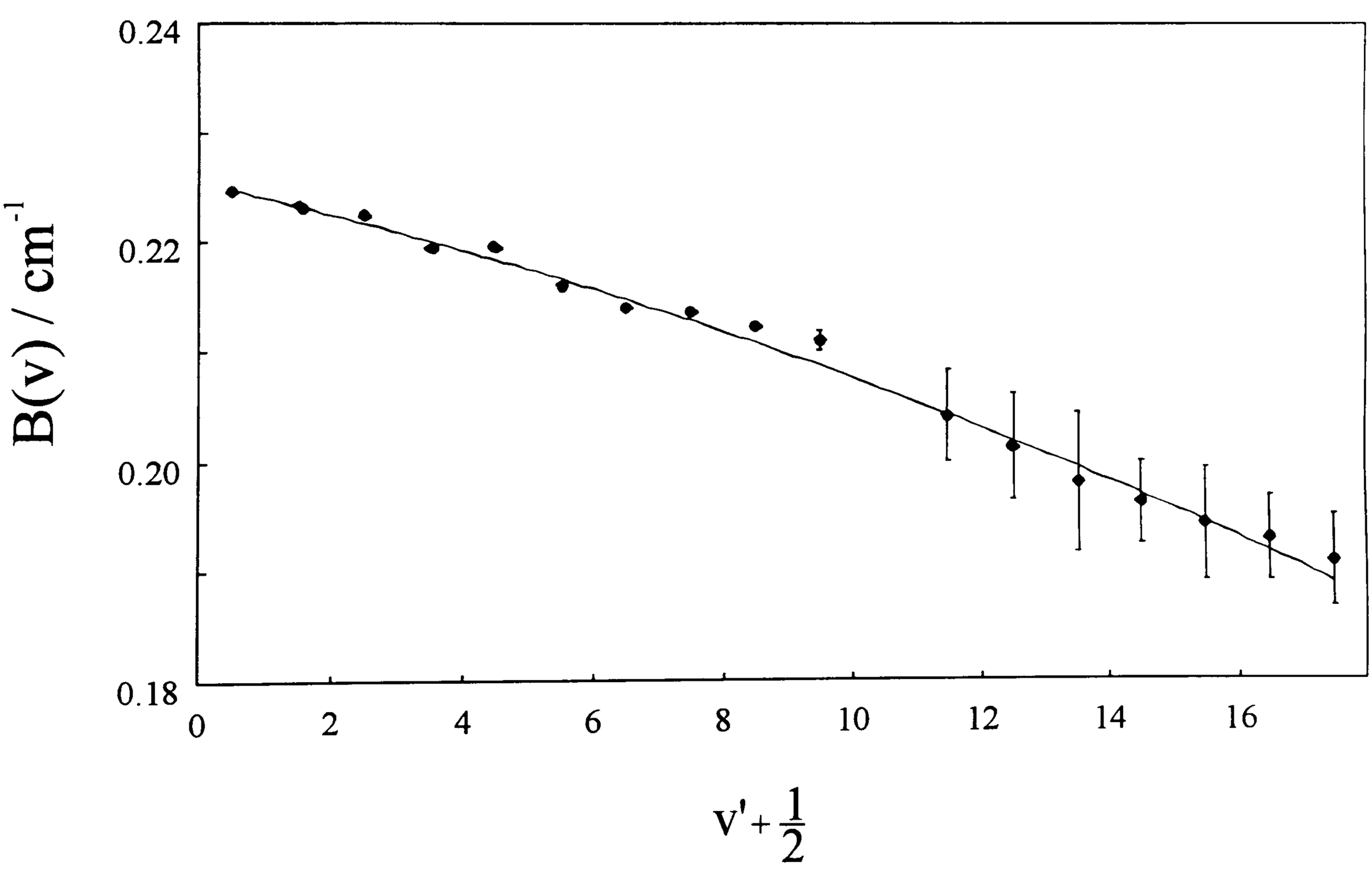

Figure 4.12 (a). Plot of B state vibrational term value G(v) against vibrational quantum number, $v'+\frac{1}{2}$
(b). Plot of B state rotational constant B(v) against vibrational quantum number, $v'+\frac{1}{2}$

	Value (cm^{-1})	Literature values (cm^{-1})	
	This work	Experimental[a]	Calculated[b]
B_e	0.2256(2)	0.2239	0.2234
α_e	0.0014(2)	0.0023	0.00198
γ_e	$-3.5\pm1.6\times10^{-5}$		
T_e	31832.7(7)	31835	31826
ω_e	435.2(3)	434.0	434.0
$\omega_e x_e$	2.72(2)	2.75	2.55

Table 4.2. Equilibrium values of molecular constants for the $B^3\Sigma_u^-$ state of S_2 derived from a weighted least squares fit of the combined data for the v' =11-20 levels (this work) and v'=0-9 levels (from references 6 and 7). Numbers in parenthesis are the standard deviation (2σ) of the parameters obtained from the fit. For comparison, literature values from experimental and theoretical studies are listed.

[a] reference 29

[b] reference 44.

4.4 Calculations

Given the detailed observations of the variation of linewidths over the wide range of vibrational levels ($10 < v' < 21$) obtained from the CRDS experiment it is now possible to try to formulate a quantitative model in order to explain the nature of the predissociation mechanisms occurring in these high vibrational levels of the $B^3\Sigma_u^-$ state of S_2. These calculations were performed in two stages: firstly, detailed *ab initio* calculations were carried out to determine the ordering of states and locate the crossing points of the possible repulsive potentials responsible for the predissociation. These repulsive potentials were then used together with an experimentally determined RKR potential for the $B^3\Sigma_u^-$ state to perform Fermi Golden Rule calculations of the predissociation rates. A comparison of calculated and experimental rates enabled us to estimate the magnitudes of the spin-orbit interactions responsible for the predissociation.

4.4.1 Determination of S_2 potentials

Ab initio potentials for the $B^3\Sigma_u^-$, and $B''^3\Pi_u$ states have been calculated previously [44], but no such potentials were available in the literature for the higher, repulsive states with a sufficient degree of accuracy for our calculations of v'-dependent predissociation rates. Therefore *ab initio* calculations of the various potential curves were carried out only for states of *u* (ungerade) symmetry (apart from the ground state) since only these states could be responsible for the predissociation, by consideration of the selection rules governing allowed interactions between electronic states [38].

The predissociating states must correlate to ground state atomic fragments i.e. $S(^3P) + S(^3P)$ and the B state is correlated to the first excited atomic limit $S(^3P) + S(^1D)$. By consideration of the Wigner-Witmer correlation rules there are 8 possible ungerade molecular states arising from these two ground state atomic fragments namely $^1\Sigma_u^-$, $^1\Pi_u$, $2\times\ ^3\Sigma_u^+$, $^3\Pi_u$, $^3\Delta_u$, $^5\Sigma_u^-$, and $^5\Pi_u$.

The ab initio calculations detailed below were performed using the commercially available package of programs MOLPRO 96 [46]. All the calculations utilised the correlation-consistent valence-quintuple-zeta (cc-VQZ) Gaussian basis set of Dunning and co-workers [47] and were carried out in D_{2h} symmetry. A restricted Hartree-Fock calculation was conducted in order to determine approximate forms for the ground state molecular orbitals. These orbitals were then used as a first guess for calculating the excited state wavefunctions and energies for a total of 21 internuclear distances in a multireference configuration-interaction (MRCI) [48,49] calculation using complete active space SCF (CASSCF) [50] orbitals. Internal contraction of core orbitals was used and the effects of higher order excitations were accounted for by using the multireference analogue of the Pople correction. All of the calculations were carried out on a Silicon Graphics SGI Power Challenge machine at the University of Bristol Computing Service. The calculations took approximately 40 minutes of cpu time to generate the energy at one internuclear distance for all 10 states.

All of the potential energy curves determined from the MRCI calculations, but shifted slightly in energy as described below, are shown in Figure 4.13 (they are also listed in Appendix 1 for reference). The potential minimum of the $X^3\Sigma_g^-$ state has been set to the zero of energy and all other potentials are referenced from this point. The *ab initio* calculation ignores the effect of spin-orbit coupling and should therefore make all eight ungerade states arising from the $S(^3P) + S(^3P)$ combination tend toward the same asymptotic limit; the calculated asymptotic energies actually lie within 880 cm^{-1} of one another. The calculations return a value for the separation of the $S(^3P) + S(^3P)$ and $S(^3P) + S(^1D)$ asymptotes of ca. 9050 cm^{-1} (taken from the mean of the calculated $S(^3P) + S(^3P)$ energies for the various potential curves) compared to a value of 9239 cm^{-1} derived from the known atomic energy levels of sulphur. For the calculation of predissociation rates it is important to have a knowledge of which repulsive molecular states correlate with which atomic limits since this will determine how much kinetic energy is imparted into the dissociating atomic fragments and therefore affect the de Broglie wavelength of the continuum wavefunctions. As will be illustrated in section 4.5, the de Broglie wavelengths and the relative phases of the bound and continuum wavefunctions are key factors in influencing the rates of predissociation of S_2 $B^3\Sigma_u^-$ v'

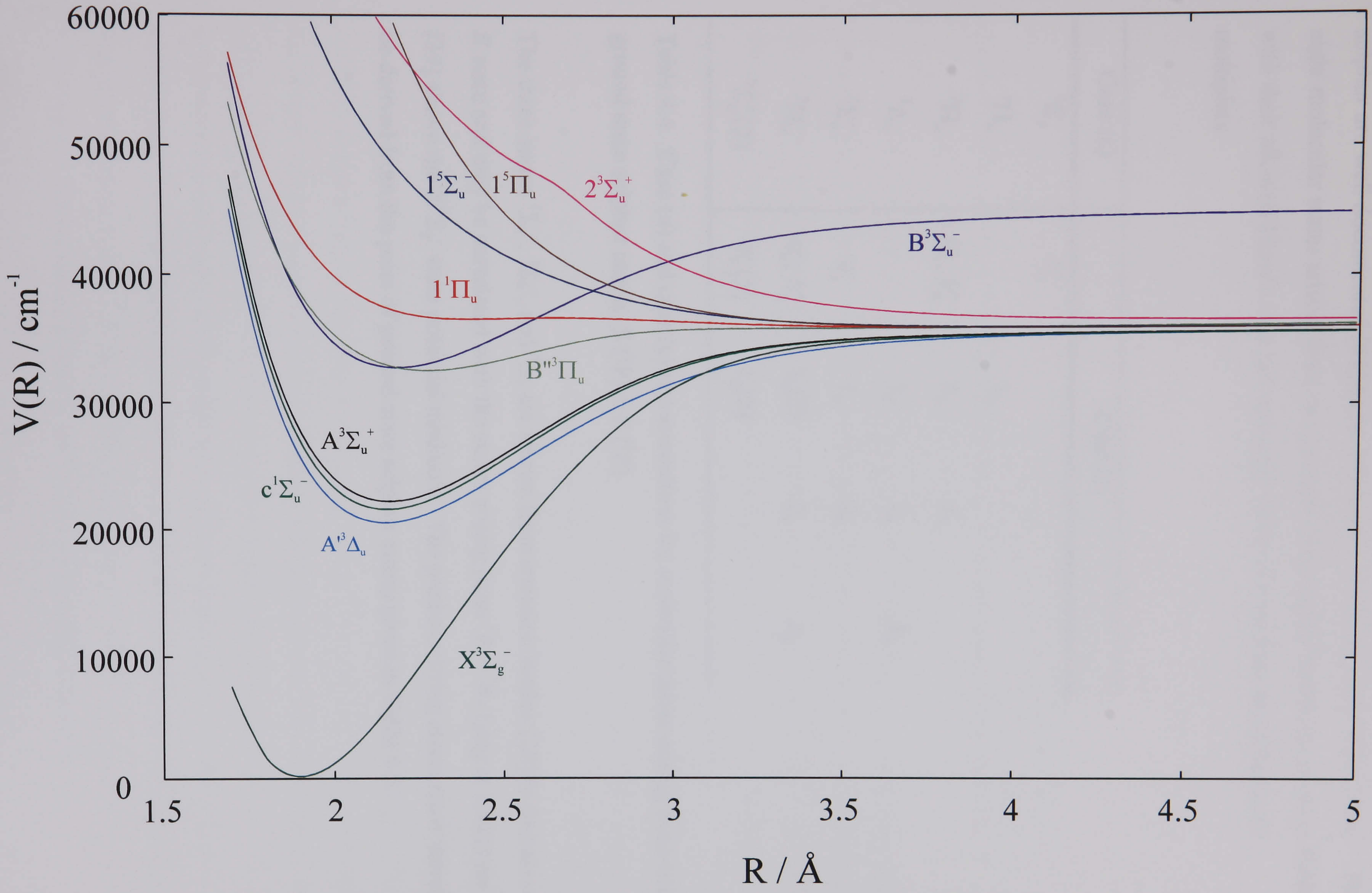

Figure 4.13. *Ab initio* potentials derived from an MRCI calculation of the ground $X^3\Sigma_g^-$ state and lowest lying ungerade (u) states of S_2.

states. The energy separation of the $^3P_1$, $^3P_0$, and ^1D atoms relative to the $^3P_2$ state of sulphur are well documented [51] to be 396.8 cm^{-1}, 573.6 cm^{-1}, and 9239.0 cm^{-1} .The eight molecular states arising from two ground state sulphur atoms are given in Table 4.4 with their allowed Hund's case (c) molecular states arising from the different Ω multiplets.

Case (a)	Case (c)			
$^1\Sigma_u^-$	0_u^-			
$^1\Pi_u$		1_u		
$^3\Pi_u$	0_u^-, 0_u^+	1_u	2_u	
$^3\Delta_u$		1_u	2_u	3_u
$^5\Sigma_u^-$	0_u^-	1_u	2_u	
$^5\Pi_u$	0_u^-, 0_u^+	$1_u(2)$	2_u	3_u
$^3\Sigma_u^+(2)$	$0_u^-(2)$	$1_u(2)$		

Table 4.4. Case (a) and case (c) representations for molecular states arising from two ground state sulphur atoms, S (^3P) + S (^3P).

The three states $^1\Sigma_u^-$, $^3\Sigma_u^+$, and $^3\Delta_u$ are known from emission studies [26] to lie below the *B* state and may be correlated with the states arising from $^3P_2$+ $^3P_2$ lying at 35602 cm^{-1} [39] above the $X^3\Sigma_g^-$ state potential minimum. The predissociating states must therefore be derived from the pairs of ground state sulphur atoms given in Table 4.5.

$S(^3P_j)+ S(^3P_j)$	Energy / cm^{-1}	Case (c) components				
$^3P_0 + {}^3P_0$		no *u* states				
$^3P_1 + {}^3P_0$	36572			1_u	0_u^-	
$^3P_1 + {}^3P_1$	36396			1_u	0_u^-	
$^3P_2 + {}^3P_0$	36175	2_u		1_u	0_u^+	
$^3P_2 + {}^3P_1$	35999	3_u	$2_u(2)$	$1_u(3)$	0_u^+	$0_u^-(2)$

Table 4.5. The energies of $S(^3P_j) + S(^3P_j)$ atoms and their case (c) components.

One other bound state that is also thought to arise from two ground state sulphur atoms is the $B''^3\Pi_u$ state. However, some confusion still exists over exactly which pair of ground state sulphur atoms this state correlates with. Recent observations [7] of B" state vibrational levels near to the first predissociation limit $S(^3P_2) + S(^3P_1)$ at 35999 cm^{-1} (proposed by Ricks and Barrow [39] to be the dissociation limit of the first predissociating state, as outlined in section 4.1) seem to suggest that not all of its Ω components are converging to this limit as was originally proposed and some are more likely to be converging to the next highest atomic limit $S(^3P_2) + S(^3P_2)$ at 36175 cm^{-1}. From these and other observations the correlation diagram for the ungerade states formed by $S(^3P) + S(^3P)$ shown in Figure 4.14 has been proposed [7]. The *ab initio* potentials were all shifted in energy (by roughly 500 - 1000 cm^{-1}) so that their asymptotes were consistent with the energy of the proposed atomic correlations. Having modified the potentials in this way, it was found that predissociation of the v'=10 level of the B state was prevented by a small calculated maximum on the $^1\Pi_u$ state potential: The calculated $^1\Pi_u$ potential shows a shallow minimum and a small maximum at 2.4 and 2.7 Å respectively, and hence additional *ab initio* points were calculated in this region to resolve these topographical features. The $^1\Pi_u$ potential curve was thus positioned such that the maximum at R≈2.7 Å lay just above the energy of the $B^3\Sigma_u^-$ v'=10 state (see later Figure), which entailed a vertical shift of the potential by -500 cm^{-1}.

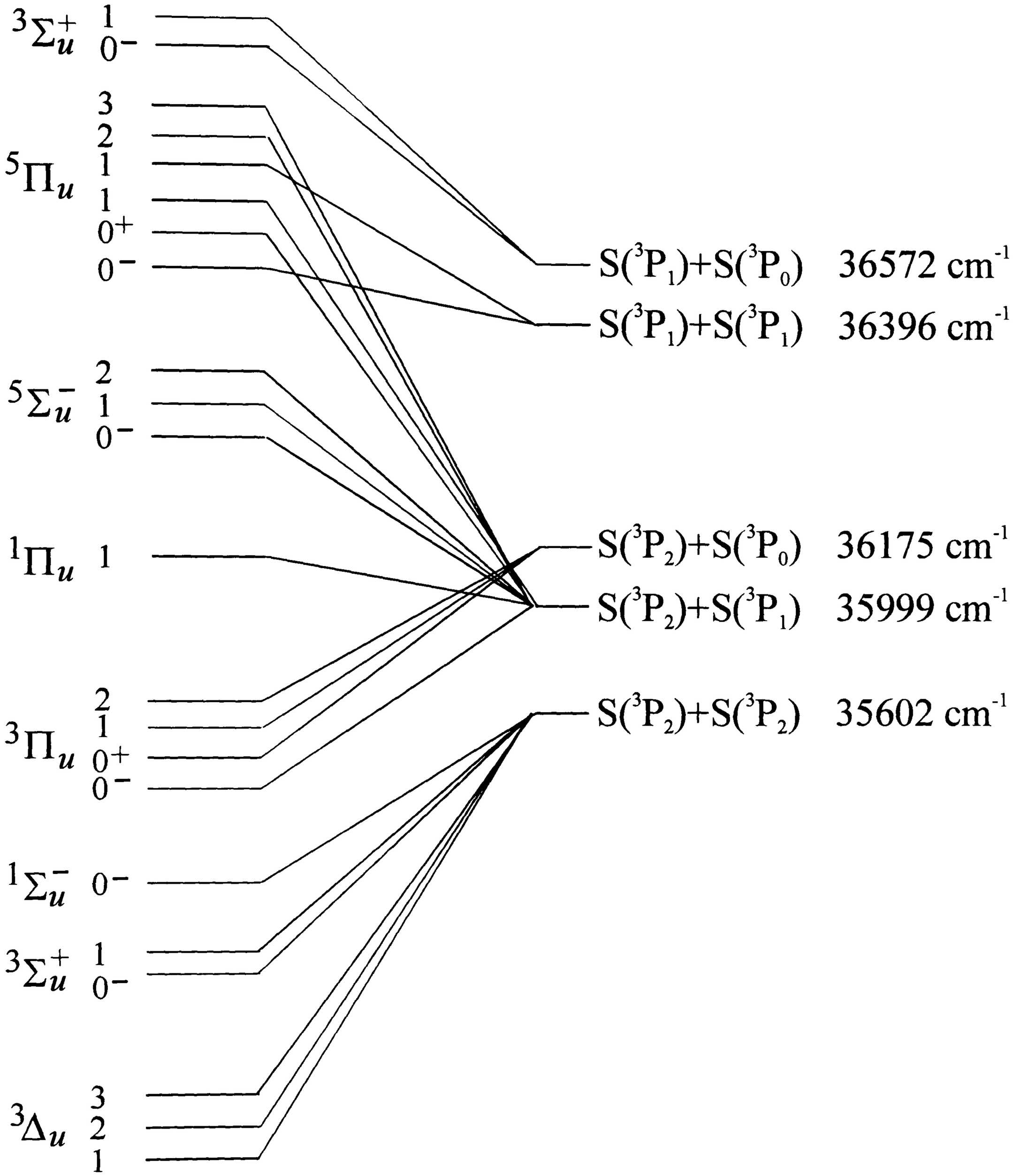

Figure 4.14. Correlation of molecular S_2 states with $S(^3P_j) + S(^3P_j)$ atomic limits from reference [7]

The ordering of the repulsive molecular states obtained from the *ab initio* calculations shown in Figure 4.13 are consistent with the correlation diagram in Figure 4.14 and follow the same pattern as is observed in O_2. The relative positions of the $^5\Sigma_u^-$ and $^5\Pi_u$ states are also in agreement with experimental evidence that implicates these states in mixing with the 0_u^- component of the B" state, thereby accounting for the observation of $^5\Sigma_g^-$ and $^3\Pi_g$ ion-pair states of S_2 from double-resonance studies via the B" state [28].

The *ab initio* potential for the $B^3\Sigma_u^-$ state was not sufficiently precise for the subsequent calculations of predissociation rates which require accurate energies of the vibrational levels of the B state. From the experimentally determined equilibrium constants for the $B^3\Sigma_u^-$ state an RKR potential was derived, for levels up to and including v' = 20, using the computer program RKR1 written by R.J. Le Roy [52]. The RKR potential obtained is shown in Figure 4.15 (and is listed in Appendix 1) along with the calculated *ab initio* potentials important in the predissociation. This Figure illustrates the accuracy of the *ab initio* calculation for such a complex, many-electron system, but the discrepancies between the RKR and *ab initio* values justify the modest corrections of the energies of the repulsive curves described above. The RKR potential appears to exhibit slightly unphysical behaviour at very high vibrational levels (due to the constants only being derived from levels with $v' \leq 20$) as can be seen from the Figure where the slope of the inner wall appears to rise very sharply at high energies. Numerical integration of the radial Schrödinger equation for the B-state RKR potential using the program LEVEL [53] generated vibrational wavefunctions and eigenvalues; the energies were compared with experimental observations and were found to be accurate to within 5 cm^{-1} even for the higher vibrational levels ($v' > 17$). The small discrepancies reflect the uncertainty with which the vibrational energy levels are calculated from the equilibrium molecular constants in Table 4.2, and the RKR potential can be concluded to be a very good approximation to the true potential.

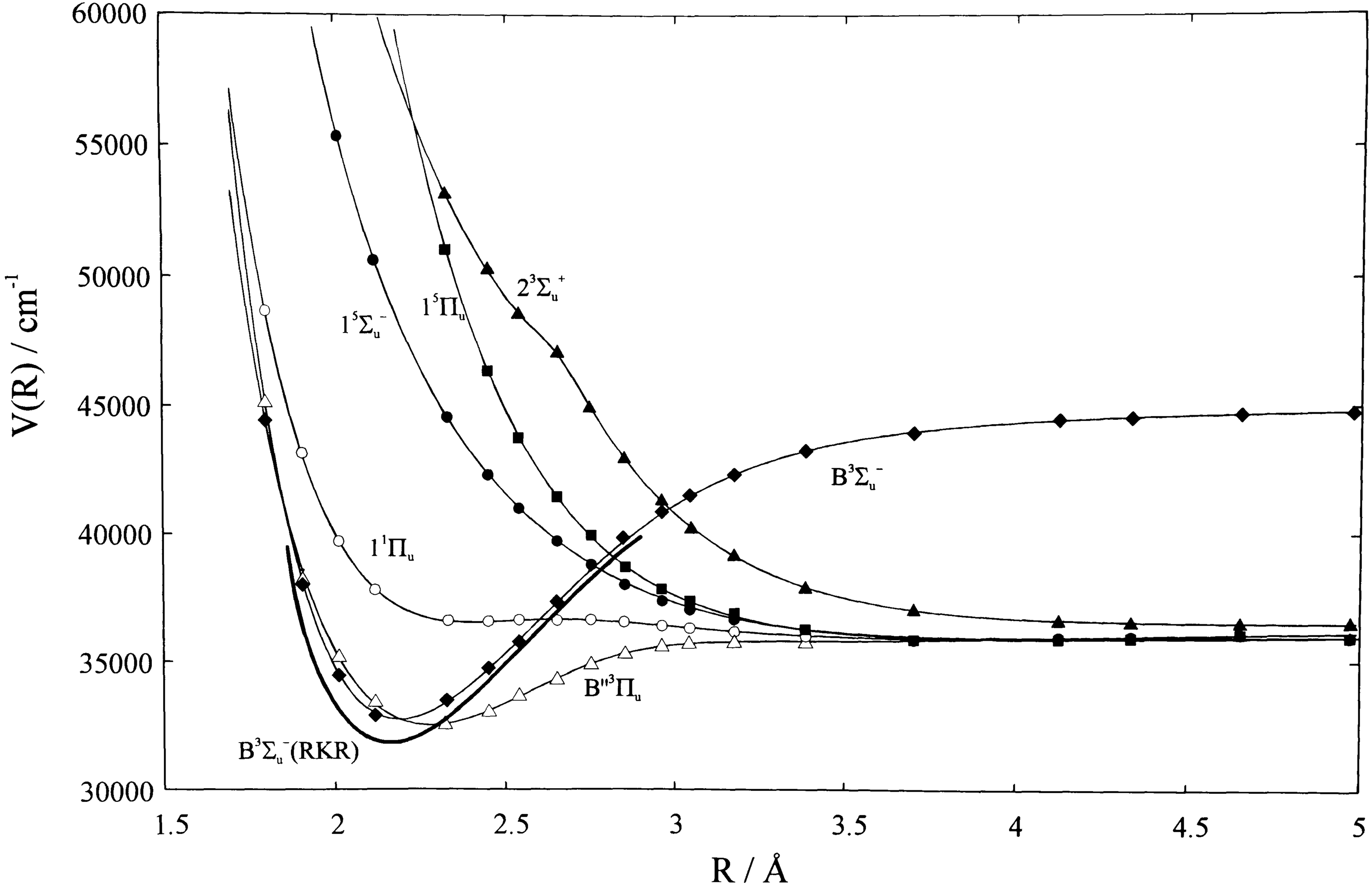

Figure 4.15. Comparison of the S_2 $B^3\Sigma_u^-$ state RKR (**bold** line) and *ab initio* potential. Also shown are the calculated potentials important in the predissociation of the B state. The symbols are the calculated *ab initio* points and the lines are generated from an 8 point piecewise polynomial interpolation.

4.4.2 Calculation of predissociation rates

Following the *ab initio* and RKR calculations of the S_2 molecular potentials of ungerade symmetry described in the preceding section, it is now possible concentrate on determining the contributions from each repulsive state to the observed predissociation rates of the $B^3\Sigma_u^-$ vibrational levels by estimating the magnitudes of the interstate spin-orbit interactions. A combination of potential curves and spin-orbit coupling functions permits Fermi golden rule calculations of the predissociation rates which can then be compared with our experimental results. Using the RKR $B^3\Sigma_u^-$ state potential together with the *ab initio* inner repulsive wall of the $B''^3\Pi_u$ bound potential and the $^1\Pi_u$, and $^5\Sigma_u^-$ repulsive potentials, predissociation rates were calculated as a function of vibrational quantum number v' using the program BCONT [54] as outlined in the previous chapter. The calculations were performed for each of the repulsive potentials individually in order to determine their relative contributions to the predissociation rate. For predissociation via the $B''^3\Pi_u$ state, the results of a spectroscopic determination [6,8] of the R-dependence of the spin-orbit coupling to the $B^3\Sigma_u^-$ state for $v' \leq 9$ are extrapolated. To avoid introducing a complicated and arbitrary parametrisation of the (unknown) spin-orbit coupling variation with internuclear separation for the $^1\Pi_u$, and $^5\Sigma_u^-$ states, however, it is assumed, for simplicity, that the spin-orbit interaction is a constant value independent of R. This approximation results in a model with just one adjustable parameter, namely the magnitude of the spin-orbit coupling between bound and repulsive states, and, as is shown below, this enables the variation of the predissociation rates with v' to be modelled in a simple fashion. The rates of predissociation are determined not only by the magnitude of the spin-orbit coupling between bound and repulsive states, but are also strongly affected by the degree of overlap between the bound vibrational wavefunctions and the continuum wavefunctions of the same energy [20].

Figure 4.16 shows the results of the calculations of S_2 $B^3\Sigma_u^-$ lifetimes compared with the experimental data. The calculations were performed for zero rotational angular momentum (N'=0) since, as discussed previously, it was not possible to determine experimentally the rotational dependence of the predissociation rates. Shown in the Figure are the linewidths that would result for predissociation via the $B''^3\Pi_u$, $^1\Pi_u$, and $^5\Sigma_u^-$ states individually; summing the calculated rates for each predissociative state and

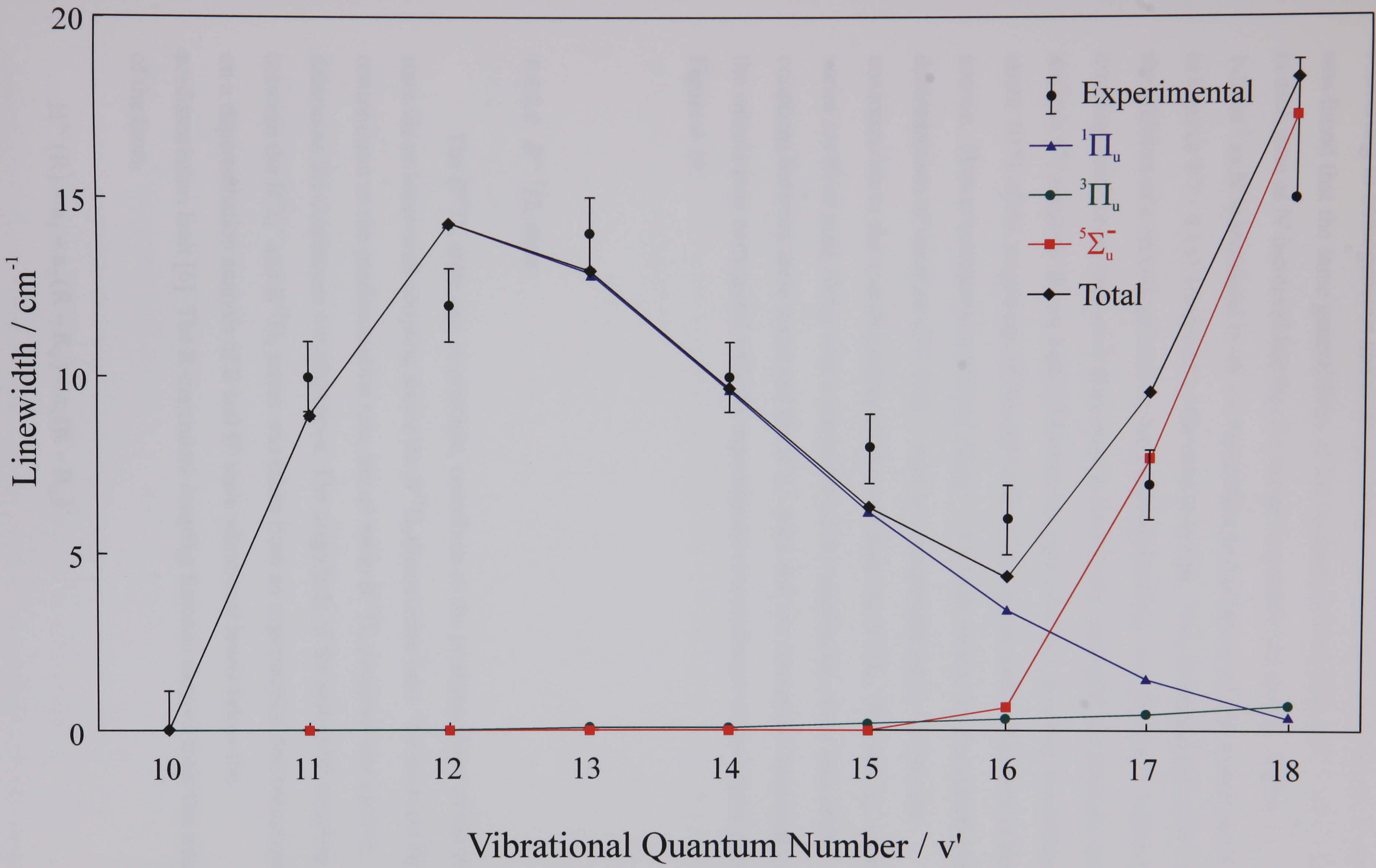

Figure 4.16. Experimentally observed variation of the linewidths of S_2 $B^3\Sigma_u^-$-$X^3\Sigma_g^-$ transitions with upper state vibrational quantum number v'. Also shown are the theoretically calculated linewidths obtained using the model described in the text for contributions to the predissociation from the $B^3\Pi_u$, $^1\Pi_u$ and $^5\Sigma_u^-$ continuum states and their sum total.

converting to homogeneous linewidths gives the total linewidth shown in the Figure. It was found that the same general form of the variation of linewidth with v' was obtained in each case as N' increased but that the actual magnitude varied only slightly (by ca. 1-2 cm^{-1} as N' is increased to 40, corresponding to the tail of the vibrational bands shown in Figures 4.7 - 4.11) compared to the total linewidth. This N-dependence arises from the addition of a centrifugal term to the potential function. An additional, J-dependent coupling mechanism may arise from the **J.L** term in the rotational Hamiltonian; previous analysis [7] suggests that at high J this term may give rise to a coupling amounting to about 10 % of the magnitude of the spin-orbit coupling interaction described in the next section. Hence, substantial rotational effects in the analysis may be discounted and the determination of variation of Γ with v' may be concentrated upon. In turn the contributions to the overall predissociation rate from the $B''^3\Pi_u$, $^1\Pi_u$, and $^5\Sigma_u^-$ states as v' varies are illustrated, along with a discussion of the magnitudes of the spin-orbit couplings between these states and the $B^3\Sigma_u^-$ state that are determined empirically so that the calculations correspond with the experimental measurements to the degree shown in Figure 4.19.

4.4.2.1 $B''^3\Pi_u$ state

The $B''^3\Pi_u$ state can, in principle, contribute to the predissociation of the $B^3\Sigma_u^-$ state via an inner-wall coupling above the $B''^3\Pi_u$ dissociation limit. To evaluate this contribution to the predissociation rate, the *ab initio* $B''^3\Pi_u$ potential was used to determine the continuum wavefunctions. The magnitude of the spin-orbit coupling between the $B^3\Sigma_u^-$ and $B''^3\Pi_u$ states was taken from an experimental determination based on a deperturbation analysis of B and B" state vibrational levels below the predissociation limit [6] The R-dependent coupling function derived from this analysis is of the form,

$$H^{SO}(R) = a_1 + a_2(R - R_e) + a_3(R - R_e)^2 \qquad (4.6)$$

where R_x, the internuclear separation about which the spin-orbit coupling function is expanded, was taken to be 2 Å, and the continued validity of this function above the dissociation limit of the B'' state is assumed. The parameters a_1, a_2, and a_3 were derived by Green and Western [6,8] from a detailed fitting procedure and the resultant values are a_1=29.9 cm^{-1}, a_2=187 $cm^{-1}Å^{-1}$, and a_3=421 $cm^{-1}Å^{-2}$. This spin-orbit coupling function results in an interaction energy of ca. 30-50 cm^{-1} at the inner wall of the B state at v' > 12. Using this coupling function and the B'' state *ab initio* potential, the calculated linewidths for the B state were determined to vary from 0.002 cm^{-1} for v'=10 to 0.98 cm^{-1} for v'=19, thus making only a small contribution to the experimentally measured linewidths throughout the range of observed vibronic levels. Therefore it may be concluded that coupling to the $B''^3\Pi_u$ state is not the dominant mechanism of predissociation of the $B^3\Sigma_u^-$ state. Barrow and du Parcq [26] suggested that the second predissociation limit of the B state arose because of the inner-wall crossing of this and the B'' state. The calculations of the potentials presented here confirm that the states do cross at an internuclear separation shorter than the equilibrium distance for the B state. The calculated rates, however, imply that the B'' state is not responsible for the second onset of predissociation at v' > 16.

4.4.2.2 $^1\Pi_u$ state

The $^1\Pi_u$ state has been postulated as being responsible for the predissociation of the S_2 $B^3\Sigma_u^-$ via an outer-wall crossing in the region of v'=11. A second predissociation limit could arise from an inner-wall crossing of the same two states at higher energy but the *ab initio* calculations suggest that this inner-wall crossing will occur at an energy well above the B-state dissociation limit. The role of the $^1\Pi_u$ state was tested by comparing our experimental data for predissociation rates with calculated rates using our RKR and *ab initio* potentials for the $B^3\Sigma_u^-$ and $^1\Pi_u$ states respectively. For the interaction between these two states, no functional form for the variation with internuclear separation of the spin-orbit coupling between the states has been determined either theoretically or experimentally. As discussed above, an approach was chosen with the intention of minimising the complexity of the model by limiting the number of

parameters. Thus a constant value of H_{so} was used independent of the internuclear separation, and it was found that with an appropriate choice of the magnitude of the spin-orbit coupling, this simple model is sufficient to match the experimental observations.

As can be seen from Figure 4.15, the gradient of the *ab initio* $^1\Pi_u$ potential is quite flat in the region of the crossing point with the $B^3\Sigma_u^-$ state, and there is a shallow minimum at shorter internuclear distances (R≈2.4Å) followed by a low maximum at R≈2.7Å. It is the combination of these topographical features that can explain the sudden jump in predissociation rate between v'=10 and 11. The flatness of the repulsive potential has the effect of making the phase difference between the bound and continuum wavefunctions critically sensitive to the variation with internuclear separation of the steep repulsive wall, and this phase difference strongly influences the overlap of bound and continuum wavefunctions and hence the calculated predissociation rates. The $^1\Pi_u$ potential was therefore moved both to shorter and longer R in an *ad hoc* fashion (though within a modest range about the calculated position) in order to reproduce the observed variation of predissociation rate with B-state vibrational level, v'. It was found that the best fit with experimental observations, and in particular the observed trend of Γ with v', was obtained by shifting the repulsive potential by 0.07 Å to a larger internuclear distance. Once the correct form of the *variation* of predissociation rate with v' had been obtained, the *magnitudes* of the linewidths were modelled by tuning the strength of the spin-orbit coupling until calculated and experimental predissociation rates were in agreement. For the calculations shown in Figure 4.16, an interaction energy of 90 cm^{-1} was used, and this value clearly gives excellent correspondence between the observed and calculated (for N'=0) linewidths of all the studied vibrational levels up to v'=16. If the *ab initio* potential without this 0.07 Å correction (but with the energy adjustments described previously) was used, the linewidth was found to oscillate more rapidly with vibrational level than is observed experimentally because of the effects of interference between bound and continuum wavefunctions. The overlap of the bound and continuum wavefunctions for the corrected potentials is discussed further and illustrated in section 4.5.

4.4.2.3 $^5\Sigma_u^-$ state

As mentioned above, the inner-wall crossing of the $B^3\Sigma_u^-$ and $B''^3\Pi_u$ states does not significantly enhance the calculated predissociation rate for v'>16 and the inner-wall crossing of the $B^3\Sigma_u^-$ and $^1\Pi_u$ states lies above the B-state dissociation limit. Therefore it is proposed that the second predissociation onset in the S_2 $B^3\Sigma_u^-$ state, which leads to increased linewidths of transitions in the $B^3\Sigma_u^-$-$X^3\Sigma_g^-$ spectrum for vibrational bands lying to shorter wavelength than the (16,0) band, is a consequence of a second outer-wall crossing of the bound state by a repulsive potential in the vicinity of the energy of v'=18. Therefore the *ab initio* $^5\Sigma_u^-$ repulsive potential was included in the model to account for the very strong predissociation occurring at around v'=18. It is worth emphasising that our *ab initio* calculations imply many interactions occurring in this region, as three repulsive curves cross the bound state in the region above the energy of v'=18 (see Figure 4.16), all of which have several Ω components. Thus the $^5\Sigma_u^-$ state was used as a representative example since it is calculated to cross the B state at an energy lower than the other states in this energy region. These calculations do not demonstrate unequivocally that the state causing the second predissociation onset has $^5\Sigma_u^-$ symmetry, but the results of our calculations for the $^5\Sigma_u^-$ state as a sample potential curve are used to demonstrate that a repulsive potential of this form, lying at this energy, can explain the rapid predissociation of the B state for v'>16 using physically reasonable magnitudes for the spin-orbit coupling. As mentioned previously, the *ab initio* $^5\Sigma_u^-$ potential curve was slightly shifted in energy to give the correct asymptotic limit for the $S(^3P_2) + S(^3P_1)$ fragments.

To reproduce the experimental predissociation rates for v'>16, a constant coupling strength between the $^5\Sigma_u^-$ and $B^3\Sigma_u^-$ states of 100 cm^{-1} was used, independent of the internuclear separation. As shown in Figure 4.16, this interaction models the experimental observations very well and provides a satisfactory explanation of the second predissociation limit using a spin-orbit coupling interaction comparable to that required to model the first predissociation limit.

4.5 Discussion

The results of the calculations described in section 4.4 and summarised in Figure 4.16 are in very good agreement with the experimentally observed variation of linewidths of B-state levels with v' ≥ 10. The *ab initio* calculations give the form of the repulsive potentials but their energies must be shifted slightly to correlate asymptotically with the energies of the correct pairs of ground state sulphur atoms. The model explaining the predissociation mechanism is physically reasonable and contains very few adjustable parameters: the only adjustments to the *ab initio* potentials were to correct for the $S(^3P_j)$ + $S(^3P_j)$ asymptotes, and to fine tune the crossing point of the $^1\Pi_u$ potential with the B state; we also determined empirically the spin-orbit interaction matrix elements between the bound $B^3\Sigma_u^-$ and repulsive $^1\Pi_u$, $^5\Sigma_u^-$ states. No rotational dependence for the predissociation rate can be inferred from the experimental observations and so all the calculations were performed with N' set to zero. The N' dependence of the linewidth was investigated using the above model and it was found that the effect of increasing N' was to cause the magnitude of the linewidths to become greater by ~ 10-20 % of the observed values, while still retaining the same trend of variation with vibrational level. Having established a model for the predissociaiton of the B state, the details of the predissociation mechanism revealed by the model are considered.

4.5.1 Mechanism of predissociation

With the extensive experimental observations given in section 4.3 and the detailed theoretical analysis outlined in section 4.4 of predissociation occurring in high vibrational levels of the $B^3\Sigma_u^-$ state of S_2, it is now possible to explain the mechanism in terms of interactions with the $B''^3\Pi_u$, $^1\Pi_u$, and $^5\Sigma_u^-$ states. The last two states are repulsive; the first state may cause predissociation via interaction with its repulsive inner wall above the dissociation limit to form $S(^3P)$ + $S(^3P)$. It must be reiterated that although the highest lying of these state is referred to as $^5\Sigma_u^-$ throughout, this choice of label is not supported by any spectroscopic evidence and is based on the outcome of the *ab initio* calculations described earlier.

The first predissociation of the $B^3\Sigma_u^-$ state, occurring slightly below v' = 10, can indeed be attributed to an interaction with a nearby $^1\Pi_u$ state, in agreement with the original conjecture of Ricks and Barrow [39]. More recent studies [7,23] detected fluorescence only from the lowest rotational levels of $B^3\Sigma_u^-$ Ω'=0 v'=10. The fact that no B-X (10,0) Ω'=1 transitions are observed in LIF lends support to the predissociation occurring via spin-orbit coupling with a 1_u state, since the $\Delta\Omega$=0 selection rule ensures that only the $^3\Sigma_u^-$ Ω=1 component of the B state can interact with the predissociating state for low rotational levels. Higher rotational levels of the $B^3\Sigma_{0u}^-$ v'=10 state can predissociate by a J-dependent S-uncoupling interaction which effectively mixes $^3\Sigma_{1u}^-$ character into the $^3\Sigma_{0u}^-$ state as rotation is increased. In the room temperature spectra presented in this work, it is legitimate to assume that all Ω' components predissociate at almost the same rate since this mixing of Ω character occurs at low J. Calculations based on the model proposed in the current work suggest a linewidth of 0.002 cm^{-1} for v'=10, N'=0 corresponding to a lifetime of 3 ns which is in very close agreement with the experimental observation of < 3 ns determined from fluorescence lifetime measurements [23]. The results of the minor modifications to the energies of the potential curves leave the v'=10 level just below the calculated crossing point of the $B^3\Sigma_u^-$ and $^1\Pi_u$ potentials. At shorter internuclear distances the (calculated) $^1\Pi_u$ state has a shallow minimum at R ≈ 2.5 Å, with a slight maximum at R ≈ 2.7 Å. These features explain the slow onset of the predissociation since there will be very little overlap of the bound v'=10 and continuum wavefunctions, as depicted in Figure 4.17(a): the continuum wavefunction is decaying in the overlap region. This poor overlap in the energy region of the crossing, and hence weak predissociation, is contrary to the common observation of a rapid increase in the predissociation rates in the vicinity of a crossing between a bound and a *steep* repulsive potential, illustrated by the study of SH $A^2\Sigma^+$ predissociation in the previous chapter.

As the amount of vibrational excitation within the B state is increased, the degree of bound-continuum wavefunction overlap increases substantially as illustrated in Figure 4.17(b) for $B^3\Sigma_u^-$ v'=11. The de Broglie wavelengths of the continuum wavefunctions, the phases of these and the bound wavefunctions, and, of course, the number of nodes in the bound wavefunction, change gradually with further vibrational excitation, causing the overlap to reach a maximum at v'=13. For vibrational levels beyond v'=13 the overlap

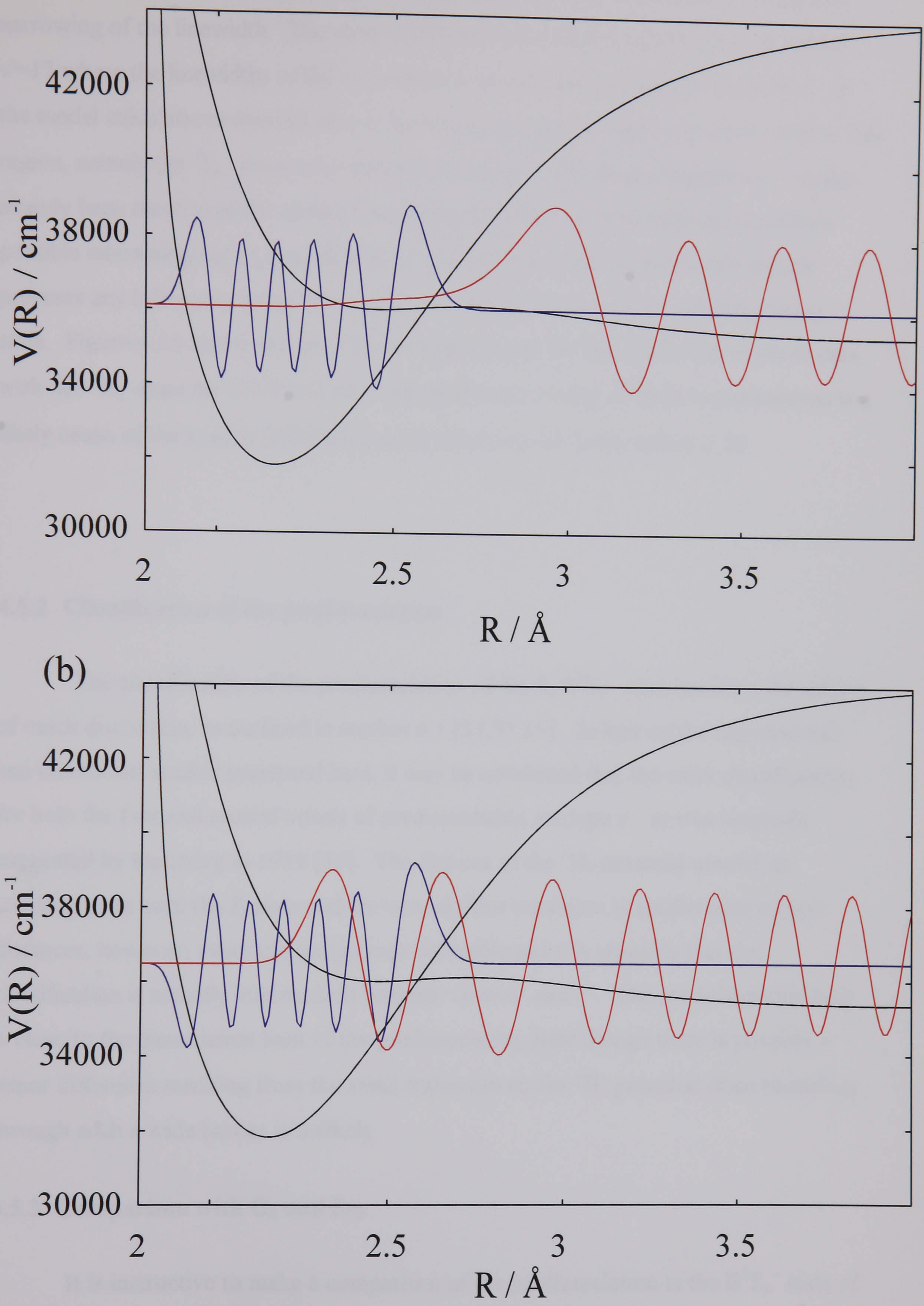

Figure 4.17. Calculated bound and continuum wavefunctions for the interaction of a $^1\Pi_u$ state with the $B^3\Sigma_u^-$ state of S_2 for (a) v'=10 and (b) v'=11

starts to decrease causing the predissociation rate to become slower and resulting in a narrowing of the linewidth. The onset of the second predissociation occurs at around v'=17 where the linewidths of the experimental spectra start to increase once more. In the model calculations detailed above, the lowest lying of the three repulsive states in this region, namely the $^5\Sigma_u^-$ state, was chosen to reproduce this second interaction. As has already been mentioned the choice was somewhat arbitrary since there are numerous possible interacting states, but the lack of any structure in the experimental spectra prevents any inferences being drawn about the precise nature of this predissociating state. Figure 4.18 shows the calculated wavefunctions for the interaction of the B state with this $^5\Sigma_u^-$ state for v'=17 and 18. The substantial overlap of these wavefunctions is a likely cause of the sudden diffuseness in the spectrum for levels with v' ≥ 18.

4.5.2 Classification of the predissociation

The classification of the predissociation of the S_2 $B^3\Sigma_u^-$ state has been the subject of much discussion, as outlined in section 4.1 [35,37,39]. In light of the experimental and theoretical studies presented here, it may be concluded that the strict classifications for both the first and second onsets of predissociation are type c^+, as was originally suggested by Herzberg in 1939 [35]. The flatness of the $^1\Pi_u$ potential around its crossing point with the B state and the very shallow minimum at smaller internuclear distances, however, make this assignment debatable and it is arguable that the classification is actually intermediate between cases a^+ and c^+. The predissociation limit is close to the dissociation limit of the predissociating state though there is possibly a minor difference resulting from the small maximum on the $^1\Pi_u$ potential since tunnelling through such a wide barrier is unlikely.

4.5.3 Comparison with O_2 and Se_2

It is instructive to make a comparison of the predissociation in the $B^3\Sigma_u^-$ state of S_2 with the well characterised predissociations in the B states of the analogous valence isoelectronic systems O_2 [55] and Se_2 [56]. In O_2 the $B^3\Sigma_u^-$ state is found to be

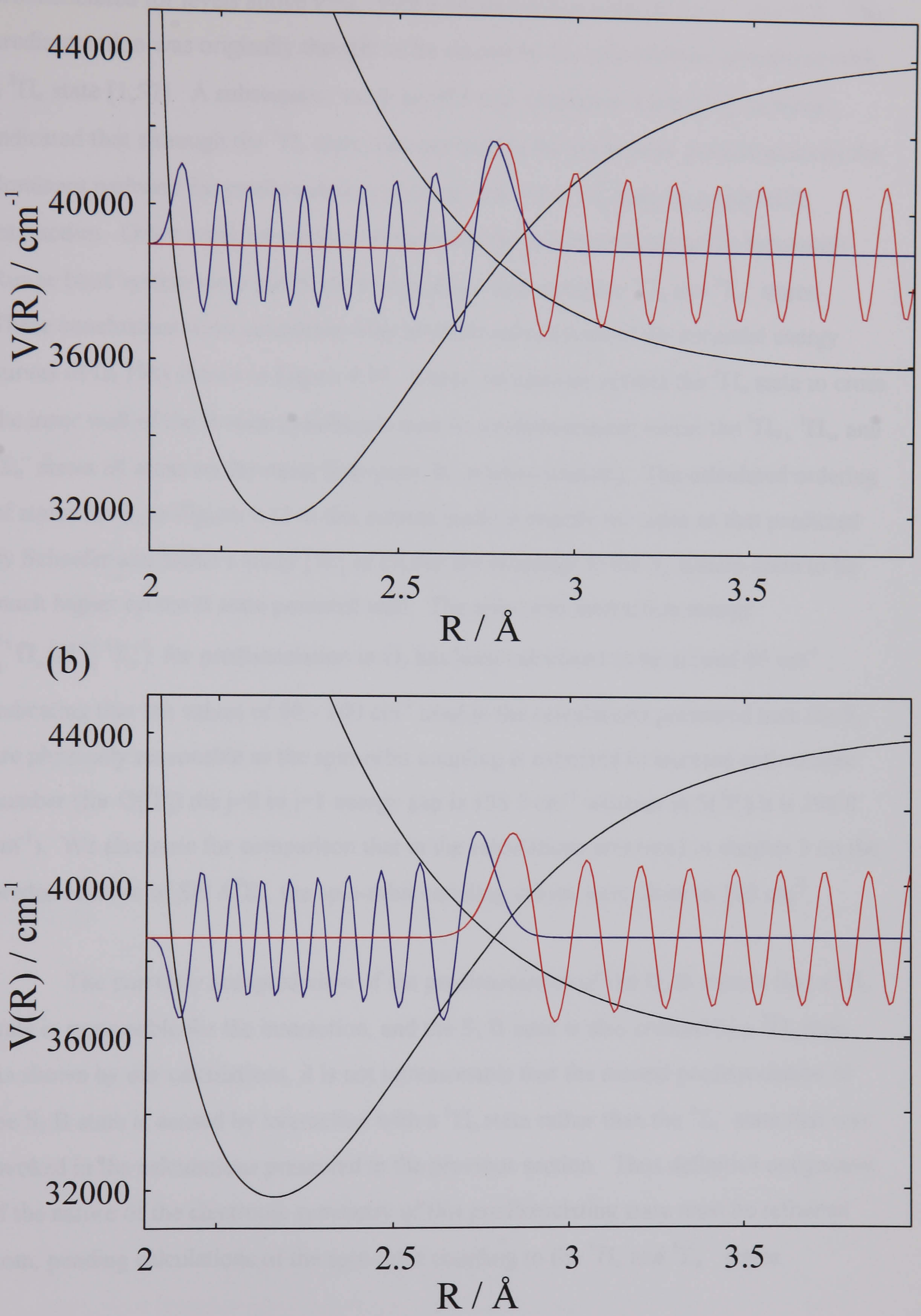

Figure 4.18. Calculated bound and continuum wavefunctions for the interaction of the $^5\Sigma_u^-$ state with the $B^3\Sigma_u^-$ state of S_2 for (a) v'=17 and (b) v'=18

predissociated for levels above v'=2, with a maximum linewidth of 3 cm^{-1} at v' = 4. This predissociation was originally thought to be caused by the spin-allowed interaction with a $^3\Pi_u$ state [1,57]. A subsequent, more careful high resolution study [55], however, indicated that although the $^3\Pi_u$ state was responsible for some weak predissociations the dominant pathway for predissociation to occur was via a $^5\Pi_u$ state by a spin-orbit interaction. Other weak interactions responsible for predissociation in the Schumann-Runge band system were attributed to crossings with repulsive $^1\Pi_u$ and $^5\Sigma_u^-$ states.

These conclusions were consistent with *ab initio* calculations of the potential energy curves of O_2 [58] shown in Figure 4.19. These calculations predict the $^3\Pi_u$ state to cross the inner wall of the B state (Mulliken's case Ic^- predissociation) whilst the $^5\Pi_u$, $^1\Pi_u$, and $^5\Sigma_u^-$ states all cross on the outer limb (case Ic^+ predissociation). The calculated ordering of states for S_2 in Figure 4.13 in this current study is exactly the same as that predicted by Schaefer and Miller's study [58] of O_2 but the crossings in the S_2 system seem to be much higher on the B state potential well. The spin-orbit interaction energy $\left\langle {}^5\Pi_u \left| H^{so} \right| {}^3\Sigma_u^- \right\rangle$ for predissociation in O_2 has been calculated to be around 65 cm^{-1}, indicating that the values of 90 - 100 cm^{-1} used in the calculations presented here for S_2 are physically reasonable as the spin-orbit coupling is expected to increase with atomic number (for $O(^3P_j)$ the j=2 to j=1 energy gap is 158.5 cm^{-1} whereas in $S(^3P_j)$ it is 396.8 cm^{-1}). We also note for comparison that in the calculations presented in chapter 3 on the predissociation of SH $A^2\Sigma^+$, the spin-orbit coupling values were close to 100 cm^{-1}.

The currently accepted view of the predissociation of the O_2 B state is that a $^5\Pi_u$ state is responsible for the interaction, and the S_2 B state is also crossed by a $^5\Pi_u$ state. As shown by our calculations, it is not unreasonable that the second predissociation of the S_2 B state is caused by interaction with a $^5\Pi_u$ state rather than the $^5\Sigma_u^-$ state that was invoked in the calculations presented in the previous section. Thus definitive assignment of the nature of the electronic symmetry of this predissociating state must be refrained from, pending calculations of the spin-orbit coupling to the $^5\Pi_u$ and $^5\Sigma_u^-$ states.

Predissociation in the $B0_u^+$ state of Se_2 by a 0_u^+ state is very strong and levels above the crossing point are so diffuse that they are not observed. In this case the predissociation manifests itself by causing large level shifts of the bound (sharp) levels.

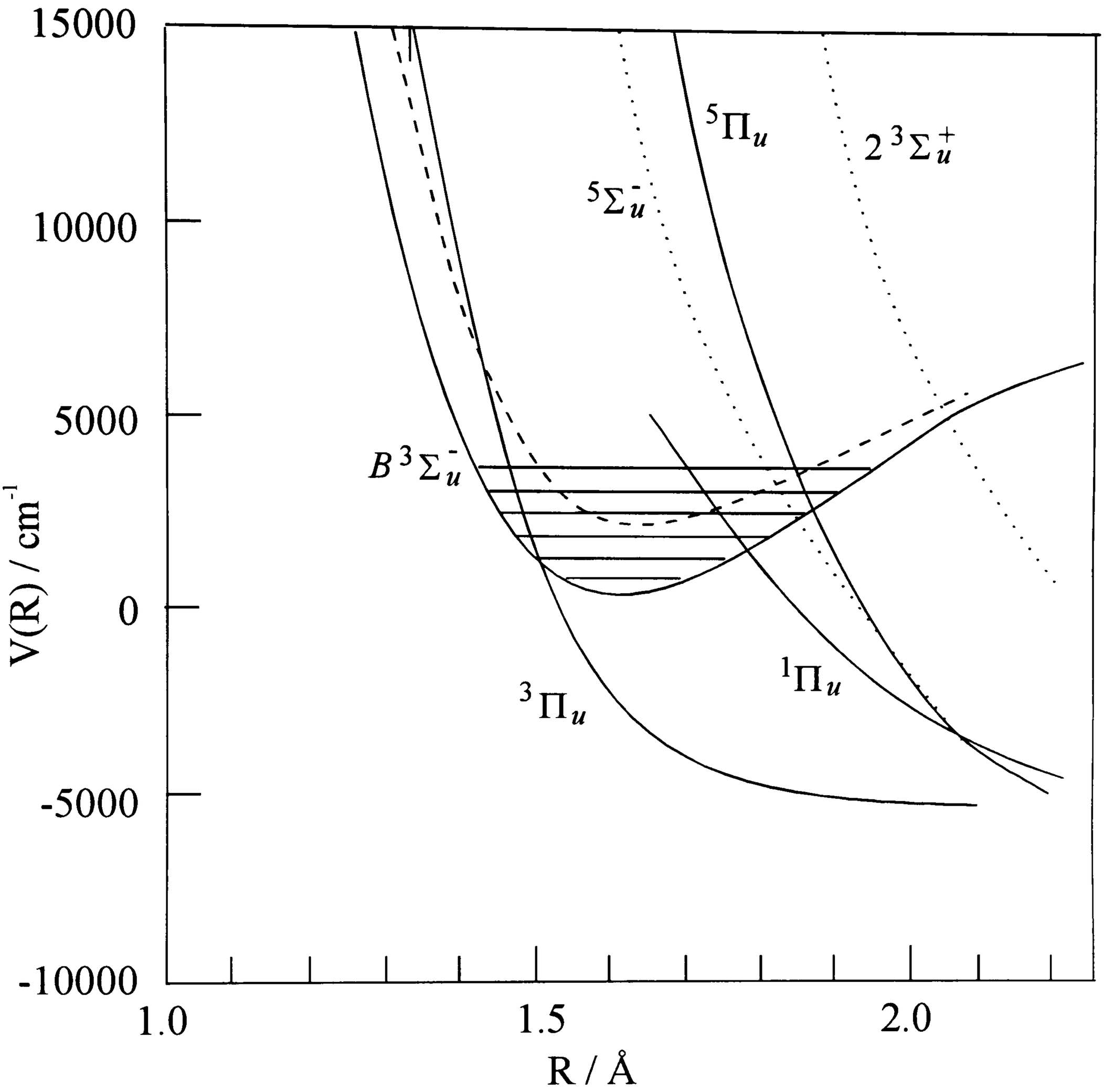

Figure 4.19. Calculated potential energy curves for O_2. The $B^3\Sigma_u^-$ RKR curve is shown by the solid line with the vibrational levels shown to v'=5. The calculated $B^3\Sigma_u^-$ curve of Schaefer and Miller [58] is shown by the dashed line. The $^3\Pi_u$ and $^1\Pi_u$ curves are also from [58]. The $^5\Pi_u$ curve is the correlated curve calculated by Julienne and Krauss [55]. The dotted lines for the $^5\Sigma_u^-$ and $2^3\Sigma_u^+$ are the calculated MC-SCF energies which are upper bounds to the actual curves.

The maximum expected linewidth has been estimated [56] to be as much as 140 cm^{-1} at v'=24. This predissociation is again caused by a spin-orbit interaction; this time the magnitude of the interaction has been calculated to be 373 cm^{-1} again lending support to the prediction of a matrix element of 90-100 cm^{-1} in S_2.

4.6 Conclusions

The technique of CRDS has been used to further characterise and clarify the predissociation mechanisms occurring throughout the $B^3\Sigma_u^-$ state of S_2 for $v' \geq 10$. In these experiments, homogeneous line broadening of spectral lines was estimated from band contour fits to various (v',0) vibrational bands with v'=10 to 19 within the S_2 $B^3\Sigma_u^-$-$X^3\Sigma_g^-$ spectrum. The lines of the (10,0) band are not broadened a great deal and the band shows sharp, as yet unassigned, rotational structure. All bands with $10 < v' \leq 17$ show diffuse structure and vary in rotational linewidth from 10 ± 1 cm^{-1} for the (11,0) band to 7 ± 1 cm^{-1} for the (17,0) band with a maximum linewidth of 14 ± 1 cm^{-1} for the (13,0) band. All bands with $v' \geq 18$ are completely diffuse, indicating the onset of a second strong predissociation at around v'=18 in the B state. For these bands only an estimate of a lower limit of 15 cm^{-1} for the linewidth is possible.

To complement this experimental study, detailed *ab initio* calculations were performed to understand the nature of the predissociating states, and, furthermore, have used the resultant calculated potentials together with an improved RKR potential for the $B^3\Sigma_u^-$ state to derive an analytical model that reproduces quantitatively the experimental data. The *ab initio* potentials were slightly shifted in energy to give the energies appropriate for the different $S(^3P_j)$ asymptotes. The model uses Fermi golden rule calculations of the predissociation rates to enable a comparison between theoretical predictions and our experimental measurements. The model indicates that the first predissociation, setting in at around v'=10, is caused by a spin-forbidden interaction with a $^1\Pi_u$ state which possesses a very shallow minimum at R=2.4 Å (just inside the crossing point of the B state potential). The observed form of the variation in linewidth with v' is reproduced if the whole *ab initio* repulsive potential is moved by 0.07 Å to larger internuclear separation, and this variation is attributed to the rapidly changing overlap of bound and continuum wavefunctions. The magnitude of the spin-orbit interaction matrix element responsible for the predissociation is estimated to be 90 cm^{-1} and is taken to be independent of R. The second predissociation is probably caused by one or more of a variety of states ($^5\Sigma_u^-$, $^5\Pi_u$ or $^3\Sigma_u^+$) since our calculations reveal that there are numerous crossings of the outer wall of the B state potential at energies around and above the

energy of the v'=18 level, and all of the states have more than one Ω component. The observed behaviour can be modelled successfully, however, if the lowest lying of these *ab initio* potentials, the $^5\Sigma_u^-$ state, is treated as a single potential (hence neglecting the Ω components) and an interaction energy of 100 cm^{-1} is invoked between it and the B state, independent of internuclear separation. A combination of the *ab initio* B" state potential and a previously determined, experimentally derived B ~ B" spin-orbit coupling function enables the conclusion to be made that coupling to the repulsive wall of the B" state constitutes at best only a very minor channel for predissociation of the B state. The theoretical model is unlikely to be the sole description of the predissociation behaviour that accounts quantitatively for the observed rates. The model is attractive, however, because it contains a minimal number of adjustable parameters and the values of those parameters can be physically justified.

Future work will include refinements to the calculated potentials by extending the basis set and an *ab initio* calculation of the spin-orbit coupling matrix elements between the B state and the $B''^3\Pi_u$, $^5\Pi_u$, $^1\Pi_u$, and $^5\Sigma_u^-$ potentials for comparison with our predictions. Further analysis of the B-X (10,0) band using fluorescence-depletion experiments to clarify the rotational assignments is already underway [45].

References

1. P. J. Flory, *J. Chem. Phys.*, **4** (1936) 23.
2. R.B.W. Pearce and A.G. Gaydon, *The Identification of Molecular Spectra*, Chapman and Hall, London (1963).
3. A. Fowler and W.M. Vaidya, *Proc. R. Soc. A*, **132** (1931) 310.
4. G. Lakshminarayana and C.G. Mahajan, *J. Quant. Spectrosc. Radiat. Transfer*, **16** (1976) 549.
5. J. I. Graham, *Proc. R. Soc. London Ser. A*, **84** (1910) 311.
6. M.E. Green and C.M. Western, *J. Chem. Phys.*, **104** (1996) 848.
7. M.E. Green and C.M. Western, *J. Chem. Soc., Faraday Trans.*, **93** (1997) 365.
8. M.E. Green, *Ph.D. Thesis*, University of Bristol (1996).
9. S.P. Sapers and D.J. Donaldson, *J. Chem. Phys.*, **94** (1990) 8918.
10. N. van Veen, P.Brewer, P. Das, and R. Bersohn, *J. Chem. Phys.*, **79** (1983) 4295.
11. K.S. Noll, M.A. McGrath, L.M. Trafton, S.K. Atreya, J.J. Caldwell, H.A. Weaver, R.V. Yelle, C. Barnet, and S. Edington, *Science*, **267** (1995) 1307.
12. S.J. Kim, M.F. Ahearn, and S.M. Larson, *Icarus*, **87** (1990) 440.
13. R.J.A. Grim and J.M. Greenberg, *Astron. Astrophys.*, **181** (1987) 155.
14. G.F. Mitchell, *Astrophys. J.*, **287** (1984) 665.
15. H.S. Liszt, *Astrophys. J.*, **219** (1978) 454.
16. S.R. Leone and K.G. Kosnik, *Appl. Phys. Letts.*, **30** (1977) 346.
17. N.D. Gibson, U. Kortshagen, and J.E. Lawler, *J.Appl. Phys.*, **79** (1996) 7523.
18. F.D. Wayne, P.B. Davies, and B.A. Thrush, *Mol. Phys.*, **28** (1974) 989.
19. H.M. Pickett and T.L Boyd, *J. Mol. Spect.*, **75** (1979) 53.
20. H. Lefebvre-Brion and R.W. Field, *Perturbations in the Spectra of Diatomic Molecules.*, Academic Press, Inc., (1986)
21. R. Schlapp, *Physic. Rev.*, **51** (1937) 342.
22. V.E. Bondybey and J.H. English, *J. Chem. Phys.*, **69** (1978) 1865.
23. C.R. Quick Jr. and R.E. Weston Jr., *J. Chem. Phys.*, **74** (1981) 4951.
24. Y. Matsumi, T. Munakata, and T. Kasuya, *J. Chem. Phys.*, **81** (1984) 1108.
25. H.J. Hurst, *D. Phil. Thesis*, Oxford University (1965).
26. R.F. Barrow and R.P. du Parcq, *"Electronic Spectrum and Electronic States of S_2" in Elemental Suphur*, edited by B. Meyer (Interscience, NewYork, 1965), Chap. 13 and references therein.
27. M. Barnes, J. Baker, J.M. Dyke, and R. Richter, *Chem. Phys. Letts.*, **166** (1992) 229.
28. M.J. Cooper and C.M. Western, *Chem. Phys. Letts.*, **267** (1997) 365.

29. K.P. Huber and G. Herzberg, *Constants of Diatomic Molecules*, Van Nostrand Reinhold Company, New York (1979).
30. J.E. Meakin and R.F. Barrow, *Can. J. Phys.*, **40** (1962) 377.
31. K.A. Meyer and D.R. Crosley, *Can. J. Phys.*, **51** (1973) 2119.
32. P. Patino and R.F. Barrow, *J. Chem. Soc., Faraday Trans.*, **78** (1982) 1271.
33. M. Heaven, T.A. Miller, and V.E. Bondeybey, *J. Chem. Phys.*, **80** (1984) 51.
34. E. Olsson, *Zeits. f. Physik*, **108** (1937) 40.
35. G. Herzberg and L.G. Mundie, *J. Chem. Phys.*, **8** (1939) 263.
36. G. Herzberg, *Ann. d. Physik*, **15** (1932) 701.
37. B. Rosen, M. Désirant and J. Duchesne, *Phys. Rev.*, **48** (1935) 916.
38. G. Herzberg, *Molecular Spectra and Molecular Structure*, Volume I - Spectra of Diatomic Molecules, Van Nostrand Reinhold Company Inc. (1950) and references therein.
39. J.M. Ricks and R.F. Barrow, *Can. J. Phys.*, **47** (1969) 2423.
40. R.W. Fair and B.A. Thrush, *Faraday Trans.*, **65** (1965) 1208.
41. G.G. Pannetier, P. Goudmand, O. Dessaux, and N. Tavernier, *J. Chem. Phys.*, **61** (1964) 395.
42. D. Kley and P. Broida, *J. Photochem.*, **6** (1976/77) 241.
43. W.C. Swope, Y-P. Lee, H.F. Schaefer III, *J. Chem. Phys.*, **70** (1979) 947.
44. A.D. Pradhan and H. Partridge, *Chem. Phys. Letts.*, **255** (1996) 163.
45. M.J. Cooper, J.M.F Elks, and C.M. Western, private communication.
46. H.J. Werner and P.J. Knowles, *Chem. Phys. Letts.*, **145** (1993) 514
47. D.E. Woon, K.A. Peterson, and T.H. Dunning, *J. Chem. Phys.*, **98** (1993) 1358, and references therein.
48. H.-J. Werner and P.J. Knowles, *J. Chem. Phys.*, **89**, 5803 (1988); H.-J. Werner and P.J. Knowles, *Chem. Phys. Lett.*, **145** (1988) 514; H.-J. Werner and E.A. Reinsch, *J. Chem. Phys.*, **76** (1982) 3144; H.-J. Werner, *Adv. Chem. Phys.* **LXIX** (1987) 1.
49. P.J. Knowles and H.-J. Werner, *Theor. Chim. Acta* **84** (1992) 95.
50. H.-J. Werner and P.J. Knowles, *J. Chem. Phys.* **82** (1987) 5053; P.J. Knowles and H.-J. Werner, *Chem. Phys. Lett.* **115** (1985) 259. See also H.-J. Werner and W. Meyer, *J. Chem. Phys.* **73** (1980) 2342 and H.-J. Werner and W. Meyer, *J. Chem. Phys.* **74** (1981) 5794.
51. C.E. Moore, *Atomic Energy Levels*, NSRDS-NBS 35 vol. 1 (1971).
52. R.J. Le Roy, RKR1, University of Waterloo Chemical Physics Research Report No. CP-425, (1992).
53. R.J. LeRoy, LEVEL 6.1, University of Waterloo Chemical Physics Research Report CP-555R (1996).
54. R.J. LeRoy, *Comp. Phys. Comm.* **52** (1989) 383; BCONT 1.4, University of Waterloo Chemical Physics Research Report CP-329R (1993).

55. P.S. Julienne and M. Krauss, *J. Mol. Spec.*, **56** (1975) 270.
56. O. Atabeck and R. Lefebvre, *Chem. Phys. Letts.*, **17** (1972) 167.
57. J.N. Murrel and J.M. Taylor, *Mol. Phys.*, **16** (1969) 609.
58. H. Schaefer III and W.H. Miller, *J. Chem. Phys.*, **55** (1971) 4107.

5. CRDS Detection of the $A^2\Pi_{3/2}$-$X^2\Pi_{3/2}$ transition in the BrO radical

5.1 Introduction

The significance of BrO in ozone catalytic destruction cycles has only been recognised comparatively recently [1]. BrO is generated in the upper atmosphere following the UV photolysis of bromine-containing compounds such as halons and CH_3Br. Once formed BrO is transported to high altitudes where it can engage in catalytic destruction of ozone via the reactions,

$$\begin{aligned} &Br + O_3 \rightarrow BrO + O_2 \\ &BrO + O \rightarrow Br + O_2 \\ &\text{net:} \\ &O + O_3 \rightarrow 2O_2 \end{aligned} \qquad (5.1)$$

and

$$\begin{aligned} &Br + O_3 \rightarrow BrO + O_2 \\ &Cl + O_3 \rightarrow ClO + O_2 \\ &BrO + ClO \rightarrow Br + Cl + O_2 \\ &\text{net:} \\ &2O_3 \rightarrow 3O_2 \end{aligned} \qquad (5.2)$$

These routes for the loss of odd oxygen species in the stratosphere are thought to be more potent than the analogous chlorine cycle and are implicated in the chemistry leading to the formation of the springtime Antarctic ozone hole [2].

The BrO radical has an inverted $^2\Pi$ ground state which has been thoroughly investigated by a combination of microwave [3] and infra-red [4] studies. Magnetic dipole transitions between the $^2\Pi_{1/2}$ and $^2\Pi_{3/2}$ components of the ground state have been observed using laser magnetic resonance (LMR) [5] experiments and a spin-orbit splitting constant of -968 cm^{-1} has been determined. The $A^2\Pi_{3/2}$ - $X^2\Pi_{3/2}$ band system shows a long progression of red-degraded bands and was first observed in emission from

an ethyl bromide flame in 1939 by Vaidya [6]. More recently the A-X band has been studied in absorption following the flash-photolysis of mixtures of Br_2-O_2 [7]. Most of the 20 observed vibrational bands were found to be unstructured though four of them, the (7,0), (12,0), (20,0), and (21,0) bands, showed some very diffuse rotational structure indicating a vibrational level dependent predissociation. Only transitions emanating from the lower spin-orbit component were observed, reflecting the large value of the spin-orbit constant A and the consequent low Boltzmann population in any thermally equilibrated sample. Detailed spectroscopic investigation of the BrO A-X band was hampered by the almost equal natural abundances of the two isotopes of Br (50.69% ^{79}Br : 49.31% ^{81}Br) causing increased spectral congestion. Further observations of the A-X band [8] using isotopically enriched $^{81}Br_2$ (98 %) allowed a rotational analysis of seven of the vibrational sub-bands to be carried out. The observed sub-bands consisted of simple overlapping P and R branches with the Q branches missing (as illustrated in Figure 5.1) since they are expected to be very weak for a case (c) $^2\Pi$-$^2\Pi$ transition by consideration of the Hönl-London factors for such a $\Delta\Lambda$=0 transition.

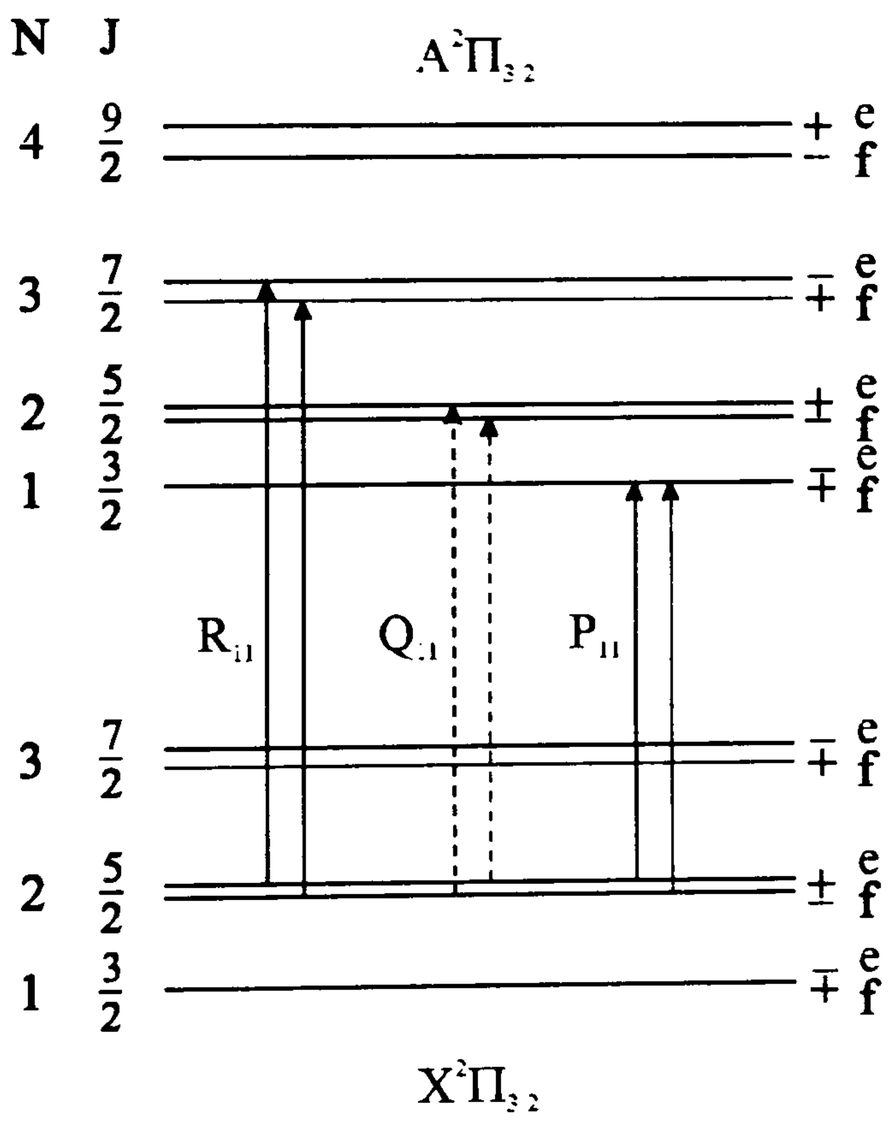

Figure 5.1. Allowed transitions for $A^2\Pi$-$X^2\Pi$ bands of BrO (note that the Q-branch is expected to be very weak and is not observed experimentally). The spin-orbit splitting is very large A=-968 cm^{-1} and transitions arising from the upper Ω component (not shown here) have not been observed.

5. *CRDS Detection of the $A^2\Pi_{3/2}$-$X^2\Pi_{3/2}$ transition in the BrO radical*

Several lower resolution studies have also been carried out in order to determine the absolute UV absorption cross sections [4,9] which are required for both laboratory and field measurements of BrO and for estimation of photolytic destruction of BrO in atmospheric models. The majority of these studies have concentrated on quantifying the absorption cross section at the strongest bandhead ((7,0) at 338.3 nm) giving a value $\sigma = 1.6 \times 10^{-17}$ cm^2 molecule^{-1} at 298 K.

The following work was conducted to test the viability of using CRDS to detect low concentrations of BrO generated by two different reaction schemes. Improved rotational constants and lifetime broadened linewidth estimates were obtained for the (7,0) and (12,0) bands from a least squares fitting procedure. Unfortunately we could not obtain isotopically enriched bromine so the analysis of the resultant spectra is made difficult by the overlapping ^{79}BrO and ^{81}BrO transitions as discussed above.

5.2 Experimental

The CRDS arrangement for recording spectra of the BrO $A^2\Pi$-$X^2\Pi$ bands was identical to that used in the previous two chapters and was described in detail in chapter 2. Two high reflectivity mirror sets were required for the experiments the first with maximum reflectivity centred at 320 nm (Research Electro Optics) and the latter at 290 nm (Virgo Lightning Optical Corp.). Again, both sets were manufactured from a quartz substrate 7.75-mm diameter, 4-mm thick and 2-m radius of curvature, the optical coating was laid down on the curved sides of the mirrors and had a specified reflectivity of >99.9% at the mirror centre. Calibration of the resultant spectra is obtained by the use of an etalon and an I_2 LIF spectrum at the fundamental dye laser wavelength recorded simultaneously with the CRD spectra.

The BrO radicals were generated in two ways in separate experiments in order to test the efficiency of both methods of production. Also, the two methods are complementary to one another depending upon which spectral region the BrO band of interest occurs in, since Br_2 absorbs strongly for $\lambda \geq 350$ nm and O_3 starts to absorb appreciably at wavelengths below 310 nm. Firstly, the following reaction was utilised,

$$O(^3P) + Br_2 \rightarrow BrO + Br\,. \qquad (5.3)$$

The ground state $O(^3P)$ atoms are formed by passing a microwave discharge through O_2 (30 % mixture in Argon) flowing into a mullite / quartz discharge tube connected to the ring-down cavity. The Br_2 (5 % in Ar) contained in a bulb is added to the ring-down cell through a glass / Teflon needle valve and Teflon tubing a few cm upstream of the $O(^3P)$ inlet and allowed to react over the length of the cell with the O atoms. Typically pressures of around 100 mTorr Br_2 / Ar and 150 mTorr of O_2 / Ar were used and the microwave generator (Microtron 200) operated at approximately 40 Watts input power. Care needed to be taken when using the quartz discharge tube as local heating by the microwave discharge tended to crack the tube very easily unless sufficient water-cooling was present. This method of production provides a very simple approach to generating

BrO with readily available starting materials. However, the general drawback with this procedure is that the reaction

$$BrO + O(^3P) \rightarrow Br + O_2 \qquad (5.4)$$

is much more rapid than reaction 5.3 and thus only moderate concentrations of BrO can be achieved.

The second reaction scheme used,

$$Br + O_3 \rightarrow BrO + O_2, \qquad (5.5)$$

should produce a steady state of BrO in much greater quantities since the reaction of BrO with O_3 ($k < 5 \times 10^{-17}$ cm^3 molecule^{-1} s^{-1}) is known to be orders of magnitude slower than with $O(^3P)$ ($k = 2.5 \times 10^{-11}$ cm^3 molecule^{-1} s^{-1}). The O_3 was synthesised using a standard method prior to use on the CRD experiment as follows. Firstly, O_2 (BOC) is passed through a trap containing phosphorous pentoxide (P_2O_5) and glass wool in order to remove any moisture present in the cylinder. The dried O_2 then flows into a commercial ozonizer (Fischer) operating at a current of 2 Amps and the resulting O_2/O_3 mixture is then transferred to a gas line via Teflon piping and swagelok fittings. The gas line was left for several minutes until it had been thoroughly purged by the gas mixture, then the outlet tap was shut off and the O_2/O_3 mixture was collected in an evacuated bulb connected to the gas line, up to a pressure of 700 Torr. A small portion of the mixture was also transferred to a 6-cm long absorption cell bounded by quartz windows. Using a UV / visible spectrometer (Perkin-Elmer) it was possible to estimate the concentration of O_3 in the O_2/O_3 mixture produced by the ozonizer to be around 2 %. The bulb of ozone diluted in oxygen was then transferred to the cavity-ring down experiment. The Br atoms are produced by a microwave discharge, operating at around 20-30 Watts, passing through 500-600 mTorr of Br_2 (5% in Ar) flowing into the ring-down cell. The Br atom discharge was left for a few moments to stabilise and then O_3/O_2 was added very gradually. BrO production was monitored by placing the laser on a known band-head and observing the ring-down time on the scope whilst O_3 was leaked into the cell. It was

found that a very small amount (< 1 mTorr) of the O_3/O_2 mixture caused the ring-down time to decrease by up to 50 % at the strongest part of the (12,0) band.

5.3 Results

Both the above methods of radical generation were found to yield sufficiently large quantities of BrO for the experiments discussed here. For the reaction of Br atoms with O_3 (equation 5.5) it was possible to determine an upper limit for the concentration of BrO radicals produced in the ring down cell to be around 6×10^{11} molecules cm^{-3}. In this estimation it is assumed that all of the O_3 is converted to BrO, which is a reasonable approximation considering the partial pressure of Br (assuming efficient conversion of Br_2 to Br in the microwave discharge) is several orders of magnitude greater than that of O_3. This estimate is consistent with the observed decrease in ring-down time from 10 μs to around 1 μs when the laser was tuned to the head of the (12,0) band. As will be evident from the signal to noise ratio of the experimental data, our detection limit for BrO is in principle substantially lower than this concentration.

A spectrum of the $A^2\Pi_{3/2}$ - $X^2\Pi_{3/2}$ (7-0) band is shown in Figure 5.2 (a) together with a 300 K simulation using the literature values for the ground state [4,5] spectroscopic constants and refined A-state constants, given in Table 5.1, derived from a least-squares fitting procedure. These refined constants were obtained by simulating the band contours of both ^{79}BrO and ^{81}BrO simultaneously and performing a least squares fit as described in chapter 4.3 in which the band origins, and rotational constants of both isotopomers, were adjustable parameters in the rigid rotor Hamiltonian matrix. The Lorentzian linewidth of 3.2 cm^{-1} derived from this spectrum corresponds to a natural lifetime of 1.7 ps indicating a fast predissociation. The next band at higher energy that shows any resolvable structure is the $A^2\Pi_{3/2}$ - $X^2\Pi_{3/2}$ (12-0) band shown in Figure 5.2 (b). Again the simulation is derived from a combination of known ground state constants [4,5] and fitted excited state constants given in Table 5.1. The calculated linewidth of 4 cm^{-1} obtained from this spectrum indicates that predissociation is stronger in this band and that the v'=12 level has a lifetime of around 1.3 ps. Attempts were also made to record the (21,0) band, another of those that had previously been reported as showing some hint of resolved rotational structure from single isotope studies, but it exhibited very little observable rotational structure for the isotopic mixture. This apparent lack of structure may be attributed to a phase effect in the rotational lines

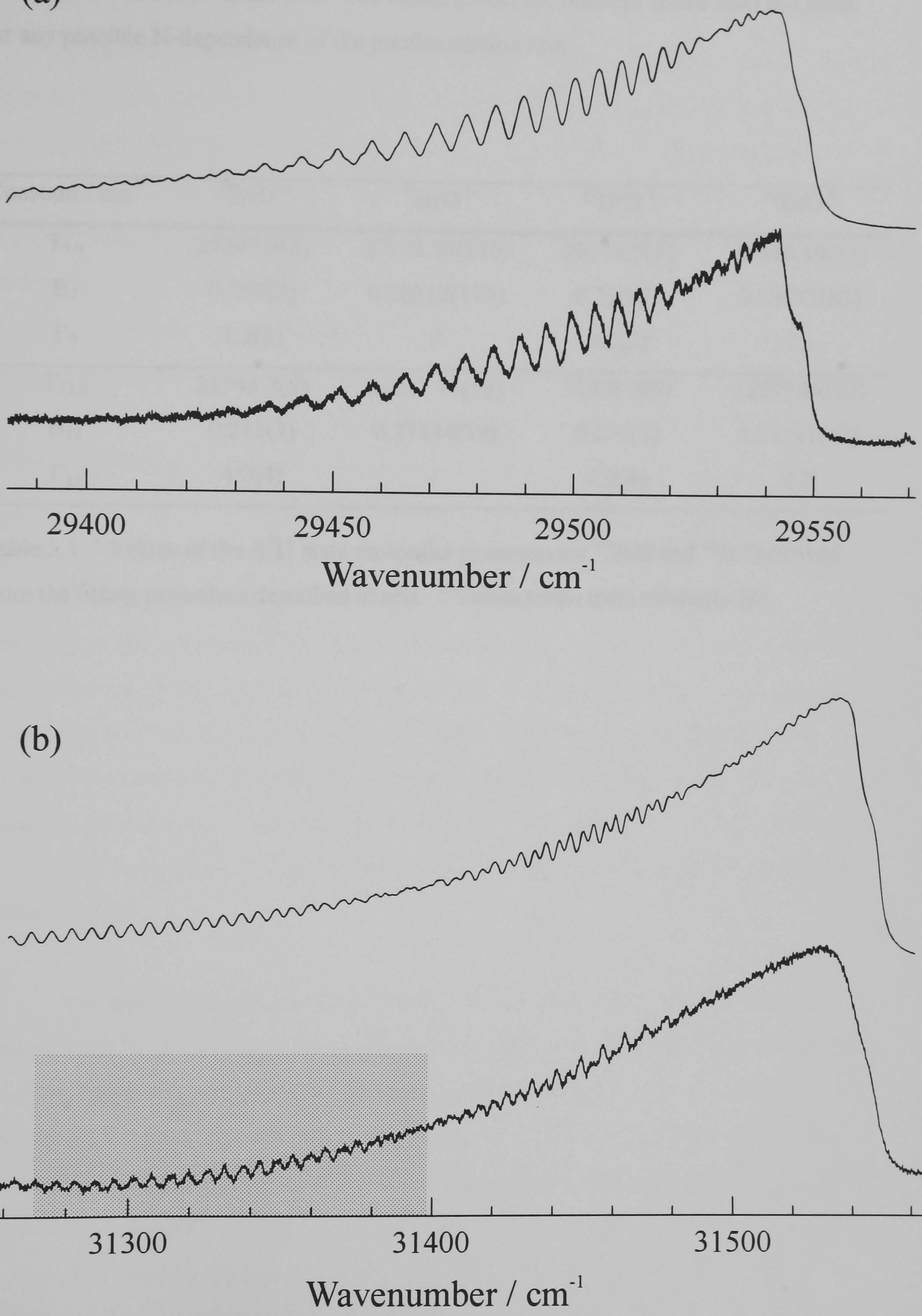

Figure 5.2 CRD spectrum and 300 K simulation of (a) (7,0) and (b) (12,0) bands of the $A^2\Pi_{3/2}$-$X^2\Pi_{3/2}$ transition of BrO. The shaded area in (b) is shown on an expanded scale in Figure 5.3.

caused by the change in rotational constants with vibrational level and is not necessarily an indication of a shorter lifetime. The fitting procedure outlined above does not allow for any possible N-dependence of the predissociation rate.

Constant / cm^{-1}	^{79}BrO [a]	^{79}BrO [b]	^{81}BrO [a]	^{81}BrO [b]
$T_{7,0}$	29547.3(8)	29543.59(110)	29542.5(8)	29538.59(71)
B_7	0.292(2)	0.28812(170)	0.290(2)	0.28672(82)
Γ_7	3.2(3)	/	3.2(3)	2.8
$T_{12,0}$	31545.7(8)	31547.74(55)	31538.5(9)	31539.88(22)
B_{12}	0.273(3)	0.27244(39)	0.271(3)	0.27141(32)
Γ_{12}	4.0(4)	/	4.0(4)	1.9

Table 5.1. [a] Values of the $A^2\Pi$ state molecular constants for ^{79}BrO and ^{81}BrO derived from the fitting procedure described in text. [b] Values taken from reference [8].

5.4 Discussion

It can be seen from Table 5.1 the $A^2\Pi$ state constants obtained from the current study are in close agreement with the original analysis of Barnett *et al* [8] for the v'=12 level. In the fitting procedure described above the values of the $A^2\Pi$ state rotational constants of both isotopomers were floated independently. However, in order for the values obtained to be physically acceptable the ratio B(^{79}BrO)/ B(^{81}BrO) must be in agreement with the fixed ratio of the reduced masses $\mu(^{81}BrO)/ \mu(^{79}BrO) = 1.0042$. This constraint therefore provides a means of checking the validity of the fitting procedure and by examination of Table 5.1 it can be seen that the isotopic ratios of both the B_7 and B_{12} constants meet this condition within the estimated experimental error. The beating of the rotational structure in the partially resolved contour of the simulation of the (12,0) band shown in Figure 5.2 (b) is very sensitive to values of the rotational constants used. Figure 5.3 (b) shows an expanded portion of the (12,0) band together with a simulation using the rotational constants derived from the fitting procedure. In order to demonstrate the sensitivity of the simulation to the values of the rotational constants Figures 5.3 (a) and (c) show the spectrum along with simulations using the values of B_{12} from Table 5.1 ± 2 %. It is evident from Figure 5.3 that even a small change in the values of the rotational constants has a dramatic effect on the shape of the contour obtained. The homogeneous component of the linewidth of 4.0 ± 0.3 cm^{-1} for transitions to the v'=12 level drawn from the current analysis is a factor of two greater than earlier estimations [8].

The values obtained from the current study for the constants of the $A^2\Pi$ v'=7 level of both ^{79}BrO and ^{81}BrO are in disagreement with the analysis of Barnett *et al.* [8]; the band origins and rotational constants deduced from present work are increased by 4 and 0.04 cm^{-1} respectively for both isotopomers. Barnett *et al.* [8] observed both the (7,1) and (7,0) bands of ^{81}BrO in their study and found that the upper state constants for the two bands differed by more than the experimental error limits. This error was thus attributed to a systematic error (possibly in the rotational numbering) caused by the blending of the P and R branches rather than a statistical error. The demonstration of the accuracy of the band contour fitting procedure used in the current analysis for the (12,0)

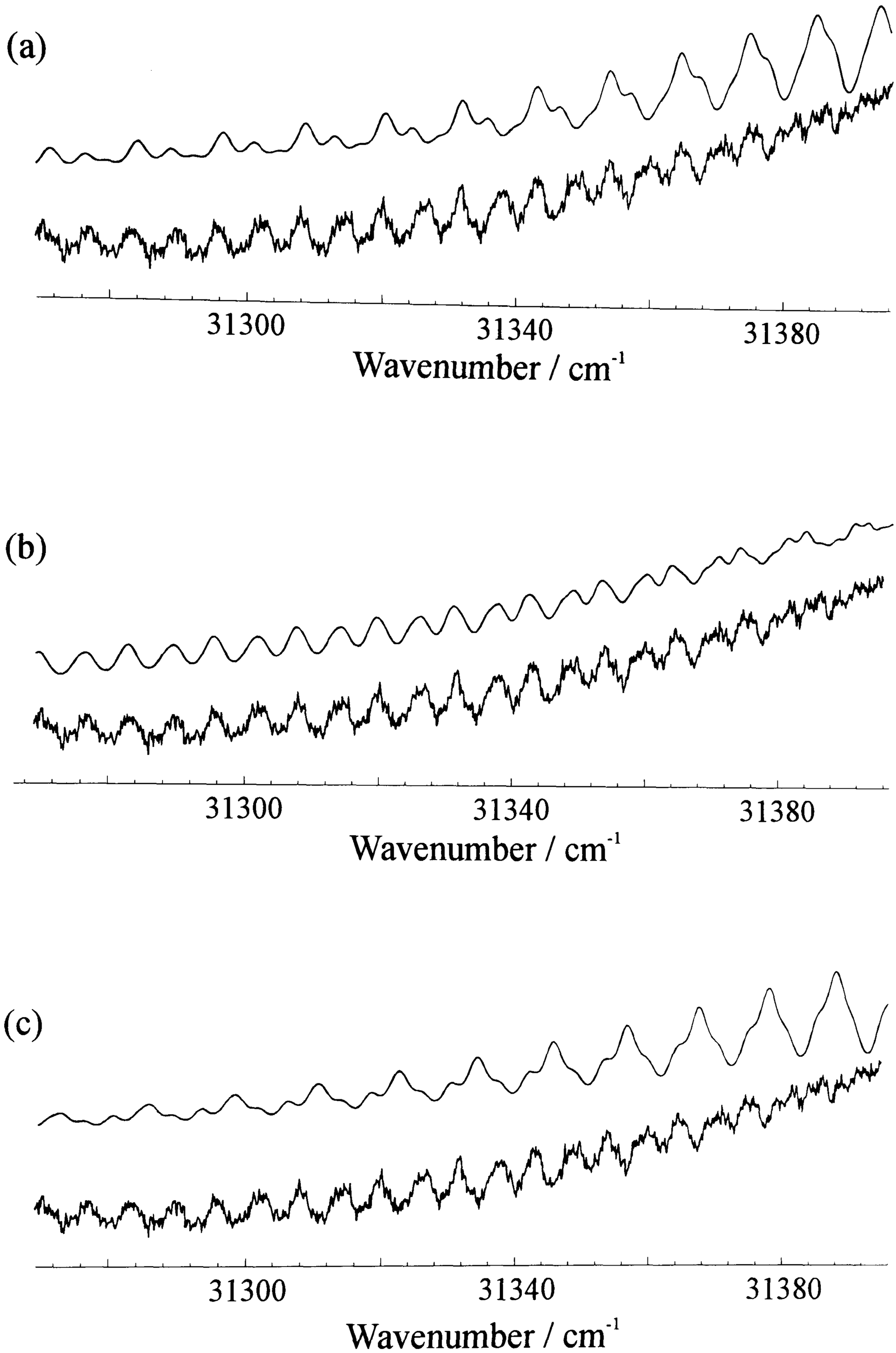

Figure 5.3. Expanded portion of the $A^2\Pi_{3/2}$-$X^2\Pi_{3/2}$ (12,0) band (boxed area in Figure 5.2 (b)). Figure (b) shows the simulation derved from the fitting process described in the text. Figures (a) and (c) show simulations with the rotational constants changed by ± 2%.

band (Figure 5.3) suggests that the derived constants for the (7,0) band are more accurate than earlier studies [8].

No *ab initio* calculations have been performed to determine the ordering of excited states of BrO and thus very little is known about the predissociation mechanisms occurring throughout the $A^2\Pi$ state. By consideration of the Wigner-Witmer correlation rules 12 states may be formed from $Br(^2P_u) + O(^3P_g)$, namely, $^2\Sigma^+$, $^2\Sigma^-(2)$, $^2\Pi(2)$, $^2\Delta$, $^4\Sigma^+$, $^4\Sigma^-(2)$, $^4\Pi(2)$, and $^4\Delta$. The ground $X^2\Pi$ state must undoubtedly correspond to one of the two $^2\Pi$ states formed from two ground state atoms. The $A^2\Pi$ excited state is predissociated and therefore cannot be correlated with the remaining $^2\Pi$ state. The $A^2\Pi$ state must therefore dissociate to $Br(^2P_{3/2}) + O(^1D_2)$ [7]. It therefore seems feasible that there are numerous potentials which may predissociate the $A^2\Pi$ state causing the observed diffuseness of bands. By interpolating the derived $A^2\Pi$ state rotational constants from table 5.1 between v'=7 and 12 (assuming a linear variation) it was possible to estimate the required predissociation rate in order for there to be no observable rotational structure. From these calculations it was found that the linewidths of transitions to $A^2\Pi$ v'=8,9,10, and 11 must be around 8-12 cm^{-1}. No further analysis could be undertaken due to the lack of both experimental and theoretical data.

5.5 Conclusions

LIF is inappropriate for studies of the kinetics of reactions of BrO since the rapid predissociation of all levels of the A-state precludes fluorescence. Using CRDS, a laser-based detection scheme for the $A^2\Pi_{3/2}$ - $X^2\Pi_{3/2}$ band system of BrO has been demonstrated, with the BrO produced via either of the reactions, $Br + O_3 \rightarrow BrO + O_2$ or $O + Br_2 \rightarrow BrO + Br$. As discussed in chapter 2, CRDS is already starting to be used as an invaluable tool for chemical kinetics measurements. This demonstration of the simplicity of detecting BrO with high sensitivity via CRDS should enable further important studies of the rates of reaction of BrO to be performed using this spectroscopic probe. The signal to noise ratio in the spectra shown in Figure 5.2(a) is around 80:1 with no signal averaging. Based upon this the sensitivity is such that concentrations of two orders of magnitude less than detected here should be easily detectable if averaging over a number of laser shots is used. Related studies on the kinetics of the IO radical using CRDS detection on its A-X (2,0) band have recently been performed [10] and further investigation is currently in progress.

The current generation of diode lasers that are available on the market claim to be powerful enough (10 mW) to be used in conjuction with frequency conversion techniques thus offering a very compact and high resolution laser source capable of UV spectral coverage. Coupling this with recent developments in cw CRDS, which can now achieve extreme sensitivities ($\alpha_{min} = 2 \times 10^{-10}$ / cm) [11], the possibility of developing a portable, inexpensive instrument for *in-situ* trace gas detection in the field is rapidly becoming a realistic prospect. Currently, indirect techniques such as resonance fluorescence of Br atoms formed by titration with NO are utilised for detection of BrO in the stratosphere and are capable of detection limits < 1ppt at these altitudes. However, the long duration of the measurement cycle (limited by the NO addition cycle of up to 32 s) in such techniques limits their spatial resolution which can be of the order of several km if the instrument is mounted on an aircraft. Using CRDS with a cw laser it should be feasible to detect 10-100 ppt with the above minimum absorption coefficient, α_{min}, in the stratosphere. CRDS also offers the added benefit of rapid data aquisition (200 Hz sampling rate [11]) which could, in principle, provide very high spatial resolution.

References

1. M.J. Prather and R.T. Watson, *Nature*, **344** (1990) 729.
2. R.P. Wayne, *Chemistry of Atmospheres*, Clarendon Press, Oxford (1991).
3. E.A. Cohen, H.M. Pickett, and M. Geller, *J. Mol. Spec.*, **87** (1981) 459.
4. J.J. Orlando, J.B. Burkholder, A.M.R.P.Bopegedera, and C.J. Howard, *J. Mol. Spec.*, **145** (1991) 278.
5. A.R.W. McKellar, *J. Mol. Spec.*, **83** (1981) 43.
6. W.M. Vaidya, *Proc. Indian Acad. Sci. A*, 7 (1938) 321.
7. R.A. Durie and D.A Ramsay, *Can. J. Phys.*, **36** (1958) 35.
8. M. Barnett, E.A. Cohen, and D.A. Ramsay, *Can. J. Phys.*, **59** (1981) 1908.
9. W.B. DeMore, S.P. Sander, D.M. Golden, R.F. Hampson, M.J. Kurylo, C.J. Howard, A.R. Ravishankara, C.E. Kolb, and M.J. Molina, *Chemical Kinetics and Photochemical Data for use in Stratospheric Modeling*, Evaluation Number 12, JPL Publication 97-4 (1997).
10. A.J. Orr-Ewing and J.W. Hudgens, *in preparation.*
11. D. Romanini, A.A. Kachanov, and F. Stoeckel, *Chem. Phys. Letts.*, **270** (1997) 546.

6. Four-wave mixing spectroscopy of molecular iodine

6.1 Introduction

6.1.1 Four-Wave Mixing Spectroscopy

Four-wave mixing (FWM) methods have traditionally been employed in the areas of optical-phase conjugation [1] and ultra-fast relaxation phenomena in liquids and solids [2]. Only in more recent years has its potential as a powerful probe in high-resolution gas-phase spectroscopy [3-6], in plasma diagnostics [7-9] and molecular photodissociation dynamics [10-12] been realised. Extensive theoretical analysis has also been carried out [13-16] in order to investigate some of the many features afforded by such experiments. The technique has been extended to the infra-red spectral region and has been used to record vibrational spectra of the fundamental and overtone bands in HF [17], and also CH overtones in both CH_4 [18] and C_2H_2 [19]. One other important area of research where FWM techniques have demonstrated promising features is in Femtosecond real-time probing of transition states using short-pulse lasers [20].

All resonant FWM techniques make use of the photo-refractive response of a medium to an applied field to generate a signal beam. The FWM mechanism relies upon the interaction of three coherent light beams to induce a non-linear polarisation in a medium via the third order non-linear susceptibility tensor $\chi^{(3)}$. In Degenerate Four-Wave Mixing (DFWM) [3,12,21] this induced polarisation then generates a fourth coherent beam. DFWM involves a similar excitation scheme to Coherent Anti-Stokes Raman Spectroscopy (CARS) as illustrated in Figure 6.1. However, the important difference to note is that DFWM is a resonant process and thus will be intrinsically more sensitive than non-resonant CARS. The important distinction about the case of DFWM is that the three input beams all have the same angular frequency ω, and so the induced polarisation, and hence the generated signal beam, also oscillates at ω. In dilute media (*e.g.* a gas) this mixing process is enhanced by many orders of magnitude in the vicinity of a resonance of a molecular (or atomic) transition. Thus a spectrum can be obtained by observing the intensity of the signal beam as a function of laser frequency.

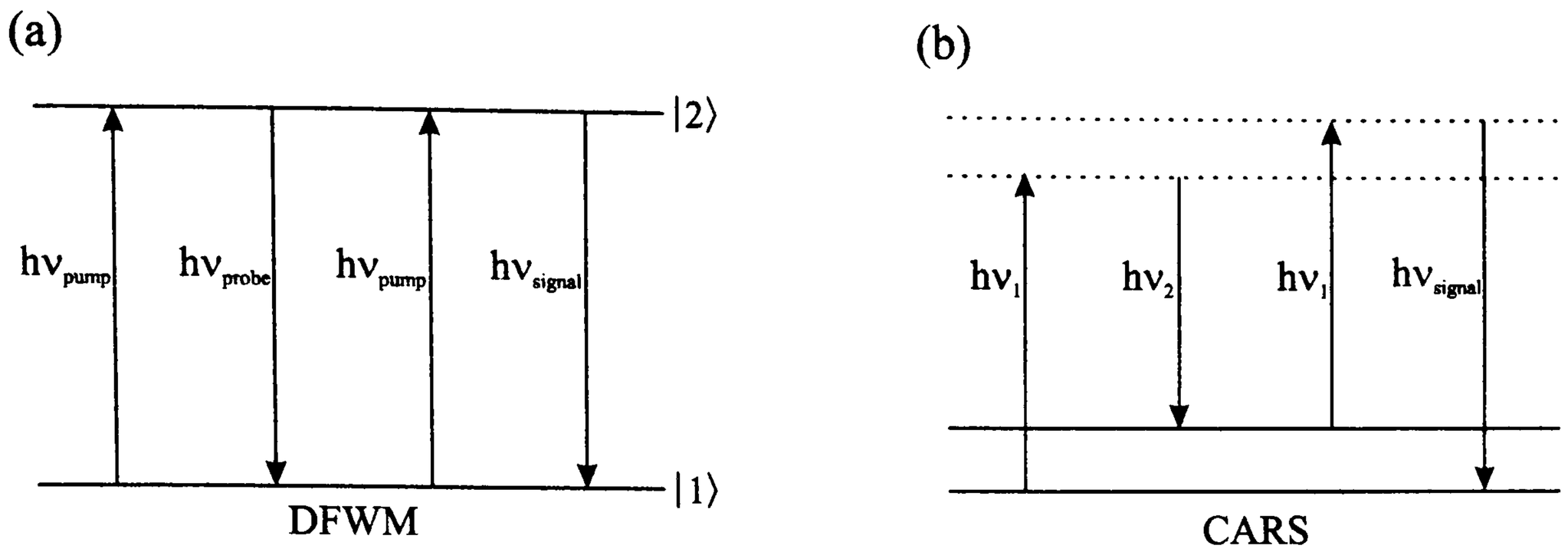

Figure 6.1. Excitation schemes for (a) Degenerate Four-Wave Mixing (DFWM) and (b) Coherent Anti-Stokes Raman Spectroscopy (CARS). The solid horizontal lines represent real states of the system whilst the dotted lines are virtual states. The energy of the signal photon in each case is given by $h\nu_{signal}$.

The most common and conceptually most pleasing qualitative interpretation of the FWM process is that of the laser-induced grating (LIG) [2] in which two laser beams (λ_{pump}) are crossed in an absorbing medium to form a spatially modulated intensity pattern, illustrated in Figure 6.2.

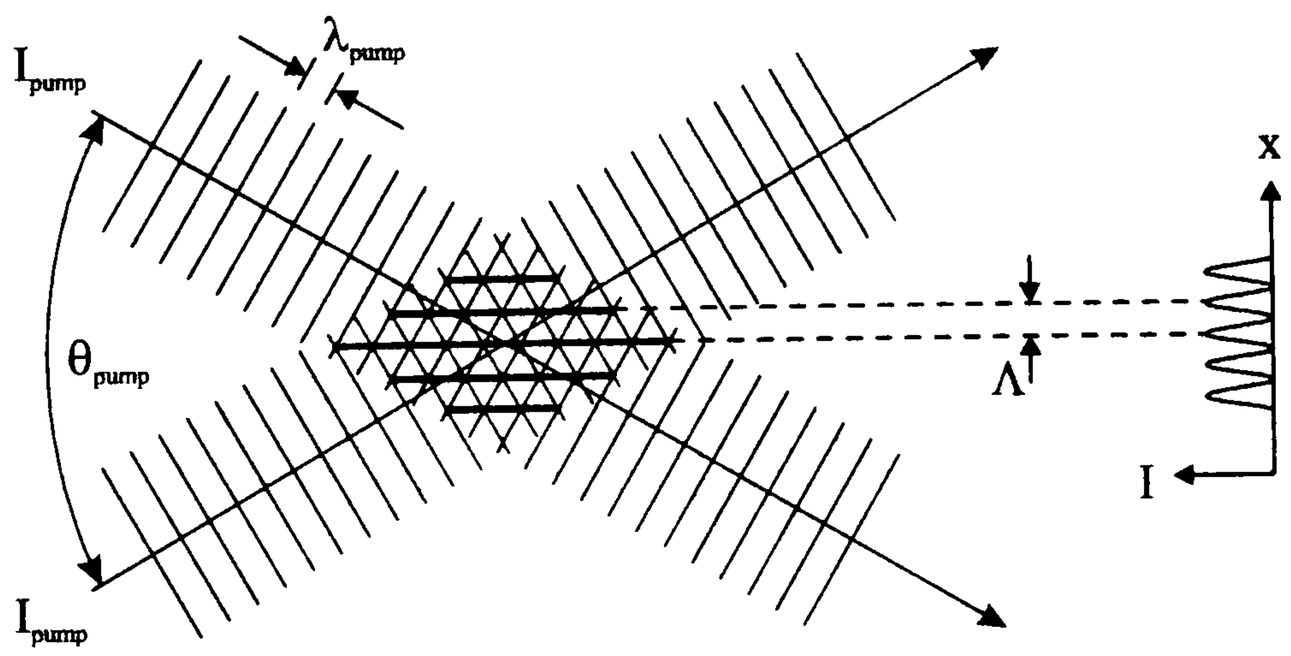

Figure 6.2. Production of a transient grating via two-beam interference.

If λ_{pump} is resonant with a molecular transition then this interference pattern is projected into the absorbing medium *i.e.* the areas of constructive interference will produce areas of excited state population whereas the reverse will be true of the destructive interference regions. This population grating then acts as a transient diffraction grating with spatial period given by

$$\Lambda = \frac{\lambda_{pump}}{2\sin(\theta/2)}, \tag{6.1}$$

where θ is the angle between the two grating-forming (pump) beams. This grating may then be probed by a third laser (λ_{probe}) to obtain a diffracted signal beam. The signal beam is only produced when λ_{probe} is resonant with a transition out of one of the levels involved in the grating forming step. This will always be the case in DFWM as both the grating-forming (pump) and probe beams have the same frequency by definition. However, if the probe beam is of a different frequency to the pump beam then a number a situations can arise that will lead to a diffracted signal beam being produced. This less common variant of FWM has been given the name Two-Colour Laser Induced Grating Spectroscopy (TC-LIGS) [12,22,23]. Figure 6.3 shows three possible cases where a TC-LIGS signal beam will be obtained. From this Figure it can be seen that the benefits so derived and the information obtained from the TC-LIGS technique closely parallel those associated with traditional double-resonance spectroscopies.

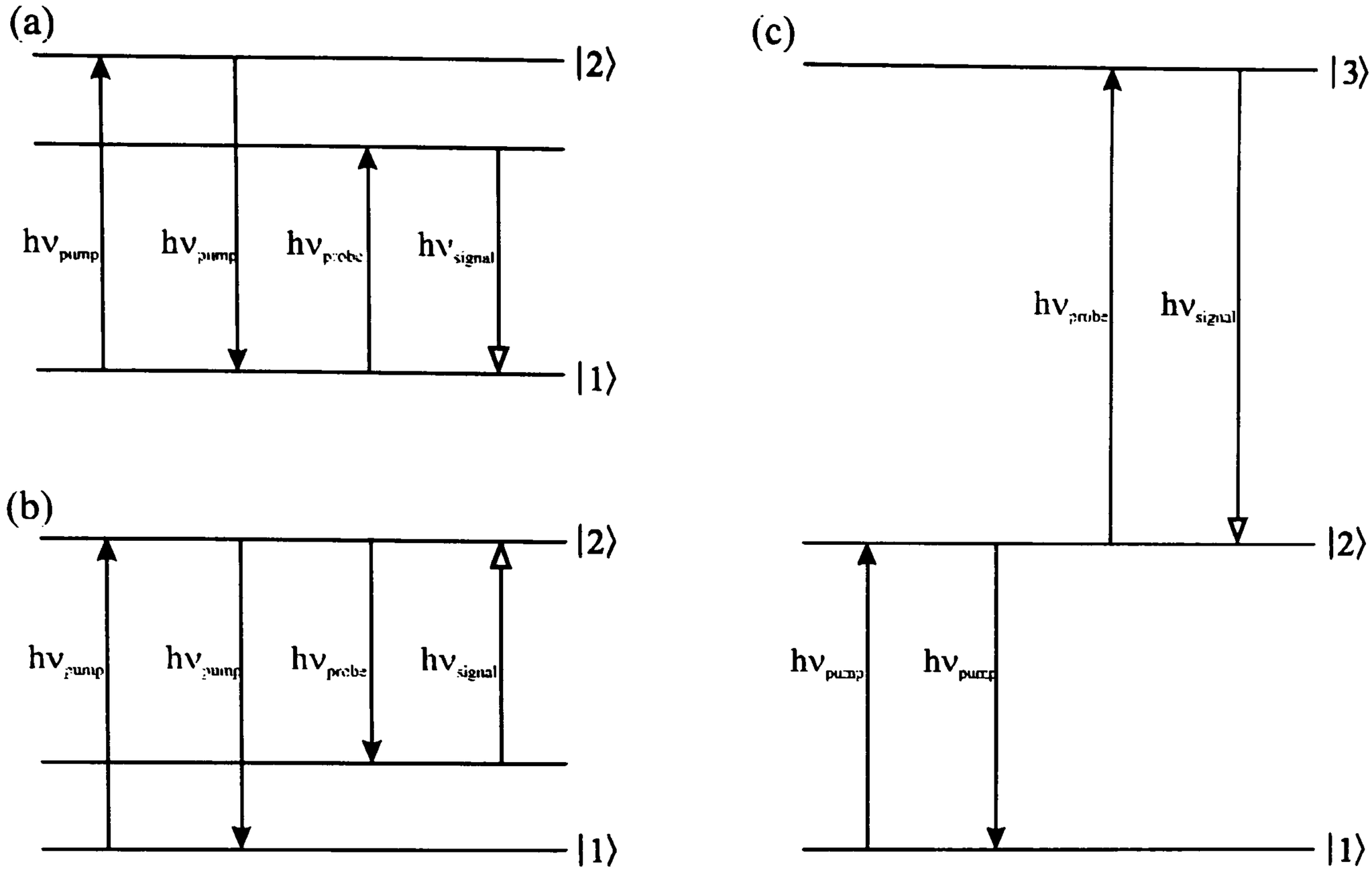

Figure 6.3. Illustration of the various excitation schemes adopted using Two-Colour Laser-Induced Grating Spectroscopy (TC-LIGS). The two pump beams ($h\nu_{pump}$) provide the grating forming transitions and: (a) the probe laser excites a transition upwards from the ground electronic state population grating, (b) the probe laser excites a transition from $|2\rangle$ to a high-lying level within state $|1\rangle$, or (c) the probe laser excites a transition from state $|2\rangle$ to a higher electronic state $|3\rangle$.

Amongst the major advantages one can foresee for LIGS methods over more conventional forms of spectroscopy are (i) the highly directional nature of the signal (thus eliminating scatter or source-background emission) and (ii) the ability to study non-fluorescing and predissociated systems [24]. A potential restriction with LIGS techniques, however, is the dependence of the signal intensity, I_s, to the initial (unperturbed) population difference, ΔN, between the two levels and the transition dipole moment, μ_{12}. This dependence has been investigated both theoretically [15] and experimentally [13,15] and is found to follow the power law,

$$I_s \propto (\Delta N \ell)^2 \mu_{12}^m \tag{6.2}$$

where ℓ is the interaction length and the exponent m depends upon the intensity, I, of the two grating forming beams. If the intensity is such that the transition is not saturated ($I << I_{sat}$) then m is approximately 8; whilst in the high field limit ($I >> I_{sat}$) m is found to be 2. Thus if the transition is very weak or the molecule of interest is only present in trace quantities then FWM signal intensity, I_s, will be very small. Under these circumstances it may prove necessary to work with high input laser powers in order to work at the high field limit thus reducing the dependence upon the transition dipole moment.

6.1.2 Ion-pair states of I_2

Part of this study is concerned with the observation and analysis of transitions involving hitherto unreported rovibrational levels of the E and f ion-pair states of molecular iodine [25-28]. Ion-pair states have attracted considerable attention in the past few years, both experimental and theoretical [28]; it is now recognised that such excited states should be identifiable for many molecules and indeed have been found in S_2 [29], and ClO [30]. Ion-pair states are generally characterised by large dissociation energies, long equilibrium bond lengths, and small vibrational level spacings. The halogens have proved to be especially popular for study, not least because their lowest lying ion-pair states lie at energies amenable to many contemporary spectroscopies. The interactions between zero-order ion-pair states, Rydberg states lying at comparable energies and (generally repulsive) valence excited electronic states, and the consequences of these interactions on the observable excited state photophysics, are proving to be a particularly fruitful area of study [28]. The first observations of ion-pair states in molecular iodine were in emission, [31] following high energy electrical discharge excitation of iodine vapour. The spectra so obtained were impenetrably complex. This is hardly surprising, given the unselective nature of the excitation scheme and the fact that, because of the much greater equilibrium bond lengths of the ion-pair states, the emission spectrum from each ion-pair state comprises a very extensive Franck-Condon progression. More selective, higher resolution data has since been obtained via a number of double resonance experiments - both in the bulk and in a beam - generally proceeding via the bound $B^3\Pi_u$ (0_u^+) valence state. This choice of intermediate state automatically limits the number of accessible ion-pair states since u $\leftrightarrow$ u transitions are dipole forbidden. This problem may be overcome, however, by double resonance excitation via perturbed levels near the dissociation threshold of the B state [32].

All 18 ion-pair states arising from the combinations I^+ ($^3P_2$) + I^- ($^1S_0$), I^+ ($^3P_{1,0}$) + I^- ($^1S_0$) and I^+ ($^1D_2$) + I^- ($^1S_0$) have now been characterised, at least partially, amongst the cluster of states lying at excitation energies *ca.* 41400 cm^{-1}, 47000 cm^{-1} and 55400 cm^{-1}, respectively. Molecular constants for many of these states are now available; the most recent and complete set of spectroscopic parameters [27] for the E 0_g^+ ($^3P_2$) and

f 0_g^+ ($^3P_0$) states span a very wide range of vibrational levels (E-state $123 \leq v \leq 346$ and f-state $40 \leq v \leq 214$), but are restricted to the non-rotating molecule.

6.1.3 Overview

The aim of the following work was to demonstrate the applicability of TC-LIGS to spectroscopic problems by adopting all three excitation schemes illustrated in Figure 6.3 to probe the X and B valence states and the high-lying E and f ion-pair states of molecular iodine.

In the first set of experiments the B(0_u^+) - X(0_g^+) transition was probed using the folded double-resonance schemes illustrated in Figure 6.3 (a) and (b) providing both state-selected absorption and emission spectra simultaneously.

In the later experiments the TC-LIGS excitation scheme shown in Figure 6.3 (c) was adopted to access levels of the E and f ion-pair states of I_2 via the excitation sequence,

$$E, f\,0_g^+, v',\ J' \xleftarrow{290-360\ nm} B\,0_u^+, v,\ J \xleftarrow{532.05\ nm} X\,0_g^+, v'',\ J'' \qquad (6.3)$$

These double resonance experiments involved selective preparation of (five) rovibronic levels of the $B^3\Pi_u$ (0_u^+) state and further excitation to levels of the E and f ion-pair states lying in the energy range 49100 - 52700 cm^{-1}. Spectroscopic analysis yielded refined term values for a range of rotational levels associated with high vibrational levels (v=100-106, 113-121, 130-140 and 150-157) of the E state, and for lower lying (v=27-66) levels of the f state.

Both sets of experiments were intended to provide benchmarks for future, more challenging systems where, for example, the species may be in trace quantities or the excited state is predissociative.

6.2 Experimental

The TC-LIGS experiment shown in Figure 6.4 consists of a pulsed dye laser system, a large collection of optical components to steer the grating-forming and probe beams into a static cell containing I_2 vapour, a photomultiplier tube (PMT) connected to data acquisition electronics and wavelength calibration equipment.

The second harmonic output of an etalon narrowed Nd:YAG laser (Quanta-Ray DCR-2) at 532.05 nm (18790 cm^{-1}) is used for two purposes. Firstly, a portion of the 532 nm beam is split off and irised to *ca.* 1 mm spot size. This beam is then further split in the ratio 60 : 40, by means of a coated beamsplitter, to produce the two grating-forming beams which are both temporally and spatially overlapped at a crossing angle of ~3° in the centre of an evacuated glass cell (windows mounted at Brewster's angle) containing iodine vapour at a pressure of ~ 308 mTorr [33]. Secondly, the remainder of the 532 nm output is employed to pump a tuneable dye laser (Quanta-Ray PDL-2, operating with Rhodamine 6G), the output of which is used as the probe beam. The probe is firstly passed through a spatial filter (incorporating a 100 μm diamond pinhole (Fort Wayne Wire-Die)) and a 6 ns optical delay before being overlapped with the grating beams. The probe beam is overlapped at an angle determined by the phase-matching requirement (discussed in section 6.3.1),

$$\frac{\sin\theta_g}{\sin\theta_p} = \frac{\lambda_g}{\lambda_p} \tag{6.4}$$

where θ_g and θ_p are the grating and probe crossing half-angles, respectively, and λ_g and λ_p are the corresponding wavelengths. The signal detection axis was aligned by placing a thin cuvette containing a dilute solution of iodine in cyclohexane in the interaction region and observing the visible signal beam that emerges. This beam was then traced along, via a number of apertures, a band pass filter to eliminate scattered light from the 532 nm beams, and a polariser to discriminate against LIF and scattered light from the probe beam before reaching a photomultiplier detector (EMI 9924QB) placed 2-3 metres from the interaction region. The output from the PMT was preamplified and passed via a linear gate (Stanford Research SR 250) and a V-F converter to a PC for data collection

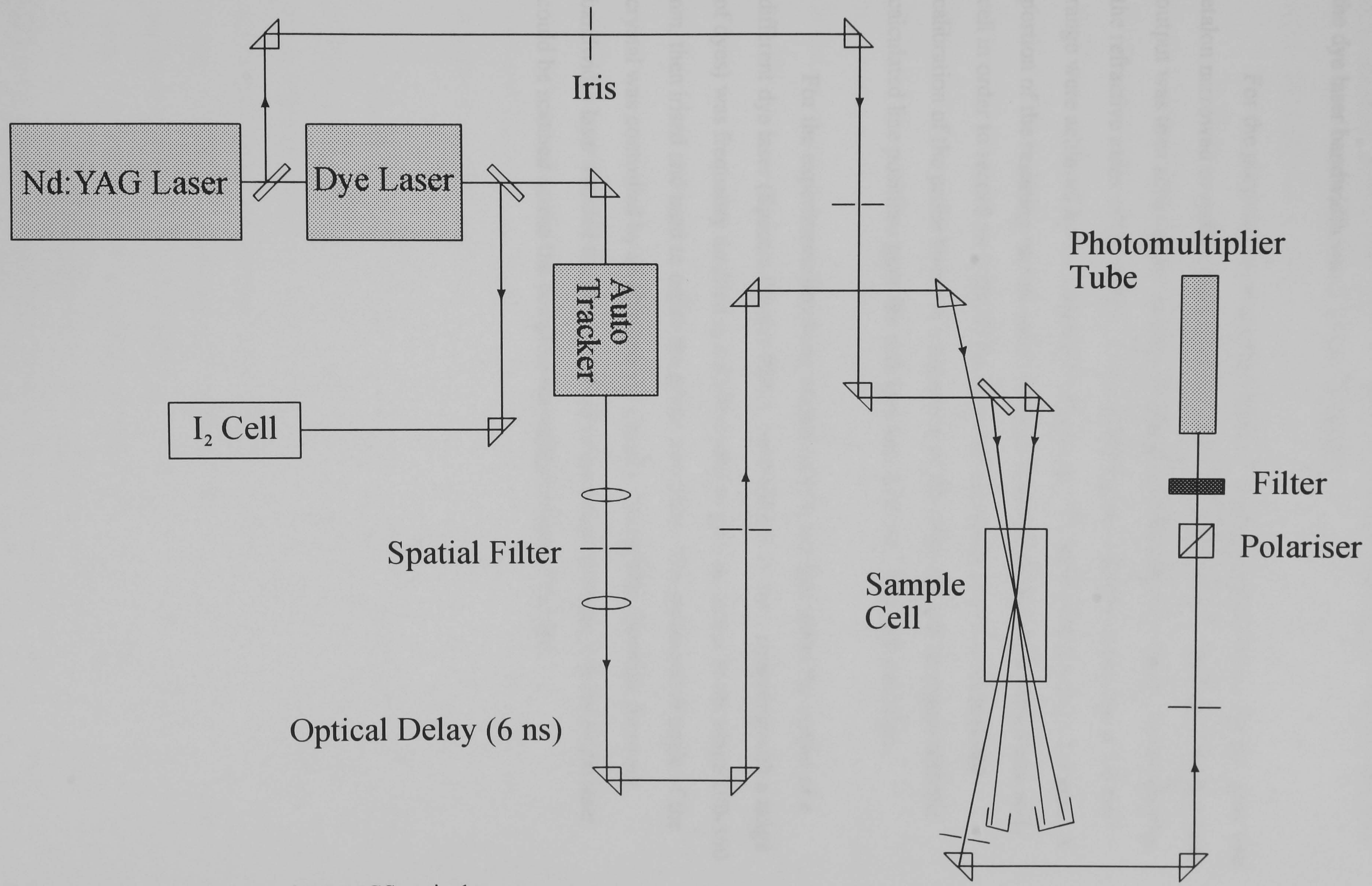

Figure 6.4. Schematic layout of TC-LIGS optical arrangement

and subsequent processing. Pulse energies were of the order of 5-10 μJ per beam and the dye laser bandwidth was 0.25 cm^{-1} FWHM.

For the purposes of obtaining calibrated high resolution spectra the dye laser was etalon narrowed to reduce the emission bandwidth to 0.05 cm^{-1}. Tuning of the dye laser output was then achieved by varying the pressure inside the laser cavity, hence varying the refractive index of the cavity. In the following experiments scans over a 7-8 cm^{-1} range were achieved by the addition of argon gas from approximately 0.2 - 1.0 atm. A portion of the resulting narrow bandwidth dye laser output was then passed into an I_2 cell in order to record an I_2 (B-X) fluorescence excitation spectrum to facilitate calibration of the probe laser. A comparison of the observed LIF spectrum with the calculated line positions gave fits with less than 0.02 cm^{-1} standard deviation.

For the experiments involving excitation of I_2 ion-pair states the output of a different dye laser (Spectra Physics PDL3, bandwidth 0.07 cm^{-1}, operating with a range of dyes) was frequency doubled in a KDP crystal to give an output in the range 290-360 nm, then irised and used to excite the probe transition. The phase-match angle of the crystal was controlled by an auto-tracker (Inrad). Using this inherently narrower bandwidth laser avoided the need for short range etalon scanning and the probe laser could be scanned across the complete wavelength range of the dye.

6.3 Results and Discussion

6.3.1 TC-LIGS of the I_2 B-X transition

In Figure 6.5 a portion of the two-colour LIGS spectrum of I_2 is shown in the range 17640-17990 cm^{-1}. Only 41 lines are discernible in this spectrum, which is an illustration of the considerable spectral simplification afforded by the TC-LIGS technique. In a conventional room-temperature I_2 absorption spectrum across the same wavenumber range some 1800 lines are observed [34]. In addition to the desired SEP-like transitions, some 'upward' (absorption like) transitions from the ground state levels depleted by the grating beams to various rovibronic levels of the B state are also present in the spectrum shown in Figure 6.5. These upward transitions are due to diffraction of the probe beam from the depleted ground state population grating, and proved invaluable in the assignment of the excited states populated following excitation at 532 nm. Identification of the upward transitions was facilitated by a separate set of experiments in which portions of the TC-LIGS spectrum shown in Figure 6.5 were recorded simultaneously with I_2 LIF spectra. Upward transitions are easily recognised since they appear in tandem with the equivalent absorption lines in the LIF spectrum. Additionally, the LIF spectra provide a calibration of the TC-LIGS spectra. As mentioned in the previous section an inter-cavity etalon was used to narrow the dye laser bandwidth to 0.05 cm^{-1} for these experiments, sufficient to resolve much of the dense rotational structure in the LIF spectra.

Figure 6.6 shows the high resolution TC-LIGS spectrum in the region 17710-17745 cm^{-1}. Assignment of the upward transitions revealed the involvement of three lower states in the depleted ground state grating, namely the v"=0, J"=52, 55, and 85 rovibronic levels. The grating beams primarily excite the I_2 B-X (33,0) R(85), and (32,0) P(52), R(55) transitions as illustrated in Figure 6.7, indicating the YAG second harmonic wavelength is 532.051(3) nm. The frequencies of these transitions span a range of 0.17 cm^{-1}, which is commensurate with the 0.2 cm^{-1} etalon narrowed bandwidth of the YAG second harmonic beam. Thus the three rovibronic levels populated by the 532 nm grating beams are v'=33, J'=86, and v'=32, J'=51, 56. In Figure 6.5 SEP-like transitions are observed from these levels to the v"=4 and 5 vibrational levels of the

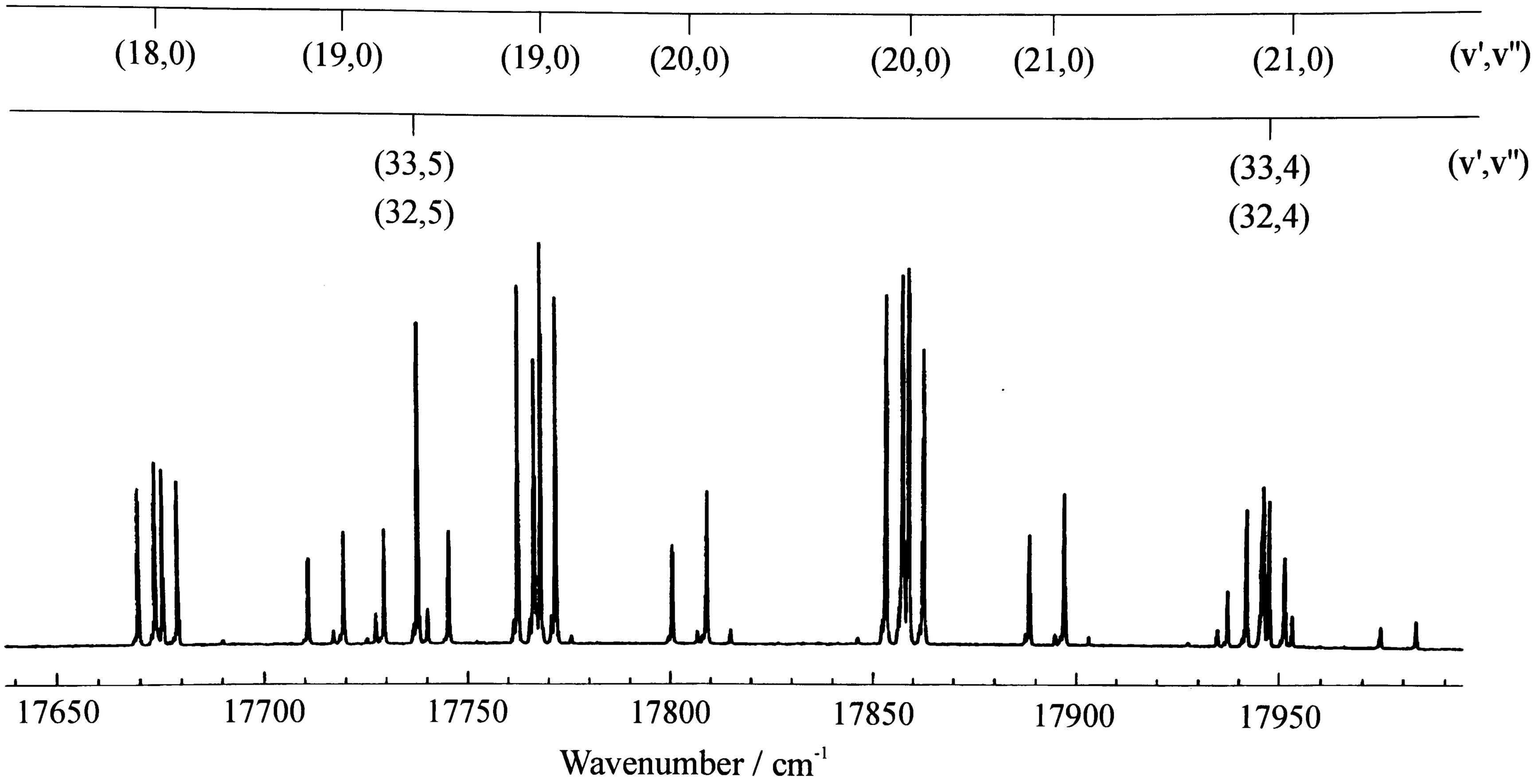

Figure 6.5. Two colour LIGS spectrum of I_2, recorded by tuning the probe laser wavenumber in the range 17640 - 17990 cm^{-1}. Two types of transition are observed: (a) absorption-like ('upward') transitions produced by diffraction of the probe beam from the grating formed via depletion of selected ground state rovibronic levels by the 532 nm beams; (b) SEP like transitions produced by diffraction from the excited state grating. The approximate positions of vibronic transitions of type (a) and (b) are indicated by the upper and lower combs respectively.

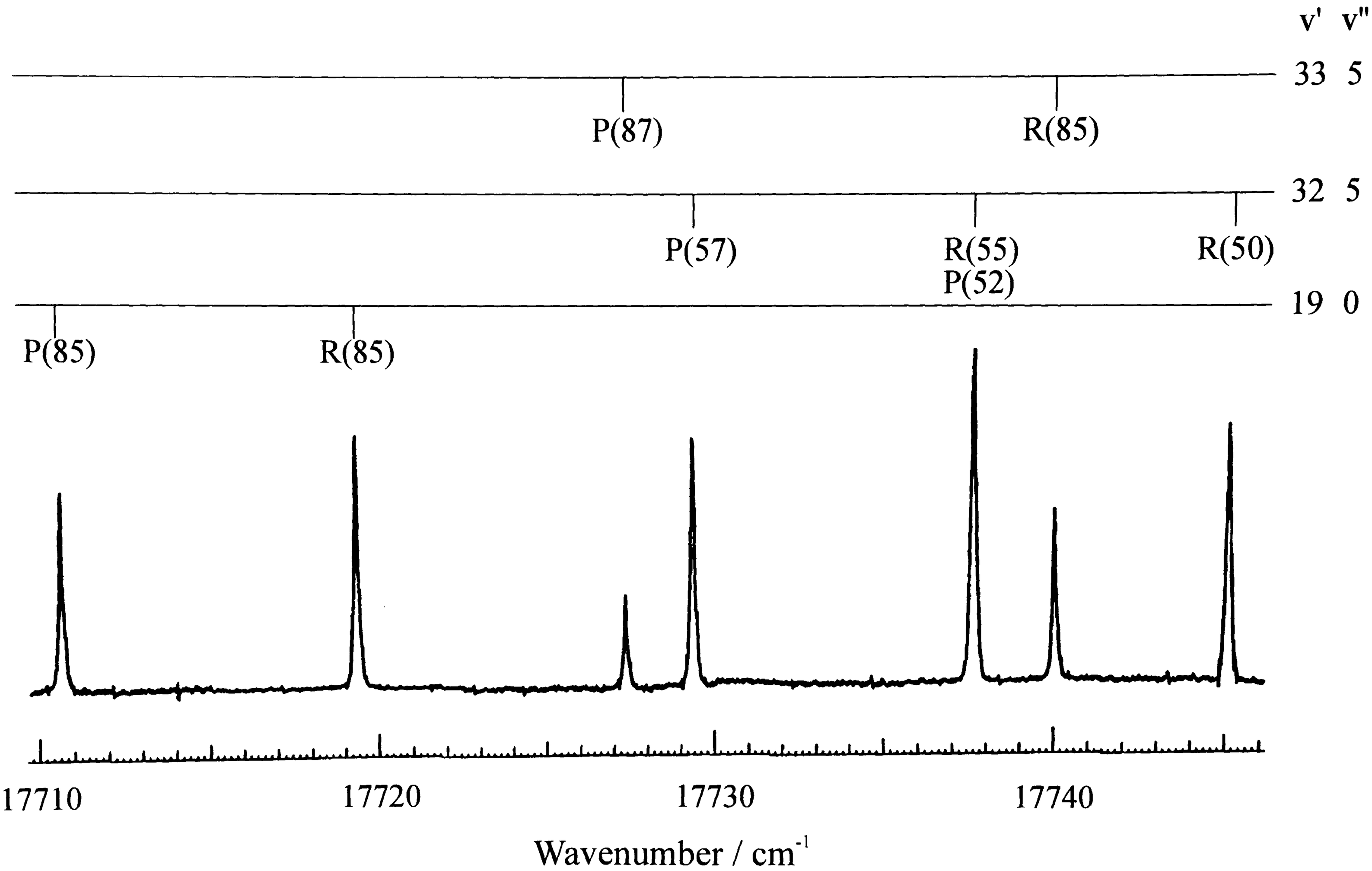

Figure 6.6. High resolution two-colour LIGS spectrum of I_2 (B-X) in the range 17710 - 17746 cm^{-1}. The spectrum is a composite of seven separate scans, each of ~ 5 cm^{-1}.

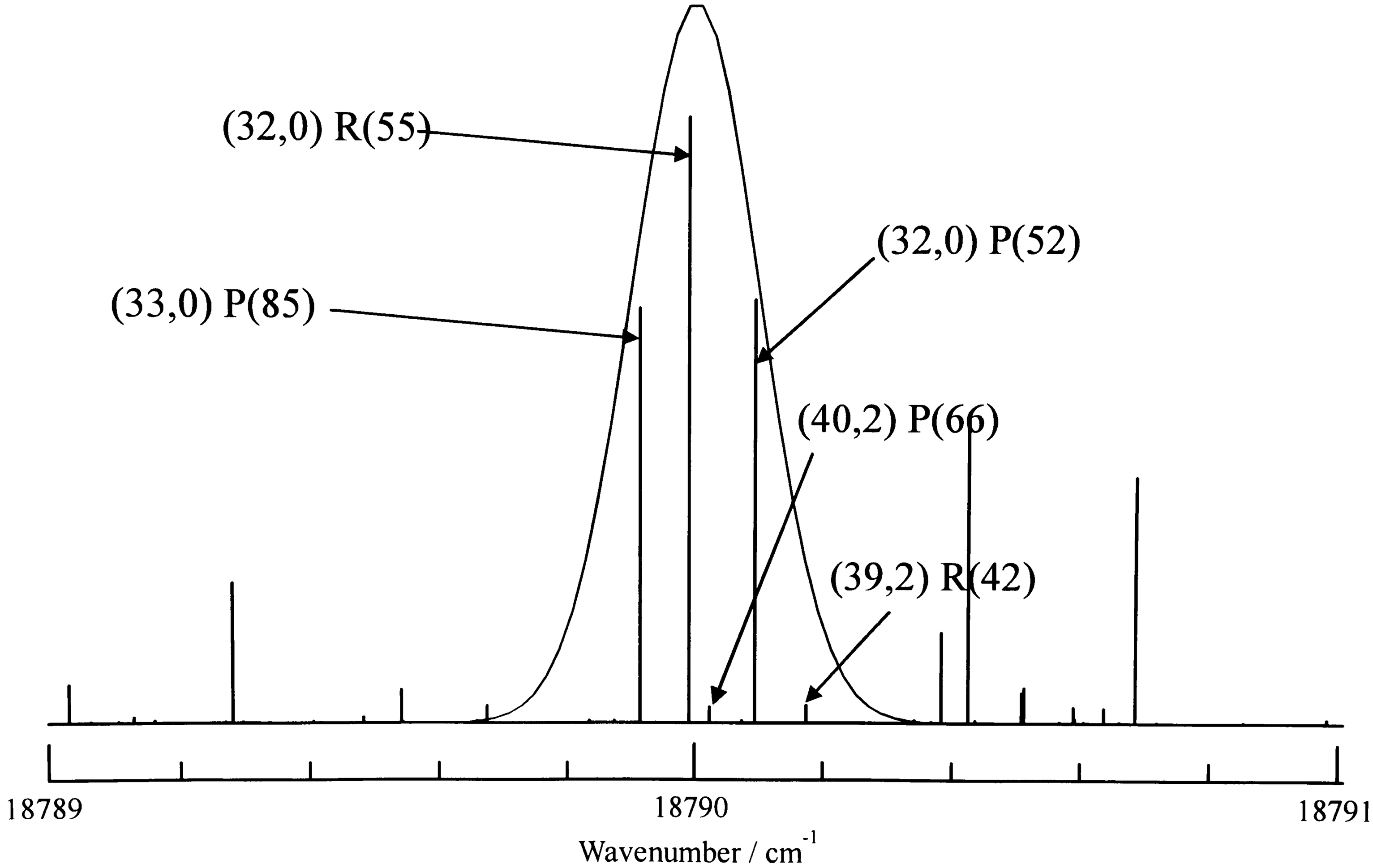

Figure 6.7. Calculated stick spectrum indicating the rovibronic transitions contributing to the room temperature I_2 (B-X) spectrum in the region of 532.05 nm (18790 cm^{-1}) excited by a 0.2 cm^{-1} FWHM laser pulse. Individual lines are labelled (v',v") $\Delta J(J")$.

electronic ground state of I_2. The signal to noise ratio of the TC-LIGS spectrum in Figure 6.6 is around 1000:1. Buntine *et al.* have also reported SEP-like TC-LIGS spectra of I_2 [35], but the signal to noise ratio in their spectrum is barely 50:1, which is not significantly better than that achieved in many conventional SEP experiments.

A potential restriction with the TC-LIGS experiment is the phase matching condition [2,5] given in equation 6.4. Viewed from the perspective of a laser-induced grating, an equivalent statement of this requirement is that, for optimum diffraction efficiency, the probe wavelength must satisfy the Bragg condition for diffraction from the grating. Buntine *et al.* [35] report that the use of a lens to overlap the beams relaxes the phase-matching condition, which leads to the expectation that one can detune the probe wavelength some way from its optimum, phase-matched value and still observe diffracted signal. We have recorded spectra with and without a lens in order to test the practicality of such an approach. We find that the use of a 50 cm focal length lens results in only a slightly larger TC-LIGS bandwidth: with unfocused beams signal is observable over a range of 550 cm^{-1}, whilst focusing with a 50 cm^{-1} focal length lens increases this bandwidth to 710 cm^{-1}. However, the magnitude of the signal is roughly 16 times greater with unfocused beams than with focused, an effect that can be traced back to the quadratic dependence of the LIGS signal on the interaction path length [1]. The use of unfocused beams would appear to be the preferable arrangement. Butenhoff and Rohlfing [5] have considered the restrictions imposed by the phase-matching condition in some detail, and have derived an expression for the FWHM bandwidth (in cm^{-1}) over which the TC-LIGS signal may be obtained in the case where the grating beam wavelength is tuned. This expression (equation 7 in ref. [5]) is,

$$\Delta\bar{\nu} \approx \frac{0.443}{\eta_p L}\left(\frac{\lambda_g}{\lambda_p}\right)^2 \frac{1}{\sin^2\theta_g} \tag{6.5}$$

where λ_g and λ_p are the wavelengths of the grating and probe beams respectively, η_p is the refractive index of the medium at λ_p, θ_g is the crossing half angle of the grating beams and L is the interaction length in cm (estimated as 2 cm in our experiment). The FWHM predicted by this equation for our experimental arrangement is 220 cm^{-1}. The complete tuning range of approximately 550 cm^{-1} measured here compares favourably

with this prediction.

6.3.2 Detection of the E and f ion-pair states of I_2

Figure 6.8 shows a portion of the TC-LIGS spectrum involving levels of both the E 0_g^+ ($^3P_2$) and f 0_g^+ ($^3P_0$) ion-pair states of I_2. The linewidth of the grating forming laser is such that we are not truly state specific in the grating forming transition as discussed in the previous section. This increases the spectral complexity, but not to the extent of causing any ambiguity in interpretation. As a result we see E ← B and f ← B features originating from B state levels with v=32, J=51 and J=56, v=33, J=84, v=39, J=43 and v=40, J=65.

Valence to ion-pair state transitions in I_2 involve significant charge transfer along the internuclear axis, and hold with the $\Delta\Omega=0$ propensity rule (Hund's case (c)) expected for such a parallel transition. As a consequence, our TC-LIGS spectra are dominated by progressions of P- and R-doublets. This may be seen more clearly in Figure 6.9, which shows a portion of the survey spectrum of Figure 6.8 with much expanded frequency resolution. Analysis of this spectrum is comparatively straightforward given accurate knowledge of the X [36] and B state [37] term values, and the available vibrational Dunham parameters of Wilson *et al.*[27] and rotational parameters of Brand *et al.* [25] and Ishiwata *et al.* [26] for the E and f states, respectively. The dominance of the f-B features serves to highlight the very different strengths of the f-B and E-B transition moments in this frequency range. In passing, it is of interest to highlight the way in which the f-B and E-B transition probabilities vary with vibrational quantum number (Figure 6.8). This marked oscillation is a well documented feature of such ion-pair ← valence excitations in the halogen molecules, and is a natural consequence of the Franck-Condon principle when applied to transitions involving highly excited vibrational levels and substantial changes in equilibrium bond length. Note also the TC-LIGS technique greatly emphasises this feature, because the intensity of each spectral line is proportional to some power (varying between 8 and 2 depending upon the intensity of the laser beams forming the grating) of the one photon transition probability as discussed in section 6.1.

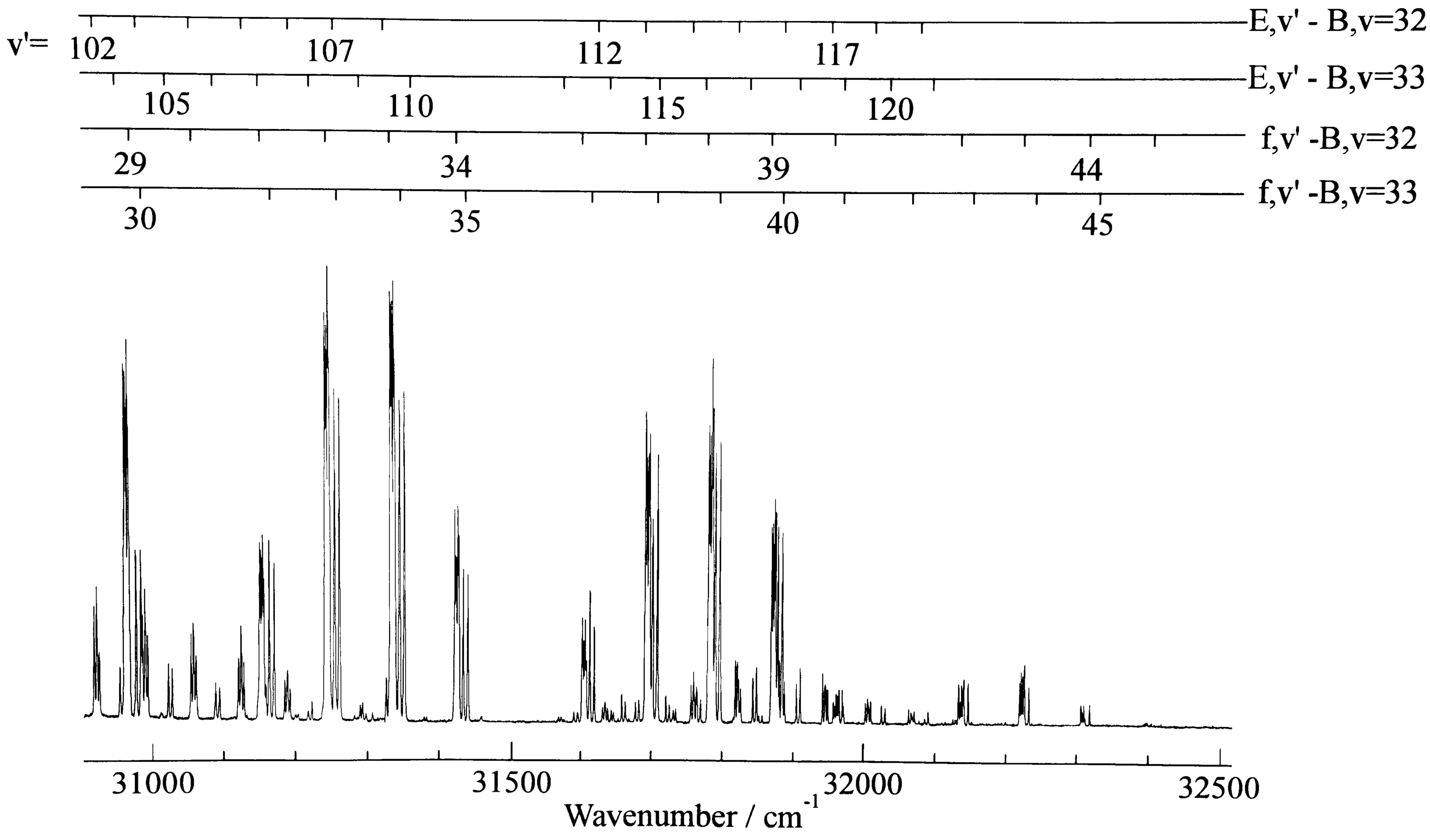

Figure 6.8. Long range two colour LIGS spectrum of the E and f ion-pair I_2 states obtained by tuning the probe laser wavenumber over the range 30900 - 32500 cm^{-1}, whilst the grating forming laser is held fixed at 18790 cm^{-1} (532.05 nm). Vibronic assignments are indicated by the combs superimposed above the spectrum.

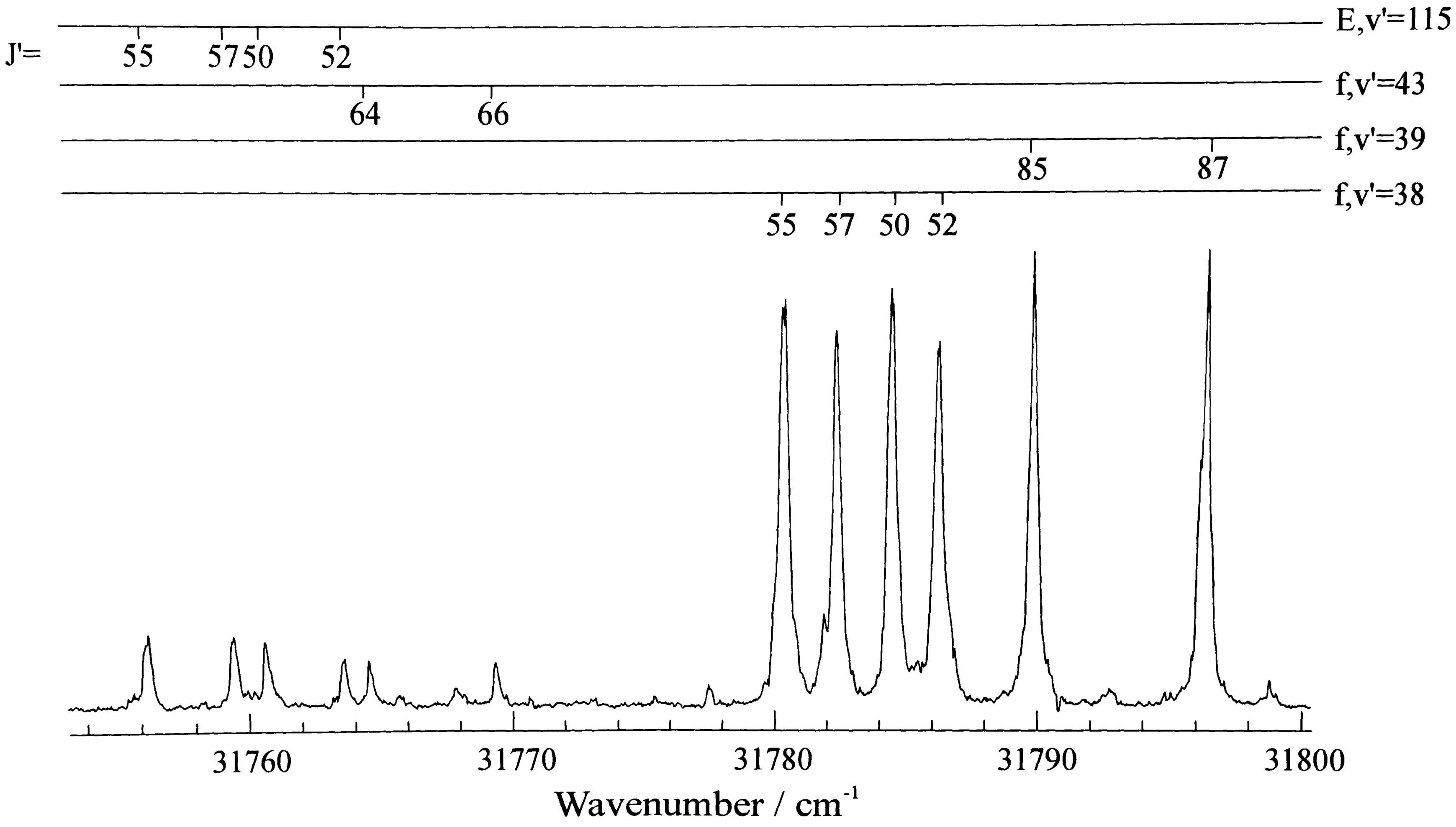

Figure 6.9. Detail of the TC-LIGS spectrum shown in Figure 6.8, plotted on a greatly expanded wavenumber scale. The combs superimposed above indicate the vibrational (v') and rotational (J') levels of the ion-pair states involved in this region of the double resonance spectrum.

Detailed analysis of the high-resolution TC-LIGS spectra such as that shown in Figure 6.9 yields f state term values in reasonable agreement with those derived using the available literature parameters [26] (maximum deviation $\Delta E(obs.-calc.) = -0.6\ cm^{-1}$); this, however, is still somewhat large given the narrow (~0.1 cm^{-1}) bandwidth of the frequency doubled probe dye laser. The situation regarding the E state is far worse: the rovibrational term values determined herein show large deviations from the values predicted, by extrapolation, using the vibrational data of Donovan and coworkers [27] and the rotational Dunham parameters of Brand and Hoy [25]. This is illustrated in Figure 6.10, which shows the vibrational dependence of this discrepancy for two different levels of rotational excitation within the E state (J'=50 and 87). The striking similarity between these two data sets strongly suggests that the error is in the vibrational part of the Dunham expansion, as might be expected since the reported parameters [28] were derived from fitting data involving vibrational levels with $v' \geq 123$ only.

These experiments involved much shorter probe wavelengths than in the two colour LIGS study of high vibrational levels of the ground state of I_2 outlined in the previous section. Equation 6.5 would predict substantially relaxed phase matching constraints for the present combination of pump and probe wavelengths ($\Delta\nu$ ~750 cm^{-1} (FWHM) at $\lambda_p = 320nm$) - a prediction fully borne out by the fact that we are able to tune over the complete frequency-doubled DCM dye range (~2000 cm^{-1}) without the need to readjust the phase-matching of the beams.

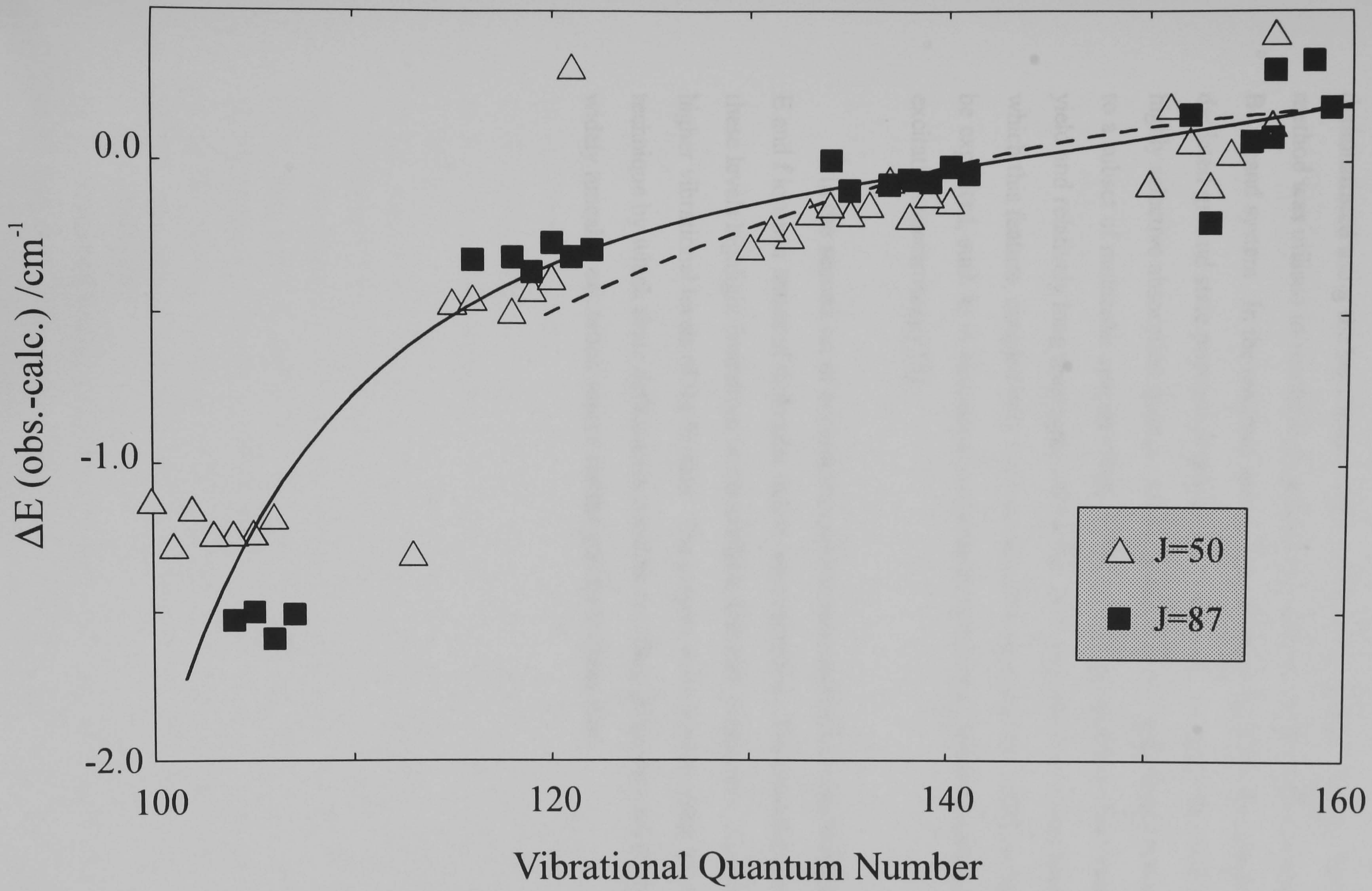

Figure 6.10. Plot showing the way in which ΔE(obs-calc), the difference between the observed and calculated [25,27] values for two different J' levels of the E state of I_2, varies with vibrational quantum number. The full line is to guide the eye through the TC-LIGS data points, whilst the dashed lines represents data from Wilson et al. [27].

6.4 Conclusions

The technique of two-colour laser induced grating spectroscopy has been demonstrated using the benchmark system of molecular iodine. Firstly, the TC-LIGS method was utilised to record high resolution, background free SEP-like spectra of the B-X band system. In the resultant spectra upward transitions are also observed from the depleted ground state population grating demonstrating the ability of LIGS to record highly selective absorption spectra. Unlike SEP, the LIGS experiment is not restricted to a subset of molecular species which fluoresce with suitably large fluorescent quantum yield and relatively long fluorescence lifetime. It is possible to conceive many ways in which this feature, coupled with the state selective nature of the LIGS technique could be exploited, such as in vibrational overtone spectroscopy [38] and photofragment excitation spectroscopy [5].

In the second set of experiments double-resonance-like excitation spectra of the E and f ion-pair states of molecular iodine were recorded. The deduced term values of these levels highlight limitations in the available Dunham parameters, especially for the higher vibrational levels of the E state. The present work indicates that TC-LIGS is one technique by which these deficiencies could be rectified, given the availability of a more widely tuneable excitation source for the grating forming step.

References

1. R.L. Abrams, J.F. Lam, R.L. Lind, D.G. Steel, P.F. Liao, Phase Conjugation and High Resolution Spectroscopy by DFWM, in *Optical Phase Conjugation*, ed. by R.L.Fischer (Academic, New York 1983), chapter 8 and references therin.
2. H.J. Eichler, P. Günter, D.W. Pohl, *Laser Induced Dynamic Gratings*, (Springer-Verlag, Berlin 1986).
3. R.L. Farrow and D.J. Rakestraw, *Science*, **257** (1992) 1894 and references therein.
4. P. DeRose, H.L. Dai, and P.Y. Cheng, *Chem. Phys. Letts.*, **220** (1994) 207.
5. T.J. Butenhoff and E.A. Rohlfing, *J. Chem. Phys.*, **98** (1993) 5460.
6. S. Williams, J.D. Tobiason, J.R. Dunlop, and E.A. Rohlfing, *J. Chem. Phys.*, **102** (1995) 8342.
7. T. Dreier and D.J. Rakestraw, *Opt. Letters*, **15** (1990) 72.
8. D.S. Green, T.G. Owano, S. Williams, D.G. Goodwin, R.N. Zare, and C.H. Kruger, *Science*, **259** (1993) 1726.
9. G.C. Herring, W.L. Roberts, M.S. Brown, and P.A. Debarber, *Applied Optics*, **35** (1996) 6544.
10. T.J. Butenhoff and E.A. Rohlfing, *J. Chem. Phys.*, **98** (1993) 5469.
11. T.A.W. Wasserman, A.A. Arias, T. Muller, and P.H. Vaccaro, *Chem. Phys. Letts.*, **262** (1996) 329.
12. P.A. Vaccaro, *Nonlinear Spectroscopy for Molecular Structure Determination*, ed. by E. Hirota, R.W. Field, J.P. Maier, and S. Tsuchiya (IUPAC, 1997), chapter 4.
13. R.L. Farrow, D.J. Rakestraw, and T. Dreier, *J. Opt. Soc. Am. B.*, **9** (1992) 1770.
14. E.J. Friedman-Hill, L.A. Rahn, and R.L. Farrow, *J. Chem. Phys.*, **100** (1994) 4065.
15. S. Williams and R.N.Zare, *J. Chem. Phys.*, **101** (1994) 1072; 1093.
16. S. Williams, E.A. Rohlfing, L.A. Rahn, and R.N.Zare, *J. Chem. Phys.*, **106** (1997) 3090.
17. R.L. Vander Wal, B.E. Holmes, J.B. Jefferies, P.M. Danehy, R.L. Farrow, and D.J. Rakestraw, *Chem. Phys. Letts.*, **191** (1992) 251.
18. G.J. Germann, R.L. Farrow, and D.J. Rakestraw, *J. Opt. Soc. Am. B.*, **12** (1995) 25.
19. Y. Tang and S.A. Reid, *Chem. Phys. Letts.*, **248** (1996) 476.
20. M. Motzkus, S. Pederson, and A.H. Zewail, *J. Phys. Chem.*, **100** (1996) 5620.
21. G. Hall and B.J. Whitaker, *J. Chem. Soc. Faraday Trans.*, **90** (1994) 1.
22. E.F. McCormack, S.T. Pratt, P.M. Dehmer and J.L. Dehmer, *Chem. Phys. Letts.*, **211** (1993) 147.
23. T.J. Butenhoff and E.A. Rohlfing, *J. Chem. Phys.*, **97** (1992) 1595.
24. G. Hall, A.G. Suits, and B.J. Whitaker, *Chem. Phys. Letts.*, **203** (1993) 277.

25. J.C.D. Brand, A.R. Hoy, A.K. Kalkar, and A.B. Yamashita, *J. Mol. Spect.*, **95** (1982) 350.
26. T. Ishiwata, J. Yamada, and K. Obi, *J. Mol. Spect.*, **158** (1993) 237.
27. P.J. Wilson, T. Ridley, K.P. Lawley, and R.J. Donovan, *Chem. Phys.*, **182** (1994) 325.
28. K.P. Lawley and R.J. Donovan, *J. Chem. Soc. Faraday Trans.*, **89** (1993) 1885.
29. M.J. Cooper and C.M. Western, *Chem. Phys. Letts.*, **267** (1997) 365.
30. M.J. Cooper, T. Diez-Rojo, L.J. Rogers, C.M. Western, M.N.R. Ashfold, and J.W. Hudgens, *Chem. Phys. Letts.*, **272** (1997) 232.
31. R.S. Mulliken, *J. Chem. Phys.*, **55** (1971) 288.
32. M.D. Danyluck and G.W. King, *Chem. Phys.*, **22** (1977) 59.
33. M.W. Chase *et al.*, *JANAF Thermochemical Tables*, 3rd ed., *J. Phys. Chem. Ref. Data*, **14** (1985) 1359.
34. S. Gerstenkorn and P. Luc, *Atlas du spectre d'absorption de la molecule d'iode* (CNRS, Paris, 1978)
35. M.A Buntine, D.W. Chandler, and C.C. Hayden, *J. Chem. Phys.*, **97** (1992) 707.
36. R.F. Barrow and K.K.Yee, *J. Chem. Soc. Faraday Trans. 2*, **69** (1973) 684.
37. P. Luc, *J. Mol. Spect.*, **80** (1980) 41.
38. M.A Buntine, D.W. Chandler, and C.C. Hayden, *J. Chem. Phys.*, **102** (1995) 2718.

7. General Conclusions and Future Work

Cavity ring-down spectroscopy has been shown to be a highly sensitive and versatile technique for the study of molecular electronic spectra and excited state predissociation dynamics. The work presented in Chapters 3 and 4 on the predissociation of $SH(A^2\Sigma^+)$, $SD(A^2\Sigma^+)$, and $S_2(B^3\Sigma_u^-)$ exemplifies the relatively simple extraction of quantitative dynamical information, such as linewidths, from CRD spectra. The availability of relatively inexpensive high reflectivity mirrors extending from the infra-red [1] to the deep ultra violet [2] is rapidly increasing the diversity of species and transitions that may be probed. Other recent developments using cw lasers demonstrate the potential of CRDS to high resolution spectroscopy limited only by the width of the cavity longitudinal modes [3,4]. At the other extreme CRDS applications with broadband laser sources (such as free electron lasers [5,6]) are also under development using a monochromator to disperse the light exiting the cavity before detection on a time and position sensitive CCD array; such methods should in principle be capable of obtaining a complete spectrum in one laser shot. However, CRDS does have some obvious limitations, such as: The method samples a column, rather than a point, which may prove restrictive when attempting spatial profiling in a very inhomogeneous environment. The only degree of selectivity open to the user is the excitation frequency; thus all absorbing species placed between the mirrors will contribute to the observed ring-down time.

Laser-induced grating spectroscopy, on the other hand, has proved somewhat less popular as time has gone on. In many ways LIGS techniques are very complementary to CRDS. LIGS can be used in a very selective manner (especially the two-colour variants) and provides high spatial resolution which are essential for many diagnostic applications involving localised temperature measurements. However, the quadratic intensity dependence of the signal on the number density and the varying dependence on transition dipole moment according to the pump field intensity make quantitative interpretation of spectral lineshapes and intensities very complex. Moreover, these dependencies can make the probing of trace species or weak

transitions inherently difficult; a problem exemplified in attempts to probe the $\tilde{A}\,^1A''$-$\tilde{X}\,^1A'$ transition of HNO by LIGS in our lab.

Bearing in mind the above discussion and the work presented in this thesis the future for both CRDS and TC-LIGS looks very promising indeed. Both techniques offer a whole host of new spectroscopic and diagnostic applications with, in all probability, many more, as yet unthought of, to come.

References

1. J.J. Scherer, K.W. Aniolek, N.P. Cernansky, and D.J. Rakestraw, *J. Chem. Phys.*, **107** (1997) 6196.
2. P. Zalicki, Y. Ma, R.N. Zare, E.H. Wahl, J.R. Dadamio, T.G. Owano and C.H. Kruger, *Chem. Phys. Lett.*, **234** (1995) 269.
3. D. Romanini, A.A. Kachanov, and F. Stoeckel, *Chem. Phys. Letts.*, **270** (1997) 538.
4. D. Romanini, A.A. Kachanov, and F. Stoeckel, *Chem. Phys. Letts.*, **270** (1997) 546.
5. R. Englen and G. Meijer, *Rev. Sci. Instrumen.*, **67** (1996) 2708.
6. R. Engeln, E. van den Berg, G. Meijer, L. Lin, G.M.H. Knippels, and A.F.G. van der Meer, *Chem. Phys. Lett.*, **269** (1997) 293.

Appendix 1

(a). S_2 potential energy curves derived from the *ab initio* calculations described in chapter 4.4.1. All potentials are referenced from the $X^3\Sigma_g^-$ state potential minimum - defined as the zero of energy.

R / Å	Energy / cm^{-1}				
	$X^3\Sigma_g^-$	$A'^3\Delta_u$	$B^3\Sigma_u^-$	$1^1\Pi_u$	$B''^3\Pi_u$
1.69334	7564.10	47011.1	56641.5	56520.5	52818.1
1.79918	1486.58	33889.3	44490.4	47408.8	43243.8
1.90501	0.0	26402.4	37527.9	41829.5	37423.8
2.01085	1249.64	22605.5	33887.8	38481.2	34011.5
2.11668	4048.02	21204.3	32363.2	36592.9	32196.9
2.32835	11535.3	22372.9	32803.4	35315.3	31431.9
2.45006	16005.9	24188.3	34094.3	35286.7	31932.1
2.54002	19137.7	25706.6	35235.6	35345.2	32485.5
2.65114	22677.9	27584.4	36697.3	35389.0	33209.2
2.75168	25495.3	29162.2	37973.4	35356.2	33771.6
2.85223	27897.8	30537.4	39121.2	35278.9	34192.6
2.96335	30037.8	31775.5	40209.8	35159.5	34471.1
3.04802	31302.0	32516.6	40903.5	35062.6	34581.3
3.17502	32657.2	33337.5	41735.3	34928.4	34650.3
3.38669	33875.6	34142.4	42670.3	34763.6	34673.2
3.70419	34573.8	34669.4	43416.8	34649.0	34711.0
4.12753	34880.9	34921.7	43864.6	34631.7	34812.7
4.33919	34949.6	34978.6	43984.7	34644.3	34864.5
4.65670	35009.0	35028.4	44100.9	34668.4	34930.6
4.97420	35040.4	35056.8	44172.4	34691.3	34981.5
5.29170	35057.6	35060.1	44198.5	34699.4	35009.3

R / Å	Energy / cm^{-1}				
	$c^1\Sigma_u^-$	$A^3\Sigma_u^+$	$2^3\Sigma_u^+$	$1^5\Sigma_u^-$	$1^5\Pi_u$
1.69334	45130.5	47995.0	94237.9	83715.8	127638
1.79918	32171.1	34740.9	80910.4	70638.3	104642
1.90501	24815.5	27134.2	71391.9	61538.9	87111.9
2.01085	21119.7	23229.1	64362.7	55053.0	73850.3
2.11668	19790.6	21730.8	59029.3	50342.5	63848.7
2.32835	21018.1	22735.2	51664.4	44248.4	50731.0
2.45006	22820.1	24473.1	48794.9	41982.6	46041.9
2.54002	24310.9	25941.0	47151.3	40676.8	43487.1
2.65114	26144.7	27763.8	45598.4	39388.0	41126.8
2.75168	27686.5	29305.7	43510.1	38464.7	39553.7
2.85223	29051.2	30642.4	41524.7	37735.9	38399.6
2.96335	30323.2	31840.2	39833.5	37111.0	37476.2
3.04802	31126.2	32551.8	38830.0	36740.1	36959.4
3.17502	32086.1	33332.0	37685.0	36320.6	36406.0
3.38669	33165.1	34083.1	36464.2	35889.7	35878.0
3.70419	34009.9	34561.3	35575.6	35613.9	35573.9
4.12753	34459.3	34789.5	35166.7	35535.9	35507.4
4.33919	34559.1	34843.1	35092.6	35538.6	35517.2
4.65670	34642.2	34891.8	35041.3	35555.4	35541.9
4.97420	34686.1	34921.8	35021.2	35574.4	35566.1
5.29170	34698.4	34931.8	34999.4	35576.2	35576.7

(b). S_2 $B^3\Sigma_u^-$ state RKR turning points derived from procedure outlined in chapter 4.4.1.

R / Å	E / cm^{-1}	R / Å	E / cm^{-1}	R / Å	E / cm^{-1}
1.864	7284.99	1.867	6951.29	2.409	1905.54
1.866	7118.84	1.871	6612.07	2.441	2313.83
1.869	6782.37	1.876	6267.32	2.472	2716.60
1.873	6440.38	1.881	5917.04	2.501	3113.85
1.878	6092.87	1.886	5561.24	2.530	3505.56
1.883	5739.83	1.892	5199.91	2.559	3891.75
1.889	5381.27	1.899	4833.06	2.586	4272.42
1.895	5017.17	1.907	4460.68	2.615	4647.56
1.902	4647.56	1.915	4082.78	2.642	5017.18
1.911	4272.42	1.924	3699.35	2.670	5381.27
1.919	3891.76	1.934	3310.39	2.697	5739.83
1.929	3505.56	1.946	2915.91	2.725	6092.87
1.940	3113.84	1.959	2515.90	2.753	6440.38
1.952	2716.60	1.974	2110.38	2.781	6782.37
1.966	2313.83	1.991	1699.32	2.810	7118.84
1.982	1905.53	2.011	1282.74	2.393	1699.32
2.000	1491.72	2.036	860.63	2.426	2110.38
2.022	1072.37	2.045	732.92	2.457	2515.91
2.039	818.11	2.058	561.87	2.487	2915.91
2.051	647.50	2.075	389.93	2.516	3310.39
2.066	476.01	2.096	217.11	2.545	3699.35
2.084	303.63	2.132	43.40	2.573	4082.78
2.110	130.36	2.194	43.40	2.601	4460.68
2.162	0.00	2.235	217.11	2.628	4833.06
2.218	130.36	2.262	389.93	2.656	5199.91
2.250	303.63	2.284	561.87	2.684	5561.24
2.274	476.01	2.304	732.92	2.711	5917.04
2.294	647.50	2.317	860.63	2.739	6267.32
2.313	818.11	2.357	1282.74	2.767	6612.07
2.337	1072.37	2.375	1491.72	2.796	6951.29